Title

Self-assembly and interdomain dynamics of natural and designed inflammasome adaptor isoforms of ASC: Implications for inflammasome regulation.

Author

Diaz-parga, Pedro

Publication Date

2022

Peer reviewed|Thesis/dissertation

University of California, Merced

Self-assembly and interdomain dynamics of natural and designed inflammasome adaptor isoforms of ASC: Implications for inflammasome regulation.

A dissertation submitted in partial satisfaction of the requirements for the degree

Doctor of Philosophy

In

Quantitative and Systems Biology

by

Pedro Diaz-parga

Committee in charge:

Professor Michael Colvin, Chair

Professor Eva de Alba

Professor Arvind Gopinath

Professor Krish Krishnan

Copyright

The Dissertation of Pedro Diaz-parga is approved, and it is acceptable in quality and form for publication on microfilm and electronically:

Eva de Alba

Arvind Gopinath

Krish Krishnan

Michael Colvin, Chair

University of California, Merced 2022

Table of Contents

Lists of figures:

List of Abbreviations:

Aβ – Amyloid beta

AD – Alzheimer's disease

APAF-1 – Apoptosis protease-activating factor 1

AIM2 – Absent in Melanoma 2 receptor

ALR – Absent in melanoma 2-like receptor

ALS – Amyotrophic lateral sclerosis

ARC - Apoptosis repressor with caspase recruiting domain

ASC – Apoptosis-associated speck-like protein containing a CARD

Bbox - zinc finger domain

BIR - Baculovirus inhibitor of apoptosis protein repeat

CARD – Caspase activation and recruitment domain

CARMA1 - CARD-containing MAGUK protein 1

CAPS – Cryopyrin-associated periodic syndromes

CC – Coiled coil domain

CD – Crohn's disease

CDL – CARD domain linker

CLR – C-type lectin receptor

COP – CARD-only protein

CRYO-EM – Cryo-electron microscopy

CSA – Chemical shift anisotropy

DAMPS – damage-associated molecular patterns

DD – Death domain

DED – Death effector domain

DLS – Dynamic light scattering

DNA - Deoxyribonucleic acid

dsDNA – double stranded DNA

FEG – Field-emission gun

FCAS – Familial cold autoinflammatory syndrome

FIIND - function-to-find-domain

FMF – Familial Mediterranean fever

HIN-200 – Hematopoietic interferon-inducible nuclear protein

IDL - interdomain linker

IL – Interleukin

IL-1β – Interleukin-1 beta

IL-18 – Interleukin-18

IBD – Inflammatory bowel disease

IFN – Interferon

IRF8 - Interferon regulatory factor 8

LeTx - Lethal Toxin

LPS – lipopolysaccharide

LRR – Leucine rich repeat

MEFV – Marenostrin

mtDNA – Mitochondrial DNA

MWS – Muckle-Wells syndrome

NAIP - Neuronal apoptosis inhibitory proteins

NLR – Nucleotide-binding domain leucine-rich repeat containing receptor

NMR – Nuclear magnetic resonance

NOD – Nucleotide binding oligomerization

NOMID – Neonatal-onset multisystem inflammatory disease

OB - Oligonucleotide/oligosaccharide binding

PAMP – Pathogen-associated molecular patterns

PD – Parkinson's disease

POP – PYD-only protein

PRR – Pattern recognition receptor

PYD – Pyrin domain

RLR – Retinoic acid inducible gene-I (RIG-I) like receptor

ROS – Reactive oxygen species

SEC – Size-exclusion chromatography

SNPs – Single nucleotide polymorphisms

T3SS - Type III secretion systems

T4SS - Type IV secretion systems

TEM – Transmission electron microscopy

TLR – Toll-like receptor

TMS1 - Target of methylation-induced gene silencing-1

TNF-α – Tumor necrosis factor alpha

TNFR1 - Tumor necrosis factor receptor 1

NF-κβ – Nuclear factor kappa beta

UC – Ulcerative colitis

UVB – Ultraviolet B

Curriculum Vitae

EDUCATION

2017-2022 **UNIVERSITY OF CALIFORNIA MERCED**
PhD Quantitative and Systems Biology

2015-2018 **CALIFORNIA STATE UNIVERSITY FRESNO**
Master in Chemistry

2010-2014 **UNIVERSITY OF CALIFORNIA IRVINE**
BS in Pharmaceutical Sciences

2006-2010 **CLOVIS EAST HIGH SCHOOL**
High School Diploma

RESAERCH EXPERIENCE

01.2018 – 08.2022 **UNIVERSITY OF CALIFONRIA MERCED**

EVA DE ALBA LAB, ASSOCIATE PROFESSOR

- Purification of Isotopically doubly labelled ^{13}C, ^{15}N ASCb and ASC3X and ^{15}N ASC, ASCb and ASC3X in M9 minimal media for use in 3D, 2D and RT-NMR experiments.
- 3D CBCACONH and HNCACB experiments for the backbone assignment of ASCb and ASC3X.
- Comparing the interdomain dynamics of ASC, ASCb and an engineered isoform ASC3X using ^{15}N relaxation techniques (T_1, T_2, and ^{15}N-^{1}H NOE).
- Investigation into the self-association kinetics of ASC, ASCb, and ASC3X over the course of 49 hrs using Dynamic light scattering (DLS) to identify the presence of multiple populations and monitor polydispersity changes over time.
- Utilization of Size-exclusion chromatography to monitor the effects of time, concentration, and pH on the oligomer size distribution of ASC, ASCb, and ASC3X.
- RT-NMR Kinetics of ^{15}N ASC, ASCb, and ASC3X at various concentrations to monitor self-association differences over the course of 65 hrs due to differences in linker length.
- Analysis of ASC, ASCb, and ASC3X filaments at physiological pH with Uranyl Acetate using Scanning electron microscopy (SEM), Transmission electron microscopy (TEM) and Scanning transmission electron microscopy (STEM).
- Formation of pH driven hydrogels utilizing inflammatory proteins (ASC and ASCc), as well as artificially engineered proteins (ASC^{CARD} and CARD-CARD).
- Characterization of hydrogels using Rheological studies, Transmission electron microscopy (TEM), and Scanning electron microscopy (SEM) for filament analysis

06. 2016 – 08.2016

10.2017 – 01.2018 **UNIVERSITY OF CALIFORNIA MERCED**

DR. WOLF LAB, ASSISTANT PROFESSOR

- Trained in various PCR techniques (Splinkerette, Inverse, etc…) with the purpose of identifying where a particular gene (GAL4), promoting water seeking activity, was being inserted into the drosophila genome. Primers were constructed to contain parts of the known sequence of GAL4 and the location was determined to be at CG4502 a 10 kb Ubiquitin Conjugating Enzyme.
- Identify where in the 10 kb Ubiquitin Conjugating Enzyme water seeking activity is being promoted. Performed restriction digest to break the 10 kb gene into 4 small fragments and performed directional TOPO cloning to insert them into a pENTR vector

11.2015 – 06.2017 **CALIFORNIA STATE UNIVERSITY FRESNO**

Dr. Goto Lab, Department Chair and Professor

- Research focus was on understanding the dynamic equilibria of a non-proteinogenic amino acid β-Methylamino-L-alanine (BMAA) and its conversion to carbamate adducts in the presence of bicarbonate and divalent metals (Zn^{2+}, Cu^{2+}, Mg^{2+}). Experiments were performed using Circular Dichroism, ^{1}H NMR, 2D NMR, PFG-NMR, and UV-Vis to verify metal-BMAA complexation.

06.2013 – 06.2014 **UNIVERSITY OF CALIFONRIA IRVINE**

DR. ROSE LAB, **Distinguished Professor & Director of NERE, Ecology & Evolutionary Biology**

- Assisted the graduate student in their Diet and Aging project for the purpose of determining how Drosophila progeny over many generations develop evolutionary traits based on their Diet.
- Responsibilities included maintaining fruit flies over the course of the year, preparing different subset of dietary foods such as Charcoal, Apple, and Banana agar plates, separation of females and males for experimental analysis and using ImageJ for egg analysis

AWARDS

09.2015 – 06.2017 **BRIDGES TO DOCTORATE PROGRAM**

04.2017 **CENTRAL CALIFORNIA RESEARCH SYMPOSIUM (CCRS) ACS HONORABLE MENTION**

09.2016 **FACULTY SPONSORED STUDENT RESEARCH AWARD**

11.2018 **NSF-FUNDED CREST CENTER FOR CELLULAR AND BIOMOLECULAR MECHANISM (CCBM) FELLOWSHIP (SPRING 2019)**

04.2020 QSB SUMMER FELLOWSHIP (SUMMER 2020)

PRESENTATIONS

09.2017 **ANNUAL BIOMEDICAL RESEARCH CONFERENCE FOR MINORITY STUDENTS (ABRCMS),**

Effects of Divalent Metal Ions on BMAA and its Carbamate Adducts

Pedro Diaz-parga, Joy Goto, V.V. Krishnan

04.2017 **CENTRAL CALIFORNIA RESEARCH SYMPOSIUM (CCRS)**

Effects of divalent metal ions on BMAA and its carbamate adducts

Pedro Diaz-parga, Joy Goto, V.V. Krishnan

05.2019 QSB RETREAT ORAL PRESENTATION

03.2020 **61ST EXPERIMENTAL NUCLEAR MAGNETIC RESONANCE CONFERENCE (ENC)**

Can linker length and domain mobility control the interacting capabilities of multidomain proteins?

Pedro Diaz-parga and Eva de Alba

08.2020 **SOUTHERN CALIFORNIA USERS OF MAGNETS (VIRTUAL CONFERENCE)**

Can linker length and domain mobility control the interacting capabilities of multidomain proteins?

Pedro Diaz-parga and Eva de Alba

03.2021 **62ND EXPERIMENTAL NUCLEAR MAGNETIC RESONANCE CONFERENCE (ENC)**

Influence of the linker length in the self-association properties of multidomain proteins

Pedro Diaz-parga and Eva de Alba

02.2022 **66TH ANNUAL BIOPHYSICAL SOCIETY ANNUAL MEETING**

Difference in self-assembly of the inflammasome adaptor isoform ASC and ASCb: insights into inflammasome regulation

Pedro Diaz-parga and Eva de Alba

PUBLICATIONS

Diaz-Parga, P., & de Alba, E. (2022). Inflammasome regulation by adaptor isoforms, ASC and ASCb, via differential self-assembly. *Journal of Biological Chemistry*, 101566.

Diaz-parga, P., Goto, J. J., & Krishnan, V. V. (2020). On the Differential Roles of Mg 2+, Zn 2+, and Cu 2+ in the Equilibrium of β-N-Methyl-Amino-L-Alanine (BMAA) and its Carbamates. *Neurotoxicity Research*, 1-11.

Diaz-Parga, P., & de Alba, E. (2019). Protein interactions of the inflammasome adapter ASC by solution NMR. *Methods in enzymology*, 625, 223-252.

Diaz-Parga, P., Goto, J. J., & Krishnan, V. V. (2018). Chemistry and chemical equilibrium dynamics of BMAA and its carbamate adducts. *Neurotoxicity research*, 33(1), 76-86.

Submitted (Accepted with revisions):

Diaz-Parga, P., Gould, A., & de Alba, E. (2022). "Natural and engineered inflammasome adaptor proteins reveal optimum linker length for self-assembly". *Journal of Biological Chemistry*

Abstract

Inflammation is governed by the inflammasome: a large multiprotein complex necessary to trigger an inflammatory response. The inflammasome adaptor ASC is responsible for mediating inflammasome formation. ASC exists as 4 isoforms: ASC, ASCb, ASCc, and ASCd. Of the four isoforms ASC and ASCb are capable of eliciting an inflammatory response, however ASC is able to produce a stronger response compared to ASCb. Structurally, ASC and ASCb are multidomain proteins containing a PYD and CARD (Death Domain proteins) necessary to participate in homotypic interactions and drive inflammasome formation. ASC contains a 23 amino acid linker separating the two domains while ASCb contains a significantly shorter linker, 4 amino acids. Self-association capabilities of ASC and ASCb as a result of linker length mediate inflammasome formation. To further study the effects of linker length, an engineered the isoform ASC3X with identical PYD and CARD connected by a 69-amino acid long linker (i.e., three-times longer than ASC's linker) was used to test the influence of linker length on the self-association capabilities of ASC3X. To understand the self-association capabilities of each isoform: real-time NMR (RT-NMR) was used to determine differences in their self-association ability. dynamic light scattering (DLS) and size-exclusion chromatography were performed to monitor their oligomer size distribution. Microstructures formed by each isoform were images using transmission electron microscopy (TEM). DLS data indicate ASC is able to form uniform structures in solution compared to ASCb and ASC3X. Interdomain dynamics of each isoforms reveal the effect of linker length on domain flexibilty. The shorter linker of ASCb restricts the PYD and CARD domain causing ASCb to tumbles as a rod. Increasing the length of linker allowed the PYD and CARD of ASC and ASC3X to tumble semi-independently of each other. Altogether, our data suggest that ASC's linker length is optimized by allowing enough flexibility to favor intermolecular homotypic interactions and simultaneously keeping both domains sufficiently close for essential participation in self-assembly. In addition, our results help explain at the molecular level the differences in inflammatory response by ASC isoforms.

Chapter 1

Introduction

1.1 Role of innate immunity in inflammation

The immune system is comprised of a large network of cells, proteins, and organs working together to protect the body from bacteria, viruses, and pollutants (1, 2). Response and removal of pathogens by the immune system is accomplished through two separate mechanisms necessary to distinguish self from non-self, innate and adaptive immunity (3, 4). Innate immunity is the first line of defense against any intruding pathogen. As the first line of defense, it is capable of recognizing a broad range of foreign agents and signals (5). Innate immunity lacks immunological memory to previous infections, instead relying on its ability to respond to pathogens effectively and rapidly (6). Adaptive immunity is highly dependent on previous exposure to pathogens, relying primarily on tailored made immune receptors from previous infections (4, 7). Immunological memory from repeated exposure to pathogenic material improves response time and removal from the host upon repeated infection (4, 6, 7). These specialized cells of the adaptive immune system include naïve T cells, memory T cells $CD4^+$ and $CD8^+$ cells and antibody-producing B cells (**Figure 1**) The innate immune system is a highly conserved defense system amongst mammals, plants, and invertebrates (8–10). Innate immunity comprises of multiple defensive barriers designed to protect against invading pathogens: skin, mucous membrane, low pH, chemical mediators, phagocytic cells and inflammatory cell death (3, 9). Innate immunity involves a wide range of various myeloid cells (macrophages, mast cells, neutrophils, basophils, dendritic cells, and natural killer cells) necessary for the detection, signaling, and activation of pro-inflammatory cytokines in response to a multitude of pathogens (**Figure 1**) (2, 11). Activation of the innate immune system leads to an inflammatory response, characterized by symptoms of redness, swelling, pain, and loss of tissue function (12). Although it is nonspecific, the innate immune system is equipped with pattern recognition receptors (PRRs) aimed in the identification of pathogen-associated molecular patterns (PAMPs) and damage-associated molecular patterns (DAMPs) (13, 14).

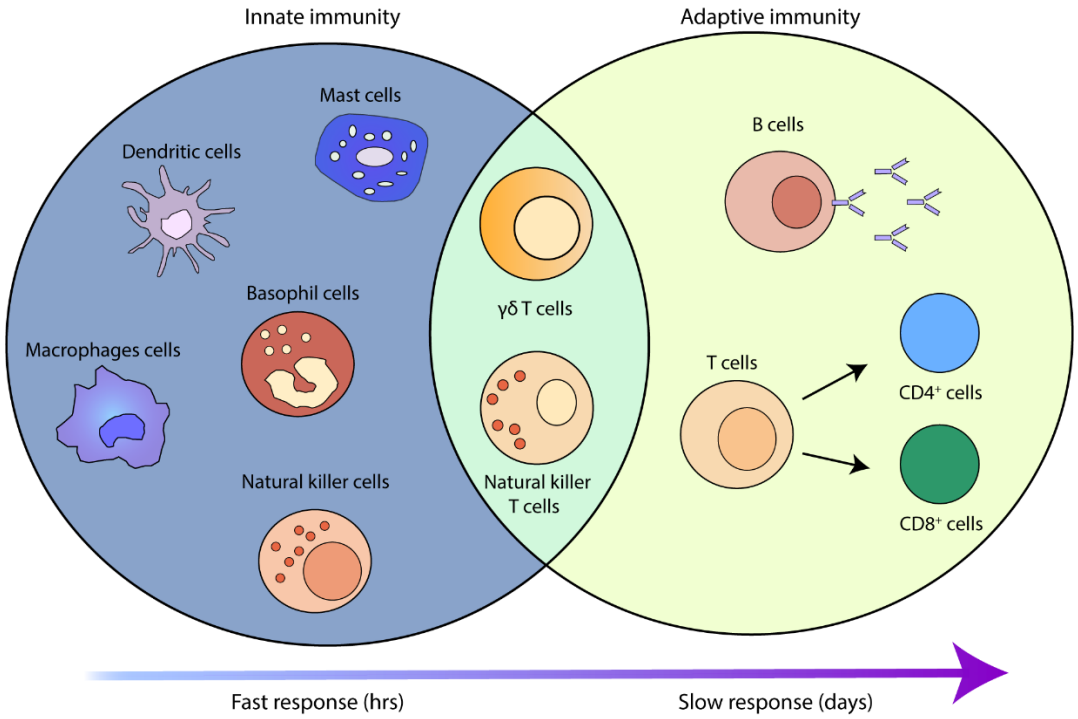

Figure 1. Cells of the innate and adaptive immune system. Innate immune system is the first line of defense against foreign objects. Initiation of the innate immune system is rapid, occurring hours within infection. Innate immune cells include macrophages, basophils, mast cells, dendritic cells, and natural killer cells. Adaptive immunity response is slower occurring days following infection. Adaptive immunity consists of antibodies secreted by B cells and $CD4^+$/$CD8^+$ cells secreted by T cells. Communication between innate and adaptive is facilitated by γδ T cells and natural killer T cells. Figure adapted from ref (15).

PAMPs are a diverse set of microbial motifs that share various recognition patterns or evolutionary conserved structures common to many pathogens (10). While DAMPs are endogenous molecules released from damaged/dying cells (10). Recognition of PAMPs and DAMPs are mediated by either membrane bound PRRs, Toll-like receptors (TLRs), C-type lectin receptors (CLRs), or one of the three intracellular sensors, RIG-I-like receptors (RLRs), NOD-like receptors (NLRs), and absent in melanoma 2 like receptor (AIM2) (14). Activation of TLRs by a PAMP or DAMP signals the activation of the inflammasome complex. Inflammasomes are large multiprotein platforms that necessitate the recruitment and activation of inflammatory caspases in the presence of PAMPs and DAMPs (15,16). Inflammasome formation is mediated by the protein adaptor ASC (apoptosis-associated speck like protein containing a CARD) (18). ASC functions as an adaptor bridging the inflammatory sensor (NLRs, Pyrin, and AIM2) to the effector procaspase-1 via homotypic interactions (18, 19). Recruitment of procaspase-1 to the inflammasome results in the autocleavage of procaspase-1 to its bioactive form caspase-1. Once active, caspase-1 initiates an inflammatory form of cell death known as pyroptosis, consisting in swelling of the cell membrane and release of pro-inflammatory cytokines to the extracellular milieu (20). Active caspase-1 cleaves immature inflammatory cytokines

pro-IL-18, and pro-IL-1β into their active form. Simultaneously, caspase-1 serves to cleave gasdermin-D into its active N-terminus form initiating the assembly of 10 – 20 nm pores on the plasma membrane causing cellular swelling and lysis of the cell (21).

1.2 Inflammation in health and disease

As mentioned previously innate immunity serves to rapidly detect and remove infectious agents/pollutants from the host via the inflammatory response. However, overstimulation of the inflammasome by either disease or genetic background can have a profound effect on the inflammatory pathway leading to excessive (chronic) inflammation or insufficient inflammation. Dysregulation of either the sensor, adaptor or effector are associated with various inflammatory diseases. Overproduction of IL-1β, due to high caspase-1 activity, is prevalent in hereditary diseases such as cryopyrin-associated periodic syndromes (CAPS), and familial Mediterranean fever (FMF) (22, 23). Dysregulation of inflammatory sensors and ASC are associated with Psoriasis (24), Type 1 (25, 26) and 2 Diabetes (27, 28), Inflammatory bowel disease (29, 30), and have been linked to Alzheimer's disease (30, 31).

1.2.1 Hereditary autoinflammatory disease

Cryopyrin-associated periodic syndromes are a spectrum of rare hereditary diseases related to inflammasome dysfunction (23). In order of severity, these include familial cold autoinflammatory syndrome (FCAS), Muckle-Wells syndrome (MWS), and neonatal-onset multisystem inflammatory disease (NOMID) (33). Mutations in the inflammasome sensor, NLRP3, result in the overstimulation of the inflammatory response leading to a higher-than-normal production of IL-1β. Overproduction of IL-1β results in repeated bouts of systemic inflammation throughout the body. Although, genetically similar each cryopyrinopathy has distinct symptoms unique to each syndrome (33, 34). FCAS is characterized by recurrent urticaria, arthralgia, and fever upon exposure to cold temperatures. MWS can appear spontaneously without any apparent trigger and is characterized by conjunctivitis and renal amyloidosis. NOMID being the most severe of cases, involves central nervous system degradation that can result in hearing loss and meningitis. Treatment of CAPS is performed by targeting IL-1β with known IL-1β inhibitors such as anakinra, rilonacept, and canakinumab (33, 34).

1.2.2 Neuroinflammation in neurodegenerative diseases

Chronic neuroinflammation is associated in the pathogenesis of Alzheimer's disease (AD), Parkinson's disease (PD), and amyotrophic lateral sclerosis (ALS) (35, 36). Neuroinflammation is characterized as the clearance of pathogens, misfolded proteins, and cellular debris from the central nervous system (CNS) (37). The CNS is composed of glial

cells, consisting of astrocytes, microglia, and oligodendrocytes serving as regulators of the inflammatory response. Currently, NLRP1, NLRP2, NLRP3, NLRC4 and AIM2 have been implicated in the progression of neurodegenerative disease. Alzheimer's is a neurodegenerative disease associated with a loss of memory and cognitive functions over time (38). Alzheimer's is characterized by the presence of Amyloid-beta plaques and tau tangles (38). Under normal conditions amyloid beta (Aβ) is cleaved into its Aβ-40 fragment by β-secretase; however, during the onset of AD, amyloid beta is cleaved into its neurotoxic form, Aβ-42, causing it to aggregate into Aβ plaques (38, 39). Accumulation of Aβ has been shown to activate the NLRP3 inflammasome in microglia (40). In addition, ASC is able to associate with Aβ clusters inducing pyroptosis in surrounding microglia leading to a mass release of ASC-Aβ clusters (31). Overproduction of IL-1β as a result of chronic inflammation induces brain damage and affects synaptic plasticity (41, 42). Several strategies have been shown to prevent and ameliorate the brain inflammatory response, such as, an IL-1β blocking antibody and small-molecule NLRP3 inhibitor (JC-124) (43, 44). Parkinson's is a neurodegenerative disorder characterized by the presence of α-synuclein and loss of dopaminergic neurons leading to a loss of motor functions. Studies have shown the ability of α-synuclein to activate the NLRP3 inflammasome in monocytes and microglia (45, 46). In agreement with these studies, the caspase-1 inhibitor AC-YVAD-CMK in NLRP3 knockout mice was shown to prevent the loss of dopaminergic neurons typical of Parkinson's (47, 48).

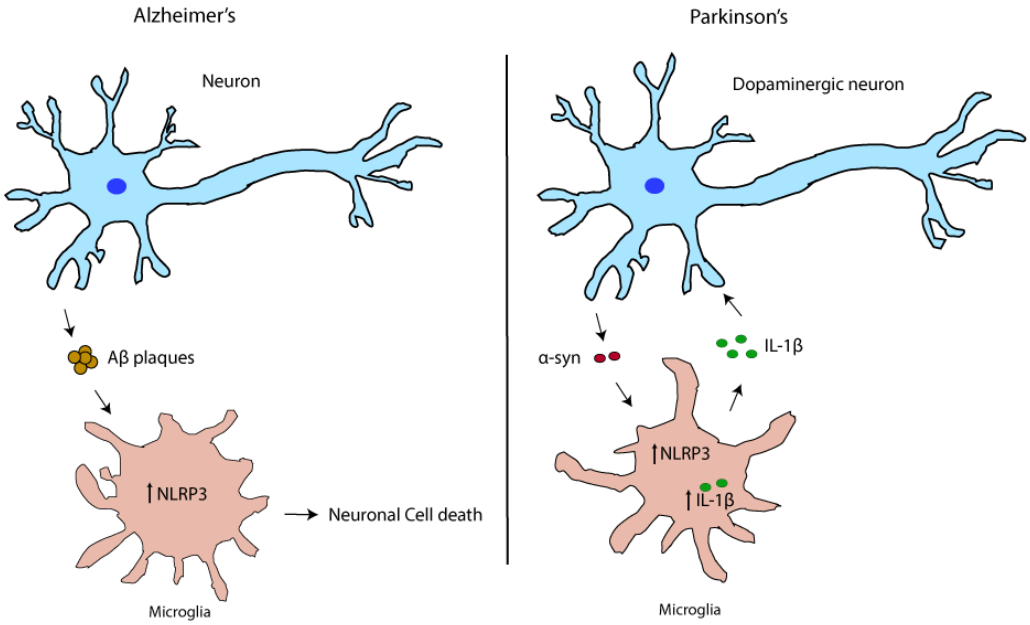

Figure 2. Inflammation in Alzheimer's and Parkinson's Disease. In Alzheimer's disease, the production of Aβ plaques induce NLRP3 inflammasome formation in microglia cells. a-synuclein produced by dopaminergic neurons are sensed by microglia cells activating the NLRP3 inflammasome producing an overabundance of IL-1β. Pyroptosis of microglia releases IL-1β causing the degeneration of dopaminergic neurons**.**

1.2.3 Inflammatory bowel disease

Inflammatory bowel disease are recurrent chronic inflammatory events of the colon and small intestine (29, 30). Damage and or disruption of the gut microbiome and mucosal barrier elicit strong inflammatory responses in the gut (49). Several studies have recently reported a role of the inflammasome sensor NLRP3 in the pathogenesis of in Inflammatory bowel diseases (49–51). IBD is comprised of ulcerative colitis and Crohn's disease. Complications in ulcerative colitis can range from abdominal pain to weight loss and lead to inflammation of joints and ultimately colon cancer. Multiple studies have linked NLRP3 SNPs (single nucleotide polymorphisms) to susceptibility of ulcerative colitis (52, 53). Interestingly, the food additive, titanium dioxide (TiO_2) nanoparticles, were reported to damage intestinal mucosal barrier resulting in the activation of the NLRP3 inflammasome and increase in IL-1β and IL-18 (54). Similarly, NLRP3 dysregulation is implicated in the progression of Crohn's disease. CARD8, a negative regulator of NLRP3, normally binds to the NLRP3 inflammasome and inhibits its binding to ASC (51). Mutations in CARD8 resulting in a loss of function were found to prevent CARD8 from binding to NLRP3 and resulted in an increase severity of Crohn's disease (51).

1.2.4 Skin disease

The skin is an essential barrier that is permanently exposed to the environment. As the interface between environment and host it is the primary defense against environmental, physical, and biological threats (55, 56). Secondly, the skin serves as a mode of thermoregulation and water retention. As such, it is composed of two main parts, the epidermis and dermis layers. The epidermis, consisting of multiple layers of tightly packed keratinocytes, functions as a strong physical barrier against external stimuli. Formation of the epidermis is driven by a programmed process of differentiation, whereas migration of keratinocytes to the surface cause morphological and biochemical changes to the cell (57). Keratinocytes serve two roles: to act as a physical barrier against bacterial and viral agents and promote the release of anti-microbial peptides and proinflammatory cytokines (58). The dermis layer contains specialized adaptive and innate immune cells as well as providing support to the epidermis layer (**Figure 3)**. Human keratinocytes have been found to express inflammatory components ASC, procaspase-1, and notably NLRP1. Exposure to ultraviolet B radiation (UVB) has been shown to induce activation of the NLRP1 inflammasome leading to sunburns (59, 60). Inflamed skin due to atopic dermatitis and psoriasis has become increasingly linked to AIM2 inflammasome activation. Abundant cytosolic DNA released by psoriatic lesions were found to trigger release of IL-1β via AIM2 inflammasome activation.

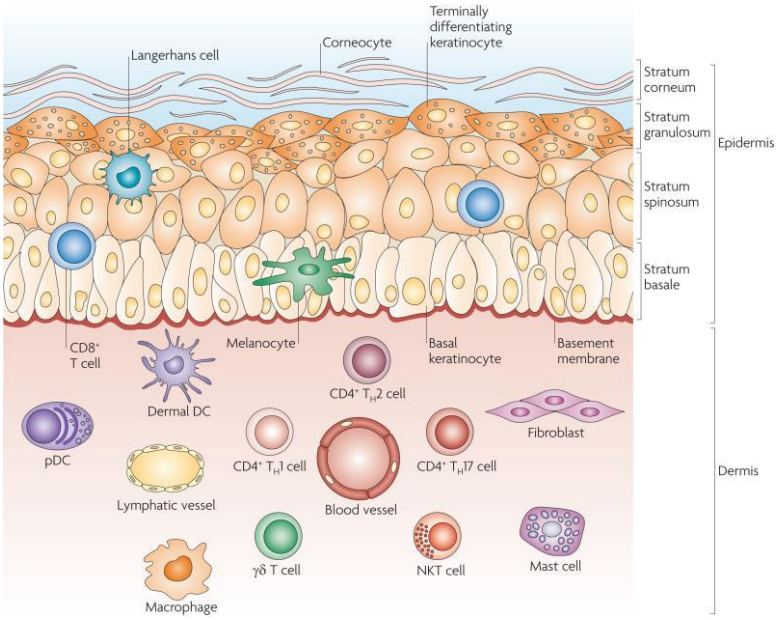

Figure 3. Immune cells of the skin. The skin is composed of two layers: the epidermis and the dermis. The epidermis is composed of four different layers made of keratinocytes in diverse differentiated states. Inflammatory producing cells include Langerhans cells, melanocytes, and keratinocytes. The dermis layer harbors immune cells of both the innate and adaptive systems. Reprinted by permission from Springer Nature Customer Service Centre GmbH: Springer Nature. Reviews Immunology. Skin immune sentinels in health and disease, Frank O. Nestle et al, Copyright (2009). (56).

Chapter 2

Molecular components involved in the inflammatory response

2.1 Death Domain Superfamily

The Death Domain superfamily is a large collection of structurally similar proteins involved in cellular death (61, 62). It is comprised of four subfamilies: death effector domain (DED), death domain (DD), caspase recruitment domain (CARD), and the pyrin domain (PYD) (61). The human genome is composed of 32 DDs, 7 DEDs, 28 CARDs, and 19 PYDs (61). A common feature amongst the death domain superfamily is the presence of six α-helices arranged in a Greek key bundle (63). The six α-helices are variable among the four subfamilies, differences in orientation and length of each helix result in differences in the structural configuration of each subfamily (61). Homotypic interactions within each subfamily facilitate the assembly of structural scaffolds necessary for the activation of either apoptosis or pyroptosis. Both apoptosis and pyroptosis are forms of cellular death, initiated in response to host infection by pathogenic or viral agents (20, 64). Apoptosis is characterized by nuclear/cytoplasmic condensation and cellular fragmentation into apoptotic bodies (65). Pyroptosis is an inflammatory form of cell death that results in the rapid swelling and rupture of macrophage cells (20, 65). The integral role of the Death Domain family in both apoptosis and pyroptosis is evidenced by the requirement of multiple death domain proteins needed for cellular signaling and self-association leading to either apoptosis or pyroptosis. Death domain members interact with each other through three distinct interactions Type I, Type II, or Type III (66–68). Self-association of death domain proteins leads to an increase in the local concentration of effector proteins involved in signal transduction such as, ubiquitin ligases, deubiquitinases, kinases, and caspases (66).

2.1.1 CARD domain

Currently, ~ 33 CARD containing proteins have been identified in humans (69). The CARD domain is a protein consisting of ~ 90 amino acids and serves to function in protein-protein interactions necessary for pyroptosis, apoptosis, and cellular signaling (61, 70, 71). Generally, CARD containing proteins are classified into two categories: adaptor proteins involved in scaffolding/signaling, and prodomain caspases containing a CARD at the N-terminus. CARD containing caspases include caspases, -1, -4, -5, and -12 involved in inflammation and caspase-8 and caspase-10 in apoptosis (64, 69, 72). As the second largest family member and mediator of both apoptosis and pyroptosis, CARD-CARD interactions are necessary for the formation of large molecular platforms for signaling processes. CARDs contain the conserved six-helical bundle common to the death domain family. Unique to the CARD family is the presence of a bent/broken H1 splitting the first helix into two separate helices termed H1a and H1b (61, 69). A comparison of CARD domains from ICEBERG, CARMA1, procaspase-1, and ARC CARD show similar structural homology and surface charge distribution (**Figure 4**). The surface charge of

CARD proteins indicates CARD proteins mainly interact through electrostatic interactions. Interactions between CARD-CARD dimers were first demonstrated from the crystal structure of Apaf-1 complexed with the CARD of procaspe-9 (**Figure 4E**) (67). The binding is primarily driven by numerous salt bridges formed between helices H1 and H4 of the CARD of procaspase-9 with helices H2 and H3 of Apaf-1. These are termed type I interactions (67). Recently, the crystal structure of apoptosis repressor with caspase recruiting domain (ARC) has also revealed an altered form of the CARD protein distinct from other death domain proteins (73). ARC CARD contains a 5-helix fold motif instead of the conserved six-helix fold unique to death domains (73). H6 was instead found to be disordered and not necessary for the function of ARC CARD. Notably, CARD containing proteins have also shown the ability to self-associate and form filaments utilizing type I, type II, and type III interactions. Cryo-EM structures of ASC^{CARD} and $NLRC4^{CARD}$ demonstrate the ability of the CARD domain to form tightly packed helical filaments of ~ 8 nm in diameter utilizing type I, II, and III interactions to self-associate (74).

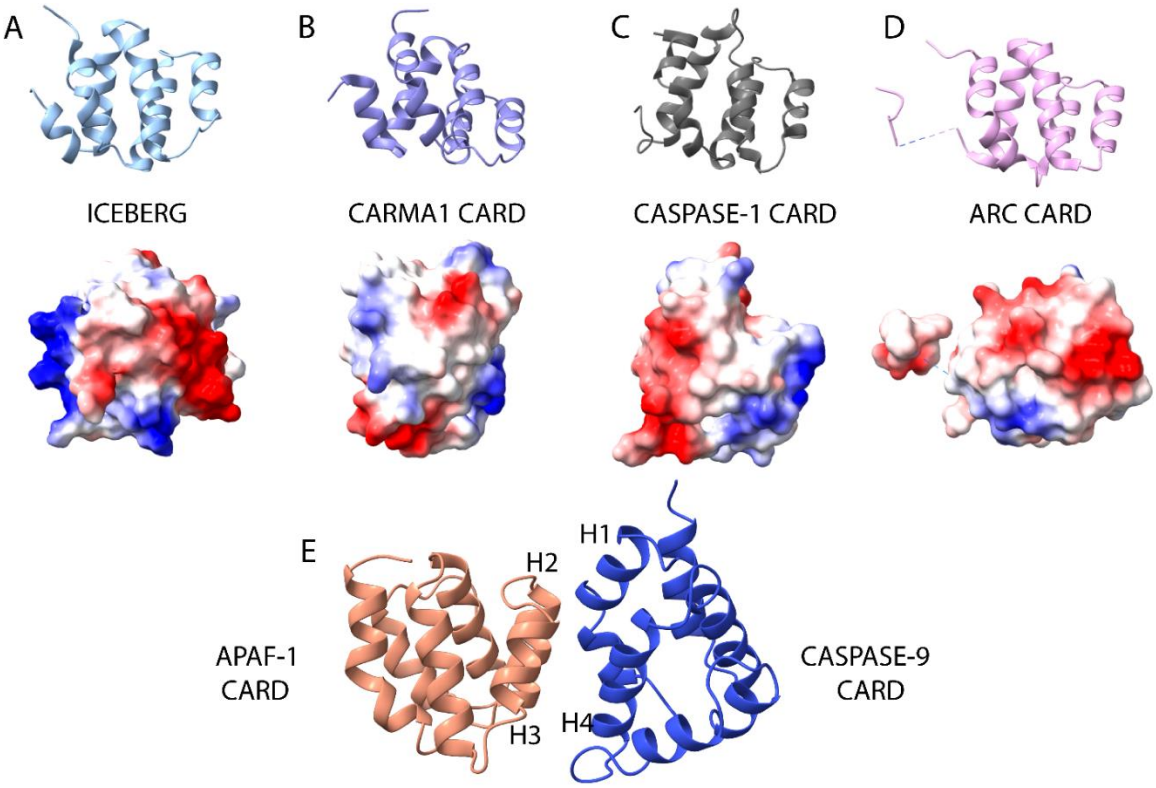

Figure 4. Structural similarities between the CARD family. (A)-(C) Structural similarity of the CARD domain from different proteins depicting the broken H1 and similar bipolar charge distribution of ICEBERG (pdb 1DGN) (75), CARMA1 (pdb 4I16) (76), Caspase-1 CARD (pdb 5FNA) (77). (D) depiction of ARC CARD (pdb 4UZ0) (73) containing the characteristics typical of CARD domains but lacking H6 common to the death domain family. Ribbon diagrams (top) and electrostatic surfaces (bottom) are shown. (E) Type I interaction between H2 and H3 of APAF-1 and H1 and H4 of Caspase-9 card (pdb 3YGS) (67). Add helix numbers in A-D.

2.1.2 Pyrin Domain

The PYD domain, originally discovered in the Pyrin protein Marenostrin (MEFV), is a 90 amino acid protein containing the six anti-parallel α-helices stabilized by a conserved central hydrophobic core (61, 78–80). The PYD domain is present in 23 human genes and appears exclusively at the protein N-terminus (79). The hydrophobic core is stabilized by residues belonging to H1, H2, H4, H5, and H6, whereas H3 does not contribute to the formation of the hydrophobic core. A structural analysis of PYDs present in the NLR family, ASC^{PYD}, ASC2, and $AIM2^{PYD}$ indicates structural homology among them, and points to a distinctive long loop connecting H2 and H3, with the exception of AIM2 with a shorter H2-H3 loop, and an overall shorter H3 compared to other death domain proteins (**Figure 5**) (79–81). Alterations in H3 of the PYD containing proteins is considered vital in PYD-PYD interactions. PYD-PYD interactions are primarily facilitated by charged and hydrophobic residues (79). PYD proteins can exist as part of multi domain proteins (NLRs, AIM2, ASC) or as PYRIN domain-only proteins (POPs) (70). POPs are small proteins (10-13 kDa) that serve as negative regulators of inflammasome formation. Presently, there are three POPs that have been identified, POP1, POP2, and POP3 (82–84). However, PYDs present as part of a multidomain protein are necessary for inflammasome formation.

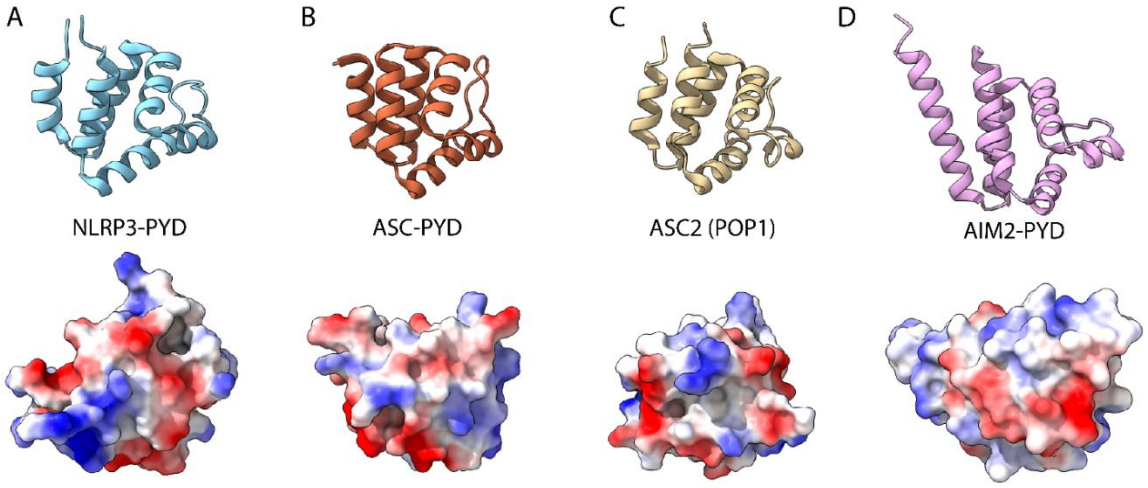

Figure 5. Structural comparison of different PYD domains. (A) 3D NMR solution structure of NNLRP3 PYD (pdb 2NAQ) (85). (B) NMR structure of ASC PYD (pdb 1UCP) (86). NMR solution structure of ASC2 (pdb 2HM2) (87). Crystal structure of AIM2 PYD (pdb 3VD8) (81). Ribbon diagrams (top) and electrostatic surfaces (bottom) are shown.

2.2 Inflammasome receptors

Formation of the inflammasome complex is necessary for caspase-1 activation and initiation of pyroptosis. Numerous cytosolic inflammasome sensors have been identified in inflammasome formation including: NLRP1, NLRP2, NLRP3, NLRC4 NLRP6, NLRP7, NLRP12 AIM2, Pyrin, and IFI16 (**Figure 6**) (17, 19, 88). Each inflammasome sensor consists of multiple subunits. Sensors can contain the following subunits: caspase activation and recruitment domain (CARD), nucleotide-binding and oligomerization domain (NACHT), Pyrin Domain (PYD), leucine rich repeat (LRR) etc... (**Figure 6**) (17, 88). Each sensor can uniquely respond to specific stimuli designating its use for inflammasome complexation. For example, NLRC4 and NLRP1 are prompted for inflammasome formation by gram-negative bacteria, while double stranded DNA (dsDNA) exclusively binds to AIM2, triggering the formation of the AIM2 inflammasome (89–91). PAMPS and DAMPS produced by Gram-negative and Gram-positive bacteria result in NLRP3, NLRP2, NLRP7, and NLRP12 inflammasome formation (92–94). Activation of these cytoplasmic sensors leads to the activation and nucleation of the adaptor protein ASC and subsequent recruitment of procaspase-1.

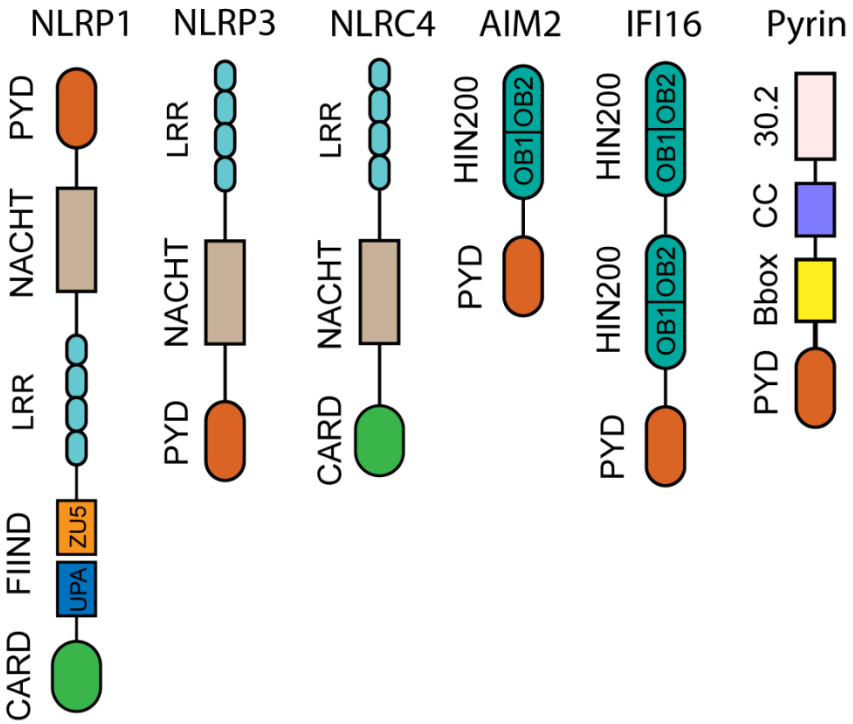

Figure 6. Inflammasome receptor. Inflammasome receptors carry multiple protein domains. Inflammasome sensors can contain a combination of the following domains: pyrin domain (PYD), nucleotide-binding and oligomerization domain (NACHT), leucine rich repeat domain (LRR), caspase activation and recruitment domain (CARD), HIN200 domain, B30.2 domain, coiled-coil domain (C-C), a B-box domain (bBox), and a function-to-find domain (FIIND).

2.2.1 NLRP3 inflammasome

The inflammasome complex is a multimeric protein complex that is composed of three primary components: a sensor, adaptor, and an effector. NLRP3 inflammasome complexation is unique in its ability to respond to a multitude of stimuli (95). NLRP3 has been shown to respond to various PAMPs such as bacterial lipopolysaccharides, O antigens, and peptidoglycan (93). Similarly, DAMPs such as ATP, monosodium urate (MSU), and calcium pyrophosphate dehydrate (CPPD), as well as notable environmental triggers such as silica, asbestos, and aluminum can activate the NLRP3 sensor (96–98). Depending on the stimulus, NLRP3 can be activated through a canonical or non-canonical pathway. Canonical activation of NLRP3 is a two-step process requiring a priming step for the transcription of NLRP3 and inflammatory cytokines pro-IL-1β and pro-IL-18 and an activation step to initiate NLRP3 inflammasome formation (**Figure 7**) (93, 99). Priming of the cell requires either a DAMP or PAMP activating TLR4 or tumor necrosis factor receptor 1 (TNFR1) to upregulate NLRP3 and pro-IL-1β and pro-IL-18 in a NF-κB-dependent way (100). Simultaneously, a second signal is needed to activate the NLRP3 sensor to trigger inflammasome assembly. The secondary signal can range from alteration in cellular concentration of K^+ through efflux, increases in intracellular Ca^{2+}, or release of mitochondrial DNA (mtDNA) to the cytosol (93, 101, 102). NLRP3 begins to self-associate through the NACHT domains and recruits ASC via its PYD domain (103). ASC subsequently recruits procaspase-1 via its CARD domain enabling the activation of procaspase-1 by proximity-induced self-cleavage into its active form . Caspase-1 cleaves pro-IL-1β and pro-IL-18 into its active forms while simultaneously cleaving Gasdermin-D into a N-terminus and C-terminus fragment (21, 104). The N-terminus is transported to the plasma membrane and forms 10-20 nm size pores (105, 106). The production of the pores causes the cell to undergo an inflammatory form of programmed cell death known as pyroptosis. During pyroptosis the cell begins to swell and eventually ruptures releasing IL-1β and IL-18.

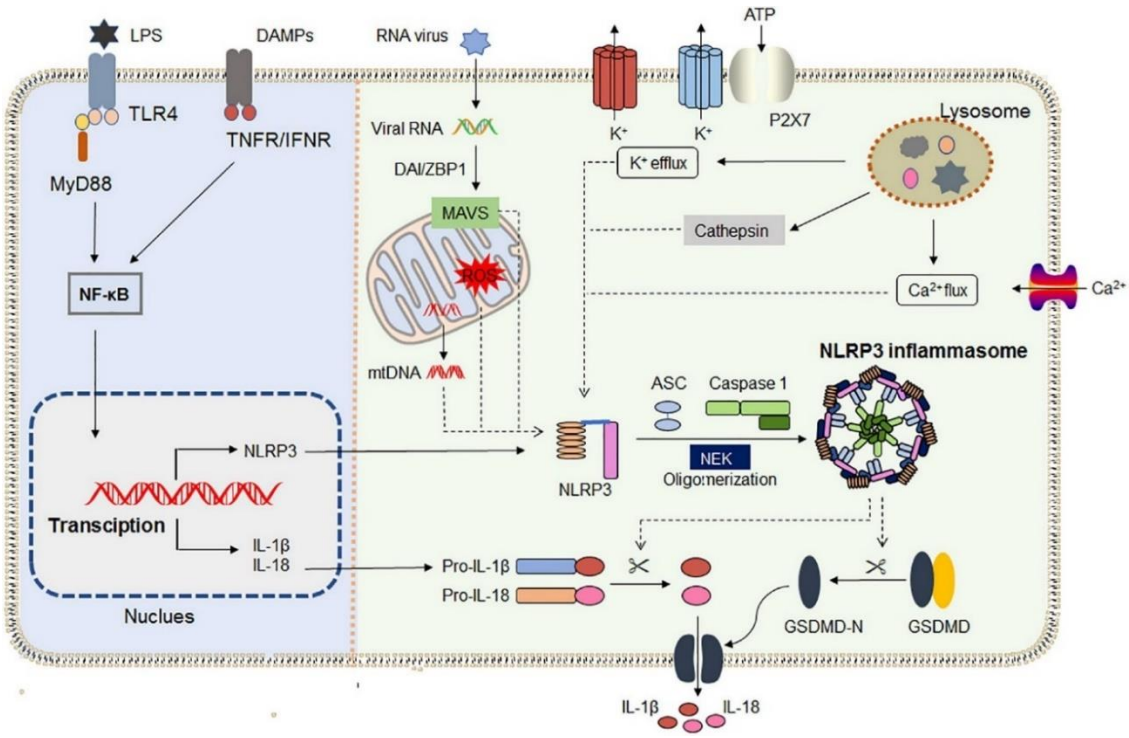

Figure 7. Canonical NLRP3 inflammasome activation. NLRP3 activation requires a priming signal (left) and an activation signal (right). Priming involves the presence of a PAMP or DAMP interacting with TLR4 or TNFR increasing the transcription of NLRP3 and proinflammatory cytokines pro-IL-1β and pro-IL-18. Activation of NLRP3 is achieved by multiple upstream signaling events: mtDNA, K^+ efflux, Ca^{2+} flux, ROS production, and lysosomal disruption. NLRP3 activation recruits ASC and caspase-1 to the inflammasome complex. Activated caspase-1 cleaves gasdermin-D, initiating gasdermin-mediated pyroptosis. Originally published in Frontiers Cell and Developmental Biology. NLRP3 Inflammasome: A Promising Therapeutic Target for Drug-Induced Toxicity. Wei Shanshan et al. © 2021. CC BY. (107).

NLRP3 inflammasome activation can also proceed through a non-canonical fashion. Specific gram-negative bacteria such as *Escherichia coli*, and *Vibrio cholerae* have been known to activate an alternative NLRP3 pathway (108). Activation of the NLRP3 non-canonical pathway is mediated by the TLR4-TRIF recognition of LPS necessary for the upregulation of Type I IFN (**Figure 8**) (109, 110). Type I and Type II IFN are required for expression of caspase-4/5/11, an important prerequisite for non-canonical inflammasome activation. In contrast to canonical inflammasome activation, caspase-4/5/11 act as both the sensor and effector molecules for LPS (111, 112). Caspase-4/5/11 are able to directly interact with LPS through their CARD domain (111, 112). Binding of caspase-4/5/11 initiates self-association into the active forms. Simultaneously, NLRP3 inflammasome formation is activated indirectly due to the stress of molecular events surrounding the cell leading to the activation of caspase-1 (112). Activated caspase-4/5/11 and caspase-1 can directly cleave gasdermin-D into its active N-terminus fragment initiating pyroptosis of the cell.

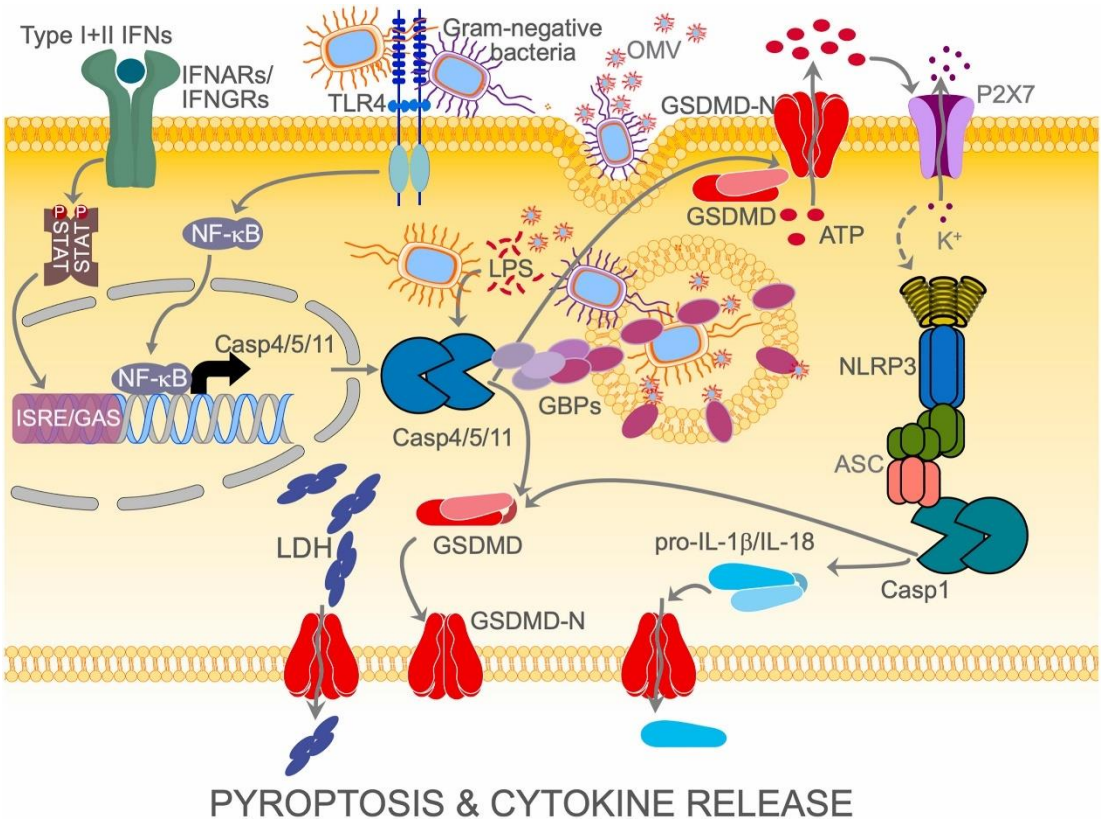

Figure 8. Non-canonical NLRP3 inflammasome activation. LPS recognition by TLR4 and Type I & II are required for the expression of casapase-4/5/11. Extracellular LPS internalized by endocytosis interacts directly with caspase-4/5/11. Simultaneously, PAMPs/DAMPs activate NLRP3 inflammasome resulting in caspase-1 activation. Caspase-1/4/5/11 can activate gasdermin-D resulting in pyroptosis of the cell. Originally published in Molecular Aspects of Medicine. An overview of the non-canonical inflammasome. Kevin P. Downs et al. © Elsevier 2020. CC BY. (112).

2.2.2 NLRP1

NLRP1 was the first cytosolic inflammasome receptor linked to the activation of proinflammatory caspases (16). Activation of inflammatory caspases was achieved by a multiprotein complex consisting of NLRP1, ASC, and caspase-1 termed the inflammasome (16). In contrast to the rest of the NLR family, NLRP1 contains two unusual features. NLRP1 possesses both a N-terminal PYD domain and a C-terminal CARD domain and a proteolytic function-to-find-domain (FIIND) required for NLRP1 inflammasome activation (**Figure 6**) (113). Only one NLRP1 gene is believed to be encoded in humans compared to the multiple NLRP1 orthologs encoded in mice (114). Understanding of human NLRP1 stems from the numerous experiments performed using the murine analogue NLRP1b. Notably, *Bacillus anthracis* Lethal Toxin (LeTx) was shown to activate murine NLRP1b inducing an inflammatory response (115). N-terminal proteolysis by *B. Anthracis* lethal toxin was necessary for the activation of murine NLRP1b, as well (116, 117). Introduction of proteasome inhibitors negated murine NLRP1b activity (118). Similarly, *Toxoplasma gondii*, *Shigella flexneria*, and *Listeria monocytogenes* have been

demonstrated to activate human NLRP1. Based on the N-terminal cleavage of NLRP1b a functional degradation model was proposed for its activation (**Figure 9**) (119). As proposed by the model, N-terminal cleavage of the PYD domain results in proteasome-dependent NLRP1b activation (119). Destabilization of the N-terminus by lethal factor (LF) cleavage and subsequent ubiquitinoylation of the N-terminus by UBR2 marks the NLRP1b sensor for degradation (119, 120). During proteasome degradation the FIIND domain auto cleaves releasing the $FIIND^{UPA}$-CARD allowing it to interact with the ASC^{CARD} and the $caspase\text{-}1^{CARD}$ forming the NLRP1b inflammasome (120).

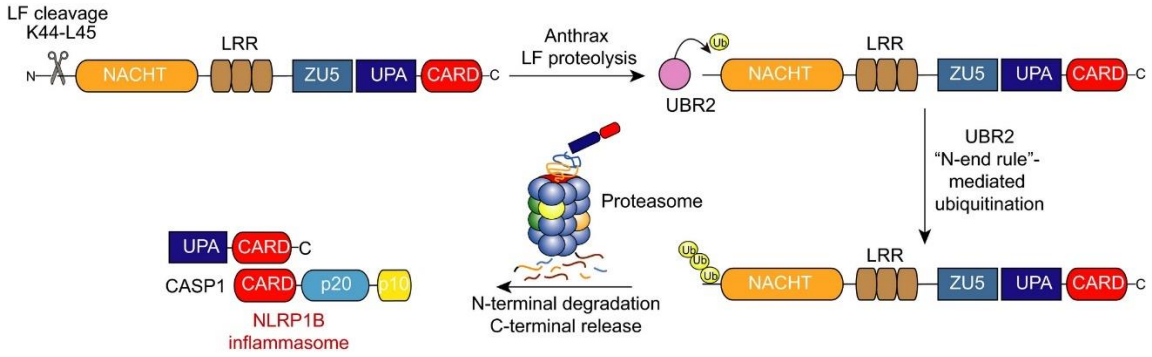

Figure 9. Functional degradation model for NLRP1b activation. Lethal factor (LF) cleaves at the N-terminus allowing UBR2 to recognize and ubiquitinate the N-terminus of NLRP1B. UBR2-mediated ubiquitination induces the proteosome degradation of NLRP1b. The C-terminal UPA-CARD is liberated and forms the NLRP1b inflammasome. Originally published in Immunological Reviews. The NLRP1 and CARD8 inflammasomes. Cornelius Y. Taabazuing et al. © John Wiley & Sons A/S 2020. CC BY. (120).

2.2.3 NLRC4 inflammasome

The organization of NLRC4 is similar to that of other NLR family members; it is composed of a C-terminal LRR, NACHT domain, followed by a N-terminal CARD domain instead of the usual PYD domain. NLRC4 is mainly activated by flagellin, type III (T3SS) and type IV secretion systems (T4SS) by various gram-negative bacteria, including *Shigella flexneri*, *Legionella pneumophila*, and *Pseudomonas aeruginosa* (121–123). To date, no association between the components of the T3SS, T4SS and flagellin have been shown to directly interact with NLRC4, instead it is presumed pathogen detection is facilitated by the upstream regulators from the NAIP (neuronal apoptosis inhibitory proteins) family (124). NAIPs are tripartite proteins containing a Baculovirus inhibitor of apoptosis protein repeat (BIR-domain), a central nucleotide binding and oligomerization domain (NOD) and C-terminal leucine rich repeat (LRRs). NAIP proteins function as co-receptors for NLRC4 by detecting specific PAMPs and initiating NLRC4 self-association (124, 125). Murine genome encodes for multiple NAIPs while the human genome only encodes a single NAIP gene (126–128). The central NOD domain of NAIPs dictates its specificity for various PAMPs. For example, NAIP5/6 are able to detect bacterial flagellin, whereas NAIP1 binds to T3SS needle protein (129, 130). Since humans encode a single

NAIP, different isoforms of the NAIP gene as a result of alternative splicing are assumed to confer similar specificity to PAMPs (128). As shown in **Figure 10** interferon regulatory factor 8 (IRF8) is present in the cell under basal conditions; in the presence of IFN/LPS IRF8 induces transcriptions of various NAIPs. Ligand bound NAIP complexes with NLRC4 initiating rapid self-association of NLRC4. It has been noted NLRC4 is able to directly interact with the CARD domain of caspase-1 without the need of the adaptor protein ASC; however procaspase-1 activation is reduced (131). Incorporation of ASC to the NLRC4 complex leads to an enhancement of procaspase-1 activation, thus promoting a higher inflammatory response.

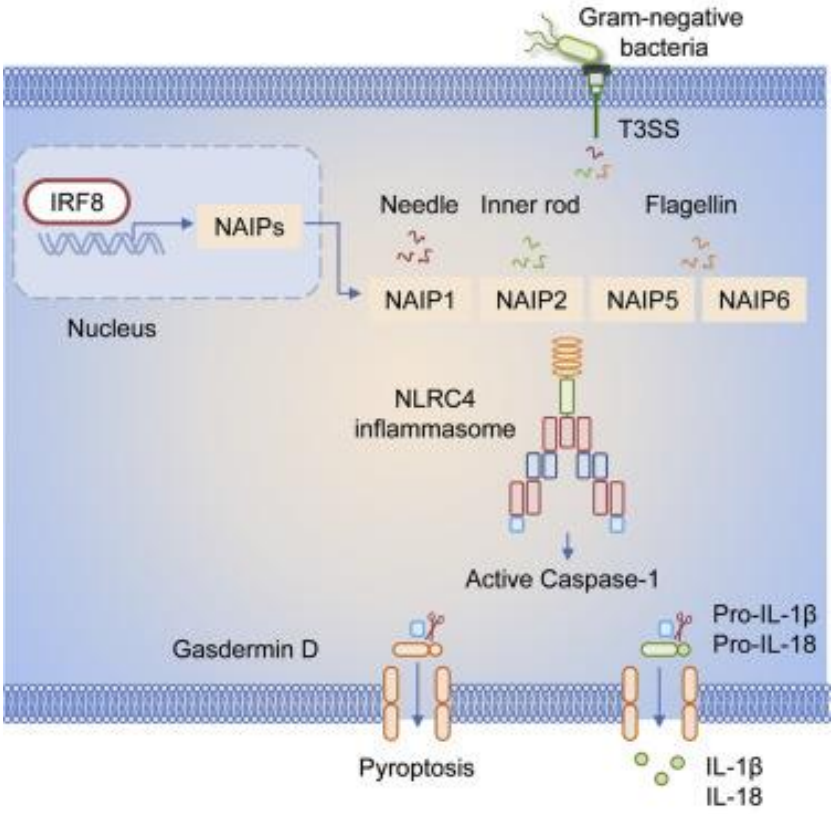

Figure 10. NLRC4 inflammasome activation. NLRC4 activation requires NAIP for PAMP recognition. Upon stimulation by IFNs and LPS, transcription factor IRF8 induces the expression of various NAIPs. NAIPS sense T3SS, T4SS, and bacterial flagellin of gram-negative bacteria. Binding of NAIP to PAMPs allows it to complex with NLRC4 initiating NLRC4 inflammasome formation. Reprinted from Cell, 173, Rajendra Karki, IRF8 Regulates Transcription of Naips for NLRC4 Inflammasome Activation, pg 920-933, Copyright 2018, with permission from Elsevier. (127)

2.2.4 Aim2 inflammasome

AIM2 is a critical inflammatory receptor necessary for the recognition of cytosolic DNA (90, 91). AIM2 consists of a N-terminal PYD domain connected to a C-terminal

hematopoietic interferon-inducible nuclear protein with a 200-amino acid repeat (HIN200) domain (81). Furthermore, the HIN200 domain is subdivided into two OB (oligonucleotide/oligosaccharide binding) folds necessary for nucleic acid binding, termed OB1 and OB2 (132). OB1 and OB2 are connected by a long linker composed of a helix-loop-helix motif (133). OB1 and OB2 folds consist of highly conserved topological arrangement of five β-strands; interaction between the two folds is accomplished through extensive hydrophobic interactions (134). A comparison of ALR HIN domains reveals structural similarities in three different sub-classes; HIN-A, HIN-B, and HIN-C, each with their own function and DNA binding affinity (135). Under basal conditions the HIN200 domain serves a secondary purpose, to keep AIM2 in an autoinhibited state through $AIM2^{PYD}$-HIN200 interactions (136). As shown in (**Figure 11**) binding of cytosolic DNA to the HIN200 domain releases it from its autoinhibited state. Both OB1 and OB2 contain positively charged patches of arginine and lysine residues that directly interact with the DNA phosphate backbone (136). Binding of HIN200 to dsDNA allows for multiple monomers of AIM2 to bind the dsDNA. Clustering of AIM2 leads to the nucleation of the $AIM2^{PYD}$ (137), which recruits ASC through $AIM2^{PYD}$-ASC^{PYD} interactions (137). This assembly carries ASC^{CARD} for caspase-1 recruitment and activation, leading to pyroptosis.

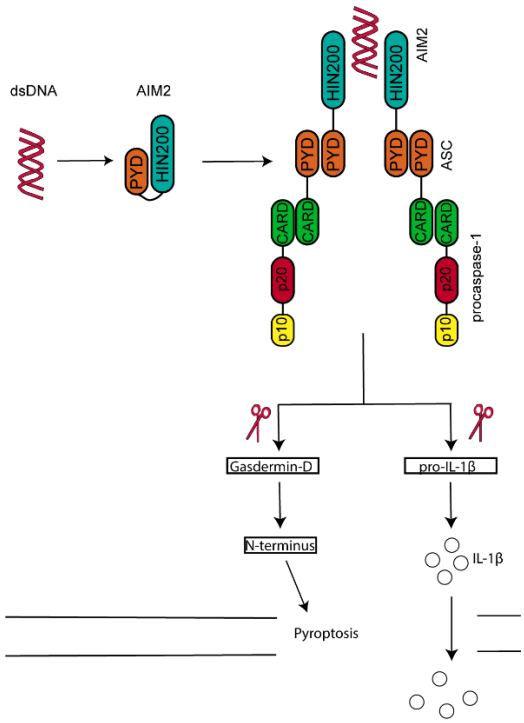

Figure 11. AIM2 inflammasome activation. Prior to AIM2 activation, N-terminal PYD and HIN200 region are complexed maintaining AIM2 in an autoinhibitory state. The presence of dsDNA activates AIM2 and interacts with the HIN200 domain of AIM2. Multiple copies of AIM2 interact with the dsDNA causing the recruitment of ASC through the $AIM2^{PYD}$ domain and procaspase-1 through the ASC^{CARD} domain forming the AIM2 inflammasome complex. Activated caspase-1 cleaves gasdermin-D and pro-IL-1β into active forms resulting in pyroptosis and release of IL-1β.

2.2.5 Pyrin

Pyrin is a large 86 kDa protein located in immune cells (138–140). Pyrin is composed of four functional domains: a pyrin domain (PYD), a zinc finger domain (bBox), coiled coil domain (CC), and a B30.2/SPRY domain (138). Unlike the rest of the inflammasome sensors Pyrin reacts to pathogen activity indirectly rather than through the direct recognition of PAMPs (141). Activation of Pyrin is dependent on the modification of Rho/A/B/C GTPases by bacterial toxins/effectors (101, 141, 142). Modification of Rho GTPases include adenylation, glycosylation, and ADP-ribosylation (141). Modified Rho GTPases haves been shown to affect microtubule dynamics, specifically actin polymerization (141, 143). Changes in actin polymerization are sensed by Pyrin, leading to its activation. Prior to Pyrin activation, Pyrin exists in an autoinhibited state. Pyrin contains two phosphorylation sites, Ser-208 and Ser-242, which are required for 14-3-3 binding (143). Following bacterial virulence and Rho GTPase modification, dephosphorylation of both serine sites removes 14-3-3 releasing Pyrin from its autoinhibited state. Once in active form, Pyrin self-associates through its coiled-coil domain, leading to the recruitment of ASC through its PYD domain and the recruitment of procaspase-1.

2.3 ASC

2.3.1 ASC Structure

The inflammasome adaptor ASC is a 195 amino acid protein consisting of a N-terminal PYD domain and a C-terminal CARD domain connected by a 23-amino acid linker (**Figure 12**) (144). Both the PYD and CARD domain of ASC adopt the six helical bundle motif typical of the Death Domain superfamily (145, 146). The PYD domain of ASC shares structural similarities common to other PYD domains, such as a long loop connecting H2 and H3, and a short H3. The ASC^{PYD} surface is highly bipolar composed of negatively charged amino acid residues located at H1 and H4, and a positively charged surface containing positively charged residues located at H2 and H3 (61, 86). The large charge-charge interaction is largely conserved among PYD domains and is the predominant interaction involved in ASC^{PYD} self-association. ASC^{PYD} type I interaction involves residues E13 (H1), D51 (H4), H5, and D48 (H3-H4 loop) interacting with residues K21(H2), R41(H3), and C-terminus of H5 (85, 137). Furthermore H2 and H3 are orientated perpendicular to H1 and H4, allowing ASC^{PYD} binding motifs to further interact with other available ASC^{PYD} during self-association (103). Additionally, ASC^{PYD}-ASC^{PYD} type I interactions are supported by various hydrophobic interactions. Three solvent exposed residues L25, P40, and L45 were found to interrupt ASC^{PYD} self-association (147). P40 is involved in a type III interaction between H2-H3 loop of one ASC^{PYD} with H1-H2 corner of another ASC^{PYD} (137). Particularly, L25A mutations have been shown to disrupt

ASC^{PYD} self-association; as confirmed by NMR-based chemical shift analysis, L25 mutations structurally perturb the preceding residue K24 resulting in the destabilization of H3, thus reducing the ability of ASC^{PYD} to self-associate (85). In addition, 11 conserved hydrophobic residues (I8, L12, L15, L20, F23, L27, L52, L56, L68, V72, M76) buried within the PYD core are necessary for the stabilization of ASC^{PYD} structure and filament formation (86, 147). Mutations at any of these amino acid residues result in loss of ASC^{PYD} self-association capabilities and collapse of the ASC^{PYD}. Cryo-EM structure of the ASC^{PYD} filament reveal the formation of a tightly packed helical filament with a hollow center of ~ 20 Å and an outer diameter of ~90 Å (137). Type I, II, and III interactions were shown to play an important role in the formation of the helical filament. The type I interaction is predominant resulting in buried surface area of 880 $Å^2$ compared to 540 $Å^2$and 360 $Å^2$ buried surface area from type II and Type III interactions, respectively (137).

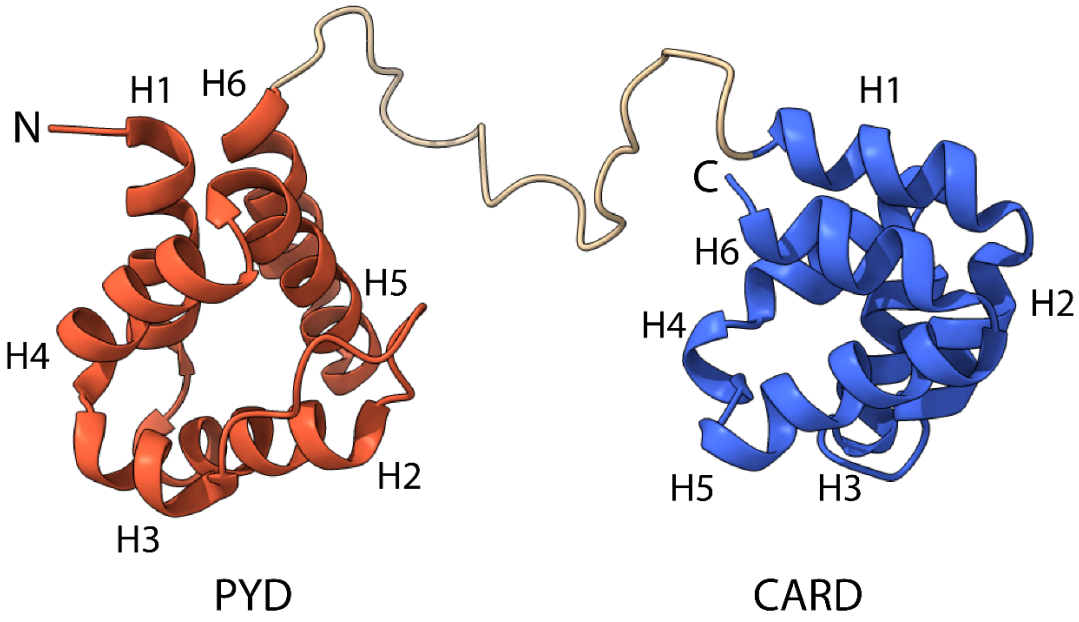

Figure 12. Structure of ASC. 3D solution structure of ASC as determined by NMR (pdb 2KN6) (145). PYD and CARD domain of ASC are shown in orange and blue, respectively. N and C denote the N-terminus and C-terminus of the protein. H1-H6 denotes the conserved six helix bundle representative of the death domain superfamily. Ribbon diagram was generated using ChimeraX (148).

ASC^{CARD} adopts the conserved six helical bundle present in death domains. However, ASC^{CARD} contains several unique features compared to other CARD containing proteins. ASC^{CARD} does not display a fragmented helix 1 (H1a and H2b), H2 and H3 have a different orientation, and the electrostatic surface has an even distribution of positive and negatively charged residues on the surface (67, 145). NMR chemical shift analysis indicates the presence of three contacting regions involved in ASC^{CARD}- ASC^{CARD} self-association; these regions located at the N- and C- terminus of H1, H6, N- and C-terminus of H5 and H6, and H2 and H3 constitute the type I, II, and III interactions involved in self-association (145). Cryo-EM structures of ASC^{CARD} indicate the ability of ASC^{CARD} to self-

associates into helical filaments with an inner diameter of ~ 10 Å and an outer diameter of ~ 80 Å (74). Similar to ASC^{PYD}, ASC^{CARD} filament formation is mediated by Type I, II, and III interactions. Type I interactions involve contacts between residues R119 (H2) with residues E130, D134, and R160 of H1 and H4 (74). These residues are complementary pairs and are the predominant interaction in filament formation. Type II interactions involve contribution from the hydrophobic residues W169 (H4-H5 loop) and Y187 (H6). Lastly, type III interactions involve residue R160 (H4) interacting with residue D143, and E144 of H3 (74). Mutations of the aforementioned residues in Type I, type II, and Type III were found to completely abolish filament formation, confirming their importance to filament formation (74).

2.3.2 ASC Function

ASC was originally discovered in leukemia HL-60 cells, it was detected as an aggregate speck-like complex in apoptotic cells indicating a role for ASC as an inducer of the apoptotic pathway in the presence of certain anti-cancer drugs such as etoposide or vincristine (144). Regulation of ASC expression was shown to be affected by aberrant methylation of its promoter region; increased methylation of the ASC promoter region effectively silences ASC expression providing breast cancer and various cancer lines the ability to escape death and continue proliferation (149, 150). As a result of its ability to be methylated in various cancer cell lines, ASC was deemed a pro-apoptotic factor and was alternatively named Target of Methylation-induced gene Silencing 1 (TMS1). Early in its inception, ASC(TMS1) was determined to be caspase-9-dependent leading to the redistribution of ASC in the cytosol to form perinuclear aggregates (ASC specks) similar to the spherical structures originally seen by Matsumoto *et al.* (151). Although ASC was originally described as a pro-apoptotic protein, it quickly became evident that it played a vital role in pyroptosis. Under basal conditions ASC localizes to the nucleus in resting macrophages (18). Activation of the inflammatory response by PAMPs or DAMPs prompts the self-association of ASC from the nucleus to the cytosol. Formation of the ASC pyroptosome is mediated mainly by ASC self-association resulting in a large molecular platform with a dimeter of ~ 1 μm necessary for procaspase-1 activation (152). It has been determined that only one ASC speck forms per cell and ASC speck formation is a fast process occurring within minutes of a PAMP/DAMP stimulus. Additionally, super-resolution microscopy studies of full-length ASC have shown that ASC self-associates to form rings (ASC specks) of ~ 0.6 - 0.7 μm that interact with similar ring-like structures of NLR, situating pro-caspase-1 in the center and initiating pyroptosis (153). Furthermore, TEM studies of full-length ASC show its propensity to form filamentous macrostructures. ASC tends to form long filaments (600- 800 nm) of 6.4 ± 0.8 nm average width (154). ASC filaments stack laterally and are composed of 2-7 filament bundles. Interestingly ring-like structures observed in TEM agree with the ASC dimer model derived from molecular docking using HADDOCK, suggesting the ASC dimer is a necessary step for ASC self-association (154).

2.3.4 ASC isoforms

Besides the ability of ASC to act as an adaptor between inflammatory sensor and effector, ASC is thought to also play a role in modulating the inflammatory response. ASC exists as four different isoforms. Canonical ASC containing a PYD, and CARD connected by a 23-amino acid linker, ASCb structurally similar to ASC, but with a 4-amino acid linker, ASCc consisting of a CARD domain and linker, but lacking H3-H6 of the PYD, and ASCd containing H1 and H2 of the PYD linked to a novel 69 amino acid domain (**Figure 13**) (18). The CARD, PYD and linker region of ASC is encoded by 3 exons. Exon 1 encodes for the PYD, exon 2 for the linker region, and exon 3 for the CARD domain (155). Generation of ASCb, ASCc, and ASCd is accomplished through alternative splicing of the 3 exons to generate the different isoforms of ASC (155). Generated isoforms display different characteristics compared to ASC.

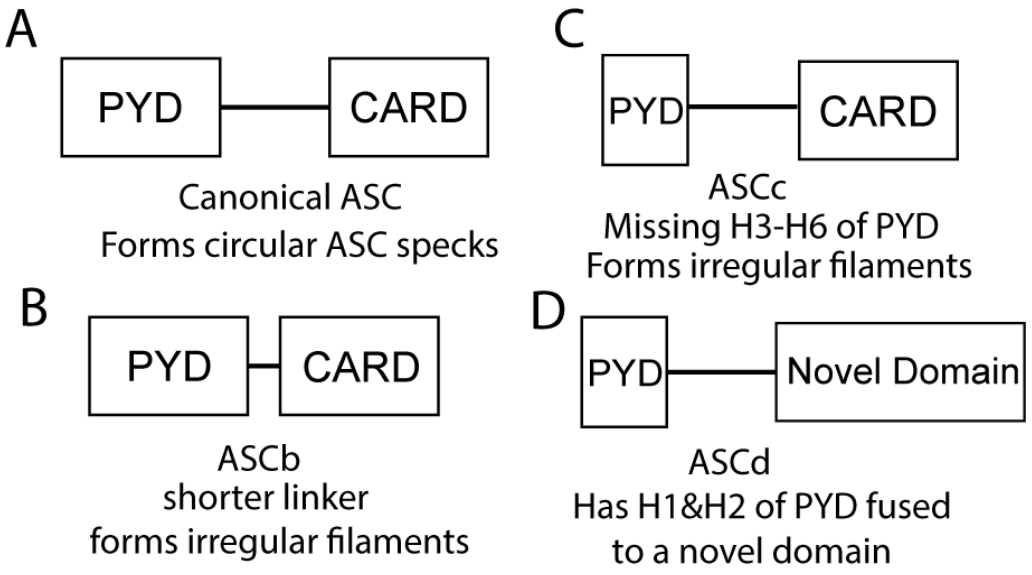

Figure 13. ASC isoforms. (A) Canonical ASC containing a PYD and CARD domain connected by a 23 amino acid linker. (B) ASCb containing both the PYD and CARD domain connected by a 4 amino acid linker. (C) ASCc contains the CARD domain and linker region but is missing H3-H6 of the PYD domain. (D) ASCd represents a novel domain connected to a partial PYD domain.

ASC is shown to localize to the nucleus in resting macrophages. During an inflammatory event, ASC migrates to the cytosol forming the ASC speck (18). Formation of the ASC speck was found to localize with NLRP3 through PYD-PYD interactions and procaspase-1 through CARD-CARD interactions, thus promoting the activation and release of IL-1β from immune cells (18). ASCb does not display a similar localization pattern to ASC, instead ASCb is diffused throughout the cytoplasm. With the only difference being the length of the linker, it is presumed a specific linker length is required for nucleus localization. Unlike ASC, ASCb is incapable of forming the prototypical ASC specks, instead forming irregular filaments. ASCb contains the CARD and PYD domain retaining its ability as an inflammasome adaptor. The preserved CARD and PYD domain

are able to interact with both NLRP3 and procaspase-1 eliciting an inflammatory response, albeit lower compared to ASC (18). Likewise, ASCc is present in the cytoplasm of resting macrophages as long filamentous structures. The lack of a PYD domain renders it incapable of interacting with the inflammasome sensor NLRP3. However, the intact CARD domain was shown to be able to interact with procaspase-1, though an inflammatory response was not produced (18). Lastly, ASCd is present diffused throughout the cytoplasm and is unable to interact with either NLRP3 nor procaspase-1 (18).

Expression of each isoform was found to vary based on the cell line used. PMA differentiated THP-1 cells were found to predominantly express ASC, ASCb, and very low levels of ASCc (18). In contrast, human peripheral blood macrophages (PBM) were shown to upregulate ASCb expression in the presence of LPS, while mouse J774A1 macrophages showed high expression of ASCc compared to ASC and no expression of ASCb was observed (18). The co-expression of multiple isoforms in either differentiated cells or LPS treatment suggest a level of regulatory control in inflammasome complexation resulting in varying efficacies. Co-expression studies of ASC, ASCb, and ASCc notably influenced the localization of each isoform. ASC co-expresses with ASCc in the perinuclear aggregates, eliminating the irregular ASC filaments observed when expressed alone. However, ASC and ASCb co-expression did not form the perinuclear aggregates seen in ASC. Instead, both ASC and ASCb were recruited to the nucleus and formed irregular perinuclear aggregates.

2.4 Caspase-1

Caspases are cysteine-aspartic proteases involved in regulating cellular death through either apoptosis or pyroptosis (156). Caspases are categorized into two distinct groups based on their ability to activate inflammatory or apoptotic pathway. Caspases involved in apoptosis include caspase-2, caspase-3, caspase-6, caspase-7, caspase-8, caspase-9, and caspase-10; whereas inflammatory caspases include caspase-1, caspase-4, caspase-5, and caspase-12 (**Figure 14**). Activation of the inflammasome complex generally involves the recruitment of procaspase-1 for pyroptosis to occur in the cell. It is synthesized in an inactive precursor. Procaspase-1 is a multidomain protein consisting of a N-terminal CARD connected to a large p20 subunit by a CARD domain linker (CDL) and a smaller p10 subunit connected to the p20 subunit by an interdomain linker (IDL). Formation of the inflammasome complex serves as a molecular platform attracting and increasing the local concentration of procaspase-1 to facilitate autocatalytic processing. As identified by cell studies, confocal imaging shows colocalization of procaspase-1 to the ASC speck. Procaspase-1 specks are smaller ~ 0.4 μm in diameter and occupies the central area of the ASC speck. Recruitment of procaspase-1 to the inflammasome complex is facilitated through CARD-CARD interactions between ASC^{CARD} and the CARD of procaspase-1. Activation of procaspase-1 to its active form requires self-processing at both its CDL and IDL to generate multiple p20/p10 fragments to form a tetramer composed of two p20 and

two p10 fragments (157). The newly formed tetramer is generally considered the active form of caspase-1. Activated caspase-1 is necessary for the activation of pro-inflammatory cytokines pro-IL-1 β and pro-IL-18 and gasdermin-D.

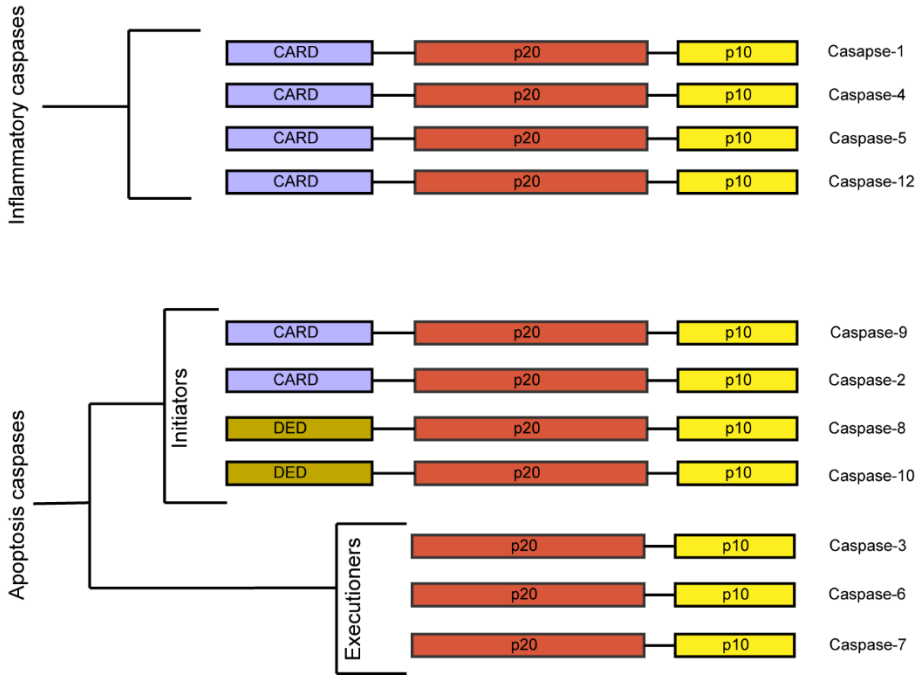

Figure 14. Hierarchal representation of caspases involved in apoptosis and inflammation. Caspases consist of a large p20 subunit, smaller p10 subunit, and a CARD or DED domain. Inflammatory caspases-1/4/5/12 contain a CARD domain allowing for direct participation in inflammasome complexation (caspase-1) or direct interaction with LPS (caspase-4/5/12) resulting in pyroptosis of the cell. Caspases involved in apoptosis are broken into two categories, imitator caspases (caspase-9/2/8/10) involved in upstream signaling events and executioner caspases (caspase-3/6/7) that facilitate apoptosis of the cell.

2.4 Gasdermin-D

The cytosolic substrate responsible for permeabilizing the cell membrane and initiating pyroptosis was identified as Gasdermin-D (GSDMD). Two independent studies confirmed the existence of gasdermin-D as the executioner in pyroptosis of the cell. A research study using genome wide CRISPR-Cas-9 knockout of murine macrophages identified a gRNA sequence highly conserved between mice and human involved in pyroptosis known as gasdermin-D (21). Simultaneously, another group identified the existence of gasdermin-D using quantitative mass spectrometry to detect molecules directly interacting with the NLRP3 inflammasome (104). Gasdermin-D is a 53 kDa protein cleaved into a 31 kDa N-terminal fragment and a 22 kDa C-terminal fragment by capsase-1. The C-terminal fragment plays an auto-inhibitory role in preventing gasdermin-

D from misfiring. The active N-terminal fragment has increased affinity for phosphatidylinositol (4)-phosphates, phosphatidylinositol (4,5)-bisphosphate, and phosphatidylserine (PS) on the cellular membrane (105). Binding of the N-terminal fragment to the cell membrane induces the formation of a pore. The pore formed is estimated to contain between 16-24 monomers of gasdermin-D with an inner diameter between 10 20 nm, allowing for the passage of IL-1β and IL-18 outside the cell and leading to pyroptosis (158, 159).

Chapter 3

Experimental Techniques

3.1 NMR spectroscopy

Nuclear magnetic resonance (NMR) spectroscopy relies on the existence of the nuclear spin, which is an intrinsic property of each nucleus that depends on the rotational motion of the nucleus about its own axis. The nuclear spin is given by the spin angular momentum *I*. The total angular momentum of each spin is quantized and represented by the angular momentum vector L (160):

$$|L| = \hbar\sqrt{I(I+1)}$$

Eq (1)

Where ħ is Planck's constant divided by 2π and I is the nuclear spin quantum number. By convention, the angular momentum in the z-direction is represented by the following equation (160, 161):

$$I_z = \hbar m$$

Eq (2)

Where *m* is a magnetic quantum number ranging from -I,-I+1,…,I-1,I representing the direction of the spin about the z-axis. For example, a spin of I = ½ will possess two possible quantized states +½ and –½ along the z-axis. All nuclei with non-zero spin quantum number possess a magnetic moment (**Figure 15A**) defined as (160–162):

$$\mu = \gamma I_z$$

Eq (3)

Where μ is the magnetic moment, γ is the gyromagnetic ratio, and *I* is the angular momentum vector. Nuclei possessing spin are classified as magnetically active, while those containing no spin are termed NMR silent (160, 162). Nuclei with odd mass numbers having a half-integer spin quantum number (^{1}H, ^{13}C, ^{15}N, ^{31}P, and ^{19}F) are considered magnetically active. Nuclei with even mass number and even atomic number have a spin value of I = 0 and are NMR silent. Nuclei with even mass number and odd atomic number have a spin value of I = 1 (^{2}H and ^{14}N).

In the absence of a magnetic field, nuclei are orientated randomly, however, in the presence of a magnetic field nuclei will adopt a specific orientation with respect to the magnetic field, either parallel (with the magnetic field) or anti parallel (against the magnetic field) (**Figure 15B**) (160, 162, 163). This effect, known as Zeeman splitting, orientates nuclei with I = ½ into a low energy state (α spin) and a high energy state (β spin) separated by an energy gap (**Figure 15B**) (160, 162). The energy needed to excite from the α state to the β state is given below (160):

$$\Delta E = \hbar y B_0$$

Eq (4)

Where ħ is Planck's constant divided by 2π, γ is the gyromagnetic ratio, and B_0 is the strength of the magnetic field. Increasing the strength of the magnetic field (B_0) increases the energy of separation. As seen in **Figure 15A** the stationary magnetic field B_0 generates a torque on nuclei possessing spin causing it to precess about the z-axis (**Figure 15A**). For reference purposes, we consider precession to be clockwise for nuclei with positive gyromagnetic ratio and counterclockwise for nuclei with negative gyromagnetic ratio. Precession about the z-axis is given by the Larmor frequency:

$$\omega = -y B_0$$

Eq (5)

In solution, nuclei with I = ½ exist in either the α or β state. For nuclei with negative gyromagnetic ratio the β state has a lower energy and is more populated at equilibrium. For nuclei with positive gyromagnetic ratio the α state is lower energy and more populated at equilibrium. The relative population of each nuclei in the α and β state can be calculated using the Boltzmann equation below (160, 161, 163). Where N_α and N_β are the number of nuclei in each state, *k* is the Boltzmann constant, and T is temperature.

$$\frac{N_\alpha}{N_\beta} = e^{\frac{-\Delta E}{kT}}$$

Eq (6)

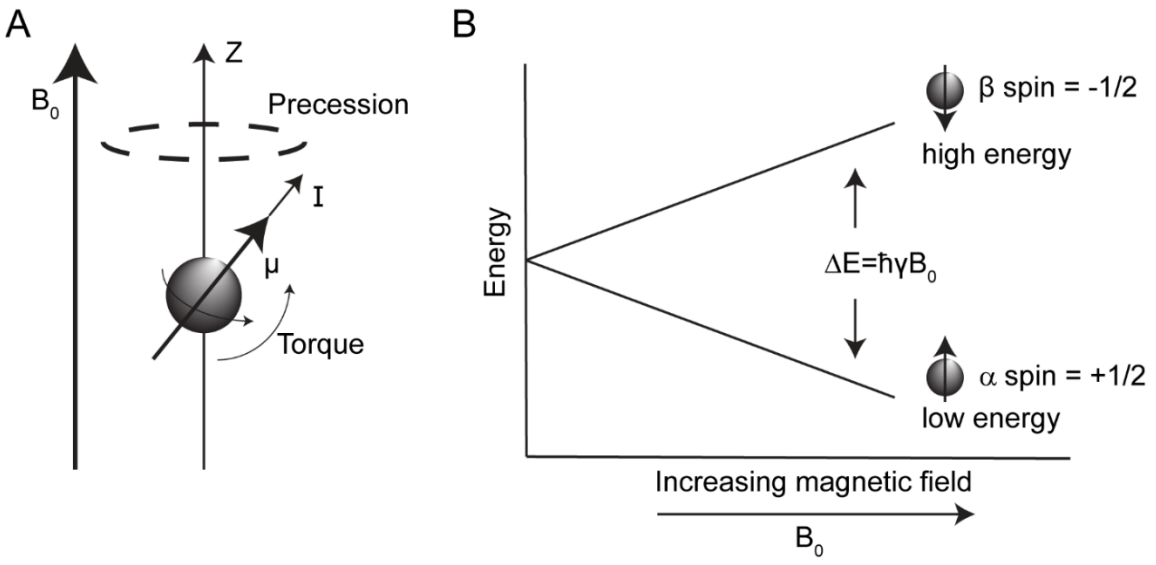

Figure 15. Precession of nuclei and Zeeman energy level diagram. (A) Stationary magnetic field B_0 generates a torque on the nuclei causing it to precess about the z-axis. (B) In a magnetic field, magnetically active nuclei with I= ½ orient with (α spin) or against (β spin) the magnetic field.

3.1.1 Chemical shift

Chemical shifts report on the local magnetic environment of the nuclei. For protein and peptide studies using NMR, chemical shifts are used for the identification of torsion angles, hydrogen bonding and secondary structure (164). The chemical shift (δ) is expressed mathematically as follows (160–162):

$$\delta(ppm) = \frac{v_i - v_{ref}}{v_{ref}} \; x \; 10^6$$

Eq (5)

Where ν_i is the frequency of the nucleus, ν_{ref} is the resonance frequency for a reference nucleus. The resonance frequencies observed are associated with differences in the chemical environment as this, in turn, influences the magnetic environment. Each nucleus experiences three major effects: shielding, dipolar coupling, and scalar coupling affecting the observed frequency (161, 163). The orbital motion of electrons around the nucleus creates a small magnetic field that opposes the applied external magnetic field, thus reducing the magnetic field experienced by the nucleus. This effect is known as shielding the nucleus from the applied magnetic field. A highly shielded nucleus (greater electron density) will absorb at lower frequency compared to a deshielded nucleus (**Figure 16D**). Because the chemical shift depends on the electron density around the nucleus,

electronegative groups attached to molecules will result in significant differences in the chemical shift of each nucleus (**Figure 16A**).

Similarly, the resonance frequency of a nuclei can be influenced by the spin state of another nucleus via a "through-space" interaction known as dipolar coupling (160, 161, 163). The dipolar coupling interaction is strongly dependent on the distance between two nuclei, at distances greater than 5 Å the effect largely disappears (161, 163). In a magnetic field, molecule can align with or against the magnetic field. As shown in **Figure 16B,** the field experienced by nucleus A can be either enhanced or decreased depending on the orientation of nucleus B. The magnitude of this effect is given by the following equation (160, 162, 163):

$$d = \frac{\mu_0 \gamma_A y_B h}{8\pi^2 r^3}$$

Eq (6)

Where μ_0 is the magnetic permeability of free space, γ_A and γ_B are the gyromagnetic ratios of each nucleus, r is the distance between the two nuclei, and h is Planck's constant. Lastly, electrons shared through chemical bonds can also alter the electron shielding of each nucleus. This effect known as scalar coupling is generally weaker compared to shielding or dipolar coupling (**Figure 16C**). Unlike dipolar coupling and shielding effects, scalar coupling does not depend on the external magnetic field and is mediated through bonds rather than the "through-space" effect of dipolar coupling. The magnitude of this effect decreases with increasing number bonds.

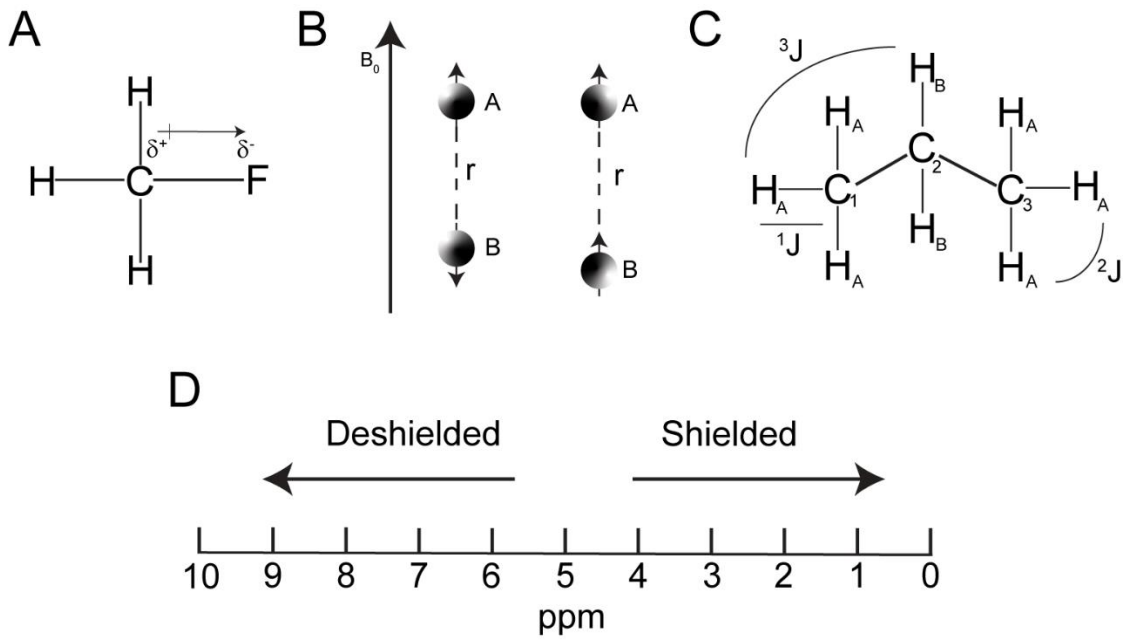

Figure 16. Factors affecting the chemical shift. (A) Shielding due to the presence of electronegative atoms. (B) Dipolar coupling between two nuclei within 5Å of each other. (C) Scalar coupling: the spin state of nearby nuclei are affected by nearby nuclei through the electrons in covalent bonds. (D) Effects of shielding and deshielding on the observed frequencies.

3.1.2 NMR relaxation

Nuclear Magnetic Resonance (NMR) allows us to obtain information related to biomolecules at the atomic scale (165, 166). Proteins are dynamic; they sample a wide range of conformational ensembles to achieve a specific functionality. NMR is uniquely suited for reporting on protein dynamics as it provides resolution at the atomic scale. The time behavior of each nuclei (spin) can be extracted to provide information related to the dynamics of the protein (162, 163, 167). Time scales relevant for protein functionality can be monitored with different NMR parameters tailored to each time regime. As shown in **Figure 17**, different motional regimes correspond to different dynamic information related to the protein. The ps-ns timescale (fast regime) describes the local motion of the protein backbone and overall tumbling (166, 167). Intermediate motion on the μs-ms timescale features important biological functions such as catalysis, ligand binding, and allostery (162, 167). Slower dynamics (ms-s timescale) include protein folding/unfolding and aggregation (167, 168). ^{15}N NMR relaxation is routinely used to obtain information related to protein dynamics (160, 161, 163). ^{15}N relaxation experiments allow for the characterization of the backbone N-H bond vector. ^{15}N relaxation is dependent on the orientational motion of the N-H vector with respect to the external magnetic field. The quantification of these motions

generally includes three types of experiments: longitudinal relaxation T_1, transverse relaxation T_2, and the heteronuclear ^{1}H-^{15}N NOE (160, 162, 163).

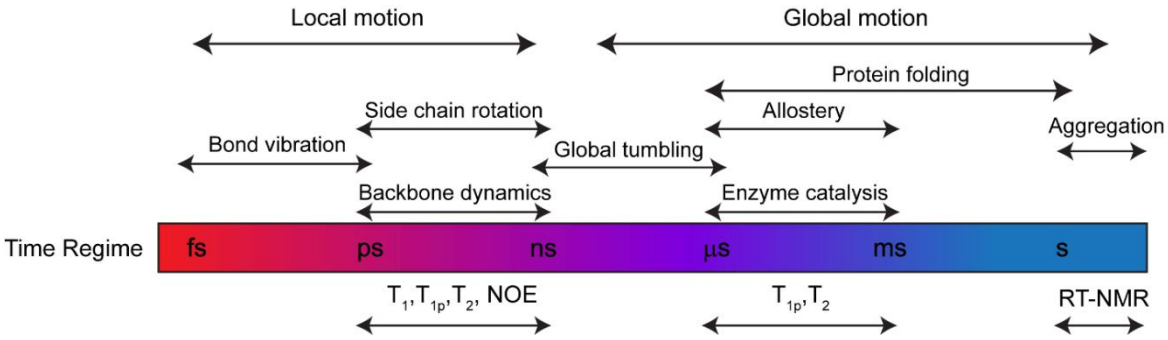

Figure 17. Timescales experienced by proteins. NMR techniques used to probe various timescales are shown above. ^{15}N relaxation experiments T_1, T_2, and NOE probe the ps-ns and µs-ms timescale.

Longitudinal relaxation (T_1) represents the time required for the magnetization to return to thermal equilibrium. T_1 is primarily affected by interactions between magnetic dipoles. As previously described, the effect of these interactions consists in the magnetic dipole of one nucleus influencing the local magnetic field of nearby nuclei (160, 161, 163). The magnitude of the dipole-dipole interaction strongly dependens on the distance between the two nuclei. The dipole-dipole interaction is stronger at distances < 5 Å (160, 161, 163). The ^{15}N-^{1}H bond distance is 1.02 Å making it the dominant relaxation mechanism. Measurement of T_1 is generally performed using 1D inversion-recovery NMR experiments. As shown in **Figure 18A,** a 180° pulse inverts magnetization from the +z axis to -z magnetization. The magnetization in the -z axis is allowed to return to thermal equilibrium at varying delay times, resulting in changes in the magnitude of the net magnetization (160, 161, 163, 165). A 90° pulse is then applied to bring the magnetization to the xy plane for acquisition. However, T_1 relaxation experiments are generally performed using a 2D ^{15}N-HSQC pulse sequence with Freeman-Hill cycling to obtain better peak resolution and avoid peak crowding (160, 165). Use of the 2D ^{15}N-HSQC T_1 pulse sequence results in an exponential decay; the longer the delay time the less signal present during acquisition (**Figure 18B**).

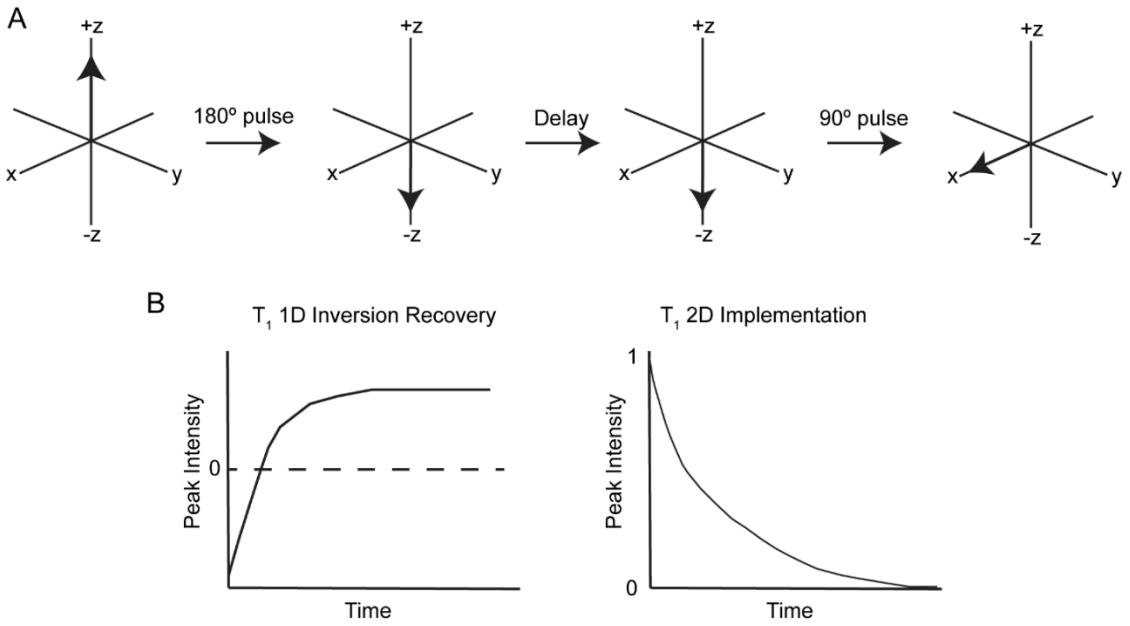

Figure 18. Measurement of T_1. (A) Vectorial representation of the inversion-recovery experiment. Longitudinal relaxation is measured as return of magnetization to equilibrium. Varying the delay results in signal intensity changes. (B) Graph showing the results of the inversion-recovery experiment. 2D ^{15}N-HSQC implementation results in an exponential decay.

Transverse relaxation (T_2) results from the loss of phase coherence of the magnetization in the x-y plane. Experimentally, T_2 is recorded via a spin echo and allows for the simultaneous quantification of motion in the ps-ns and μs-ms timescales **(Figure 19)** (160, 161, 165). The predominant factor affecting T_2 relaxation is the anisotropy of the chemical shift (CSA) and its orientation rate with respect to the external magnetic field. The electron density surrounding the ^{15}N nucleus is anisotropic, resulting in chemical shift anisotropy. The asymmetric distribution of electrons around the ^{15}N nucleus causes the amide to experience different local magnetic fields depending on its orientation, thus resulting in a loss of phase coherence in the transverse plane. In contrast to solid-state NMR, molecules tumble fast enough in solution that the CSA effect is averaged over time in chemical shift measurements. However, the CSA effect can be determined in relaxation experiments in solution, particularly for large macromolecules such as proteins that tumble slowly, which enhances magnetic relaxation via CSA (160–162). As shown in spin echo experiment (**Figure 19),** the magnetization in +z is rotated to the x-y plane using a 90° pulse; modulating the delay affects the loss of coherence, afterwards, a 180° pulse is applied to refocus magnetization followed by a delay of equal length to the first one, acquisition is then recorded after the echo, varying the delay allows for determination of T_2 (161–163).

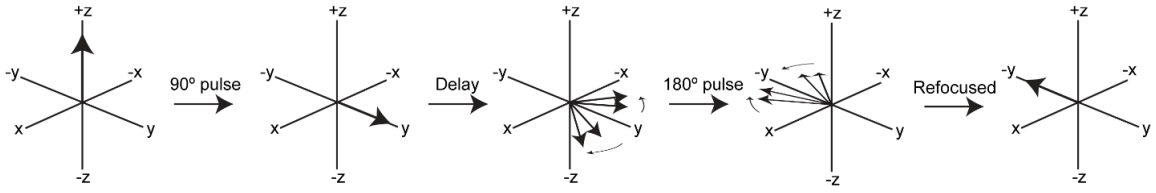

Figure 19 Measurement of T_2. Vectorial representation for experimentally determining T_2 via a spin echo. A 90° pulse is applied to place the magnetization in the transverse plane (x-y plane). During the delay, the spins lose coherence. After the delay, a 180° pulse inverts the spins refocusing them. Varying the delay time directly affects signal intensity, allowing for the determination of T_2.

The steady-state [^{15}N-^{1}H]-NOE represents the cross-relaxation occurring between the backbone ^{15}N-^{1}H bond. The ^{15}N-^{1}H NOE gives information in the ps-ns timescale **(Figure 17)**. The ^{15}N-^{1}H distance is fixed at 1.02 Å and variations within the NOE correlate to differences in motion (165). Fast motions, NOE values < 0.6 are indicative of flexible loops, linkers, and disordered regions, while NOE values > 0.8 reflect rigid regions such as the presence of secondary structures. NOE data is typically acquired using two different spectra: with and without proton saturation. Experimentally, the NOE ratio is typically determined using two experiments: a saturated experiment in which the NOE is occurring by saturating (making equal) the populations of one spin and measuring the change in intensity of nearby nuclei (< 5 Å apart), and an unsaturated experiment used as reference where the NOE does not occur because no saturation is applied. The NOE is calculated using the following equation (161, 165, 166):

$$NOE = \frac{\text{I\_Saturated}}{\text{I\_Unsaturated}}$$

Eq (7)

Where I_Saturated is the intensity of the NMR signal corresponding to the nucleus affected by NOE, and I-Unsturated is the intensity of the NMR signal corresponding to the same nucleus in the absence of NOE (no saturation).

The equations relating the relaxation parameters, T_1, T_2, and NOE, with the spectral density functions (J(ω)) can be derived from the perturbing Hamiltonian of the relaxation mechanisms affecting the spins. These equations, reflecting the amount of motion at each frequency (ω), are shown below:

$$R_1 = \frac{1}{T_1} = 3AJ(\omega_n) + AJ(\omega_H - \omega_n) + 6AJ(\omega_H + \omega_N) + BJ(\omega_N)$$

Eq (8)

With A representing the dipolar constant:

$$A = \frac{\mu_0 \gamma_A y_B h}{8\pi^2 r^3}$$

Eq (11)

J(ω) representing the motion at a particular frequency:

$$J(\omega) = \frac{\tau_c}{1 + \omega^2 \tau_c^2}$$

Eq (12)

$$R_2 = \frac{1}{T_2} = 2AJ(0) + \frac{A}{2}J(\omega_H - \omega_N) + \frac{3A}{2}J(\omega_n) + 3AJ(\omega_H) + 3AJ(\omega_H + \omega_N) + \frac{2B}{3}J(\omega_n) + \frac{B}{2}J(0)$$

Eq (13)

B representing the effects of anisotropy:

$$B = \frac{(\Delta_\sigma)^2 (B_0 y_N)^2}{3}$$

Eq (14)

$$NOE = 1 + \frac{y_H}{y_N}\frac{\sigma}{R_1}, \sigma = -AJ(\omega_H + \omega_N) + 6AJ(\omega_H - \omega_N)$$

Eq (15)

3.1.3 Model-free

The model-free formalism is commonly used to extract dynamic information from relaxation parameters. In this approach, a correlation function is approximated and used to calculate the spectral density functions. Thus, no specific model of the motion is assumed, hence "model-free." The correlation function of the model-free formalism assumes that the internal motion of each N-H vector is independent from the overall motion of the protein (169). The correlation function $C(\tau)$ in the model-free formalism adopts the form:

$$C(\tau) = C_0(\tau)C_I(\tau)$$

Eq (16)

Overall tumbling of the protein for isotropic diffusion is given by C_0

$$C_0 = \frac{1}{5}e^{\frac{-\tau}{\tau_m}}$$

Eq (17)

and internal motion is given by C_I

$$C_I(t) = S^2 + (1 - S^2)e^{\frac{-\tau}{\tau_e}}$$

Eq (18)

S^2 is a generalized order parameter measuring the amplitude of motion of the N-H bond vector, τ_e is the internal correlation time, and τ_m is the overall tumbling motion for isotropic diffusion ($1/\tau_m = 6D$) (169). Considering molecules with isotropic diffusion, the spectral density function adopts the form shown below:

$$J(\omega) = \frac{S^2\tau_m}{1 + (\omega\tau_m)^2} + \frac{(1 - S^2)\tau}{1 + (\omega\tau)^2}$$

Eq (19)

With $J(\omega)$ is the spectral density function, ω is the frequency, τ_m is the overall motion, with τ defined as:

$$\frac{1}{\tau} = \frac{1}{\tau_m} + \frac{1}{\tau_e}$$

Eq (20)

The first term represents the overall tumbling of the molecule with contributions from S^2. The generalized order parameter (S^2) can range in values from 0 to 1. S^2 value of 0 represents a completely unrestricted motion of the N-H bond vector, while a value of 1 represents a fully restricted N-H bond vector (165, 169). The second term reflects the overall tumbling of the molecule with contributions from the internal motion. However, the model-free does not consider slow motions that can occur between the ns-ps timescale and motions closer to global tumbling. An extended model-free spectral density function

is used to account for these motions by adding an additional exponential term to account for these motions (170):

$$J(w) = \frac{S^2\tau_m}{1+(\omega\tau_m)^2} + \frac{\left(1-S_f^2\right)\tau_f}{1+\left(\omega\tau_f\right)^2} + \frac{\left(S_f^2-S^2\right)\tau_s}{1+(\omega\tau_s)^2}$$

Eq (21)

With

$$\frac{1}{\tau_i} = \frac{1}{\tau_m} + \frac{1}{\tau_i}$$

Eq (22)

With i = f, s.

3.2 Transmission Electron Microscopy

3.2.1 Electron wavelength

Transmission electron microscopy (TEM) is a powerful technique that uses a beam of electrons to obtain images of matter at a resolution typically higher than that achieved with optical microscopy. The high resolution allows for imaging at the angstrom level, but it is also used for visualization of cells, organelles, viruses, and nanoparticles (171). Theoretically, for a given optical system the resolution limit of the system is given by Rayleigh's criterion (172, 173):

$$\delta = \frac{0.61\lambda}{n\sin\alpha}$$

Eq (23)

δ is the resolution limit, λ is the wavelength, *n* is the refractive index between the sample and lens, and α is the angle of collection of the magnifying lens. *n*sinα is commonly referred to as the numerical aperture (NA). Utilization of shorter wavelengths increases the resolution limit according to Rayleigh's criterion. In regular optical microscopy, it is typically not possible to lower the resolution under 200 nm (172). To overcome this limitation, electrons are used in TEM due to their wave-like properties according to the de Broglie wave equation (172, 174):

$$\lambda = \frac{h}{p} = \frac{h}{mv}$$

Eq (24)

Where p is the momentum of the electron, *m* is mass of electron, ν is the velocity of the electron and *h* is Planck's constant. the kinetic energy in electron volts of an electron subjected to an electric potential difference (V) created by an electric field is shown below (172, 174):

$$eV = \frac{mv^2}{2}$$

Eq (25)

Where *e* and *m* and v are the charge, mass and velocity of the electron.

Rearranging the equation gives the electron wavelength:

$$\lambda = \frac{h}{\sqrt{2meV}}$$

Eq (26)

At high electric potential (> 100 kV), the total kinetic energy of the electron increases substantially as ν increases (relativistic mass) and must be taken into account (174). Considering the relativistic effects of the electron at higher energies the relativistic wavelength of the electron is given (172, 174):

$$\lambda = \frac{h}{2m_0 eV\left(1 + \frac{eV}{2m_0 c^2}\right)}$$

Eq (27)

Where h is Planck's constant (6.626×10^{-34} N·m·s), m_0 is the rest mass of the electron (9.109×10^{-34} kg), e is the charge of electron (-1.602×10^{-19} C), V is the acceleration voltage (V), and c is the speed of light in a vacuum (2.998×10^8 m/s). As shown in **Table 1,** increasing the accelerating voltage decreases the wavelength of the electron beam. At an accelerating voltage of 200 kV the electron wavelength is 2.51 pm, which increases the resolution limit according to the equation 20.

Table 1 Voltage and corresponding wavelength

Accelerating voltage (kV)	Electron wavelength (nm)
100	0.00370
120	0.00335
140	0.00307
160	0.00285
180	0.00267
200	0.00251

3.2.2 Electron sources

The electron beam can be generated from two main sources, a thermoionic gun or a field-emission gun (FEG). A thermionic gun generates electrons when heated at temperatures. Thermionic sources use materials such as tungsten filaments, lanthanum hexaboride (LaB_6), or cerium hexaboride (CeB_6) that are capable of being heated to temperatures over 1,700 K (172, 174). Tungsten filaments are easier to maintain and cheaper but have poor resolution due to the high operating temperature needed to produce electrons. LaB_6 crystals have a lower operating temperature, a 1 μm fine tip, and a higher current density compared to tungsten filaments. The result is an electron source capable of working at lower temperatures increasing its operating life, brightness levels (10x) greater than tungsten filaments, and a smaller crossover (minimum cross-sectional area of the beam) angle improving the coherence of the electron beam (172). However, due to the volatile nature of LaB_6 a higher vacuum is needed to reduce carbon contamination. FEG's uses an applied electric field on a tungsten needle with a tip radius of < 0.1 μm to emit electrons (173, 174). FEG's can provide ~ 100 times brightness, highly coherent beam, and a smaller beam size compared to thermoionic guns. Two types of FEG's are commonly used; a Schottky FEG or a cold FEG. Schottky FEG uses a tungsten emitter or, in the case of hot-FEG, a zirconium oxide (ZrO_2) coated tip to increase electrical conductance (173, 174). Typically, these FEG's have an operating temperature between 1,600 – 1,800 K and offer an energy spread of 1 eV. For energy spreads lower than 0.5 eV a cold FEG is used at a significantly lower operating temperature (300K) compared to other electron sources (174).

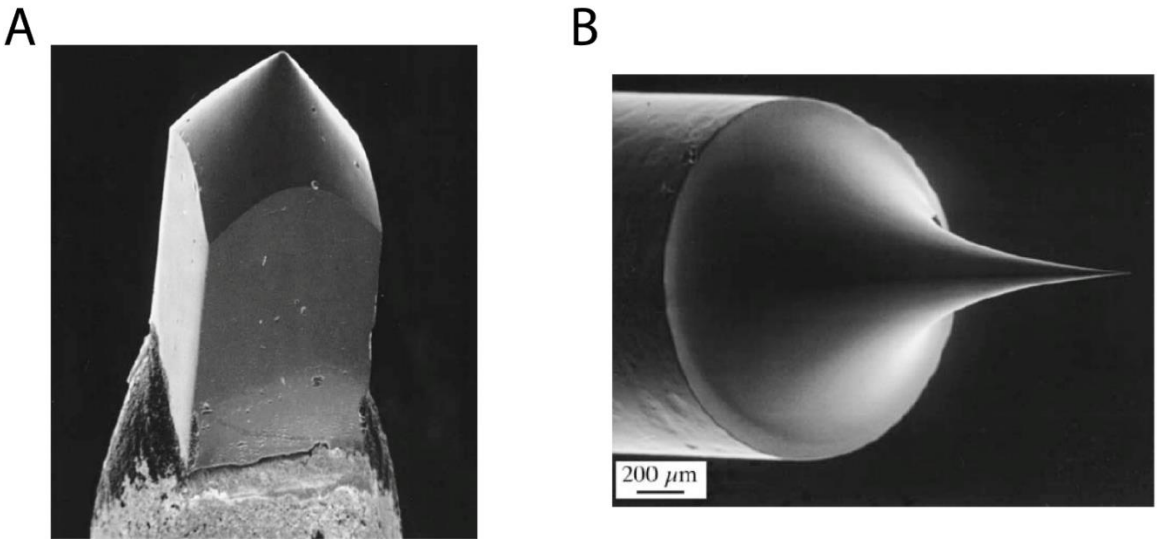

Figure 20. SEM images of electron sources. (A) LaB_6 crystal electron source and (B) A FEG displaying the fine tip of the tungsten needle. Reprinted by permission from Springer Nature Customer Service Centre GmbH: Springer Nature. Springer eBook. Electron Sources, David B. Williams, C. Barry Carter, Copyright (2009). (172).

3.2.3 Electromagnetic lenses

The TEM is equipped with electromagnetic lenses capable of focusing the electron beam. As shown in **Figure 21** the electron beam travels down the optical axis as it is refocused and magnified several times by multiple magnetic lenses. Magnetic lenses are constructed using two soft iron materials wrapped in Cu coils to generate a magnetic field (173, 174, 174). The magnetic field aids in converging the beam to a focal point. The electron beam passes through a first set of lenses; the condenser lenses C1 and C2. The C1 lens controls the spot size of the electron beam. The C2 lens is used to control beam brightness and converges the beam onto the sample. The diffraction of the electron beam from the specimen is then passed through the objective lens. The objective lens is necessary for focusing and magnifying the specimen and further magnification of the image is accomplished by the intermediate lens and projector lens. It should be noted the electromagnetic lenses presented above suffer from both spherical aberrations (C_s) and chromatic aberrations (C_a) (172, 174). Spherical aberrations are the result of electrons deviating from the optical axis affecting the focus of the sample. Chromatic aberrations are due to differences in electron energies as they are accelerated. The different electron energies form a disk instead of a focal point making it difficult to properly focus the image.

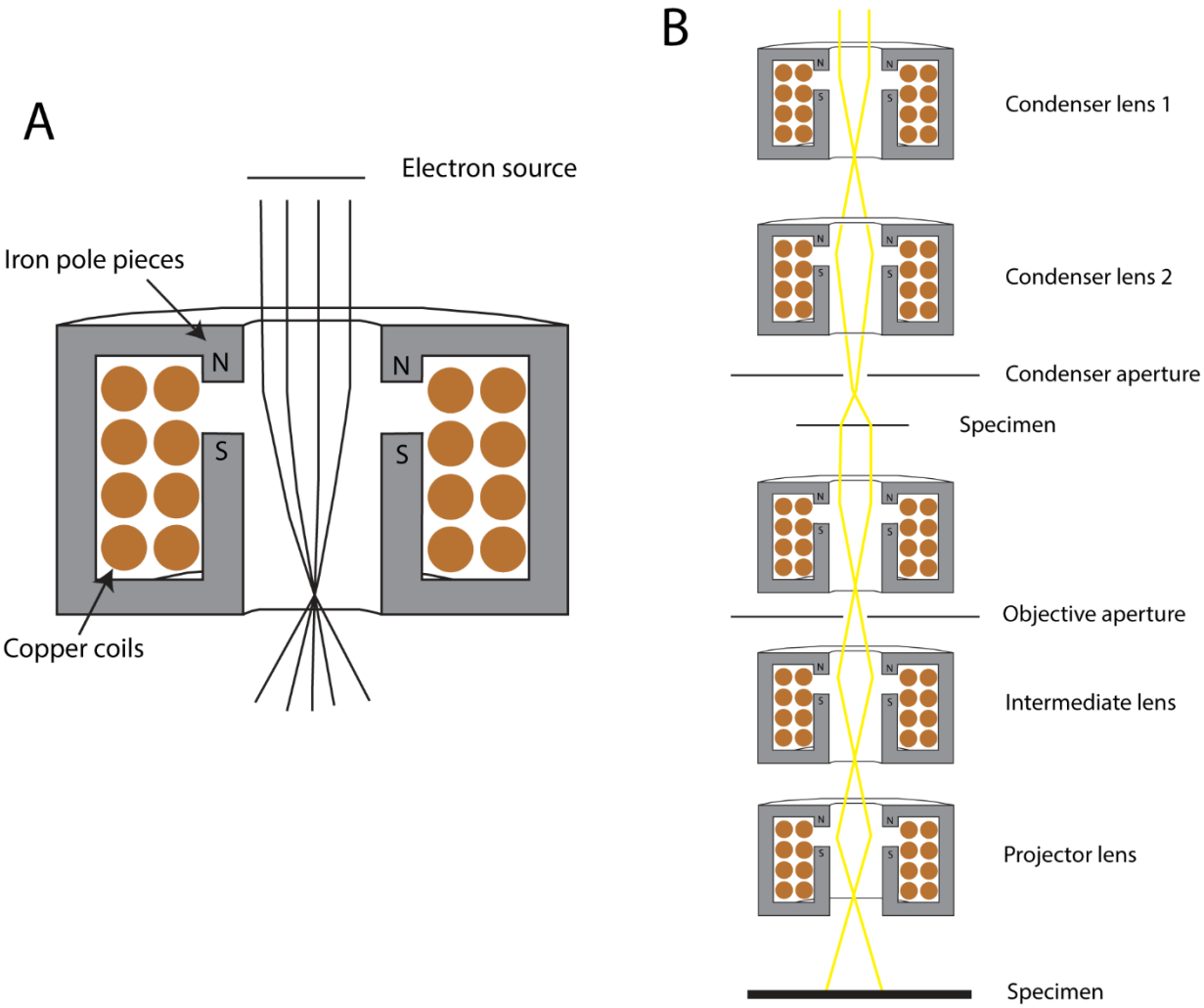

Figure 21 Electromagnetic lenses used in TEM. (A) Schematic diagram of electromagnetic lenses. Current passing through the copper coils magnetizes the iron pole pieces deflecting electrons back to the optical axis. (B) Ray diagram of a TEM microscope showing the multiple electromagnetic lenses and apertures used.

3.2.4 TEM sample preparation

TEM grids are commonly used for sample support. They can be composed of a variety of materials (Cu, Ni, Au, Mo, Ti, Be, and stainless steel) and can be further modified by coating the grid with different support films (carbon, formvar, SiO, etc..) of varying thickness (173). Copper grids with carbon films are commonly used due to their low cost, nonmagnetic properties, chemical stability, and electrical conductivity. TEM grids are 3 mm in diameter and range in thickness from 5 – 30 μm (173). Samples composed of polymers, biological materials and specific light elements (C, O, H, and N) that are too thin or transparent can be negatively stained to enhance their contrast (175). Negative staining involves the use of heavy metals such as phosphotungstic acid (PTA) or uranyl acetate to

surround the sample with dense metals, blocking incoming electrons around the sample (175). Because electrons cannot pass through the dense material the sample appears brighter relative to the dark background. Positive staining involves enhancing the contrast

of a sample by coupling a heavy metal (lead citrate, osmium tetroxide) to polymers, and biological samples(175).

3.3 Dynamic light scattering

Dynamic light scattering (DLS) uses a monochromatic light source to illuminate particles in solution. The scattered light reports on the shape and size of macromolecules (176). The benefits of DLS are its versatility in using a wide range of buffers and temperatures. In addition, DLS only requires a small sample size. DLS is widely used in the characterization of micelles, proteins, nanoparticles, and nucleic acids. Assuming a spherical shape, DLS is routinely used to determine the size of molecules and nanoparticles in solution as well as the homogeneity of the sample (176, 177). Additionally, DLS is useful in monitoring aggregate sizes and distribution due to the scattering intensity being proportional to sixth power of the molecular radius (178). Therefore, different populations of oligomers can be reported. Furthermore, protein-protein interactions, protein-RNA interactions, and protein-small molecule interactions can be monitored in solution (176). Changes in hydrodynamic sizes are readily observed and correlated to protein complexes.

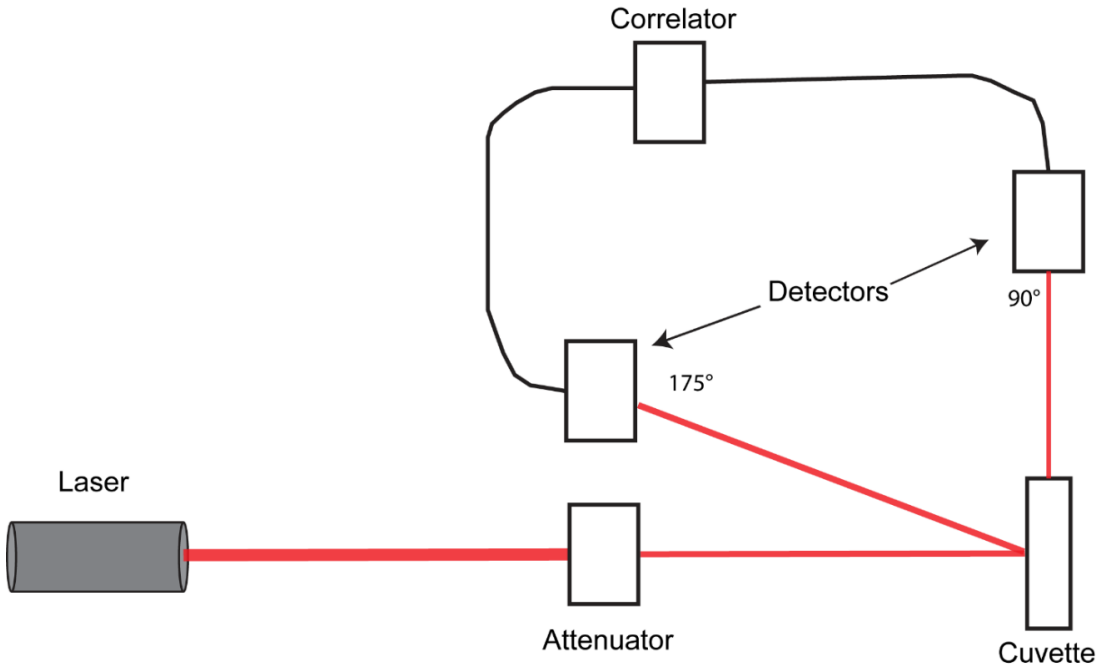

Figure 22. Schematic representation of a DLS instrument. **A laser is used as a light source. The laser passes through an attenuator to reduce the intensity of light prior to illuminating the sample. Detection can be accomplished either with a backscatter detector at 175° degree or at 90°. Finally, the scattering intensity is processed through a correlator.**

3.3.4 Dynamic light scattering theory

DLS relies on the principle of Brownian motion for determining particle size. Larger molecules diffuse slowly whereas smaller molecules tend to diffuse rapidly (**Figure 23**). When molecules are illuminated by a monochromatic source, in this case an infrared laser, the intensity of the scattered light fluctuates as a function of time given by the correlation function G(τ) (176):

$$G(\tau) = I(t)I(t+\tau)$$

Eq (28)

Where τ is the difference in time between the two measurements. The average of the function with time, shown in equation 26, provides a measure of how fast the intensity of the scattered light decays and how fast it changes orientation (176, 177):

$$g(\Delta\tau) = \frac{f(t)f(t+\tau)}{f(t)f(t)}$$

Eq (29)

The dependence of the correlation function with time is approximated to an exponential function where B is the baseline, A is the amplitude, and Γ is the decay rate of the scattered intensity (**Figure 23**) (176, 177):

$$G(\tau) = B + Ae^{(-2\Gamma\tau)}$$

Eq (30)

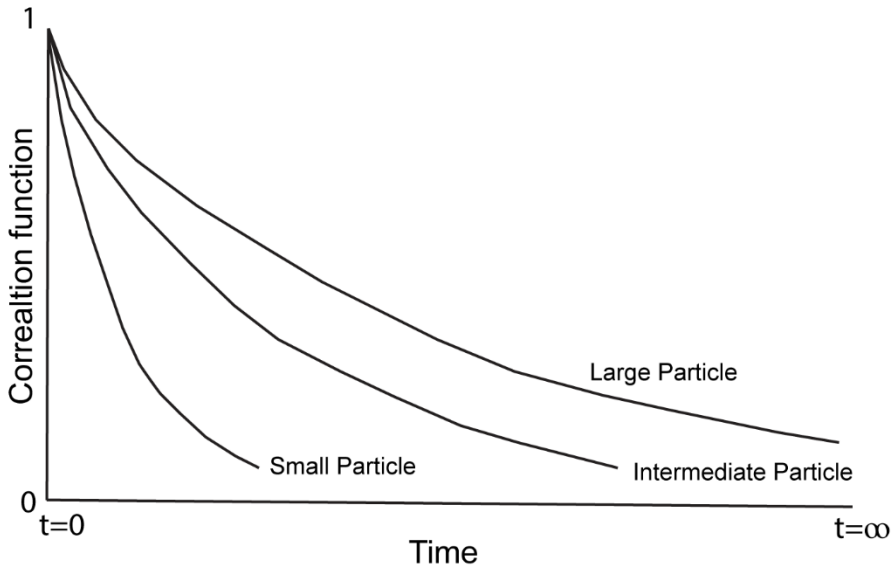

Figure 23. Dependence of the correlation function with time. The decay rate of the intensity of the scattered light changes depending on the particle size. The intensity of the scattered light decays faster for smaller particles compared to larger particles.

Γ is proportional to the scattering vector (q) and the diffusion constant (D) with the scattering vector being proportional the refractive index (η), the wavelength of the light (λ) and the scattering angle (θ) (176, 177).

$$\Gamma = Dq^2 = D\left(\frac{4\pi\eta \sin\frac{\theta}{2}}{\lambda}\right)^2$$

Eq (31)

Determination of the diffusion constant (D) allows for the calculation of the hydrodynamic radius (particle size) using the Stokes-Einstein equation (176, 177):

$$D = \frac{k_B T}{6\pi\eta r_h}$$

Eq (32)

Where k_B is Boltzmann constant (1.380×10^{-23}kg.m^2.s^{-2}.K^{-1}), T is the absolute temperature, η is the viscosity of the medium and r_h is the hydrodynamic radius of the molecule

4. Project aims

The objectives of this doctoral thesis are as follows:

1. Objective 1: Determine a biological role for the ASC isoform, ASCb, using biophysical techniques.
    a. Determine the capabilities of ASC and ASCb in regulating inflammasome complexation at the molecular level.
    b. Identify differences in ASC and ASCb that affect their ability to self-associate.

2. Objective 2: Determine the role played by the protein interdomain linker in the self-association capabilities of ASC and ASCb. Can this linker be optimized to increase inflammasome activity.?
    a. Develop an engineered isoform of ASC, called ASC3X, to monitor the effects of linker length on protein self-association.
    b. Determine whether there is an optimal linker length by comparing ASC, ASCb and ASC3X behavior at the molecular level.
    c. Determine the influence of the linker length on the interdomain dynamics between the PYD and CARD.

5. Results

Objective 1

Publication 1

Diaz-Parga, P., & de Alba, E. (2022). Inflammasome regulation by adaptor isoforms, ASC and ASCb, via differential self-assembly. *Journal of Biological Chemistry*, 298, 101566.

Objective 2

Publication 2

Diaz-Parga, P., Gould, Andrea & de Alba, E. (2022). Natural and engineered inflammasome adaptor proteins reveal optimum linker length for self-assembly. *Journal of Biological Chemistry*.

Publication 1

This research was originally published in the Journal of Biological Chemistry. Pedro Diaz-parga, and Eva de Alba. Inflammasome regulation by adaptor isoforms, ASC and ASCb, via differential self-assembly. J Biol Chem. 2022; 298:101566.

JBC RESEARCH ARTICLE

Inflammasome regulation by adaptor isoforms, ASC and ASCb, *via* differential self-assembly

Received for publication, July 14, 2021, and in revised form, December 30, 2021 Published, Papers in Press, January 8, 2022,
https://doi.org/10.1016/j.jbc.2022.101566

Pedro Diaz-Parga[1,2] **and Eva de Alba**[1,*]

From the [1]*Department of Bioengineering, School of Engineering, and* [2]*Quantitative Systems Biology Ph.D. Program, University of California, Merced, Merced, California, USA*

Edited by Peter Cresswell

ASC is an essential adaptor of the inflammasome, a micrometer-size multiprotein complex that processes proinflammatory cytokines. Inflammasome formation depends on ASC self-association into large assemblies *via* homotypic interactions of its two death domains, PYD and CARD. ASCb, an alternative splicing isoform, activates the inflammasome to a lesser extent compared with ASC. Thus, it has been postulated that adaptor isoforms differentially regulate inflammasome function. At the amino acid level, ASC and ASCb differ only in the length of the linker connecting the two death domains. To understand inflammasome regulation at the molecular level, we investigated the self-association properties of ASC and ASCb using real-time NMR, dynamic light scattering (DLS), size-exclusion chromatography, and transmission electron microscopy (TEM). The NMR data indicate that ASC self-association is faster than that of ASCb; a kinetic model for this oligomerization results in differing values for both the reaction order and the rate constants. Furthermore, DLS analysis indicates that ASC self-associates into more compact macrostructures compared with ASCb. Finally, TEM data show that ASCb has a reduced tendency to form densely packed filaments relative to ASC. Overall, these differences can only be explained by an effect of the linker length, as the NMR results show structural equivalence of the PYD and CARD in both proteins. The effect of linker length was corroborated by molecular docking with the procaspase-1 CARD domain. Altogether, our results indicate that ASC's faster and less polydisperse polymerization is more efficient, plausibly explaining inflammasome activation differences by ASC isoforms at the molecular level.

Inflammation is a vital physiological process that protects organisms from pathogens and injury. The inflammatory response is triggered by a myriad of stimuli that have been classified as pathogen- and damage-associated molecular patterns (PAMPs and DAMPs, respectively) (1, 2). The presence of these danger signals prompts the formation of a multimeric protein complex known as the inflammasome. The assembly of the inflammasome is driven by self-association and oligomerization of three types of proteins: sensor, adaptor, and effector. There are different families of inflammasome sensors that show specificity for certain PAMPS and DAMPS. Cytosolic sensors are mainly represented by the NLRs (nucleotide-binding domain leucine-rich repeat containing receptors) and ALRs (absent in melanoma 2-like receptors) families and pyrin (3–6). Inflammasome sensors are modular and typically contain protein–protein interacting death domains: PYD (pyrin domain) and CARD (caspase activation and recruitment domain) (7, 8). Inflammasome sensors self-associate upon activation by danger signals and prompt the oligomerization of the inflammasome adaptor ASC (apoptosis-associated speck-like protein containing a CARD), a bimodular protein with an N-terminal PYD and a C-terminal CARD (3, 4, 9, 10). The inflammasome adaptor acts as a molecular glue by self-associating and tethering multiple copies of the sensor and the effector procaspase-1 (3, 11, 12) (Fig. 1). Inflammasome assembly leads to the activation of procaspase-1, rendering it capable of cleaving pro-IL-1β and pro-IL-18 into their active forms, which are secreted to the extracellular environment to trigger the inflammatory response. Inflammasomes are ∼0.5 μm-size perinuclear puncta formed in the cytosol of activated cells by the oligomerization and self-association of sensor, adaptor, and procaspase-1 (13).

The NLR member NLRP3 is one of the most well-known inflammasome sensors. NLRP3 is expressed in myeloid, muscle and endocrine cells, and neurons (14). NLRP3 remains in an autoinhibited form in the resting state and becomes activated upon stimulation, assembling into a large, micrometer-size cytosolic complex together with the adaptor ASC. NLRP3 becomes functional in a two-step process: priming and activation (15). In the priming step, Toll-like receptors (TLRs) or NODs (nucleotide binding oligomerization domain) and cytokines such as TNF-α trigger the activation of the transcription factor NF-κB promoting the expression of the inflammasome components: NLRP3, procaspase-1, and pro-IL-1β (15, 16). Subsequent posttranslation modifications (ubiquitylation, phosphorylation, and sumoylation) of NLRP3 stabilize the protein in a signal-competent, autosuppressed inactive state that transforms into an activated state upon stimulation (17). Once activated, NLRP3 assembles into the inflammasome: a mature multiprotein-complex particle also composed of ASC and procaspase-1 (the NLRP3 inflammasome), capable of activating IL-1β and IL-18.

* For correspondence: Eva de Alba, edealbabastarrechea@ucmerced.edu.

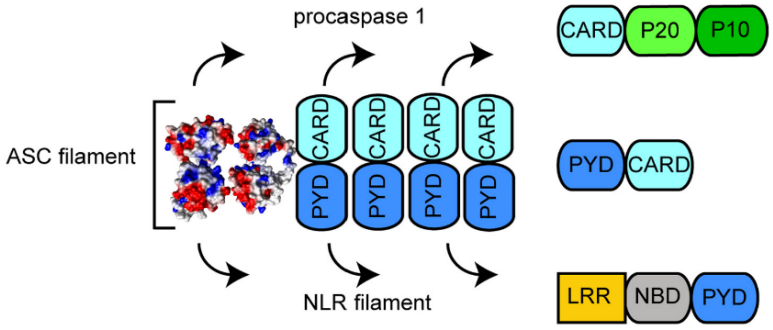

Figure 1. Model for ASC-dependent inflammasome assembly. ASC dimer shown as the filament minimal building block. The ASC filament shows two interacting sides, one for recruiting procaspase-1 CARD and the other for interaction with the PYD of NLRs sensor proteins (12).

The dysregulation of the inflammasome is linked to uncontrolled inflammation as the culprit of an increasing number of inflammatory diseases including rheumatoid arthritis, type I diabetes, asthma, psoriasis, atherosclerosis, and neurodegenerative disorders (18, 19). Therefore, gaining insight into the mechanisms involved in inflammasome regulation and assembly is critical to identify potential targets for therapeutic treatment. Protein isoforms share highly similar amino acid sequences and structures and are known to participate in regulatory roles by tuning and modulating protein function. Thus, the study of the molecular bases underpinning function modulation by protein isoforms is particularly relevant to understand regulation at the molecular level. The inflammasome adaptor ASC has four isoforms: canonical ASC, ASCb, ASCc, and ASCd, which differ in amino acid composition (20). ASC and ASCb are the most similar as both retain the two protein–protein interacting domains, PYD and CARD (Fig. 2*A*), and only differ in the length of the interdomain linker (23 and three amino acids for ASC and ASCb, respectively). ASCc retains the CARD and a fragment of the PYD. ASCd bears only a partial PYD and no CARD. It has been reported that only ASC and ASCb are inflammasome-activating isoforms, as both promote the release of IL-1β (21) and have been shown to colocalize with NLRP3 and procaspase-1 (20). However, ASCb activates the inflammasome to a lesser extent as determined by the amount of IL-1β released and cannot form the typical puncta characteristic of canonical inflammasomes, forming instead filamentous aggregates (20). In contrast, ASCc and ASCd do not colocalize with NLRP3 and cannot generate mature IL-1β, leading to the conclusion that these isoforms are not inflammasome activators. In fact, the release of IL-1β by ASC is diminished in the presence of ASCc, which suggests that the latter acts as an inflammasome inhibitor (20). No clear effect on inflammasome activity has been identified for ASCd, and thus, the function of this isoform is still unknown (20).

To understand the modulation of inflammasome assembly by the activating isoforms, ASC and ASCb, we have studied the self-association properties of both proteins using several biophysical and biochemical techniques. By multidimensional solution NMR, we obtained the ^{15}N and ^{13}C chemical shifts of ASCb's polypeptide backbone to compare to previously published data for ASC (22), revealing that the PYD and CARD structures of both isoforms are very similar as expected due to the identical amino acid sequence. NMR signal intensity decay resulting from oligomerization was monitored by real-time NMR at the individual residue level for both proteins over a period of 65 h. Based on these studies, we determine that ASC and ASCb follow different kinetics for self-association. Moreover, NMR data indicate that the PYD and CARD of ASC behave differently during self-association, whereas no differences were observed for the two domains in ASCb. Oligomer size distribution was analyzed by dynamic light scattering in ASC and ASCb solutions as a function of time during the self-association process, revealing different tendencies in polydispersity that agree with observations from the cell studies. The effect of protein concentration, pH, and time on the oligomerization processes was studied by size-exclusion chromatography (SEC), showing that ASC has a stronger self-association capability compared with ASCb. Additionally, the characteristics of the macrostructures formed by ASCb were investigated by negative-staining transmission electron microscopy (ns-TEM) and compared with previously reported TEM data for ASC. The analysis of ns-TEM micrographs reveals that ASCb also forms filaments of similar thickness to those formed by ASC; however, ASC tends to form bundles composed of a larger number of stacked filaments. Finally, the impact of linker length on the interaction between ASC or ASCb and the CARD of procaspase-1 was studied *in silico* by creating structural models *via* molecular docking.

Results

ASC and ASCb differ only in the linker length at the structural level

The previously reported 3D NMR structure of ASC revealed that the PYD and CARD domains adopt the six-helix bundle motif common to other death domain folds. The two domains are connected by a 23 amino acid–long linker (10). We expect that the structures of the PYD and CARD of ASC and ASCb would be almost identical because the two isoforms only differ in the linker length, and the PYD and CARD of both proteins share 100% amino acid sequence identity (Fig. 2*A*). To

compare structural information of the two isoforms derived from the NMR data, we assigned the ^{15}N and ^{13}C backbone chemical shifts of ASCb (Table S1) and compared this assignment with that reported for ASC (22).

In protein NMR, the [^{1}H-^{15}N]-HSQC spectrum correlating the amide ^{1}H and ^{15}N chemical shifts of the protein backbone is known as the protein fingerprint because it is unique for each protein (11). Figure 2*B* depicts an overlay of the [^{1}H-^{15}N]-HSQC spectra showing that the signals of the PYD and CARD of ASC and ASCb substantially overlap as expected. The more crowded region of the ASC spectrum around 8.5 ppm (for the ^{1}H chemical shift) reflects the additional signals from the longer, semiflexible linker. The average difference in chemical shifts for ^{15}N and ^{1}H of ASC and ASCb *versus* the residue number is very small (Fig. 2*C*), indicating that both PYD and CARD in ASCb are properly folded into the six-helix bundle motif. Amino acids that are close to the linker region in the amino acid sequence or in the 3D structure are expected to show deviations in chemical shifts for both isoforms. This is the case for amino acids H90, Q91, and L112; however, T16 and R33 (ASC numbering) show significant chemical shift variations even though these amino acids are not close to the linker region. We can speculate that the origin of these changes could be related to the oligomerizing properties of ASC and ASCb. In addition, a comparison of the $^{13}C_{\alpha}$ and $^{13}C_{\beta}$ chemical shifts for both isoforms (Fig. S1) indicates that the secondary structure of both proteins is identical, as expected.

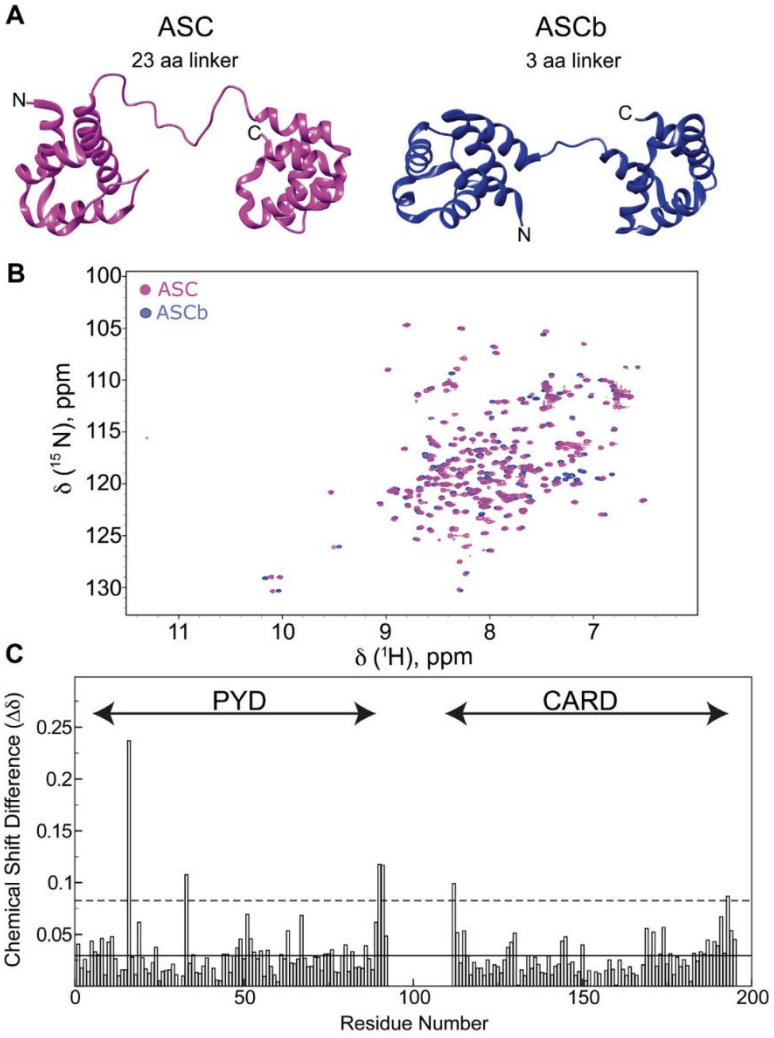

Figure 2. ASC and ASCb structure comparison by NMR. *A*, ribbon diagram of the polypeptide backbone structure of ASC (10) and ASCb (model created with the program Chimera (23) based on the PDB structure of ASC (10)). *B*, 2D-[^{1}H-^{15}N]-HSQC (NMR protein fingerprint of ASC and ASCb showing almost complete signal overlap). *C*, combined-average amide ^{1}H and ^{15}N chemical shift differences between ASC and ASCb as described in the Experimental procedures section (*solid line*: 1 SD; *dashed line*: 2 SD).

Different oligomerization kinetics for ASC and ASCb from real-time NMR

ASC has a strong tendency to oligomerize and polymerizes forming filaments and filament bundles at neutral pH (12). This behavior is a consequence of ASC function as the inflammasome adaptor, which involves self-association and tethering multiple copies of the inflammasome components *via* protein–protein interactions. It has been reported that ASC self-association is reduced at acidic pH (pH 3.8) and concentration values <200 μM; conditions used for the 3D structure determination of ASC by solution NMR techniques (10, 11). However, ASC significantly self-associates at concentrations >200 μM even under acidic conditions. As previously reported, ASC self-association can be detected by a decrease of NMR signal intensity with time (10). This observation results from the formation of large oligomeric species that are "invisible" in solution NMR due to their slow tumbling rate, hence no longer contributing to the signal arising from the monomeric species (24, 25). We have leveraged this behavior to monitor changes in signal intensity upon ASC and ASCb self-association by real-time (RT) NMR. Protein samples are in lyophilized form after purification and start to oligomerize as soon they are dissolved in the NMR buffer. A series of 2D-[^{1}H,^{15}N]-NMR spectra were acquired as a function of time after NMR sample preparation for 65 h. The RT-NMR kinetic experiments were performed on ^{15}N-labeled protein samples at different concentration values (~300–700 μM) to investigate the influence of protein concentration on the kinetics of self-association. The first 1D projection of the 2D experiment reflects the overall signal intensity of the spectra, which significantly decreases with time (Fig. 3*A*) for ASC and ASCb due to the formation of high-order oligomers. The slow tumbling rate of these large oligomers renders them "invisible" in NMR, resulting in signal intensity decrease upon protein self-association. However, careful analysis of the intensity decrease with time reveals that ASC oligomerizes faster than ASCb (Fig. 3*B*). Protein concentration is an important factor prompting polymerization for both ASC and ASCb, as self-association rates are significantly diminished at ~300 μM *versus* ~700 μM (Fig. 3*B*). ASC oligomerizes slightly faster than ASCb at the lowest concentration, but the difference between the two isoforms is small compared with the kinetics at ~700 μM. It is important to note that we have not observed signal broadening nor the

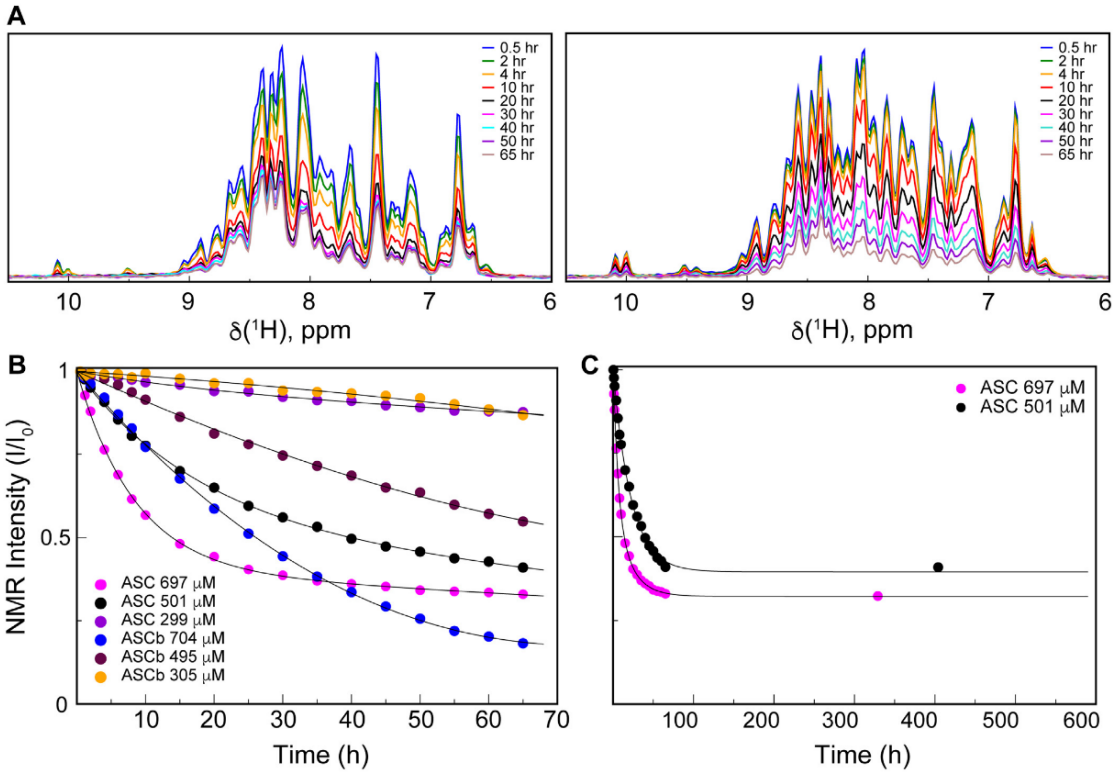

Figure 3. Oligomerization kinetics of ASC and ASCb by RT-NMR. *A*, overall NMR signal decay as a function of time for the oligomerization of ASC (~697 μM; *left panel*) and ASCb (~704 μM; *right panel*). Time points are color-coded as indicated. *B*, normalized overall NMR signal intensity decay *versus* time for ASC and ASCb at the indicated color-coded concentrations. *C*, as in (*B*) for the same ASC samples at the concentrations indicated and time point at approximately 2 weeks after sample preparation.

presence of new signals arising upon ASC or ASCb self-association (Fig. S2). There are several possible explanations for these results: 1) the oligomers formed during the kinetic experiment are already too large to be detected by NMR, 2) intermediate-size oligomers that could give rise to new signals are formed but do not live long enough to be detected.

The overall intensity decays were fitted to single- and double-exponential equations (Equations 1 and 2, respectively) to estimate apparent oligomerization rate constants (k_1 and k_2). It is important to mention that Equations 1 and 2 are logistic functions a priory not related to the underlying self-association mechanism but are particularly useful for comparing the polymerization kinetics of both proteins. Fitting of the NMR intensity decay to a double-exponential *versus* single-exponential improves for ASC but not for ASCb. This result suggests that ASC oligomerization involves at least two steps with different rate constants. The fitting to a double-exponential results in fast and slow rate constants for ASC: k_{1ASC} = 0.15 ± 0.03 h^{-1} and k_{2ASC} = 0.04 ± 0.01 h^{-1}, respectively (Table 1). Thus, one kinetic phase in ASC oligomerization is 3.75 times faster than the other assuming other conditions are identical. This result could reflect the fast formation of an initial oligomer (a nucleation step) that continues growing at a slower rate forming a polymer. The overall signal decay for ASC at ~700 μM reaches 33% of the original intensity at steady-state conditions resulting from the fraction of monomer concentration still present at the end of the kinetic experiment (65 h). Two weeks later, the intensity remains at this same value (Fig. 3*C*).

In contrast, the fitting of the ASCb NMR signal intensity decay to a double-exponential does not result in any significant difference compared with a single-exponential fitting. Thus, ASCb appears to oligomerize with a single kinetic phase with an apparent rate constant k_{ASCb} = 0.02 ± 0.01 h^{-1}. Interestingly, at the final stage of the kinetic experiment, the remaining fraction of ASCb monomeric species is 18%. The fitting of signal intensity decay for ASC and ASCb (~700 μM) to the exponential functions includes a baseline value (A_1 in Equations 1 and 2) that results in 31% and 18% of residual monomeric population for ASC and ASCb, respectively, in agreement with the experimental data. Several parameters indicative of the goodness of the fit are shown in Table 1.

$$y = A_0\, e^{-x\,k} + A_1 \quad (1)$$

$$y = A_0\, e^{-x\,k_1} + A_2\, e^{-x\,k_2} + A_1 \quad (2)$$

To study potentially different behaviors of the two death domains in protein polymerization, we have analyzed the signal intensity decay of the two isoforms at the amino acid level. Figure 4*A* shows, as examples, the fitting of several amino acids located in the PYD and CARD of ASC and ASCb to the exponential equations (Equations 1 and 2). Amino acids in the PYD and CARD of ASC show different behavior, whereas this difference is not observed for ASCb. The k_1 and k_2 values of individual amino acids plotted *versus* the residue

Table 1
Kinetic parameters from logistic Equations 1 and 2

	Protein isoform	
Rate constants	ASC	ASCb
k_1[a]	0.15 ± 0.03	0.02 ± 0.01
k_2[a]	0.04 ± 0.01	0.02 ± 0.01
$k_{1avePYD}$	0.21 ± 0.04	0.0269 ± 0.0009
$k_{2avePYD}$	0.05 ± 0.02	0.0269 ± 0.0009
$k_{1aveCARD}$	0.12 ± 0.02	0.0288 ± 0.0009
$k_{2aveCARD}$	0.02 ± 0.01	0.0288 ± 0.0009
Goodness of fit		
χ^2	0.000327961	0.00059583
r	0.999812	0.999806

[a] Reported values are averaged and SD obtained from fitting the logistic equations to the RT-NMR data at ~700 and 500 μM for each isoform. Units for rate constants are in h^{-1}.

sequence clearly show that the two death domains of ASC behave differently in the faster step (Fig. 4*B*). The k_1 values of the PYD are larger than those of the CARD: $k_{1avePYD}$ = 0.21 ± 0.04 h^{-1} and $k_{1aveCARD}$ = 0.12 ± 0.02 h^{-1} (Table 1). However, the k_2 values are similar for both domains: average value, $k_{2avePYD}$ = 0.05 ± 0.02 h^{-1} and $k_{2aveCARD}$ = 0.02 ± 0.01 h^{-1} (Table 1). This higher value for $k_{1avePYD}$ *versus* $k_{1aveCARD}$ suggests that PYD-PYD interactions could drive the first steps in the oligomerization reaction, and that both domains participate equally in subsequent polymerization steps. In contrast, the PYD and CARD domains of ASCb show very similar values of the oligomerization rate constant (k = 0.02 ± 0.01 h^{-1}) (Fig. 4*B* and Table 1), which points to equivalent participation of both domains in the different steps of the polymerization reaction. This rate constant is slower than the slower rate constant for ASC self-association (k_2), again indicating that ASCb polymerizes at a slower rate compared with ASC. The monoexponential behavior in ASCb could be explained by an initial nucleation step and subsequent polymerization with analogous rate constants. The oligomerization of ASC is a complex process as shown by our recent studies combining NMR techniques and ns-TEM, indicating that ASC dimers are the building blocks of ASC filaments and that the latter tend to form bundles comprising laterally stacked filaments. The ASC dimer involves homotypic interactions between the PYDs and CARDs of the two protomers. PYD and CARD domains have several protein–protein interacting regions that facilitate further association and polymerization.

Kinetic model for ASC and ASCb self-association

The exponential Equations 1 and 2 used for comparing the self-association behavior of ASC and ASCb report on the presence of different kinetic phases and allow the identification of similitudes and differences in the self-association process of the individual domains; however, these equations are not necessarily connected to the oligomerization kinetic mechanisms. We have attempted to propose a simple kinetic model for ASC and ASCb self-association based on previously reported models for protein oligomerization.

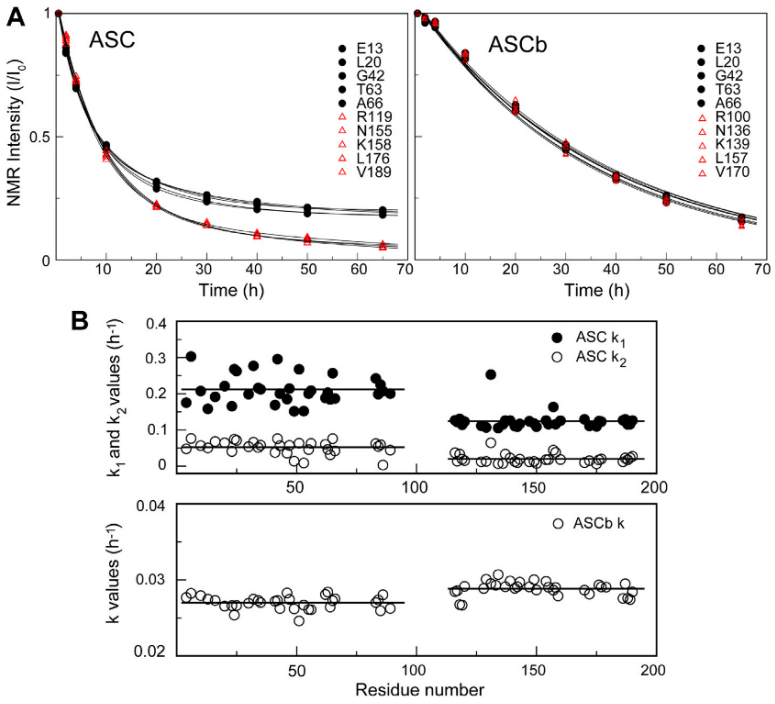

Figure 4. RT-NMR oligomerization kinetics of ASC and ASCb at the amino acid level. *A*, normalized intensity decay of ASC (*left panel*) and ASCb (*right panel*). *B*, rate constants of the PYD and CARD domains *versus* residue number for ASC (*top*) and ASCb (*bottom*).

The oligomerization mechanisms of numerous protein systems have been studied in depth using different kinetic models of polymerization (26–28). The nucleation/polymerization model proposed by Hofrichter *et al.* has been frequently used and adapted to describe the oligomerization of different proteins (29–33). According to this model, individual kinetic steps of single-monomer additions result in the formation of an oligomer of a specific size: critical nucleus size or seed. These first steps constitute the nucleation phase of the mechanism. Once the critical nucleus is formed, the addition of new monomers to this critical-size oligomer is thermodynamically favorable, thus leading to subsequent polymerization (29). To account for the high complexity of protein self-association, this and similar models based on single-monomer addition have been complemented with other equilibria involving polymer fragmentation and association (34). In addition, other models contemplate the formation of polymers or the critical-size nucleus based on the association of smaller oligomers of potentially different size (35–37). In general, originally proposed models are typically further modified to include additional steps that allow better fitting of the resulting kinetic equations to the experimental data (34).

Recently, a model has been proposed to explain the kinetic diversity of amyloid oligomers. A Petri net (38) form is used to depict the different steps potentially involved in the oligomerization process (39). According to this model, the primary nucleation phase that results in fibril formation involves two steps: (1) the initial formation of an oligomer from the association of a certain number of monomer molecules; a process that is considered reversible, and (2) the addition of a number of monomers to this critical-size oligomer resulting in fibrils; a process that is assumed to be irreversible (39). The formed fibrils can be elongated by monomer addition to both ends of the fibril. Secondary pathways, such as fibril fragmentation and oligomer formation by clustering of monomers into preexisting fibrils, are also contemplated (39). Analytical equations derived from this model successfully describe reported experimental kinetic data on oligomer concentration and fibril mass concentration during amyloid fibril assembly. We have used a simplified version of this model, which considers the basic reactions involving the formation of fibrils (filaments) but assumes that filament elongation by single-monomer addition and secondary processes such as fragmentation are negligible. Similarly, the model is represented in Petri net form in Figure 5.

The kinetic equations associated to the chemical reactions considered in Figure 5 are as follows:

$$d[M]/dt = -k_a[M]^m - (k_b[M]^n - k_{-a})[O] \quad (3)$$

$$d[O]/dt = k_a[M]^m - (k_b[M]^n + k_{-a})[O] \quad (4)$$

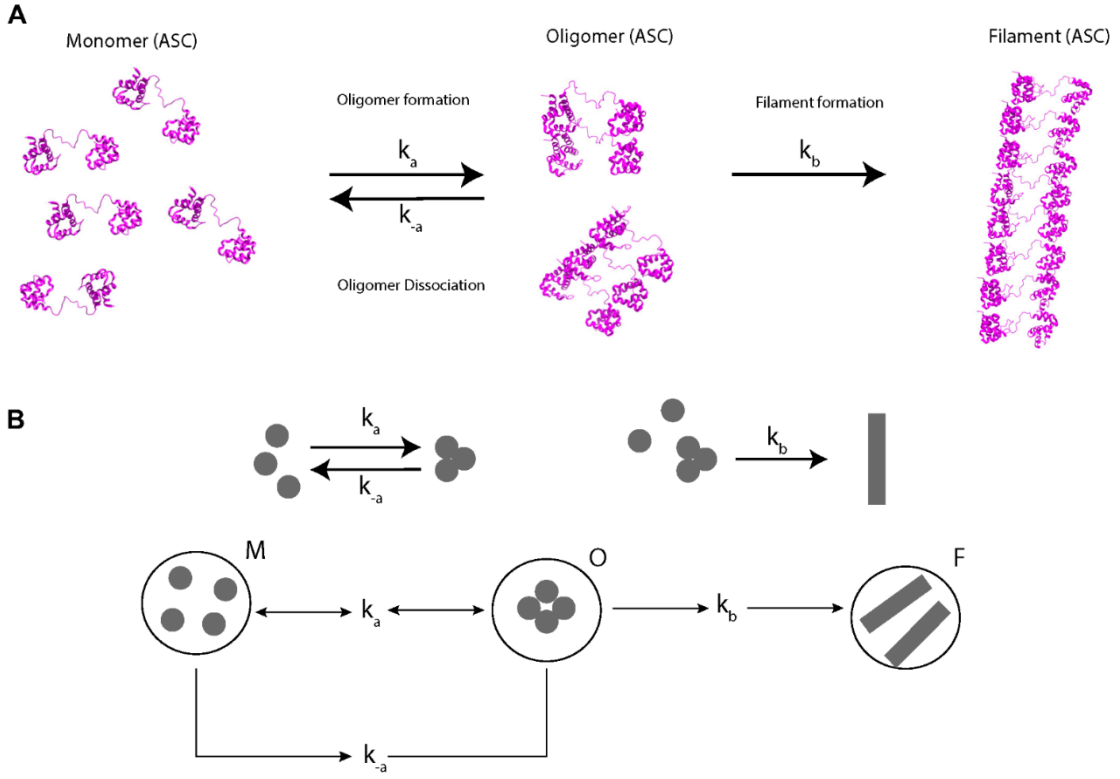

Figure 5. Kinetic model of ASC and ASCb oligomerization. *A*, monomeric ASC forms oligomers at rate k_a. Oligomers can dissociate back to monomers at rate k_{-a} or further self-associate to form filaments at rate k_b. *B*, filament formation represented in Petri net form.

$$d[F]/dt = k_b[M]^n[O] \quad (5)$$

Where M, O, and F, represent the monomer, oligomer of critical-size and filament, respectively; k_a and k_{-a} are the forward and backward reaction rate constants for the formation of the oligomer (step 1), and k_b is the rate constant for the forward reaction of filament formation (irreversible step 2). The model also assumes that protein concentration does not influence the kinetic parameters of these reactions. However, it has been previously reported that the critical size of the oligomer can depend on monomer concentration (33). Analogously to other kinetic analysis of protein oligomerization, these equations become linear by assuming that the initial concentration of monomer is constant at early stages of the self-association process. Under this assumption, the solution of the differential equations results in an expression of the normalized concentration of monomer at time t ($[M]_t$) as follows:

$$[M]_t/[M]_0 = 1 - B_0 + B_1 \; t + B_2 \, e^{-t\,B_3} \quad (6)$$

With no other assumptions and counting with the RT-NMR data reporting the decrease of monomer concentration as self-association proceeds, the fitting of the experimental data to Equation 6 allows obtaining the values of k_a and k_{-a} for the formation of the oligomer (Fig. 5) (Table 2). Both rate constants are larger for ASC than for ASCb. Specifically, k_a is close to two orders of magnitude larger for ASC, whereas k_{-a} is approximately one order of magnitude larger. This result could imply that ASC has a stronger tendency to form oligomers compared with ASCb, and that once formed, the latter has less tendency to return to monomeric form. The k_a values are similar at different protein concentration (~700 μM and ~500 μM) as expected, whereas the k_{-a} values show variations (Table 2). We attribute these variations to the assumption made in considering that the protein concentration will not affect oligomer critical size and thus the pertinent rate constants.

In addition, an estimate of the reaction rate order for oligomer formation can be obtained by applying the initial rate approximation. Under these conditions, the concentration of oligomer is assumed to be zero, and thus, Equation 3 is simplified to:

$$V_0 = -k_a\,[M]^m \quad (7)$$

The initial velocity (V_0) of the reaction was determined from the slope of the straight line formed by the first four points of

Table 2
Kinetic parameters for the self-association of ASC and ASCb from kinetic model equations

Conditions/Parameters	Protein isoform			
	ASC		ASCb	
Protein concentration[a]	697	501	704	495
k_a[a]	6.05×10^{-8}	4.74×10^{-8}	8.69×10^{-10}	8.60×10^{-10}
k_{-a}[a]	0.12	0.05	0.001	0.005
Reaction order	3.1	3.1	3.6	3.6

[a] Concentration units: μM. Time units: h.

the NMR signal intensity decay at the three concentration values for ASC and ASCb (Fig. 3*B*). Subsequently, the data at the three concentrations values were used to obtain the reaction order "*m*" from Equation 7 (m = 3.1 for ASC and m = 3.6 for ASCb). These results indicate that the formation of ASCb oligomers (O) has a slightly stronger dependence on the monomer concentration compared with ASC. Altogether, the results from the kinetic model help to further compare the oligomerization behavior of ASC and ASCb with more detail. However, the reaction rate constants and the order rate values are approximate as several assumptions were made.

The remaining NMR signal observed several weeks after that start of protein oligomerization (Fig. 3*C*) could indicate that filament formation is a reversible process. In contrast, because the second step in the proposed kinetic model is irreversible (Fig. 5*A*), the model seems to disagree with the NMR experimental data. However, a very small value of k_b could lead to an extremely slow and barely detectable decrease of the NMR signal. In fact, the natural oligomerization of ASC and ASCb is greatly diminished under the acidic conditions of the RT-NMR experiments, which could result in the reversibility of the filament-formation step or in very small values of the rate constant of the irreversible reaction (second step in Fig. 5). Both possibilities could validly explain the observed residual NMR signal.

It is also interesting to test whether potential chemical modifications in ASC and ASCb influence the kinetics of the self-association process. For this purpose, the oligomerized ^{15}N-labeled samples were subjected to liquid chromatography (reverse phase) coupled to mass spectrometry. The mass spectrum for ASC indicates the presence of monomer and dimer with molecular weights of 23,959.9 and 47,927.6 g/mol (Fig. S3). However, the mass spectrum for ASCb only reveals a monomer with molecular weight of 22,282.8 g/mol (Fig. S3). The mass spectrometry data match the theoretical molecular weights of the monomers (23,958.7 and 22,278.9 g/mol) of ^{15}N-labeled ASC and ASCb, respectively, thus ruling out chemical modifications during self-association. The oligomerized ASC and ASCb samples are treated with formic acid and undergo unfolding by the reverse-phase chromatography step prior to mass spectrometry, which should dissociate noncovalent oligomers into monomers. Therefore, the presence of an ASC dimer was unexpected. The mass spectrometry data indicate that ASC is capable of forming dimers stable enough to sustain the harsh unfolding conditions. This result agrees with our previous data on the oligomerization of ASC using NMR and TEM, which indicate that the ASC dimer is the building block of the ASC filament (12). Importantly, the persistence of a dimer in ASC, but not in ASCb, suggests that a potential ASCb dimer is not as stable, highlighting another difference in the self-association process of the two isoforms.

ASC has a stronger tendency to oligomerize compared with ASCb from size-exclusion chromatography analysis

Using SEC, we have attempted to study the oligomer size distribution in ASC and ASCb self-association. In particular, we have studied three factors critical in death domain oligomerization (40): time (80 min and 2 days after sample preparation), protein concentration (50 μM and 150 μM), and pH (3.8, 4.3 and 4.8). For this purpose, we have used an SEC column (Superdex 200 10/300 GL) with a molecular weight range of 10–600 kDa. The protein solutions and equilibration buffers in these experiments contained 150 mM NaCl to avoid nonspecific interactions between the proteins and the chromatographic matrix. Using NMR and analytical ultracentrifugation, we reported previously that the presence of NaCl enhances death domain oligomerization, particularly in studies involving the association of the PYD domains of ASC and of the inflammasome sensor NLRP3 (40). Thus, protein self-association significantly increases under these conditions compared with those used in the kinetic RT-NMR experiments without NaCl. Samples for chromatographic analysis are typically filtered through ≥0.2 μm; however, ASC and ASCb samples that were filtered prior to column loading did not give rise to any signal in the chromatogram under most conditions (pH > 3.8 and/or protein concentration >50 μM and/or sample preparation >2 days), thus indicating that the oligomers were trapped in the filter. Therefore, protein samples were not filtered in our SEC studies and instead were centrifuged at 5,000 rpm for 1 min to pellet down precipitated material. Precipitation and centrifugation result in lack of homogeneity in the starting conditions of the protein samples, which is reflected in variations in the absorbance values for identical protein concentration, thus rendering the interpretation of the SEC results significantly challenging.

Protein samples at 50 μM concentration were injected in the SEC column 80 min after preparation, resulting in absorbance peaks (at a wavelength of 280 nm) corresponding to ASC and ASCb at an elution time of ∼38 min (Fig. 6*A*). According to the SEC column calibration and assuming a spherical rotor, monomeric and dimeric forms of ASC and ASCb should elute at ∼33 and ∼30 min, respectively. The discrepancy between the expected and experimental elution times is likely due to the multidomain nature of the two isoforms, thus deviating from ideal spherical conditions. The experimental elution time at ∼8 min most likely corresponds to the monomeric forms of both ASC and ASCb as the NMR data do not suggest the presence of a stable dimer (10). The protein samples were injected again 2 days after preparation and both ASC and ASCb eluted at the void SEC time (∼17 min) with similar intensity. This result indicates that the oligomers formed by ASC and ASCb are >600 kDa, which is the upper limit for the molecular weight of the SEC column (Fig. 6*A*). Therefore, the

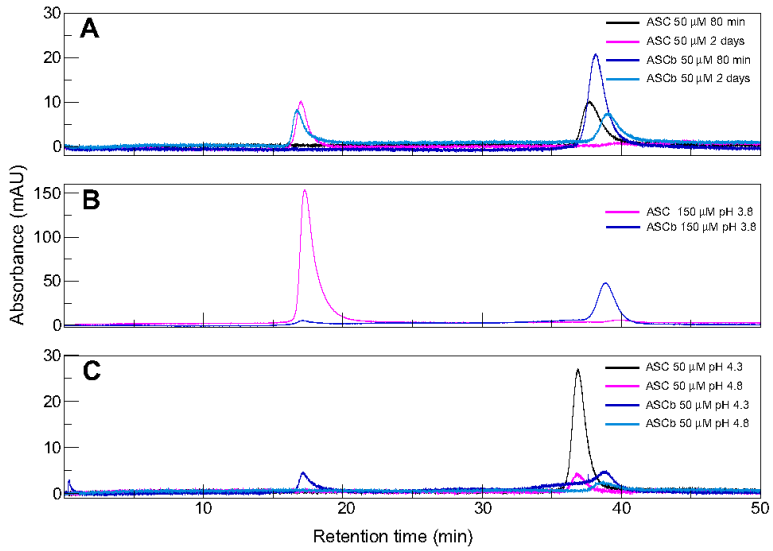

Figure 6. ASC and ASCb oligomer size distribution by SEC. *A*, oligomer formation of ASC and ASCb 80 min and 2 days after sample preparation. *B*, effect of concentration on oligomer distribution at 150 μM. *C*, influence of pH on the oligomerizing capabilities of ASC and ASCb at pH 4.3 and 4.8.

lower limit of the number of protomers in the ASC and ASCb oligomers is ~30, based on the molecular weight of the monomeric proteins. ASCb, but not ASC, still shows an absorbance signal at an elution time ~38 min in the chromatogram obtained 2 days after sample preparation, which suggests that certain population of ASCb is still monomeric under these conditions. In contrast, our RT-NMR data indicate that both ASC and ASCb are mainly monomeric at ~300 μM in the absence of NaCl, thus corroborating our original results on the enhancing effect of NaCl in death domain self-association.

The influence of protein concentration on oligomer distribution was also tested. At 150 μM protein concentration, ASC elutes mainly in the void volume (Fig. 6*B*) with a minor population at ~38 min. ASCb behaves in the opposite way showing a minor peak at the void volume and a major peak at ~38 min. This result suggests a higher tendency of ASC to oligomerize compared with ASCb. We also attempted to study the effect of pH on ASC and ASCb oligomerizing capabilities. SEC experiments on ASC and ASCb at pH values higher than 3.8 were very challenging to perform because of abundant protein precipitation; an effect originally observed for ASC (10, 40). At pH 4.3, ASC shows an absorbance signal at ~38 min, but the signal at the void volume is no longer present (Fig. 6*C*). In contrast, ASCb shows two signals barely above the baseline: one appearing at ~38 min and the other one at the void volume (Fig. 6*C*). At a higher pH value (pH 4.8), only one signal is still present for both isoforms appearing at ~38 min with very low absorbance (~2 mA units) (Fig. 6*C*). These results suggest that high-order oligomers formed by ASC and ASCb are more populated at higher pH values. These large oligomers mostly precipitate out of solution, explaining why they are no longer observed in the SEC chromatogram, thus resulting in single signals at ~38 min.

The SEC data are difficult to interpret due to the dynamics of the oligomerization process and protein precipitation in the presence of NaCl and at pH > 3.8. Nonetheless, we can derive information indicative of different oligomerizing behavior for ASC and ASCb. Overall, the SEC results suggest that ASC has a higher tendency to self-associate compared with ASCb based on the stronger effect of time, pH, and protein concentration to promote oligomerization. The SEC results also indicate that oligomers of MW > 600 kDa are observed, which implies that oligomers <600 kDa are not sufficiently populated and/or have a short half-life.

ASC self-association results in less polydisperse solutions compared with ASCb

Dynamic light scattering (DLS) was used to monitor the self-association of ASC and ASCb as a function of time. The intensity of the scattered light *versus* particle size was obtained for ASC and ASCb solutions at different time points ranging from 30 min to 49 h after sample preparation (Fig. 7). The intensity of the observed peaks depends on the population of the different particles and is proportional to the sixth power of the particle radius. Therefore, larger particles will result in peaks with higher intensity of the scattered light compared with smaller particles at equal population. It is important to mention that a perfect spherical particle is assumed for the mathematical determination of particle size from the correlation functions derived from the dependence of photon counts *versus* time in DLS. ASC oligomers are not spherical but filamentous, and thus this condition is not applicable (12).

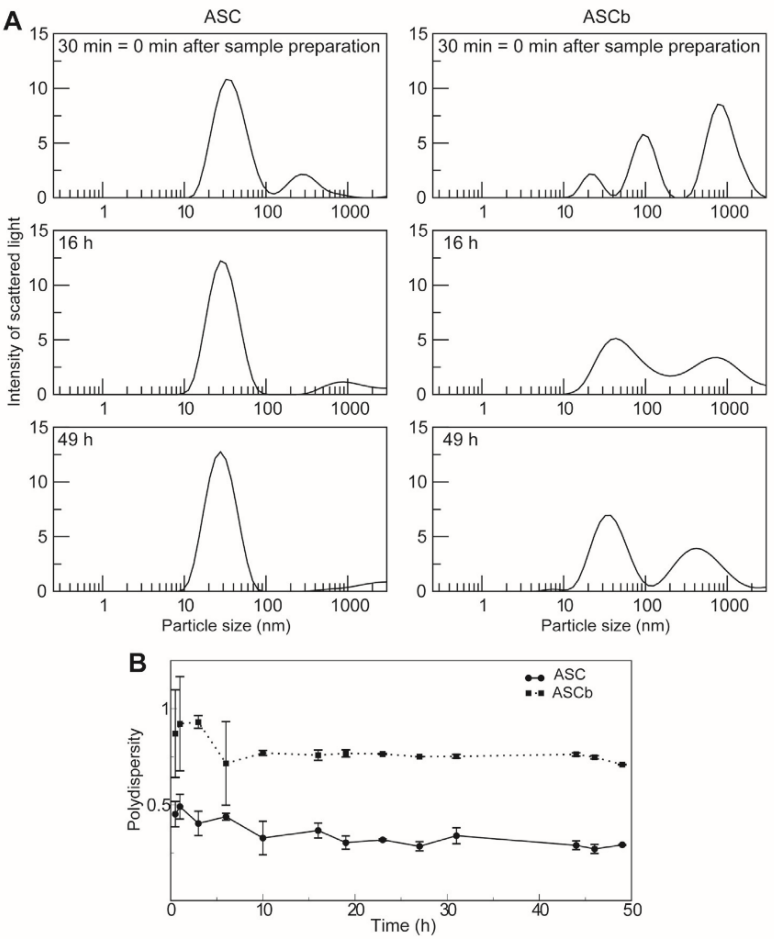

Figure 7. Time-dependent population distribution of ASC and ASCb oligomers by dynamic light scattering. *A*, changes over time in population (intensity of scattered light) and apparent size of ASC and ASCb oligomers. *B*, changes in polydispersity values of ASC and ASCb solutions during the oligomerization process. Data in (*A*) and (*B*) are an average of three measurements and error bars in (*B*) represent SD. The 30 min time point can be considered as 0 min time point after sample preparation.

Therefore, the specific dimensions obtained assuming spherical particles do not report on the real size of the oligomers. However, the data are very useful to identify particle populations of different size and their change in population during the kinetic experiment.

DLS data for ASC 30 min after sample preparation show one major and one minor peak with an overall diameter of ~40 nm and ~300 nm, respectively, (Fig. 7*A*). The population of ASC monomers detected in the RT-NMR experiments is not observed in the DLS data likely being masked by the intense signal resulting from the large oligomeric species present in solution. The former peak slowly decreases to ~28 nm at the end of the kinetic experiment, which could indicate that the oligomers are becoming more compact. In addition, the intensity of the peak at ~300 nm decreases with time. Because the larger species shows very low intensity compared with the smaller species, we can conclude that the population of the ~300 nm species is very small. At the end of the kinetic experiment, ASC shows mainly one species at ~28 nm (Fig. 7*A*). The disappearance of the ~300 nm peak is concomitant to the increase in intensity of the ~28 nm signal. Thus, we speculate whether the ~300 nm species has become more compact by forming filamentous rings and contributes to the intensity of the ~28 nm species. In contrast, DLS data for ASCb 30 min after sample preparation show three main peaks at ~20, ~100 nm, and ~900 nm, the latter one being more intense. As the kinetic experiment progresses, the three peaks consolidate into two major peaks with diameters of ~30 and ~400 nm.

In general, ASC and ASCb form species of different size and population under the same conditions during self-association. These different species tend to consolidate to a smaller number at the end of the kinetic experiment reflecting the dynamics of the polymerization process and a tendency to

form oligomers of more uniform size. Importantly, the overall polydispersity values (p) for ASC and ASCb during the DLS kinetic experiments are significantly different: p_{ASC} = 0.35 ± 0.04 and p_{ASCb} = 0.79 ± 0.06 (Fig. 7*B*). This result is remarkable as it reflects that ASC self-associates into oligomers of very similar size, whereas ASCb oligomerizes with considerably higher polydispersity. Interestingly, it has been reported that ASC and ASCb oligomerize into different macrostructures inside the cell: ASC forms a speck of uniform size and ASCb forms clustered and disordered filaments (20). The conditions for oligomerization in the cell assays are different from our *in vitro* studies in terms of protein and salt concentration, pH, and other uncontrolled factors in the cell cytosol. However, cell studies agree with our DLS results indicating that ASC is capable of forming monodisperse polymers, whereas ASCb is not.

Differences in ASC and ASCb macrostructures by transmission electron microscopy

An analysis of the macrostructures formed by ASC using negative-staining Transmission Electron Microscopy (ns-TEM) has been previously reported (12). According to this study, ASC tends to form filaments with an average width of 6.4 ± 0.8 nm and length varying between 600 and 800 nm (12). The filaments form bundles of 2–7 filaments; with three- and four-filament bundles being more abundant. Bundle width is always a multiple of the width of the individual filament matching the number of filaments in the bundle, thus indicating that the bundles are formed by lateral stacking of filaments. Importantly, the TEM micrographs show that ASC filaments are formed by stacked rings with the size of an ASC dimer. In addition to forming part of the individual filaments, these rings are abundantly observed attached to preexisting filaments suggesting a possible mechanism for filament and bundle growth.

A similar ns-TEM analysis was performed for ASCb to identify potential differences in the characteristics of the macrostructures (Fig. 8). ASCb also polymerizes into filaments that tend to form bundles. However, some differences were observed: ASCb bundles are typically composed of 1-, 2-, and 3-filaments. The analysis of 72 filaments indicates the following populations: 26.3% of individual filaments, 48.7% of two-filament bundles and 25% of three-filament bundles. Thus, for ASCb, two-filament bundles are significantly more abundant. The average width of individual filaments, two- and three-filament bundles is 7.0 ± 0.2 nm, 14.1 ± 0.4 nm, and 21.2 ± 0.4 nm, respectively. These values indicate that ASCb individual filaments are of similar width compared with those observed for ASC and that bundles are also formed by lateral stacking of individual filaments. Filament length was found to be in the 200–400 nm range, thus slightly shorter than ASC filaments. Interestingly, rings attached to preexisting filaments were not observed for ASCb.

It is important to mention that the experimental conditions for ASC and ASCb filament formation are different from the conditions used for protein oligomerization using RT-NMR. Filament formation is enhanced at neutral pH and diminished under the acidic conditions used for NMR experiments. However, our previous TEM results indicate that ASC can form filaments under acidic conditions of similar appearance to the filaments formed at neutral pH albeit less compacted and defined (12).

Steric factors dependent on the linker length result in different interactions between ASC and ASCb with procaspase-1 CARD

In addition to self-association, ASC and ASCb tether sensors and procaspase-1 molecules as part of their function in inflammasome assembly. Thus, both isoforms also participate in oligomerization processes involving other proteins. We investigated potential differences between ASC and ASCb in this function at the computational level. In an attempt to mimic the initial steps of inflammasome formation, we used docking and rigid body minimization protocols (41) to study the binding of ASC and ASCb to several CARD domains of procaspase-1 (procaspase-1^{CARD}). We first generated dimers of ASC and ASCb with one procaspase-1^{CARD} using the most prominent interactions between death domains (*i.e.*, type Ia and type Ib interactions (42) that involve helices 1 and 4 of one domain and helices 2 and 3 of the other domain). Thus, each CARD domain in ASC or ASCb is capable of interacting with two procaspase-1^{CARD} molecules *via* the surfaces composed by helices 1,4 and 2,3. The resulting dimers (ASC/procaspase-1^{CARD} and ASCb/procaspase-1^{CARD}) were used to generate trimers by including one additional procaspase-1^{CARD} molecule. The structures of the trimers were analyzed and compared with the structure of a procaspase-1^{CARD} trimer with type I interactions extracted from the cryo-EM 3D structure of the procaspase-1 CARD polymer (43).

The structures of the CARD and PYD domains of ASC and ASCb are identical, thus, conferring flexibility to the linker is critical to allow different orientations of the PYD and CARD domains that could influence the capability of interaction with procaspase-1^{CARD} molecules. Therefore, we assigned full flexibility to the 23- and three-residue linker of ASC and ASCb, respectively, in the docking protocol used to generate all models. The structures of the dimers and trimers resulting from docking and rigid body minimization are shown in Figure 9. Briefly, molecules at the right-hand side of panels A and C represent the dimer structures of ASC with the type I interaction, ASC (helices 1, 4): procaspase-1^{CARD} (helices 2, 3); and ASC (helices 2, 3): procaspase-1^{CARD} (helices 1, 4), for panels A and C, respectively. Analogously, molecules at the right-hand side of panels B and D represent equivalent interactions between ASCb and procaspase-1^{CARD}.

ASC and ASCb are capable of binding one procaspase-1^{CARD} molecule *via* type I interactions in a similar fashion (Fig. 9, right-hand side in all panels: ASC and ASCb in navy blue ribbon, procaspase-1^{CARD} in light orange). The orientation of this procaspase-1^{CARD} molecule is close to the expected position indicated by the cryo-EM 3D structure of the procaspase-1^{CARD} polymer (43) (Fig. 9, left-hand side in all panels: light purple ribbon). However, when a second procaspase-

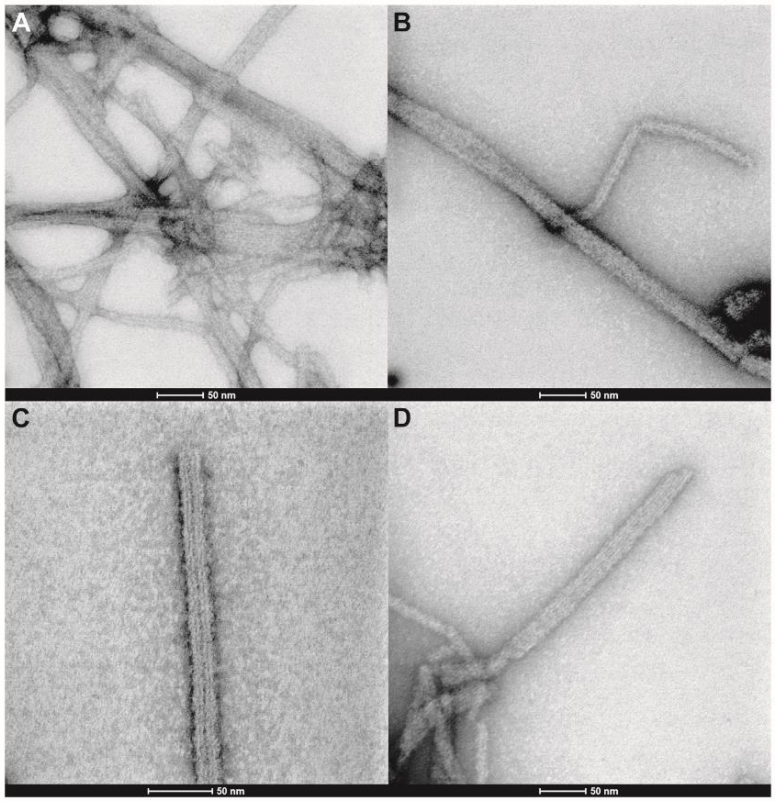

Figure 8. Filament and filament bundles formed by ASCb. *A*, ns-TEM micrograph of networks of filaments of various sizes. *B–D*, ns-TEM images showing one-filament (*B*), two-filament (*C*), and three-filament (*D*) bundles of ASCb.

1^{CARD} molecule is included, only the trimers formed by ASC resemble the expected arrangement of the additional CARD based on the cryo-EM structure (Fig. 9, *A* and *C*). The second procaspase-1^{CARD} molecule in the ASCb trimer is located in a position that significantly deviates from the polymeric CARD arrangement (Fig. 9, *B* and *D*). In fact, it is clear from the superimposed structures in Figure 9*B* (center) that the second procaspase-1^{CARD} molecule would clash with the PYD of ASCb if located in the position of the polymeric CARD. Analogously, the ASCb trimer with type one interactions, procaspase-1^{CARD} (helices 2, 3): ASCb (helices 1, 4): procaspase-1^{CARD} (helices 2, 3) shown in Figure 9*D*, results in the position of the second procaspase-1^{CARD} in a region where there is not interference with the PYD of ASCb, but deviates from the expected structure based on the cryo-EM trimer.

In summary, ASC and ASCb interact differently when several procaspase-1 molecules are involved in an oligomeric assembly resembling the formation of the inflammasome. The proximity between the PYD and CARD domains of ASCb hinders interactions of $ASCb^{CARD}$ with procaspase-1^{CARD}. In contrast, ASC's significantly longer linker results in lack of interference between the two domains, thus facilitating interactions with potential partners. Overall, the models generated with the docking protocols help to illustrate a tentative, simple mode of oligomerization of ASC and ASCb with procaspase-1. Preassembled ASC and ASCb could also interact with procaspase-1 during inflammasome formation, which would lead to a smaller number of interacting regions available for procaspase-1 in ASC^{CARD} and $ASCb^{CARD}$. In this situation, the hindering effect caused by PYD and CARD in ASCb might gain more relevance. Finally, based on the proximity-induced model for procaspase-1 autoactivation, a different structural arrangement of ASC *versus* ASCb oligomers could result in differences in the local concentration of the procaspase and thus in its autoactivation.

Discussion

It has been previously reported that ASC and its isoform ASCb are able to interact with NLRP3 and procaspase-1 (20, 21). Although both isoforms are incorporated into the inflammasome complex, ASCb leads to an overall reduction in inflammasome activity compared with ASC based on the release of smaller amounts of interleukin-1β (20). The difference in inflammasome activity between ASC and ASCb can

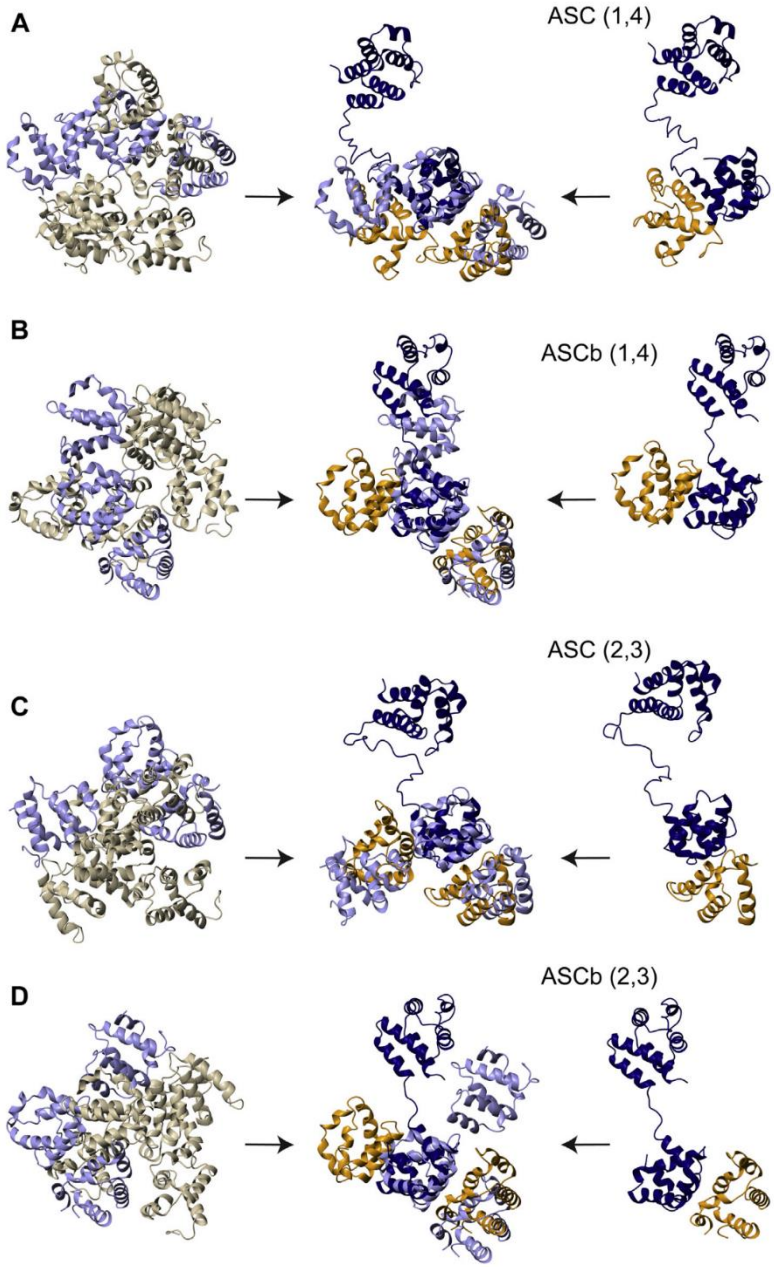

Figure 9. Steric hindrance in the interactions of ASCb with the CARD of procaspase-1. In all panels, *Left*: Different orientations of the polymeric cryo-EM structure of the CARD of procaspase-1 (procaspase-1^{CARD}) (43). The CARD trimer formed by type I interactions is highlighted in *light purple*; Center: trimer structure of ASC or ASCb (*navy blue*) from molecular docking (41) with two molecules of procaspase-1^{CARD} (*light orange*). In *light purple*, the CARD trimer superimposed in the same orientation shown in the left; *Right*: dimer structure of ASC or ASCb (*navy blue*) from molecular docking with one molecule of procaspase-1^{CARD} (*light orange*). *A* and *C*, trimer and dimer structures starting with ASC interacting helices 1 and 4 (*A*), and 2 and 3 (*C*); *B* and *D*, trimer and dimer structures generated starting with ASCb interacting helices 1 and 4 (*B*), and 2 and 3 (*D*). The CARD trimer (*purple*) in the *left* of all panels shows different orientation to facilitate comparison to the CARD trimer superimposed to ASC(ASCb)-CARD-CARD trimers shown in the center.

have relevant effects on the regulation of the inflammatory response. Therefore, it is important to understand this regulatory mechanism at the molecular level. The main function of ASC as an inflammasome adaptor is to self-associate and oligomerize with the sensors and procaspase-1. Thus, we hypothesized that the modulation of function regarding

inflammasome activation depends on the different self-association/interaction properties in ASC and ASCb. In this work, we have tested this hypothesis by studying the self-association behavior of ASC and ASCb using different techniques for a more thorough analysis.

The monitorization of ASC and ASCb self-association by RT-NMR allowed to identify overall kinetic phases by fitting the obtained data to single- or double-exponential equations. The results of the fitting indicate that ASC self-associates with two major kinetic phases, whereas ASCb follows a single kinetic phase or two phases with identical or very similar rate constant. Our data indicate that ASC oligomerization follows a fast kinetic phase and a slower second kinetic phase. In contrast, the single kinetic phase experienced by ASCb is slower than both kinetic phases of ASC. Furthermore, NMR allows atomic-resolution studies of the kinetics of the self-association process. We leveraged this unique quality of NMR to investigate differences in oligomerization at the atomic-residue level. Importantly, we found that the self-association capabilities of the PYD and CARD domains of ASC and ASCb are different. Specifically, the PYD and CARD of ASC show two different apparent kinetic rate constants facilitating oligomer formation. The higher k_1 values of the PYD domain relative to the CARD suggest that during the initial kinetic phase, the interactions involved in the conversion from monomer to oligomer are primarily driven by PYD-PYD binding followed by CARD-CARD interactions. The second kinetic phase is dictated by the simultaneous participation of both the PYD and CARD domains as indicated by their similar k_2 values. In contrast, the PYD and CARD domains of ASCb show equivalent kinetic rate constants, suggesting that both domains participate equally in the formation of the oligomeric species.

Previously reported data on ASC macrostructure characterization by ns-TEM show that ASC dimers are the building blocks of ASC polymerization into filaments (12). It is plausible that short-lived dimers are formed and rapidly assemble into oligomers of a critical nucleation size that further develop into filaments. The kinetic data obtained for ASC suggest that PYD-PYD interactions could drive dimer formation ($k_{1avePYD} > k_{1aveCARD}$), additionally stabilized by CARD-CARD binding. Contrary to the results of canonical ASC, the kinetic data for ASCb suggest that the PYD and CARD have the same oligomerization tendency. Death domain oligomerization depends on the presence of the different interacting regions in the PYD and CARD domains and on the possibility of these regions to find their interacting partners for which domain reorientation might be important. The PYD and CARD of ASC and ASCb are identical based on our structural data and the 100% amino acid sequence identity. Thus, the different behavior of the two domains in ASC is potentially related to the long linker connecting the two domains. ASC long linker will facilitate domain reorientation to a greater extent compared with ASCb. Therefore, it is reasonable to suggest that the increased oligomerization tendency observed in ASC for the PYD relative to the CARD is diminished in ASCb due to potential restrictions of domain reorientation as a result of the much shorter linker. To test the effect of the linker length, we created *via* molecular docking and rigid body minimization structural models of trimers composed of ASC or ASCb and two procaspase-1^{CARD} molecules (41). The models indicate that ASCb short linker causes steric hindrance, resulting in an arrangement of the procaspase-1^{CARD} molecules that differs from the experimental structure of the polymer (43).

The DLS kinetic study demonstrates that ASC and ASCb self-associate into different oligomer populations. Specifically, DLS data reveal the presence of a single monodisperse population present at 16 h after the start of ASC oligomerization. The low polydispersity of the protein solution suggests the formation of oligomers of similar size. In contrast, ASCb solution is more polydisperse as evidenced by the presence of two populations of oligomers 49 h after the beginning of the self-association process. These results are in agreement with previously published work on intracellular ASC and ASCb polymerization studies by fluorescence microscopy, indicating that ASC forms a filamentous speck or ring of ~0.5 μm in diameter upon macrophage activation, whereas ASCb polymerizes forming linear filaments (13, 20).

ASC and ASCb also show differences at the macrostructural level. The ns-TEM image analysis reveals shorter filaments formed by ASCb compared with ASC and a lower tendency to assemble into bundles formed by a large number of laterally stacked filaments. This result could be related to the different polymerized macrostructures observed in the cell environment for ASC and ASCb. Furthermore, utilizing SEC we show that solution pH, oligomerization time, and protein concentration are important factors governing ASC and ASCb oligomerization. SEC studies indicate that ASC has a higher tendency to self-associate compared with ASCb. We have not observed small-size oligomers or dimers in the SEC studies but instead oligomers >600 kDa consisting of at least 30 protomers; a behavior similar to both ASC and ASCb. This result agrees with single-molecule fluorescence studies indicating that ASC massively oligomerizes into micron-size clusters of >500 proteins at above a critical concentration value in a cell-free system capable of expressing ASC at different concentrations (44). These studies also indicate that smaller oligomers are not detected (44), which matches our conclusion from RT-NMR kinetic data and SEC analysis that dimers and small oligomers have a short half-life. Nonetheless, the presence of an ASC dimer in the mass spectrum, likely resulting from the dissociation of large oligomers under the harsh unfolding conditions of the liquid chromatography–mass spectrometry experiment, points to its higher stability compared with ASCb.

Altogether, our data indicate that ASC oligomerizes faster and is capable of assembling into oligomers of more uniform size compared with ASCb. In this study, we show that these differences are only attributable to the specific structure/function of ASC and ASCb with no intervention of other proteins that could have an influence in the different polymerized macrostructures observed in the cell cytosol (20). The only difference at the amino acid level is the linker length,

which seems to be optimized in ASC to enhance self-association and the formation of more compact oligomers. This different behavior intrinsic to ASC and ASCb can have important implications in the regulation of the inflammatory response. Upon macrophage activation as a result of the presence of pathogens and/or chemical signals indicative of cell dysfunction, the expression of the sensor protein, procaspase-1, and ASC is upregulated. The three proteins colocalize forming a filamentous ring-like structure, the inflammasome, consisting of self-associated and oligomerized sensor, ASC, and procaspase-1. The assembly of the inflammasome acts as platform for the activation of procaspase-1, purportedly due to an induced local increase of the caspase concentration resulting in its autoactivation (45). Therefore, ASC formation of monodisperse structures *versus* ASCb assembly into polydisperse filaments could be critical in procaspase activation. Our results indicate that ASC self-association is likely driven first by the PYD-PYD interactions followed by CARD-CARD binding, suggesting the possibility of domain reorientation that finally leads to the assembly of uniform oligomers. In contrast, the slower and weaker tendency of ASCb to oligomerize could delay the overall activation of the inflammasome. Furthermore, the polydisperse nature of ASCb oligomers could result in a less effective localization of increased procaspase-1 concentration, thus causing an overall reduction in inflammasome activity.

Experimental procedures

Expression and purification of unlabeled and isotopically labelled ASC and ASCb

E. coli BL21(DE3) cells were transformed with pET15b vectors encoding for either protein, ASC or ASCb. ^{15}N- and ^{15}N,^{13}C-labeled proteins were cultured in M9 minimal media, using $^{15}NH_4Cl$ and/or ^{13}C-glucose as sole nitrogen and carbon sources, respectively. *E. coli* cells were induced using 1 mM IPTG and incubated at 37 °C for 4 h. Cells were harvested by centrifugation at 8000 rpm for 30 min at 4 °C. Cell pellet was resuspended in resuspension buffer (6 M Guanidine-HCl, 20 mM Tris, 5 mM Imidazole, 500 mM NaCl, pH 8) and was homogenized five times at 30 s intervals to lyse the cells. The cell lysate was then ultracentrifuged at 35,000 for 30 min at 4 °C. The supernatant was filtered through a 0.45 μm filter. ASC and ASCb were purified using nickel affinity HPLC. The protein was eluted using elution buffer (20 mM Tris-HCl pH 8, 500 mM NaCl, 500 mM imidazole, and 6 M guanidinium hydrochloride) and subsequently dialyzed to remove excess of imidazole, salt, and chaotropic agent. ASC and ASCb were further purified by reverse-phase HPLC with a C4 column. Eluted protein solutions were lyophilized to remove organic solvents and stored at 4 °C. Expression of unlabeled ASC and ASCb was performed in LB media, and the purification protocol was identical to the one described for the isotopically enriched proteins. Information dependent on the amino acid sequence such as molecular weight, amino acid composition, theoretical extinction coefficient, and isoelectric point was obtained from the ExPASy server.

Structure of ASC and model of ASCb

The solution structure of ASC (PDB 2KN6) (10) was used as template to create a model of the 3D structure of ASCb using the program Chimera (23). For this purpose, 20 amino acids were removed from the linker region of ASC leaving only three amino acids (QGL) corresponding to the linker region of ASCb.

Chemical shift assignment of ASCb by NMR spectroscopy

ASCb NMR samples were prepared at 200 μM in a volume of 300 μl containing 5% D_2O, 20 mM glycine, and 1 mM TCEP at pH 3.8. NMR experiments were acquired at 298 K in a Bruker 800 MHz spectrometer equipped with a triple-resonance cryoprobe at UC Santa Cruz's NIH-NMR facility. Backbone assignment of ASCb was obtained from the following experiments: 2D [^{1}H-^{15}N]-HSQC, 3D [^{1}H-^{15}N]-NOESY-HSQC, 3D HNCACB, and 3D CBCA(CO)NH (46, 47). Data were processed with NMRPipe and spectra were analyzed with Sparky (48, 49). Previously published chemical shift assignments of ASC were used to identify potential differences (22). The chemical shift differences ($\Delta\delta^{av}$) between ASC and ASCb were calculated using the ^{1}H and ^{15}N chemical shifts according to Equation 8 (50).

$$\Delta\delta^{av} = \left[\left(\delta_{1H\_ASC} - \delta_{1H\_ASCb}\right)^2 + \left(\frac{\delta_{15N\_ASC} - \delta_{15N\_ASCb}}{5}\right)^2 \right]^{1/2} \quad (8)$$

RT-NMR experiments

ASC and ASCb samples were prepared in 5% D_2O/H_2O and 1 mM TCEP at pH 3.8. Oligomerization kinetics of ASC and ASCb was monitored using RT-NMR at a concentration of ~700 μM, ~500 μM and ~300 μM. Exact concentration values of both ASC and ASCb were determined by absorbance at 280 nm prior to commencing the experiment. Eighteen individual 2D [^{1}H-^{15}N]-HSQC experiments were acquired at time points: 30 min, 1 h 10 min, 2 h, 4 h, 6 h, 8 h, 10 h, 15 h, 20 h, 25 h, 30 h, 35 h, 40 h, 45 h, 50 h, 55 h, 60 h, and 65 h after sample preparation at 298K on a Bruker Avance III 600 MHz spectrometer equipped with a z-axis gradient cryogenic probe (UC Merced NMR facility). The overall intensity of the first 1D projection of the amide region for each [^{1}H-^{15}N]-HSQC spectrum was used to monitor signal decay over time. 1D projections were baseline-corrected from 12.8 ppm to 4.8 ppm, and the signal intensity of each 1D projection was calculated by integration from 9.5 ppm to 6 ppm using TOPSPIN 4.1 (Bruker). Intensity values for both ASC and ASCb were normalized with respect to the first 2D experiment (with an assigned intensity of 1) and were plotted as a function of time. The decays with time of NMR signal intensity were fitted to logistic mono- and double-exponential Equations 1 and 2 (Results section) for an overall identification of potentially different kinetic phases. RT-NMR data were also fitted to the analytical Equation 6 (Results section) derived from the kinetic model (Figure 5) to obtain values of the kinetic parameters. In

addition, amino-acid-specific intensity decays *versus* time for ASC and ASCb at ~700 μM and ~500 μM for the PYD and CARD domains (n = 66) were determined by obtaining the peak height value at half-height using Sparky (48). Intensity values were normalized and fitted to Equation 2. All fittings were performed with the program Qt-Grace (QTGroup, Helsinki, Finland). Goodness of fit values are shown in Table 1.

Size-exclusion chromatography

Analytical SEC was performed using a Superdex 200 Increase 10/300 GL at a flow rate of 0.5 ml/min. Prior to use, the column was calibrated with a gel filtration high molecular weight kit from GE Life Sciences. The column was equilibrated using equilibration buffer (150 mM NaCl, pH 3.8, 0.2 μm-filtered, degassed). ASC and ASCb were prepared at 50 μM and 150 μM protein concentration in 150 mM NaCl buffer, pH 3.8. Kinetic experiments of ASC and ASCb were performed at 50 μM protein concentration and loaded into the column at two different time points: 80 min and 2 days after sample preparation. The effect of protein concentration on ASC and ASCb oligomerization was tested at 150 μM (pH 3.8). Protein samples were centrifuged for 1 min at 5000 rpm and loaded into the column right after preparation. Protein absorbance values were monitored at a wavelength of 280 nm. The resulting chromatograms were plotted with QtGrace (QTGroup, Helsinki, Finland).

Dynamic light scattering

DLS experiments were performed using a Malvern Panalytical Zetasizer Pro at 25 °C, using a laser wavelength of 632.8 nm. The refractive indices of ASC and ASCb were determined to be 1.3327 using an Abbe Mark III refractometer (Reichart). The absorbance value of ASC and ASCb at 632.8 nm was 0.1089. ASC and ASCb samples were prepared at a concentration of ~700 μM by weight in HPLC-grade water at pH 3.8. Sample concentration was accurately measured prior to each experimental run by absorbance at 280 nm for both ASC and ASCb. Samples were placed in a ZEN0040 cuvette (Malvern Panalytical) for small volumes and equilibrated for 2 min at 25 °C prior to each measurement. Measurements were taken at 30 min, 1 h, 3 h, 6 h, 10 h, 14 h, 16 h, 19 h, 23 h, 26 h, 31 h, 32 h, 44 h, 46 h, and 49 h after sample preparation. Photon counts of the scattered light *versus* time are fitted to correlation functions by the ZS Xplorer software, from which the size distribution and polydispersity values are obtained. Three measurements of the scattered light were taken at each time point, and the resulting data were plotted and analyzed with QtGrace (QTGroup, Helsinki, Finland).

Transmission electron microscopy

ASCb protein filaments were prepared by dissolving lyophilized ASCb (50 μM) in a buffer containing 6 M Guanidine-HCl, 20 mM Tris pH 7, and 100 mM NaCl. The buffer was filtered with 0.2 μm-pore size filter prior to dissolving ASCb. The concentration of the protein was determined by absorbance at 280 nm. The protein solution was dialyzed against 100 mM NaCl and 20 mM Tris pH 7, and the dialysis buffer was changed three times after reaching equilibrium (3 h). A volume of 4 μl of the protein solution was deposited on a carbon-coated copper grid. After 10 min, the grid was washed in three 40 μl droplets of HPLC water (10 s each) and stained in three 40 μl droplets of 2% uranyl acetate (10 s each). The copper grid was stained for 5 min and then wipe-dried to remove excess of the staining solution. Images of ASCb filaments were obtained using a Talos F200C G2 Transmission Electron Microscope equipped with a Field Emission Gun (X-FEG) at 200 kV. A Ceta 16M Camera of 4k × 4 pixels was used for image acquisition. Analysis of ASCb filaments and bundle dimensions was performed with ImageJ.

Mass spectrometry

NMR samples of ^{15}N-labeled ASC and ASCb at ~500 μM used for the RT-NMR experiments (several months after the start of the oligomerization process) were injected in an electrospray ionization mass spectrometer (Q-Exactive Hybrid Quadrupole-Orbitrap, Thermo) coupled to an UHPLC system (Vanquish, Thermo). The protein samples were diluted with a solution containing 95% acetonitrile, 4.9% water, 0.1% formic acid and were injected in a reverse-phase column (Acclaim 200 C18, 3 μm, Thermo) at a flow rate of 0.3 ml/min. The spectra with signal intensity *versus* mass/charge were analyzed with BioPharma 2.0 software (Thermo).

Molecular docking

Molecular docking was performed with the program HADDOCK (41) using full-length ASC solution structure determined by NMR (PDB code 2KN6, (10)), the ASCb model structure created with Chimera (23), and a procaspase-1 CARD protomer extracted from the 3D structure of the polymeric CARD determined by cryo-EM (43). Firstly, four sets of dimer models composed of ASC or ASCb and one procaspase-1^{CARD} were created selecting complementary surfaces of active residues to guide the molecular docking, following the type I interactions (helices 1 and 4 of one CARD with helices 2 and 3 of the adjacent CARD and vice versa). The generated sets of dimers are dimer-set 1= ASC (helices 1, 4): procaspase-1^{CARD} (helices 2, 3); dimer-set 2 = ASC (helices 2, 3): procaspase-1^{CARD} (helices 1, 4); dimer-set 3 = ASCb (helices 1, 4): procaspase-1^{CARD} (helices 2, 3); dimer-set 4 = ASCb (helices 2, 3): procaspase-1^{CARD} (helices 1, 4).

The best dimer structure of each of the previous four sets based on the best HADDOCK score was used to create sets of trimers by the addition of another procaspase-1^{CARD} molecule as follows: trimer-set 1 = procaspase-1^{CARD} (helices 2, 3): ASC (helices 1, 4): procaspase-1^{CARD} (helices 2, 3); trimer-set 2 = procaspase-1^{CARD} (helices 1, 4): ASC (helices 2, 3): procaspase-1^{CARD} (helices 1, 4); trimer-set 3 = procaspase-1^{CARD} (helices 2, 3): ASCb (helices 1, 4): procaspase-1^{CARD} (helices 2, 3); trimer-set 4 = procaspase-1^{CARD} (helices 1, 4): ASCb (helices 2, 3): procaspase-1^{CARD} (helices 1, 4). The best trimer structure

of each of the previous four sets (based on the best HADDOCK score) is depicted in Figure 9. In all HADDOCK runs, the 23- and 3-amino acid linker of ASC and ASCb, respectively, was set fully flexible to allow for domain reorientation. The N and C termini were considered charged. The number of starting structures was 1000, out of which 200 were considered for refinement. Solvated docking was used with water as solvent for the iterations. The top clusters for the different runs were analyzed and inspected with ChimeraX (51).

Data availability

The data that support the findings of this study are contained within the article and the supporting information. All source data generated for this study are available from the corresponding author (Dr Eva de Alba; edealbabastarrechea@ucmerced.edu) upon reasonable request.

Supporting information—This article contains supporting information.

Acknowledgments—We are grateful to Dr Mourad Sadqi (NSF CREST Center for Cellular and Biomolecular Machines at the University of California, Merced) for mass spectrometry data. We would like to thank UC Merced Imaging Facility. We are grateful to Professor Son C. Nguyen for letting us use the dynamic light scattering equipment in his laboratory. The National Institutes of Health has funded the UC Santa Cruz NMR facility (award 1S10OD018455) used to obtain NMR data reported in this work.

Author contributions—E. d. A. conceptualization; P. D-P. and E. d. A. formal analysis; E. d. A. funding acquisition; P. D-P. and E. d. A. investigation; P. D-P. and E. d. A. methodology; E. d. A. project administration; E. d. A. supervision; P. D-P. and E. d. A. validation; P. D-P. and E. d. A. visualization; P. D-P. and E. d. A. writing—original draft; P. D-P. and E. d. A. writing—review and editing.

Funding and additional information—This research was funded by the National Institute of Allergy and Infectious Diseases of the National Institutes of Health under award number R15AI146780 to E. d. A., and by the NSF-CREST: Center for Cellular and Biomolecular Machines at the University of California, Merced (NSF-HRD-1547848) to P. D-P. The content of this publication is solely the responsibility of the authors and does not necessarily represent the official views of the National Institutes of Health or the National Science Foundation.

Conflict of interest—The authors declare that they have no conflicts of interest with the contents of this article.

Abbreviations—The abbreviations used are: ALR, absent in melanoma 2-like receptor; ASC, apoptosis-associated speck-like protein containing a CARD; CARD, caspase activation and recruitment domain; DAMPS, damage-associated molecular patterns; DLS, dynamic light scattering; IL-1β, interleukin-1 beta; IL-18, interleukin-18; NF-κβ, nuclear factor kappa beta; NLR, nucleotide-binding domain leucine-rich repeat containing receptor; NMR, nuclear magnetic resonance; NOD, nucleotide-binding and oligomerization domain; PAMP, pathogen-associated molecular patterns; PYD, pyrin domain; SEC, size-exclusion chromatography; TEM, transmission electron microscopy; TLR, toll-like receptor; TNF-α, tumor necrosis factor alpha.

References

1. Kawai, T., and Akira, S. (2009) The roles of TLRs, RLRs and NLRs in pathogen recognition. *Int. Immunol.* **21**, 317–337
2. Man, S. M., and Kanneganti, T.-D. (2015) Regulation of inflammasome activation. *Immunol. Rev.* **265**, 6–21
3. Sharma, M., and de Alba, E. (2021) Structure, activation and regulation of NLRP3 and AIM2 inflammasomes. *Int. J. Mol. Sci.* **22**, 872
4. Sharma, D., and Kanneganti, T.-D. (2016) The cell biology of inflammasomes: Mechanisms of inflammasome activation and regulation. *J. Cell Biol.* **213**, 617–629
5. Malik, A., and Kanneganti, T.-D. (2017) Inflammasome activation and assembly at a glance. *J. Cell Sci.* **130**, 3955–3963
6. Schroder, K., and Tschopp, J. (2010) The inflammasomes. *Cell* **140**, 821–832
7. Park, H. H., Lo, Y.-C., Lin, S.-C., Wang, L., Yang, J. K., and Wu, H. (2007) The death domain superfamily in intracellular signaling of apoptosis and inflammation. *Annu. Rev. Immunol.* **25**, 561–586
8. Jin, T., and Xiao, T. S. (2015) Activation and assembly of the inflammasomes through conserved protein domain families. *Apoptosis* **20**, 151–156
9. Masumoto, J., Taniguchi, S., Ayukawa, K., Sarvotham, H., Kishino, T., Niikawa, N., Hidaka, E., Katsuyama, T., Higuchi, T., and Sagara, J. (1999) ASC, a novel 22-kDa protein, aggregates during apoptosis of human promyelocytic leukemia HL-60 cells. *J. Biol. Chem.* **274**, 33835–33838
10. de Alba, E. (2009) Structure and interdomain dynamics of apoptosis-associated speck-like protein containing a CARD (ASC). *J. Biol. Chem.* **284**, 32932–32941
11. Diaz-Parga, P., and de Alba, E. (2019) Protein interactions of the inflammasome adapter ASC by solution NMR. *Methods Enzymol.* **625**, 223–252
12. Nambayan, R. J. T., Sandin, S. I., Quint, D. A., Satyadi, D. M., and de Alba, E. (2019) The inflammasome adapter ASC assembles into filaments with integral participation of its two death domains, PYD and CARD. *J. Biol. Chem.* **294**, 439–452
13. Man, S. M., Hopkins, L. J., Nugent, E., Cox, S., Gluck, I. M., Tourlomousis, P., Wright, J. A., Cicuta, P., Monie, T. P., and Bryant, C. E. (2014) Inflammasome activation causes dual recruitment of NLRC4 and NLRP3 to the same macromolecular complex. *Proc. Natl. Acad. Sci. U. S. A.* **111**, 7403–7408
14. Duez, H., and Pourcet, B. (2021) Nuclear receptors in the control of the NLRP3 inflammasome pathway. *Front. Endocrinol.* **12**, 630536
15. Kelley, N., Jeltema, D., Duan, Y., and He, Y. (2019) The NLRP3 inflammasome: An overview of mechanisms of activation and regulation. *Int. J. Mol. Sci.* **20**, 328
16. Elliott, E. I., and Sutterwala, F. S. (2015) Initiation and perpetuation of NLRP3 inflammasome activation and assembly. *Immunol. Rev.* **265**, 35–52
17. Barry, R., John, S. W., Liccardi, G., Tenev, T., Jaco, I., Chen, C.-H., Choi, J., Kasperkiewicz, P., Fernandes-Alnemri, T., Alnemri, E., Drag, M., Chen, Y., and Meier, P. (2018) SUMO-mediated regulation of NLRP3 modulates inflammasome activity. *Nat. Commun.* **9**, 3001
18. Friker, L. L., Scheiblich, H., Hochheiser, I. V., Brinkschulte, R., Riedel, D., Latz, E., Geyer, M., and Heneka, M. T. (2020) β-amyloid clustering around ASC fibrils boosts its toxicity in microglia. *Cell Rep.* **30**, 3743–3754.e6
19. Pirzada, R. H., Javaid, N., and Choi, S. (2020) The roles of the NLRP3 inflammasome in neurodegenerative and metabolic diseases and in relevant advanced therapeutic interventions. *Genes* **11**, 131
20. Bryan, N. B., Dorfleutner, A., Kramer, S. J., Yun, C., Rojanasakul, Y., and Stehlik, C. (2010) Differential splicing of the apoptosis-associated speck like protein containing a caspase recruitment domain (ASC) regulates inflammasomes. *J. Inflamm.* **7**, 23
21. Matsushita, K., Takeoka, M., Sagara, J., Itano, N., Kurose, Y., Nakamura, A., and Taniguchi, S. (2009) A splice variant of ASC regulates IL-1 β

release and aggregates differently from intact ASC. *Mediators Inflamm.* **2009**, 1–6
22. de Alba, E. (2007) 1H, 15N and 13C backbone and side chain chemical shifts of human ASC (apoptosis-associated speck-like protein containing a CARD domain). *Biomol. NMR Assign.* **1**, 135–137
23. Pettersen, E. F., Goddard, T. D., Huang, C. C., Couch, G. S., Greenblatt, D. M., Meng, E. C., and Ferrin, T. E. (2004) UCSF Chimera–a visualization system for exploratory research and analysis. *J. Comput. Chem.* **25**, 1605–1612
24. Sengupta, I., Bhate, S. H., Das, R., and Udgaonkar, J. B. (2017) Salt-mediated oligomerization of the mouse prion protein monitored by real-time NMR. *J. Mol. Biol.* **429**, 1852–1872
25. Fawzi, N. L., Ying, J., Torchia, D. A., and Clore, G. M. (2010) Kinetics of amyloid β monomer-to-oligomer exchange by NMR relaxation. *J. Am. Chem. Soc.* **132**, 9948–9951
26. Kamihira, M., Naito, A., Tuzi, S., Nosaka, A. Y., and Saitô, H. (2000) Conformational transitions and fibrillation mechanism of human calcitonin as studied by high-resolution solid-state 13C NMR. *Protein Sci.* **9**, 867–877
27. Eigen, M. (1996) Prionics or the kinetic basis of prion diseases. *Biophys. Chem.* **63**, A1–A18
28. Oosawa, F., and Kasai, M. (1962) A theory of linear and helical aggregations of macromolecules. *J. Mol. Biol.* **4**, 10–21
29. Hofrichter, J., Ross, P. D., and Eaton, W. A. (1974) Kinetics and mechanism of deoxyhemoglobin S gelation: A new approach to understanding sickle cell disease. *Proc. Natl. Acad. Sci. U. S. A.* **71**, 4864–4868
30. Ferrone, F. A., Hofrichter, J., Sunshine, H. R., and Eaton, W. A. (1980) Kinetic studies on photolysis-induced gelation of sickle cell hemoglobin suggest a new mechanism. *Biophys. J.* **32**, 361–380
31. Ferrone, F. A., Hofrichter, J., and Eaton, W. A. (1985) Kinetics of sickle hemoglobin polymerization: II. A double nucleation mechanism. *J. Mol. Biol.* **183**, 611–631
32. Wegner, A., and Engel, J. (1975) Kinetics of the cooperative association of actin to actin filaments. *Biophys. Chem.* **3**, 215–225
33. Goldstein, R. F., and Stryer, L. (1986) Cooperative polymerization reactions. Analytical approximations, numerical examples, and experimental strategy. *Biophys. J.* **50**, 583–599
34. Morris, A. M., Watzky, M. A., and Finke, R. G. (2009) Protein aggregation kinetics, mechanism, and curve-fitting: A review of the literature. *Biochim. Biophys. Acta* **1794**, 375–397
35. Thusius, D. (1975) Mechanism of bovine liver glutamate dehydrogenase self-assembly: II. Simulation of relaxation spectra for an open linear polymerization proceeding *via* a sequential addition of monomer units. *J. Mol. Biol.* **94**, 367–383
36. Flyvbjerg, H., Jobs, E., and Leibler, S. (1996) Kinetics of self-assembling microtubules: An "inverse problem" in biochemistry. *Proc. Natl. Acad. Sci. U. S. A.* **93**, 5975–5979
37. Serio, T. R., Cashikar, A. G., Kowal, A. S., Sawicki, G. J., Moslehi, J. J., Serpell, L., Arnsdorf, M. F., and Lindquist, S. L. (2000) Nucleated conformational conversion and the replication of conformational information by a prion determinant. *Science* **289**, 1317–1321
38. Meisl, G., Rajah, L., Cohen, S. A. I., Pfammatter, M., Šarić, A., Hellstrand, E., Buell, A. K., Aguzzi, A., Linse, S., Vendruscolo, M., Dobson, C. M., and Knowles, T. P. J. (2017) Scaling behaviour and rate-determining steps in filamentous self-assembly. *Chem. Sci.* **8**, 7087–7097
39. Dear, A. J., Michaels, T. C. T., Meisl, G., Klenerman, D., Wu, S., Perrett, S., Linse, S., Dobson, C. M., and Knowles, T. P. J. (2020) Kinetic diversity of amyloid oligomers. *Proc. Natl. Acad. Sci. U. S. A.* **117**, 12087–12094
40. Oroz, J., Barrera-Vilarmau, S., Alfonso, C., Rivas, G., and de Alba, E. (2016) ASC pyrin domain self-associates and binds NLRP3 protein using equivalent binding interfaces. *J. Biol. Chem.* **291**, 19487–19501
41. van Zundert, G. C. P., Rodrigues, J. P. G. L. M., Trellet, M., Schmitz, C., Kastritis, P. L., Karaca, E., Melquiond, A. S. J., van Dijk, M., de Vries, S. J., and Bonvin, A. M. J. J. (2016) The HADDOCK2.2 web server: User-friendly integrative modeling of biomolecular complexes. *J. Mol. Biol.* **428**, 720–725
42. Ferrao, R., and Wu, H. (2012) Helical assembly in the death domain (DD) superfamily. *Curr. Opin. Struct. Biol.* **22**, 241–247
43. Lu, A., Li, Y., Schmidt, F. I., Yin, Q., Chen, S., Fu, T.-M., Tong, A. B., Ploegh, H. L., Mao, Y., and Wu, H. (2016) Molecular basis of caspase-1 polymerization and its inhibition by a new capping mechanism. *Nat. Struct. Mol. Biol.* **23**, 416–425
44. Gambin, Y., Giles, N., O'Carroll, A., Polinkovsky, M., Hunter, D., and Sierecki, E. (2018) Single-molecule fluorescence reveals the oligomerization and folding steps driving the prion-like behavior of ASC. *J. Mol. Biol.* **430**, 491–508
45. Salvesen, G. S., and Dixit, V. M. (1999) Caspase activation: The induced-proximity model. *Proc. Natl. Acad. Sci. U. S. A.* **96**, 10964–10967
46. Cavanagh, J., Fairbrother, W. J., Palmer, A. G., III, and Skelton, N. J. (1995) *Protein NMR Spectroscopy: Principles and Practice*, Elsevier, San Diego, CA
47. Bax, A., and Grzesiek, S. (1993) Methodological advances in protein NMR. *Acc. Chem. Res.* **26**, 131–138
48. Lee, W., Tonelli, M., and Markley, J. L. (2015) NMRFAM-SPARKY: enhanced software for biomolecular NMR spectroscopy. *Bioinformatics* **31**, 1325–1327
49. Delaglio, F., Grzesiek, S., Vuister, G. W., Zhu, G., Pfeifer, J., and Bax, A. (1995) NMRPipe: A multidimensional spectral processing system based on UNIX pipes. *J. Biomol. NMR* **6**, 277–293
50. Williamson, M. P. (2013) Using chemical shift perturbation to characterise ligand binding. *Prog. Nucl. Magn. Reson. Spectrosc.* **73**, 1–16
51. Pettersen, E. F., Goddard, T. D., Huang, C. C., Meng, E. C., Couch, G. S., Croll, T. I., Morris, J. H., and Ferrin, T. E. (2021) UCSF ChimeraX: Structure visualization for researchers, educators, and developers. *Protein Sci.* **30**, 70–82

Supporting Information:

Inflammasome regulation by adaptor isoforms, ASC and ASCb, via differential self-assembly

Pedro Diaz-Parga [1,2] and Eva de Alba[1]*

[1] Department of Bioengineering. School of Engineering, [2] Quantitative Systems Biology Ph.D. Program. University of California, Merced. 5200 North lake Road. Merced, CA-95343.

Table S1: ^{15}N, $^{1}H_N$, $^{13}C_\alpha$, and $^{13}C_\beta$ Chemical Shifts of ASCb

Residue	^{15}N (ppm)	^{15}NH (ppm)	$^{13}C_\alpha$ (ppm)	$^{13}C_\beta$ (ppm)
M1	120.855	8.351	55.545	32.931
G2	110.838	8.573	45.344	-
R3	120.126	8.298	57.169	30.706
A4	124.233	8.676	55.527	18.167
R5	117.364	8.616	60.275	29.572
D6	117.29	7.643	56.994	39.86
A7	122.56	7.682	54.961	18.713
I8	120.933	8.175	66.204	38.585
L9	119.726	7.93	57.862	41.49
D10	115.962	7.919	56.738	40.234
A11	119.79	7.361	54.875	17.946
L12	114.663	8.283	57.77	41.242
E13	116.624	8.825	57.634	28.236
N14	116.116	7.326	53.636	39.844
L15	119.528	6.919	54.396	41.168
T16	113.68	8.566	60.957	70.63
A17	123.284	8.914	55.804	17.753
E18	117.661	8.568	59.335	29.074
E19	119.996	7.72	58.498	30.089
L20	121.86	9.059	57.829	40.582
K21	118.615	7.529	60.324	32.152
K22	118.698	7.601	59.746	32.498
F23	122.026	8.791	61.562	39.464
K24	117.256	8.094	60.548	33.149
L25	115.925	7.748	57.822	41.29
K26	120.626	8.127	58.091	31.98
L27	120.829	7.91	57.634	41.026
L28	116.116	7.326	56.246	41.622
S29	110.993	7.473	58.029	65.378
V30	124.342	7.857	-	-
L32	122.663	8.231	52.021	45.837
R33	121.21	7.625	56.509	31.566
E34	122.296	8.507	57.978	28.889
G35	111.344	8.693	44.748	-
Y36	118.122	7.435	58.08	40.66
G37	108.985	8.979	43.625	-
R38	118.354	8.481	53.804	31.231
I39	128.577	8.222	-	-
R41	124.291	8.358	60.046	30.454
G42	104.679	8.795	46.698	-
A43	121.765	7.183	53.693	18.363

L44	116.405	7.768	57.148	43.04
L45	116.405	7.768	58.858	41.243
S46	111.827	7.69	58.709	63.892
M47	119.956	7.175	57.882	34.453
D48	122.522	8.699	51.216	39.476
A49	118.365	8.544	55.997	18.244
L50	121.456	7.811	58.426	41.434
D51	119.092	8.284	56.828	39.679
L52	120.398	8.681	57.547	41.907
T53	117.897	7.94	69.482	68.1
D54	118.414	7.661	57.316	39.634
K55	122.605	8.327	57.511	31.287
L56	120.678	8.957	58.95	42.483
V57	115.265	7.964	65.826	31.238
S58	116.719	8.207	61.484	63.639
F59	120.036	8.452	60.748	38.83
Y60	115.834	8.039	57.928	38.953
L61	111.573	7.377	57.107	40.518
E62	116.133	8.558	61.208	29.951
T63	112.084	7.974	65.871	67.627
Y64	122.782	8.683	58.175	35.835
G65	106.757	7.965	47.795	-
A66	124.228	7.691	55.535	18.175
E67	121.366	7.757	59.419	29.678
L68	120.766	8.91	57.818	41.979
T69	114.396	7.488	67.776	67.776
A70	122.194	8.076	55.904	17.81
N71	117.615	8.347	56.007	37.561
V72	121.861	8.398	67.217	30.918
L73	118.554	8.356	58.099	41.045
R74	119.138	8.446	60.802	28.655
D75	122.202	8.026	56.642	40.445
M76	116.396	7.869	56.725	34.891
G77	107.353	7.943	44.673	-
L78	124.775	8.055	52.748	38.774
Q79	118.785	7.833	59.746	27.83
E80	121.314	8.809	59.532	27.783
M81	119.892	8.054	59.026	33.36
A82	121.665	8.038	55.356	19.133
G83	105.003	8.28	46.889	-
Q84	122.342	7.93	58.401	28.104
L85	122.56	7.682	58.426	41.434
Q86	119.092	8.284	59.187	28.655
A87	121.665	8.038	54.808	17.856
A88	119.252	7.835	53.952	19.065

T89	105.602	7.481	62.262	69.482
H90	118.73	7.668	55.331	28.535
Q91	120.855	8.351	56.46	30.679
G92	110.244	8.403	45.019	-
L93	120.933	8.175	54.201	43.481
H94	126.073	9.453	58.753	31.624
F95	130.295	8.281	62.856	40.664
I96	115.582	11.305	64.64	37.89
D97	117.693	7.202	56.467	41.806
Q98	119.919	8.23	58.014	28.973
H99	110.594	7.134	53.056	28.106
R100	121.581	6.514	60.483	30.822
A101	118.432	8.187	55.415	17.59
A102	121.161	7.866	54.514	19.713
L103	116.777	8.125	57.745	41.701
I104	118.253	8.089	65.704	38.276
A105	115.138	7.125	53.901	20.056
R106	112.028	7.86	56.797	34.132
V107	121.13	7.769	64.697	31.74
T108	116.229	8.369	60.224	70.452
N109	119.482	8.093	52.433	36.911
V110	119.014	8.027	65.646	31.515
E111	119.366	8.651	60.324	28.19
W112	118.263	7.612	60.927	29.392
L113	116.116	7.326	57.776	41.18
L114	115.699	8.166	57.817	40.867
D115	117.798	8.165	56.562	38.736
A116	121.658	7.602	54.009	17.91
L117	114.23	7.427	54.801	43.303
Y118	126.432	8.006	60.816	37.653
G119	120.059	8.404	46.079	-
K120	120.131	7.478	57.858	33.737
V121	112.717	7.485	63.252	34.347
L122	117.325	7.216	53.646	44.5
T123	113.144	8.009	60.117	70.59
D124	120.509	8.897	58.603	40.887
E125	117.364	8.616	59.615	28.686
Q126	119.79	7.361	58.207	29.102
Y127	119.461	8.585	61.925	39.315
Q128	115.775	8.571	58.429	27.668
A129	121.161	7.866	54.881	18.371
V130	116.575	7.965	66.687	31.05
R131	117.528	7.814	59.354	29.81
A132	116.469	7.158	52.701	19.001
E133	119.515	7.463	-	-

T135	106.476	7.096	58.384	73.086
N136	120.788	9.53	-	-
S138	111.8	7.353	62.442	62.442
K139	125.318	8.717	60.802	34.898
M140	116.332	8.511	55.395	30.688
R141	120.664	8.785	60.526	30.228
K142	120.172	7.679	57.055	30.69
L143	123.004	8.586	58.265	41.541
F144	114.066	8.445	60.659	37.547
S145	118.414	7.661	60.915	62.397
F146	119.607	7.156	56.513	38.467
T147	110.187	6.84	-	-
A149	115.138	7.125	51.59	19.357
W150	120.626	8.127	55.458	30.772
N151	118.851	8.08	51.115	38.637
W152	120.664	8.785	61.594	28.999
T153	113.123	7.866	66.492	68.621
C154	119.649	7.989	63.729	26.577
K155	118.615	7.529	61.206	28.974
D156	120.081	8.537	57.167	39.663
L157	123.13	7.837	58.085	41.04
L158	120.635	7.441	58.394	40.58
L159	120.485	8.205	58.208	42.571
Q160	119.51	8.674	58.89	27.822
A161	121.456	7.811	54.989	17.924
L162	121.314	8.465	57.964	42.119
R163	119.497	8.514	60.25	29.689
E164	114.773	7.756	57.998	29.538
S165	110.242	7.461	59.085	64.819
Q166	124.392	8.577	55.064	28.787
S167	118.174	8.442	62.192	62.192
Y168	118.36	7.776	59.592	36.744
L169	122.963	6.894	57.209	41.393
V170	117.15	7.086	67.461	31.25
E171	116.688	8.089	58.967	28.591
D172	118.375	7.806	56.884	41.27
L173	117.903	7.863	56.558	41.701
E174	117.256	8.094	57.75	29.411
R175	117.891	7.314	56.562	30.531
S176	121.21	7.625	-	-

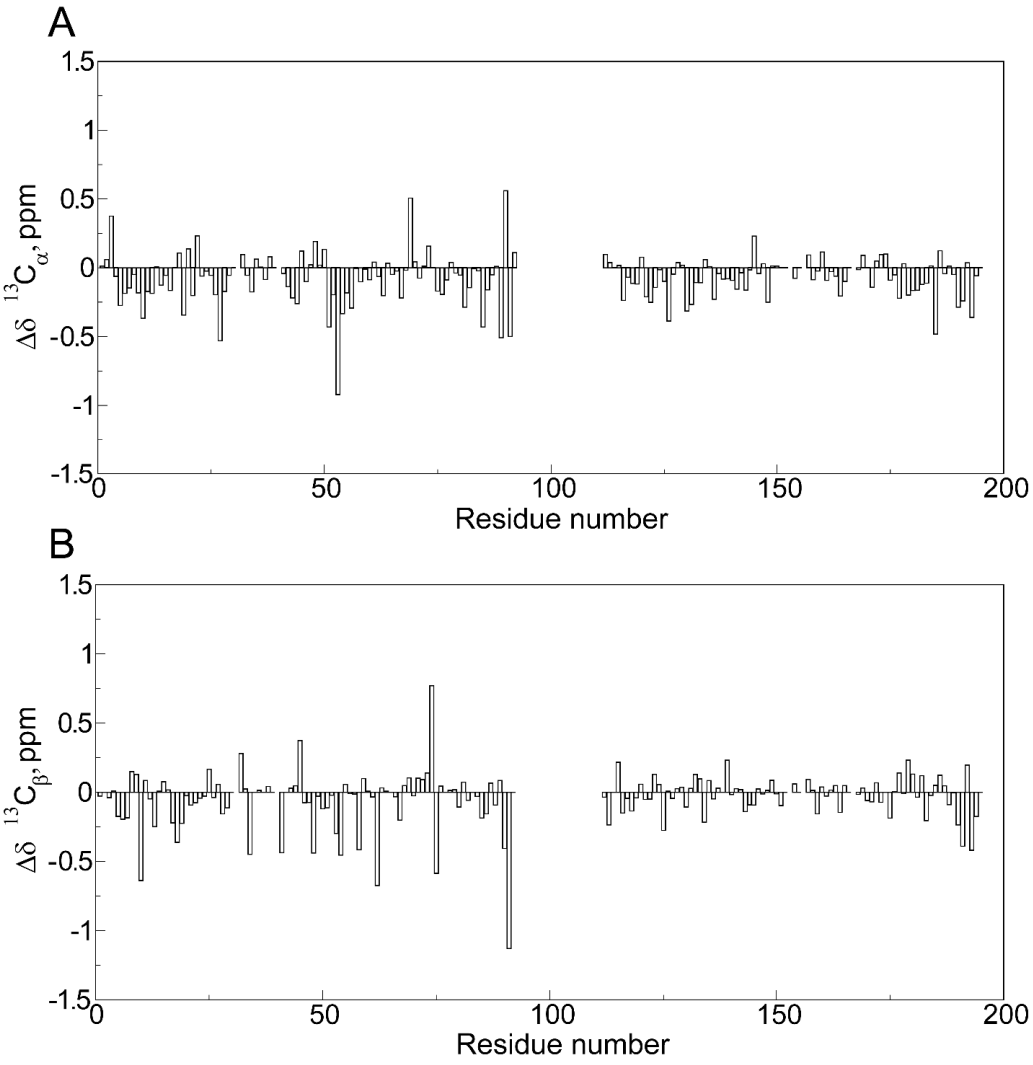

Figure S1. Comparison of ASC and ASCb ^{13}C chemical shifts. *(A) $^{13}C_\alpha$ chemical shift differences between ASC and ASCb. (B) $^{13}C_\beta$ chemical shifts differences between ASC and ASCb.*

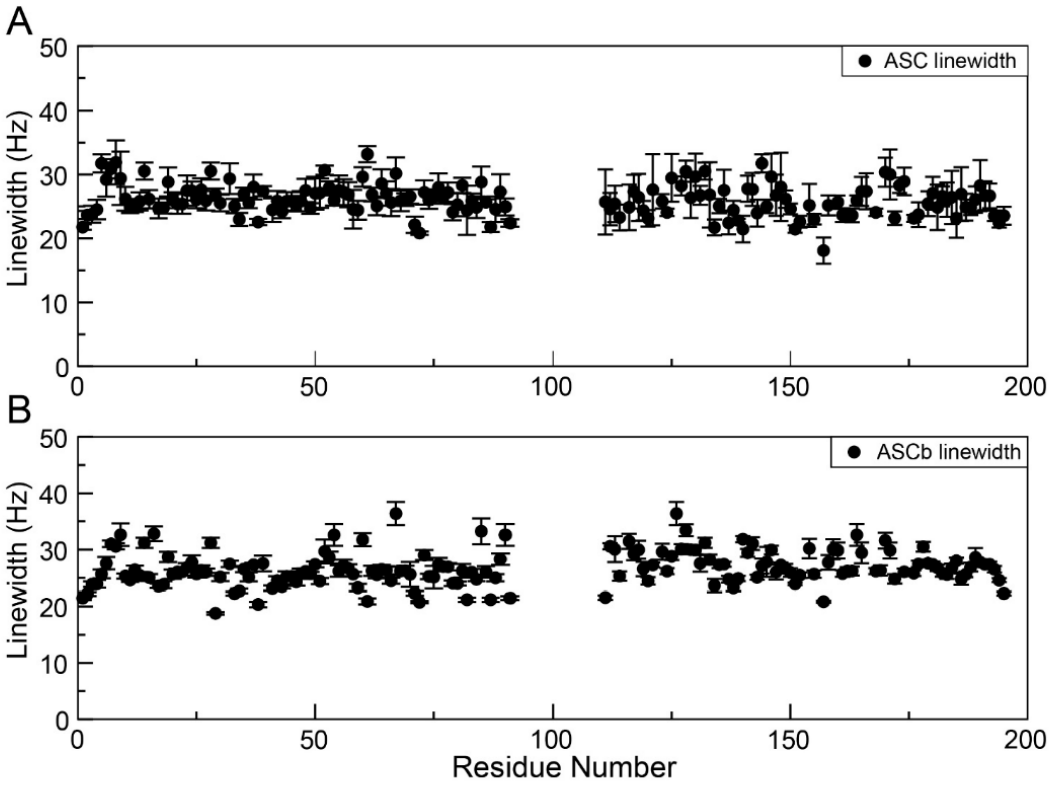

Figure S2. Comparison of ASC and ASCb NMR signal linewidth. *[^{1}H-^{15}N]-HSQC signal linewidth at half-height versus amino acid sequence for ASC (A) and ASCb (B): amino acids T16, I115, L122, V126, M159, W169, D175, and L178 for ASC, and I96, L103, T147, C154, and D156 for ASCb are excluded due to signal overlap.*

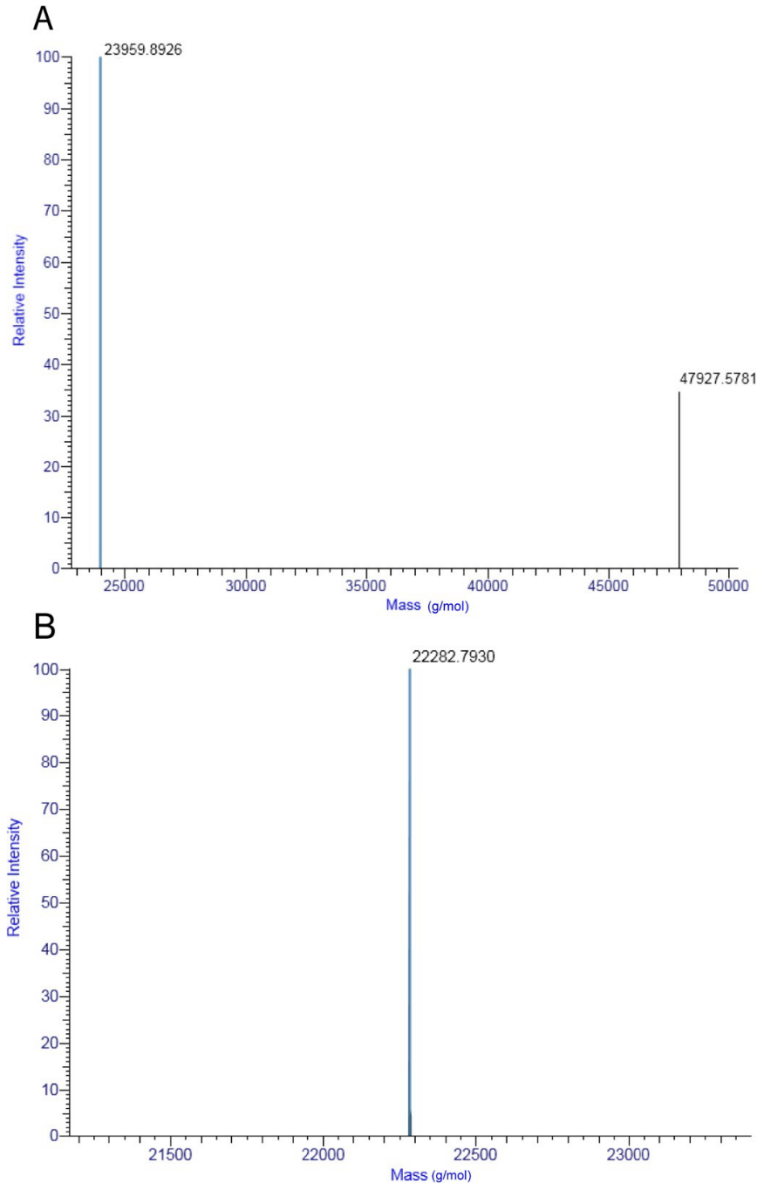

Figure S3. ASC dimer might be more stable than ASCb dimer during protein self-association. *Mass spectrometry of ^{15}N-labeled ASC (A) and ASCb (B) several months after the start of oligomerization. Mass spectrometry data in tandem after reverse phase chromatography show ASC monomer and dimer (A), whereas ASCb dimer is not present (B), suggesting higher stability of the former.*

Publication 2

This research was originally published in the Journal of Biological Chemistry. Pedro Diaz-parga, Andrea Gould and Eva de Alba. Natural and engineered inflammasome adaptor proteins reveal optimum linker length for self-assembly. J Biol Chem. 2022 © the American Society for Biochemistry and Molecular Biology

Natural and engineered inflammasome adaptor proteins reveal optimum linker length for self-assembly

Pedro Diaz-Parga[1,2], Andrea Gould[1,3] and Eva de Alba[1]

[1] Department of Bioengineering, School of Engineering, University of California Merced, CA, USA.
[2] Quantitative Systems Biology Ph.D. Program, University of California Merced, CA, USA.

[3] Current address: Revolution Medicines. 700 Saginaw Dr. Redwood City, CA, USA.

Corresponding author: Eva de Alba. Department of Bioengineering, School of Engineering, University of California Merced. CA, USA.

Short title: ASC's linker length is optimum for self-assembly
Keywords: inflammasome adaptor; ASC; protein self-assembly; interdomain dynamics; interdomain linker; NMR relaxation; multidomain protein function

Abstract

The inflammasome is a multiprotein complex that triggers the activation of proinflammatory cytokines. The adaptor ASC and its isoform ASCb mediate inflammasome assembly via self-association and oligomerization with other inflammasome proteins by homotypic interactions of their two identical Death Domains, PYD and CARD, connected by a linker of different length: 23 (ASC) and 4 (ASCb) amino acids long. However, ASC is a more potent inflammasome activator compared to ASCb. Thus, adaptor isoforms might be involved in the regulation of the inflammatory response. As previously reported, ASC's faster and less polydisperse self-association compared to ASCb points to interdomain flexibility resulting from the linker length as a key factor in inflammasome regulation. To test the influence of linker length in self-association, we have engineered the isoform ASC3X with identical PYD and CARD connected by a 69-amino acid long linker (i.e., three-times longer than ASC's linker). Real-time NMR and dynamic light scattering data indicate that ASC3X polymerization is less effective and more polydisperse compared to ASC or ASCb. However, transmission electron micrographs show that ASC3X can polymerize into filaments. Comparative interdomain dynamics of the three isoforms obtained from NMR relaxation data reveal that ASCb tumbles as a rod, whereas the PYD and CARD of ASC and ASC3X tumble independently with marginally higher interdomain flexibility in ASC3X. Altogether, our data suggest that ASC's linker length is optimized for self-association by allowing enough flexibility to favor intermolecular homotypic interactions, but simultaneously keeping both domains sufficiently close for essential participation in filament formation.

Introduction

Protein structure and dynamics determine function and operating mode. Protein dynamics is relevant for multi-domain proteins as interdomain motion plays a critical role in protein function. The combination of different domains is a frequent strategy to naturally develop new functions using minimal resources (1, 2); therefore, approximately 80% of eukaryotic proteins are predicted to be composed of multiple domains (3). The function and overall three-dimensional structure of multidomain proteins depend on the concerted action of the different domains working together (4, 5). Stretches of amino acids that connect the different domains (interdomain linkers) may facilitate interdomain communication (6). Based on amino acid composition and length, interdomain linkers can support transient secondary structures or remain intrinsically disordered, hence conferring different degrees of interdomain flexibility (7). Therefore, linker length and structure have a strong impact on domain separation and orientation, leading to changes in the

biological function of multi domain proteins. For instance, it has been reported that linker flexibility or lack thereof has a direct influence on catalytic sites, degree of domain separation, interdomain orientation, and coordinated binding in protein-ligand interactions (4, 7). In some cases, linker flexibility might be required to grant a greater amount of domain mobility, allowing the different domains to function independently of each another. The critical role of interdomain linkers is evidenced by studies showing that changes such as deletions and mutations directly impact the biological function of multidomain proteins (8–10).

Members of the Death Domain superfamily are ideal examples of multidomain proteins (11). Here we focus on the Death Domain protein ASC (11–14), which plays a critical role in the assembly of the multiprotein complex inflammasome that triggers the inflammatory response (14–17). Inflammasome assembly is mediated by homotypic interactions between multiple copies of three proteins: sensor, adaptor ASC, and the effector procaspase-1 (17, 18). Death Domain superfamily members typically carry several CARDs (caspase activation and recruitment domain), PYDs (pyrin domain), and DEDs (death effector domain), which are prevalent in a wide range of proteins necessary for the assembly and activation of inflammatory and apoptotic complexes (11, 17, 19). Inflammasome sensors are generally grouped based on their structural features as NLRs (Nucleotide-binding domain leucine-rich repeat containing receptors), ALRs (Absent in melanoma 2-Like receptors) or pyrin (20–22). NLRP3, from the NLR family, is one of the best well characterized inflammasome sensors that has been implicated in the development of several autoimmune and inflammatory diseases such as multiple sclerosis, type 2 diabetes, atherosclerosis and cryopyrin-associated periodic syndrome (23).

Inflammasome activation is a tightly controlled system involving a two-step process: priming and activation (24, 25) (**Figure 1**). The priming signal triggers toll-like receptors to initiate the nuclear factor NF-kβ pathway that results in the expression of NLRP3, pro-IL-1β, pro-IL-18 and procaspase-1 (24–26). Simultaneously, a secondary signal (activation) is required to prompt inflammasome assembly. The secondary signal is triggered by a variety of stimuli such as changes in cellular concentration of K^+, increase in intracellular Ca^{2+}, internalization of flagella through endocytosis, pore-forming toxins, and lysosomal disruption, among others (25–28). Activation and oligomerization of the NLRP3 sensor leads to the recruitment of the adaptor ASC and effector procaspase-1 to the inflammasome complex, which ultimately results in procaspase-1 autocleavage into its active form (**Figure 1**). Caspase-1 processes proinflammatory cytokines into their active forms, as well as the protein Gasdermin-D into its active N-terminus form (29, 30). Once cleaved, the N-terminus of Gasdermin-D self-associates forming large pores in the plasma membrane causing the cell to undergo an inflammatory form of death known as pyroptosis (30–33), which facilitates the release of active proinflammatory cytokines into the extracellular matrix.

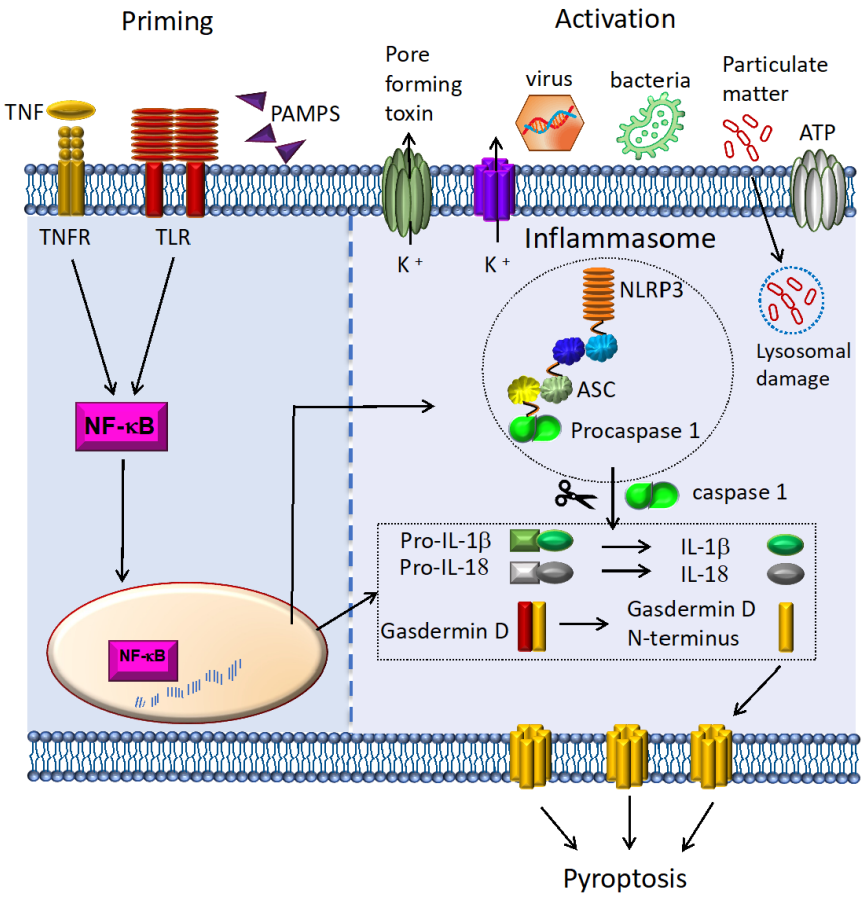

Figure 1. NLRP3 inflammasome priming and activation. *Priming (left) results from the activation of cell receptors by pathogen-associated molecular patterns (PAMPS) and cytokines, leading to the expression of inflammasome components (sensor (NLRP3), ASC, procaspase-1) and cytokine zymogens (pro-IL-1β and pro-IL-18). Activation (right) by different stimuli such as changes in K^+ efflux, lysosomal damage, or nucleic acids from virus and bacteria, leads to inflammasome assembly and the activation of the procaspase-1. Sensor and procaspase-1 are bridged by the adaptor ASC. Upon activation, caspase-1 cleaves the proinflammatory cytokines and Gasdermin-D. The N-terminus of the latter forms pores in the plasma membrane facilitating cell death by pyroptosis.*

ASC functions as a mediator between the sensor and procaspase-1 during inflammasome formation and regulates proper inflammasome assembly (14, 17, 34). ASC is a multi-domain protein consisting of a N-terminal PYD and C-terminal CARD connected by a 23 amino acid linker (14, 21, 35). ASC exists in four different isoforms: canonical ASC, ASCb, ASCc, and ASCd (14). ASC and ASCb are structurally similar, differing only in the length of their linker (23 amino acids versus 4 amino acids, respectively) (13, 14). During activation ASC localizes with sensor and procaspase-1 forming the inflammasome, which adopts the shape of a micrometer-size ring or speck (ASC speck) in the cytosol (36). Colocalization of ASC with caspase-1 and NLRP3 produces a strong inflammatory response measured by IL-1β release to the extracellular milieu (14). In contrast, ASCb is not able to assemble into the typical filamentous ASC speck,

forming instead irregular filaments. It has been reported that ASCb is a less potent activator of the inflammasome compared to ASC (14). Interestingly, ASCc, which retains the intact CARD, but not the PYD, acts as an inhibitor of the inflammasome complex, whereas the function of ASCd is still currently unknown (14).

Previously, we have reported using real-time NMR and dynamic light scattering that ASC and ASCb show stark differences in their ability to self-associate (16). We also showed using high-resolution NMR that the PYD and CARD of ASC and ASCb are identical at the structural level. Thus, differences in self-association must be associated with the length of the linker connecting both domains and with interdomain flexibility. Interdomain dynamics of multi-domain proteins can be quantified using ^{15}N NMR relaxation techniques to determine local and global dynamics. ^{15}N relaxation of the protein backbone provides dynamic information that can be correlated to protein function (37). Our previous studies on the structure and dynamics of ASC suggest that interdomain flexibility could facilitate protein-protein interactions by enabling the two domains to act semi-independently of each other, thus allowing each domain to sample a large volume of space without interfering with each other's binding capability (35).

We report herein the study and comparison of the interdomain dynamics of ASC and ASCb using high-resolution NMR relaxation techniques. Protein rotational correlation times derived from NMR relaxation data indicate that ASCb tumbles as a rod with little interdomain flexibility, whereas ASC domains are semi-independent. Thus, interdomain flexibility correlates with improved self-association observed for ASC relative to ASCb (35). We hypothesize whether a longer linker would confer additional flexibility and thus better interacting capabilities. To test this hypothesis and further understand the influence of linker length on the function of the inflammasome adaptor, we generated an artificial isoform, herein referred to as ASC3X, with a significantly increased linker length (69 amino acids, corresponding to 3 times the length of ASC linker). The rationale behind the use of a 3X linker is to determine the effect of linker length on the interdomain dynamics at one extreme scenario as a direct contrast to ASCb's very short linker. We show by NMR that the PYD and CARD of ASC3X retain the six-helix bundle motif common to death domain proteins. However, real-time NMR data of ASC3X self-association indicates a significantly different behavior compared to ASC and ASCb (16). In addition, dynamic light scattering studies reveal higher polydispersity compared to the natural isoforms. Size-exclusion chromatography analysis of ASC3X shows monomer, low-order, and high-order oligomers, whereas the low-order species was not observed in ASC and ASCb. We reported previously that both PYD and CARD in ASC are integral part of the filament structure. Here, negative-staining transmission electron microscopy (ns-TEM) studies show that ASC3X also assembles into filament bundles with analogous structural characteristics to those formed by ASC and ASCb. Finally, NMR relaxation techniques reveal that interdomain flexibility in ASC3X is only slightly larger than that of ASC. The modest increase in interdomain flexibility in ASC3X compared to ASC suggests that an intermediate sized protein such as ASC2X (46 amino acid linker) would not lead to significant changes. Altogether, our results point to a critical role played by the length of the ASC linker in fast self-association and close to monodisperse oligomerization that involves both interdomain flexibility but also sufficient proximity of the PYD and CARD to form part of the filament structure. In contrast, ASC3X interdomain flexibility is comparable to that of ASC but the two domains are separated by a very long linker, likely slowing down filament and filament bundle formation.

Results

ASC3X design and structural comparison with canonical ASC

We reported recently that ASC's faster and less polydisperse self-association compared to ASCb is related to its longer linker (23 and 4 amino acids for ASC and ASCb, respectively) (amino acid sequences shown in **Figure S1**) (16). We aimed at testing whether a longer linker would further improve the interacting capabilities of ASC isoforms. With this purpose, we engineered an artificial isoform that shares identical N-terminal PYD and C-terminal CARD albeit connected by a linker three-times longer (69 amino acids) (amino acid sequence shown in **Figure S1**) than ASC's linker; hereinafter referred to as ASC3X (**Figure 2A**).

We showed previously that ASC and ASCb share the same six-helix bundle motif in the PYD and CARD (11, 16). For an analogous structural comparison between ASC and ASC3X, the NMR chemical shift assignments of ASC3X were inferred from the chemical shifts reported for ASC (39) and checked by triple-resonance NMR. ASC3X ^{1}H, ^{15}N, $^{13}C_{\alpha}$ and $^{13}C_{\beta}$ chemical shifts are shown in **Table S1** and have been deposited in the Biomagnetic Resonance Bank with ID 51509.

The overlay of the amide [^{1}H-^{15}N]-HSQC spectra of ASC and ASC3X shows signal overlap of most amino acids in the PYD and CARD regions, thus indicating structure equivalence (**Figure 2B**). The 69-amino acid long linker in ASC3X results in intense signals in the ^{1}H chemical shift interval between 8.0 and 8.5 ppm, which corresponds to amide ^{1}H chemical shifts of disordered protein regions (40). Combined amide ^{1}H-^{15}N chemical shift deviations between ASC and ASC3X are small with a standard deviation value lower than 0.025 ppm (**Figure 3A**). Larger deviations are expected for residues close to the linker in the amino acid sequence or in the 3D structure. In addition, the $^{13}C_{\alpha}$ chemical shift differences from tabulated random coil values indicate the presence of two six-helix bundle motifs for the PYD and CARD of ASC3X as previously observed for ASC (**Figure 3B**).

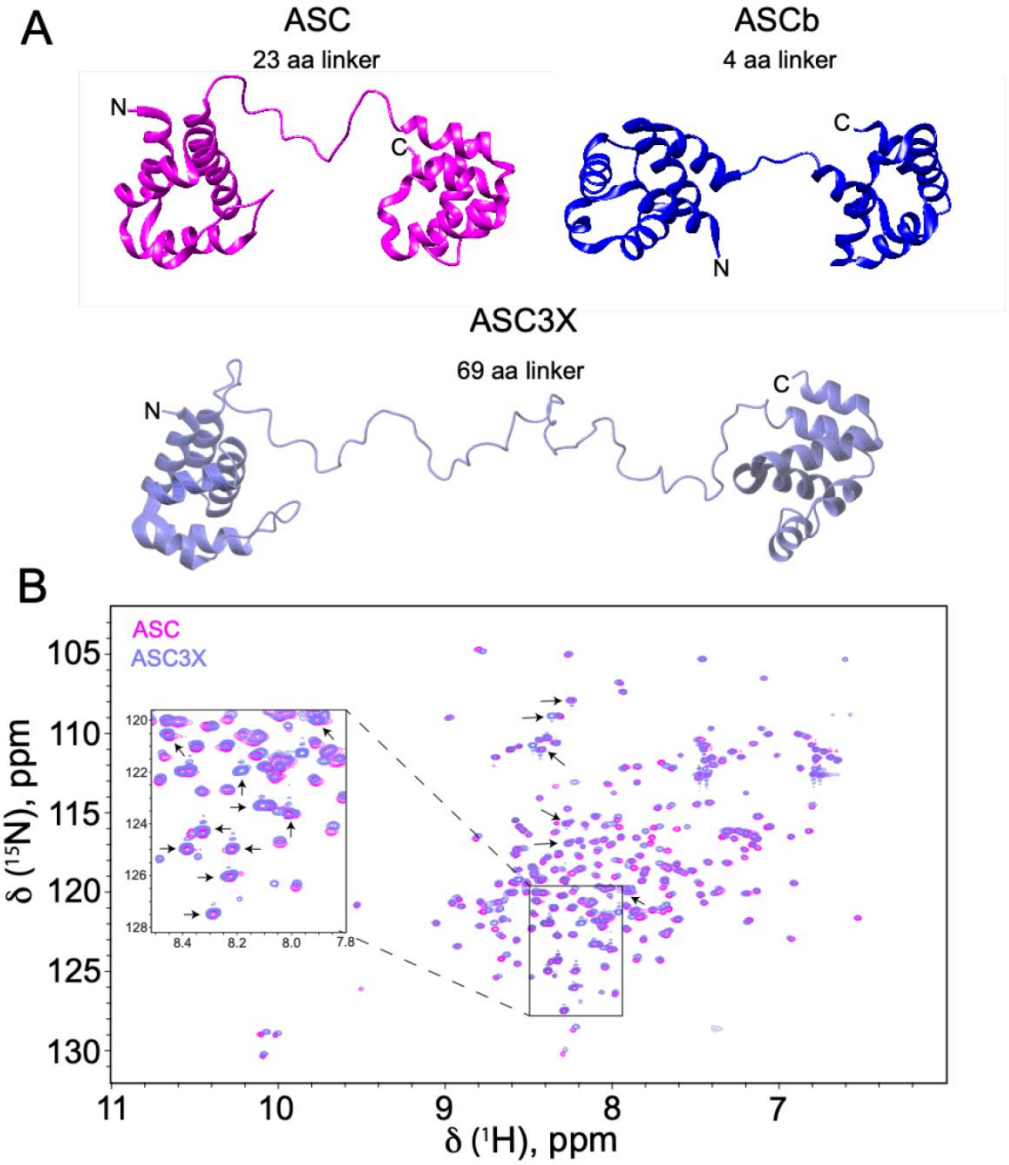

Figure 2. Structure comparison between ASC3X, ASCb and ASC. *(A) Structures of ASC* (35)*, ASCb* (16)*, and ASC3X (model created with Chimera* (38) *based on the structure of ASC* (35)*) in ribbon form. (B) 2D-[^{1}H-^{15}N]-HSQC (NMR protein fingerprint of ASC and ASC3X showing almost complete signal overlap in the PYD and CARD). A region of the spectrum is zoomed in for clarity. Unassigned peaks of the linker are indicated with arrows.*

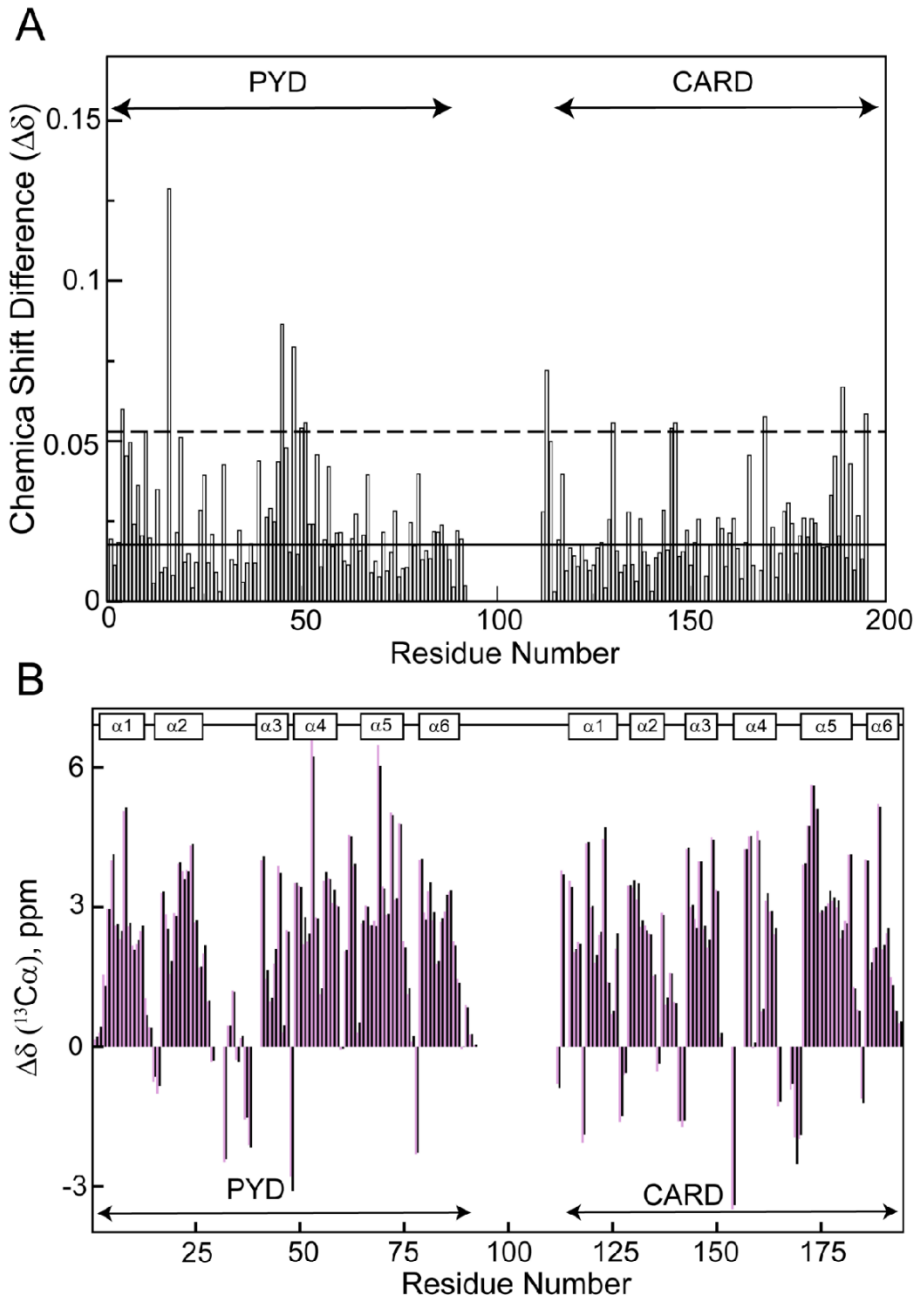

Figure 3. ASC3X and ASC share equivalent structures of the PYD and CARD domains. *(A) Combined ^{1}H and ^{15}N chemical shift differences between ASC and ASC3X versus residue number. (Solid line: 1 SD; dashed line: 3 SD). (B) Secondary shifts of ASC (pink bars) and ASC3X (black bars), indicating the six helices characteristic of the Death Domain fold.*

Different oligomerization kinetics of ASC3X compared to ASC and ASCb by real-time NMR

ASC and ASCb have a strong tendency to polymerize forming filaments and filament bundles under physiological conditions in accord with their function as inflammasome adaptors (14–16). In addition to pH and protein concentration (35), other factors such as temperature and the presence of salt were identified as important determinants in ASC's oligomerization process based on analytical centrifugation (41) and size-exclusion chromatography (16).

Upon ASC and ASCb oligomerization, NMR signal intensity decreases with time because large protein assemblies are formed and have slow tumbling rates not contributing to signal intensity (16). As a result, NMR signal intensity follows an exponential decay as protein self-association progresses. An analogous effect has also been observed in amyloid β-peptide and prion protein oligomerization (42, 43). Previously, we found that ASC oligomerizes following two kinetic phases. In contrast, a single slower kinetic phase was observed for ASCb. Because the only difference between ASC and ASCb is the length of the linker, we could expect that ASC3X behaves like ASC.

To study ASC3X oligomerization by RT-NMR, we have followed the same protocol used for ASC and ASCb (16). Briefly, pure ^{15}N-labeled protein in lyophilized form is dissolved in the NMR buffer at a concentration of ~ 700 μM to start the oligomerization process. A series of 2D-[^{1}H,^{15}N]-NMR spectra were acquired as a function of time for 65 hours. The overall signal intensity of the spectra decreases with time due to oligomerization (**Figure 4A**). The decrease of NMR signal intensity in ASC3X is analogous to that found in ASC (16), although to a significantly lesser extent, and different from ASCb behavior (**Figue 4B**). Apparent steady state conditions are reached approximately 20 h after the start of ASC3X oligomerization resulting in a plateau at ~ 75% of the original intensity.

Single- and double-exponential equations (Equations 1 and 2, respectively) were used to fit the overall intensity decay. Fitting to a double-exponential was better, which suggests that at least two steps with different rate constants take place in ASC3X oligomerization. Fast and slow rate constants for ASC3X were obtained: $k_{1\,ASC3X}$ = 0.5 h^{-1} and k_{2ASC3X} = 0.09 h^{-1}, respectively (**Table 1**). This result can be explained by protein assembly into different types of oligomers at different rates. The k_1 and k_2 values indicate that the initial decay is faster compared to ASC and ASCb; however, polymerization is less effective (plateau reached at ~ 75% of the original intensity). These results suggest that initial ASC3X oligomerized species form fast, but subsequent polymerization to higher-order oligomers is not as efficient.

$$y = A_0 e^{-x\,k} + A_1 \qquad \text{eq. 1}$$

$$y = A_0 e^{-x\,k_1} + A_2 e^{-x\,k_2} + A_1 \qquad \text{eq. 2}$$

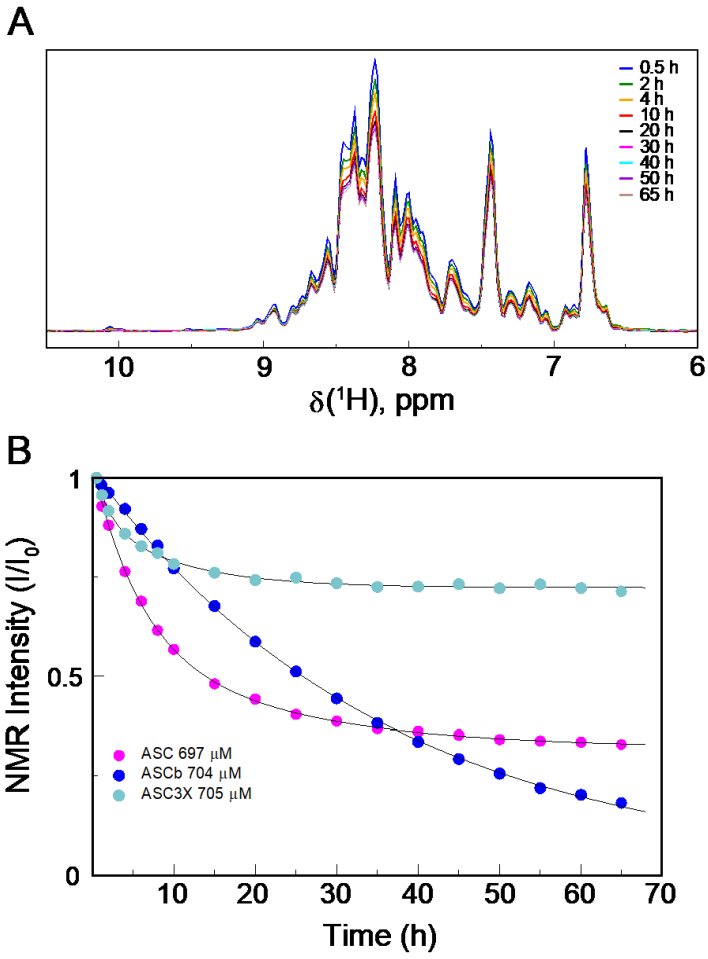

Figure 4. Less effective oligomerization of ASC3X compared to ASC and ASCb. *(A) Overall NMR signal decay from 1D projections of 2D spectra as a function of time for the oligomerization of ASC3X. (B) Normalized overall NMR signal intensity decay versus time for ASC3X, ASC* (16) *and ASCb* (16) *at approximately 700 μM protein concentration.*

By performing this analysis at the amino acid level, we reported previously that the PYD and CARD domains of ASC show different behavior in the first kinetic phase with k_1 values of the PYD larger compared to the CARD (**Table 1**). However, the k_2 values are similar for both domains. This behavior was not observed for ASCb (**Table 1**). Our results led us to suggest that PYD-PYD interactions drive the first step in the oligomerization reaction of ASC, followed by PYD and CARD participation in subsequent polymerization steps. In contrast, equivalent participation of both domains is apparent in the polymerization reaction of ASCb.

For ASC3X, we selected amino acids representative of the protein secondary structure that give rise to well-resolved NMR signals. Specifically, we selected residues in the PYD from helices 1 (E13), 2 (L20), 3 (G42),

5 (T63 and A66) and in the CARD from helices 1 (R119), 4 (N155, K158), 5 (L176) and 6 (V189) (numbering follows ASC sequence, Figure S1). The fitting of NMR signal intensity decay of the individual amino acids to the exponential equations reveals that the PYD and CARD follow different behaviors **(Figure 5)**. The average rate constants (k_1 and k_2) of 33 analyzed signals from each domain (5 residues in each of the 6 helices and 3 amino acids in the long loop connecting helices 2 and 3) are similar (**Figure 6A, Table 1**); however, the intensity of CARD signals decreases to values close to zero (~ 6%), whereas PYD signals show much smaller decrease to values ~ 76% of the initial intensity (**Figure 5**). In addition, k_1 and k_2 rate constants for individual amino acids in PYD and CARD are smaller than the values obtained for the overall intensity decay when all amino acids are included (**Table 1**). This discrepancy could be attributed to contributions of the long linker to signal intensity and to the significantly different kinetic behavior of the PYD and CARD.

Table 1. Kinetic parameters from exponential equations 1 and 2

	Protein isoform		
Rate (h^{-1})	ASC3X[a]	ASC[b]	ASCb[c]
k_1	0.503 ± 0.007	0.15 ± 0.03	0.02 ± 0.01
k_2	0.097 ± 0.007	0.04 ± 0.01	0.02 ± 0.01
$k_{1avePYD}$	0.30 ± 0.14	0.21 ± 0.04	0.0269 ± 0.0009
$k_{2avePYD}$	0.03 ± 0.02	0.05 ± 0.02	0.0269 ± 0.0009
$k_{1aveCARD}$	0.33 ± 0.06	0.12 ± 0.02	0.0288 ± 0.0009
$k_{2aveCARD}$	0.05 ± 0.03	0.02 ± 0.01	0.0288 ± 0.0009
Goodness of fit			
χ^2	0.00044850	0.00032796	0.00059583
r	0.998312	0.999812	0.999806

a: reported error from fitting. b,c: retrieved from ref (16).

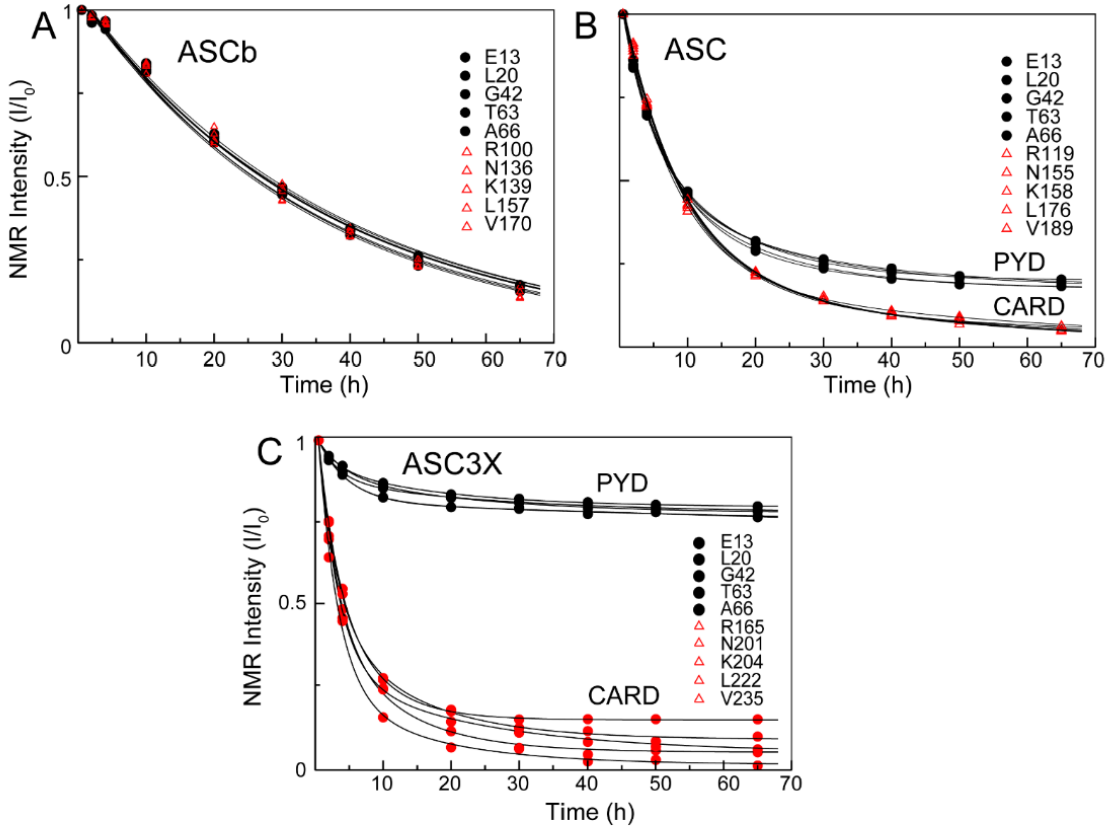

Figure 5. PYD and CARD domains display larger differences in self-assembly kinetics as linker length increases. *(A) PYD and CARD domain of ASCb show similar oligomerization kinetics (16). (B) Increase in linker length affects the oligomerization kinetics of the PYD and CARD domain of ASC (16). (C) The presence of a 3X linker has a significant effect on the oligomerization of the CARD domain. The helix to which each amino acid belongs is indicated in the main text.*

The substantial decrease in CARD signal intensity contrasting the much smaller decrease for the PYD is explained by CARD participation in homotypic interactions resulting in the formation of initial oligomeric species in which the PYD is not involved. These first oligomers will have highly mobile PYDs connected to oligomerized CARDs by the very long linkers. The higher mobility will result in intense signals from amino acids in the PYDs. To further investigate the abrupt intensity decay in CARD signals, we have monitored amide signal linewidth for both ^{1}H and ^{15}N in the of 2D-[^{1}H-^{15}N]-HSQC spectra for all time points for the PYD and only up to 10 h after the start of the experiment for the CARD because signal intensity for the latter is close to baseline level after 10 hours (**Figure 6B**). The average signal width at half height is similar for both domains (**Figure 6B**). However, while there is almost no variability in signal width with time for the PYD, significant variations (~ 5 Hz) are observed for the CARD. This variability might reflect a larger error in the CARD due to the abrupt loss in signal intensity, as well as an effect of the kinetics of CARD oligomerization in signal broadening. This dynamic effect occurs when the exchange rate (interconversion rate) between monomer and initial oligomeric species is similar in magnitude to the difference in resonance frequency for CARD nuclei in the different species. This behavior was not observed

for ASC and ASCb oligomerization and indicates that ASC3X self-association follows different kinetics and possibly the formation of initial species with different half-lives.

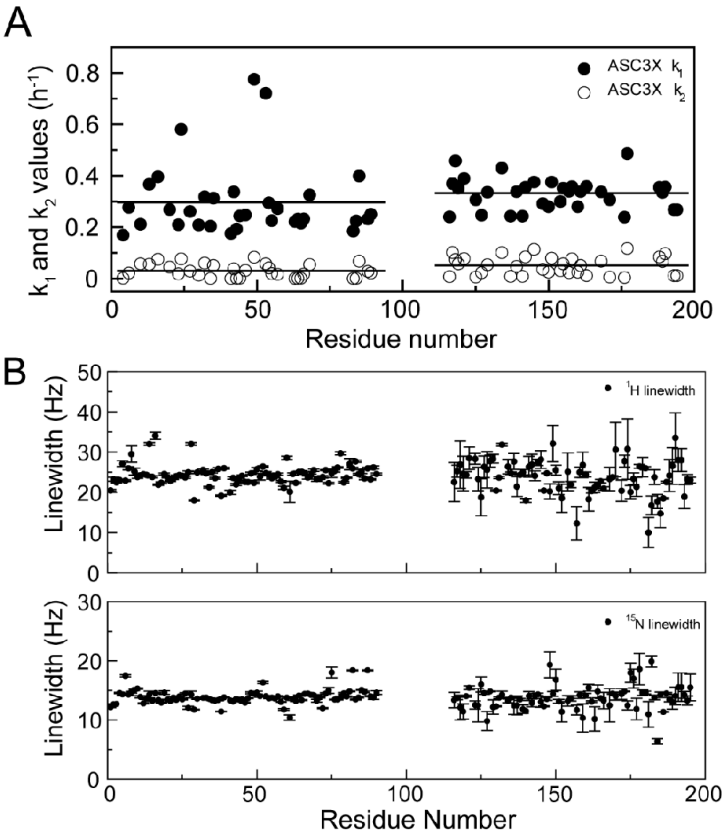

Figure 6. RT-NMR kinetics of ASC3X self-assembly reveals an important role of the CARD domain *(A) Rate constants (k_1 and k_2) of 33 signals from the PYD and 33 signals from the CARD (from 5 amino acid per helix and 3 amino acids in the long loop connecting helices 2 and 3) versus residue number. Solid black lines are averages obtained for each data set. (B) Differences in linewidth (at half-height) are average values for all time points for the PYD and time points up to 10 h for the CARD for ^{1}H (top) and ^{15}N (bottom) amide signals in 2D-[^{1}H-^{15}N]-HSQC. Error bars are standard deviations.*

We have shown previously that both PYD and CARD are integral part of the ASC filament (15), whose formation is facilitated if the two domains are not very far apart. In ASC, the two domains are connected by a linker sufficiently long to allow for reorientation, thus favoring multiple interactions, but also sufficiently short for the readily participation of the PYD and CARD in filament formation (15). In contrast, the participation of both domains in filament formation for ASC3X could be hindered by the large separation between the two domains. Overall, RT-NMR results indicate that the engineered isoform follows different kinetics for oligomerization compared to the natural isoforms. For ASC3X, the CARD domain appears to be the initial driving force of the polymerization, followed by the PYD. Based on the low

intensity decay of the PYD in ASC3X compared to the PYD in ASC (16), the oligomerization capabilities of the engineered isoform have diminished, suggesting that an interdomain linker longer than the natural one does not enhance polymerization but is in fact disruptive.

To test whether chemical modifications influence the kinetics of ASC3X self-association, we used mass spectrometry on protein samples prepared several weeks after oligomerization started. Using liquid chromatography (reverse phase) coupled to mass spectrometry, the ASC3X spectrum shows a single peak that corresponds to the monomeric species (data not shown). The molecular weight from mass spectrometry (28,204.6 g/mol) matches the theoretical molecular weight of ^{15}N-labeled monomeric ASC3X (28,202.9 g/mol), thus ruling out chemical modifications during self-association. The oligomerized ASC3X sample was also studied by mass spectrometry avoiding the unfolding step of the reverse phase column. In this case, both monomer and dimer were observed (**Figure S2**).

ASC3X forms oligomers of different sizes detected by size-exclusion chromatography

Size-exclusion chromatography (SEC) was used to study oligomer size distribution of ASC3X at different conditions of polymerization: time, protein concentration and pH. We reported previously using NMR and analytical ultracentrifugation that NaCl and high protein concentration promotes ASC self-association (41). Protein samples for the chromatographic analysis contain 150 mM NaCl to avoid non-specific interactions with the chromatographic matrix. The samples were not filtered to allow detection of large size oligomers. Instead, the samples were centrifuged for 1 minute to pellet down potential precipitated material.

ASC3X samples at 50 μM concentration and pH 3.8 were subjected to SEC (Superdex 200 10/300 GL: molecular weight range of 10 – 600 kDa) 30 and 80 minutes, and 2 days after preparation. The resulting chromatograms show absorbance peaks (at a wavelength of 280 nm) at elution times of ~ 17, ~ 33 and ~ 39 minutes for samples at 20 and 80 minutes after sample preparation (**Figure 7A,B**). The first elution peak matches the void volume of the column, thus corresponding to oligomers with molecular weight > 600 kDa. According to the SEC calibration ASC3X dimer and monomer should elute at ~29 min and ~32 min, respectively, considering a globular protein. However, ASC3X has a very long linker and thus increased retention times are expected, as this effect has been reported for ASC (16). Because retention times of 33 and 39 minutes are significantly different than the expected values, we cannot derive conclusions on the oligomeric state of the protein in each peak.

ASC3X behavior differs from that of ASC and ASCb in SEC studies, as the former assembles into long-lived oligomers of different size, whereas only oligomers > 600 kDa and monomeric species were observed for the latter (16). The peak at 33 minutes in ASC3X chromatogram is absent in the chromatogram obtained 2 days after sample preparation, and only the peaks at 17 and 39 minutes of elution time remain (**Figure 7C**). This result indicates that the oligomer at 33 minutes finally disappears with time to form higher-order oligomers.

We also tested the influence of protein concentration in the oligomerization behavior of ASC3X. At higher protein concentration (150 μM) and 30 minutes after sample preparation, the monomer peak is absent from the chromatogram (**Figure 7D**) and the long-lived oligomer is observed. This result indicates that the lon-lived oligomer is favored at higher protein concentration. To test the reversibility of the oligomerization process, the peaks at 17 minutes (high-order oligomers) and 33 minutes (long-lived, low-order oligomer) minutes were collected and reinjected in the SEC column. The resulting chromatograms show peaks at the same elution times (**Figure 7E**). In the latter chromatograms, the signal to noise ratio has decreased due to protein dilution during the SEC process. This result suggests that once the low-order or high-order

oligomers are formed, the equilibrium is significantly shifted toward these species and thus the monomer cannot be detected by absorbance. The data in **Figure 7E** corroborate the high stability of the low-order oligomer inferred from its presence in the chromatograms shown in A, B and D and from the NMR data.

To investigate by SEC the effect of pH in the oligomerization of ASC3X, we acquired chromatograms at pH 4.8 and 5.3. Significant precipitation occurs when the pH increases from 3.8 to 4.8 and 5.3. However, the chromatogram at 4.8 resulting from the supernatant after centrifugation shows three peaks at elution times equivalent to those observed at 3.8 (**Figure 7F**). As expected, the three peaks show lower absorbance values because of protein mass lost upon precipitation. In contrast, at pH 5.3, only the peak corresponding to the low-order oligomer at 33 minutes remains (**Figure 7G**), suggesting that the monomer is no longer stable under this less acidic pH and that the high-order oligomers, possibly more populated and larger, fall out of solution. It is important to note that the presence of the peak at the void volume indicates that ASC3X oligomers are > 600 kDa, corresponding to a lower limit of ~ 21 protomers in ASC3X oligomers.

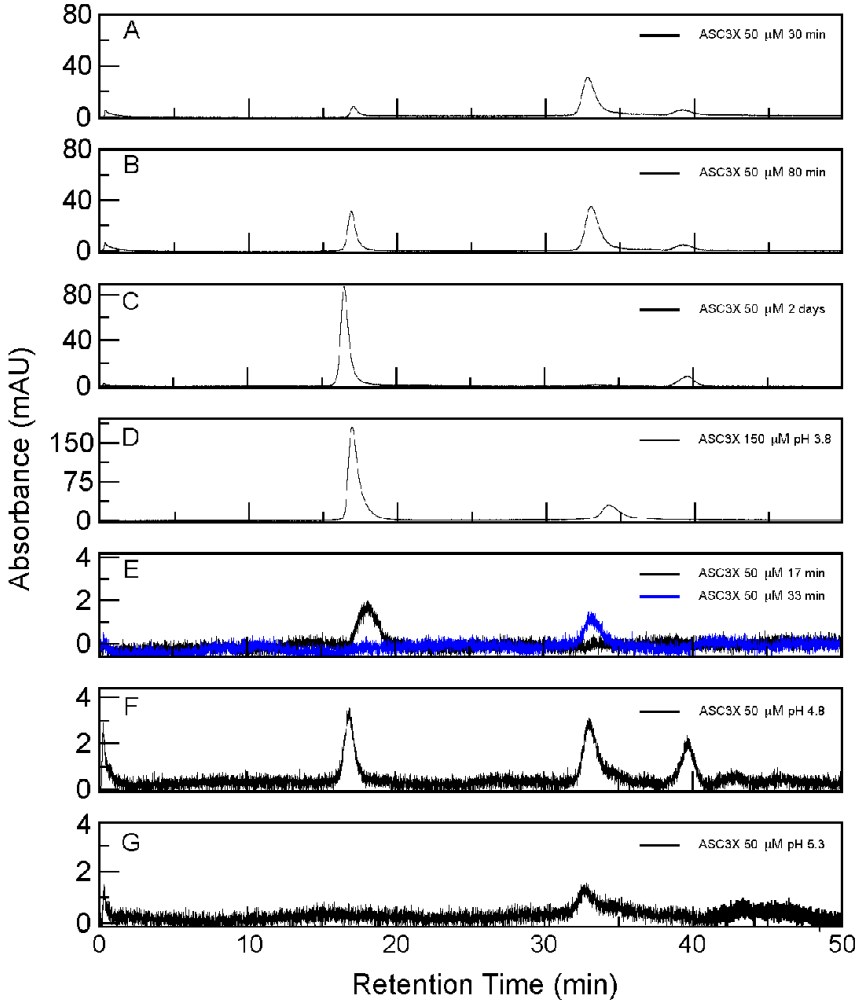

Figure 7. ASC3X oligomer size distribution by size-exclusion chromatography. *(A, B, C) ASC3X monomer, low-order and high-order oligomers retention times 30 and 80 minutes, and 2 days after sample preparation (50 μM, pH 3.8), respectively. (D) ASC3X oligomer formation at 150 μM, pH 3.8. (E) Chromatograms resulting from the injection of peaks collected at elution times of 33 and 17 minutes from (A). (F,G) ASC3X (50 μM) monomer and oligomer elution times at pH 4.8 and 5.3, respectively.*

ASC3X polymerizes forming filaments of similar width compared to ASC and ASCb

The analysis of ASC and ASCb macrostructures using negative-staining Transmission Electron Microscopy (ns-TEM) has been reported previously (15, 16). Both proteins readily form filaments with an average width of ~ 7 nm (15, 16) frequently stacked forming bundles. Bundles composed of 3- and 4-filaments are more abundant for ASC, whereas 2-filament bundles are prominent in ASCb. Bundle width is a multiple of the width of the individual filament and matches the number of filaments in the bundle, thus indicating that filaments align laterally. ASC filaments are formed by stacked rings with the size of an ASC dimer, suggesting a possible mechanism for filament growth. (15),

An analogous analysis by ns-TEM indicates that ASC3X has high propensity of forming 2-filament bundles (**Figure 8**). In contrast to ASC and ASCb, individual, isolated filaments were not observed for ASC3X and three-filament bundles were very infrequent. An average bundle width of 15.19 ± 0.53 nm was measured based on the analysis of 50 ASC3X filament bundles composed of two filaments. The width of individual filaments obtained from the 2-filament bundles is 6.94 ± 0.22 nm. These results indicate that despite the very long linker, ASC3X can form filaments of similar width to those formed by ASC and ASCb. Combining the RT-NMR and ns-TEM results, we can conclude that the long linker in ASC3X modifies the oligomerization kinetics but not the basic capability to polymerize forming filaments. The analysis of multiple macrostructures clearly shows a predominance of 2-filament bundles; exceptionally few three-filament bundles were observed (**Figure 8**). Therefore, additional lateral stacking of filaments forming multiple-filament bundles is hindered in ASC3X.

It is worth to note that the experimental conditions used for filament formation (TEM) and RT-NMR experiments are different. Neutral pH is needed in the former and acidic pH is required in the latter to shift oligomerization equilibria toward monomeric and lower-order oligomeric species that lead to appreciable NMR signal. The ns-TEM analysis shows that the less effective oligomerization of ASC3X is partially overcome at neutral pH. However, the lack of multiple-filament bundles in ASC3X compared to ASC suggests that additional oligomerization is hindered in the former. At this point we can only speculate whether ASC3X long linker is responsible for the preponderance of two-filament bundles (almost exclusively present) and the lack of individual filaments and bundles with multiple (>2) filaments.

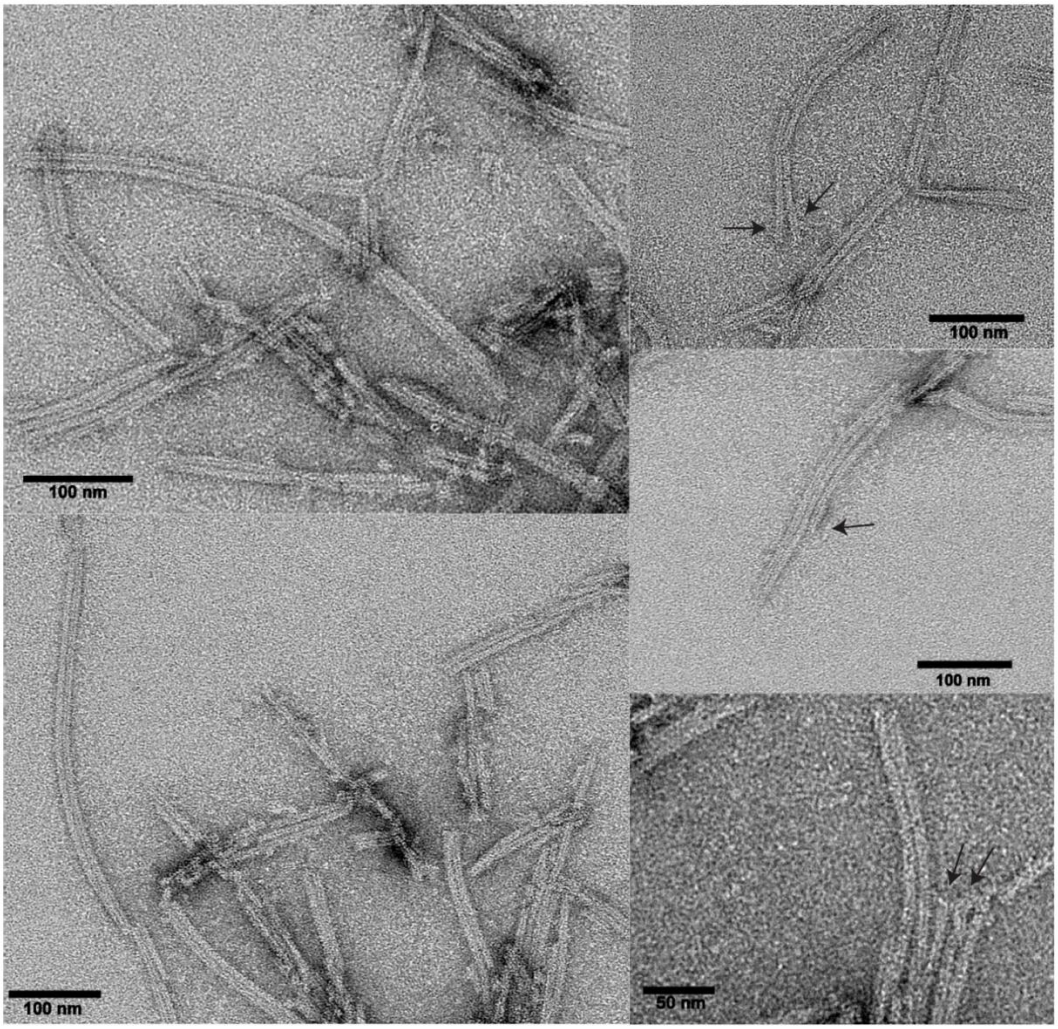

Figure 8. ASC self-assembles predominantly into two-filament bundles. *ns-TEM micrographs showing ASC3X bundles at different magnification. Arrows point to the separation of a two-filament bundle into individual, constituent filaments (up), and infrequent three-filament bundles (bottom).*

ASC3X self-association is more polydisperse compared to ASC and ASCb

Dynamic light scattering (DLS) was used to study the kinetics of ASC3X oligomerization. Figure 9 shows the intensity of the scattered light versus particle size at different time points. The intensity of the observed peaks depends on the population of the different particles present in solution and is proportional to the sixth power of the particle radius. A perfect sphere is assumed in the calculation of particle size. However, ASC3X oligomers are filamentous (**Figure 8**), thus the dimensions shown in **Figure 9** do not correspond to the real oligomer size. Nonetheless, the DLS data help identify populations of different assembly size and how they change as self-assembly proceeds.

According to the DLS data, ASC3X forms species categorized in three group sizes: ~ 10, 40 and 400 nm, 30 minutes after sample preparation, which is the time required to obtain the first DLS measurements (**Figure 9A**). As oligomerization progresses, small variations in the population and size of these species are observed, reaching steady state 49 hours after oligomerization started with peaks at ~ 10, 30 and 300 nm (**Figure 9B**). The ASC3X species detected by RT-NMR could correspond to the peak at ~ 10 nm, with high-order oligomers represented by the other two peaks. As oligomerization proceeds, the peaks at ~ 40 and 400 nm decrease in size, suggesting that the oligomers are more close-packed. At the end of the kinetic experiment, ASC3X still shows three species of different size, whereas ASC showed only one species and ASCb showed 2 (**Figure 9A**) (16). Importantly, the overall polydispersity value (p) of the ASC3X solution at the end of the polymerization experiment is fairly constant and close to 1 ($p_{ASC3X} = 0.934 \pm 0.0509$) (**Figure 9B**), contrasting with the lower polydispersity values of ASC and ASCb ($p_{ASC} = 0.35 \pm 0.04$ and $p_{ASCb} = 0.79 \pm 0.06$) (16).

Previously reported DLS data on ASC and ASCb polymerization agree with the former forming a speck of unform size and the latter polymerizing into clustered and disordered filaments inside the cell (14, 16). A behavior closer to that of ASC was expected for ASC3X. However, polymerization of the artificial isoform leads to the largest polydispersity observed. Altogether, results from cell assays, RT-NMR and DLS suggest that the length of ASC linker is optimal for faster polymerization leading to solutions of lower polydispersity. In addition, ASC shows higher tendency to form multiple-filament bundles based on ns-TEM data (15), which might be required for the formation of ASC filamentous ring-specks with an approximately 150 nm wide rim (36). We may attribute the slower polymerization kinetics, higher polydisperse oligomers and less densely packed macrostructures of ASCb and ASC3X to the very short and very long linkers of the former and latter, respectively.

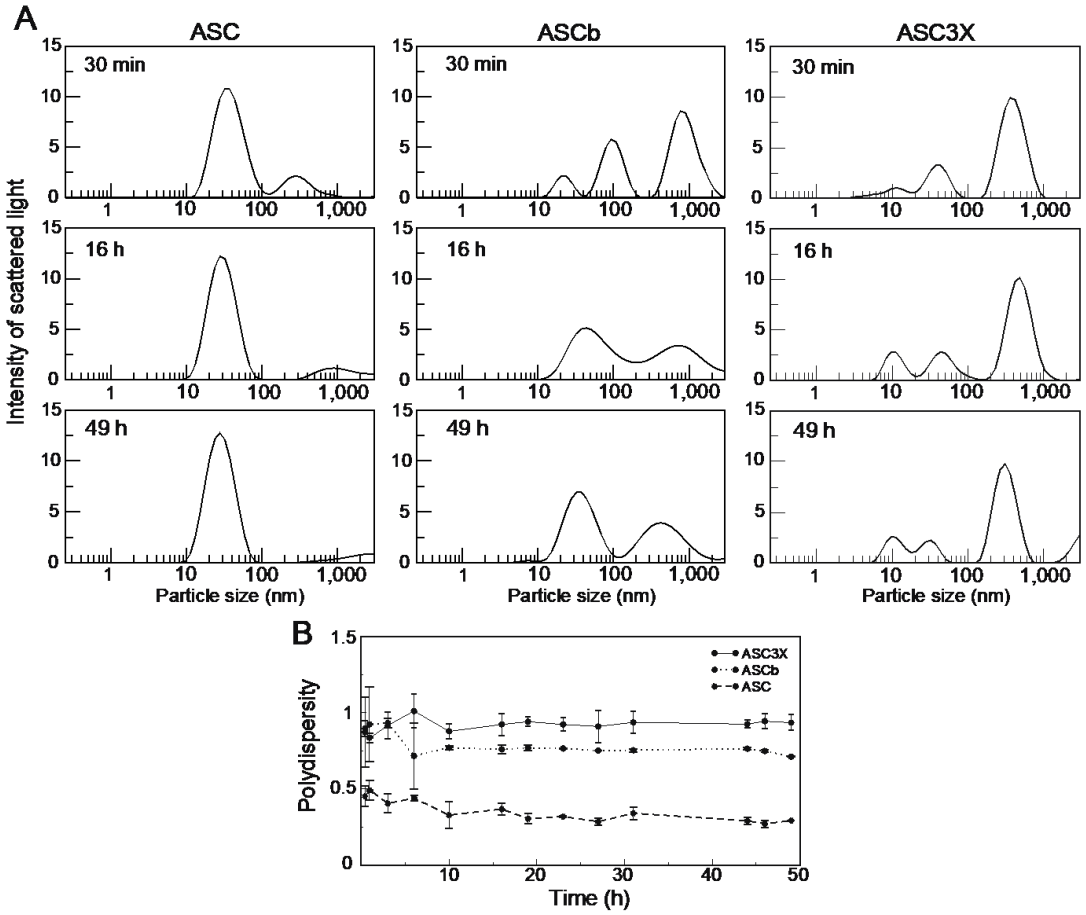

Figure 9. Time-dependent population distribution of ASC, ASCb and ASC3X oligomers by dynamic light scattering. *(A) Changes over time in intensity of scattered light vs. size of ASC, ASCb (16) and ASC3X oligomers. (B) Changes in polydispersity values of ASC, ASCb* (16) *and ASC3X solutions during the oligomerization process. Data in (A) and (B) are an average of 3 measurements and error bars in (B) represent SD. The 30 min time-point can be considered as 0 min time-point after sample preparation.*

Interdomain dynamics in ASC isoforms increases with linker length

We hypothesized previously that the linker in ASC plays an important role in interdomain dynamics (16, 35), which in turn could have an effect on the interacting capabilities of the PYD and CARD domains. Recently, we have shown using molecular docking that the proximity of the PYD and CARD in ASCb, due to the short linker, hinders its interactions with the CARD of procaspase-1 (16). This result was not observed for ASC where the two domains are sufficiently separated by the much longer linker (16). In addition, we showed based on previous NMR relaxation studies that the two domains in ASC have different rotational correlation times due to the flexibility of the linker (35). We have performed analogous studies to investigate

the influence of the linker length in the interdomain dynamics of the natural and designed isoforms, ASCb and ASC3X, respectively.

Information on NMR relaxation properties of the protein backbone amide (^{15}N) was obtained by measuring the heteronuclear Overhauser effect ([^{1}H]-^{15}N-NOE), as well as the longitudinal (T_1) and transverse (T_2) relaxation times for the three isoforms (**Figure 10**). These three parameters depend on the amide ^{15}N-H bond dynamics and the rotational diffusion of the molecule (37, 44). Information on backbone dynamics is readily inferred from heteronuclear NOE experiments as residues adopting regular secondary structure show NOE values in the 0.78 - 0.83 range, compared to values lower than ~ 0.65 for residues located in more flexible regions such as linkers and loops (45, 46). For better comparison, these studies have been performed for the three proteins, ASC, ASCb and ASC3X under the same experimental conditions, including same magnet, and using identical NMR pulse programs designed to avoid water interference that results in increased measurement errors (47). Previously reported NMR relaxation data for ASC were obtained with pulse programs that did not avoid water interference as this effect was not known at the time (35).

The average heteronuclear NOE values for the PYD and CARD regions in ASC3X, ASC and ASCb are the values expected for two rigid structures (**Table 2**, **Figure 10A**). In contrast, these values start to decrease in the regions close to the PYD C-terminus and the CARD N-terminus toward the linker center (**Figure 10A**). The very long linker in ASC3X shows severe NMR signal overlap and chemical shifts could only be assigned for a few amino acids; however, the trend toward low or negative heteronuclear NOE values in this region is clear. These results indicate that the linker undergoes local motions on a fast time scale compared to molecular tumbling. The heteronuclear NOE data indicate that ASC, ASCb and ASC3X comprise two well-ordered, rigid domains.

Clear differences are observed in the average T_1 values for ASCb compared to ASC and ASC3X (**Table 2, Figure 10B**). If interdomain motion is not considered and we assume globular shape for the isoforms, the T_1 values should decrease concomitantly with a decrease in the protein molecular weight (MW). Thus, the largest T_1 values would correspond to ASC3X (highest MW) and the lowest values to ASCb (lowest MW). We observe the opposite: average T_1 values are largest for ASCb and lowest for ASC3X. This result is a consequence of the non-globular shape and responds to the presence of interdomain dynamics. As interdomain mobility increases, the NMR relaxation parameters approximate to values expected for the individual domains. Thus, we suggest two extreme models for interdomain dynamics of the three isoforms: 1) each domain is dynamically independent; 2) both domains tumble as a single rigid body.

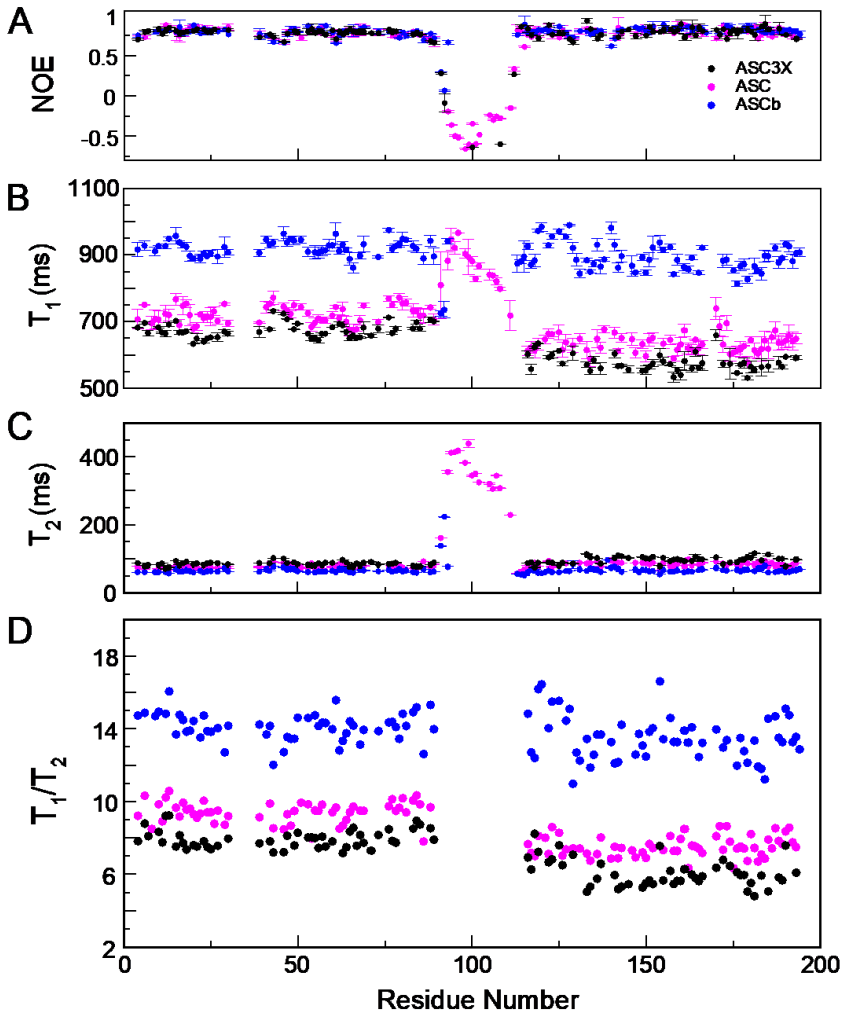

Figure 10. Interdomain dynamics in ASC3X, ASC and ASCb from ^{15}N amide NMR relaxation. *(A) Heteronuclear NOE. (B) longitudinal (T_1), (C) and transverse (T_2) relaxation times. (D) T_1/T_2 ratios of ASC (magenta), ASCb (blue), and ASC3X (black).*

We can expect significant interdomain flexibility in ASC3X due to the 69-amino acid long linker. Thus, T_1 values for both PYD and CARD are the smallest (**Table 2**), as the two domains could almost be considered independent from one another. T_1 values for PYD (MW = 9,951.5 Da) are ~ 100 ms larger than for the CARD (MW = 9,737.1 Da) because of the larger MW of the former compared to the latter. This result reflects the dynamic independence of one domain from the other. An analogous situation is found for ASC, with the 23-amino acid long linker also conferring interdomain flexibility. The T_1 values in ASC are slightly higher compared to ASC3X (**Table 2**) because the PYD and CARD feel the drag from each other more pronouncedly than in ASC3X. The shorter linker in ASC results in slightly less interdomain flexibility. The T_1 values for the PYD are also larger than for the CARD in ASC, but the difference between the average

values is ~ 80 ms. The decrease in T_1 values difference is again a consequence of the shorter linker in ASC compared to ASC3X. In contrast, NMR relaxation results for ASCb are very different. The linker connecting the PYD and CARD of ASCb is only 4 amino acids long, and therefore we expect a great reduction in interdomain flexibility. In fact, the average T_1 values for ASCb are the largest out of the three isoforms, even though ASCb molecular weight is the smallest. In this case, the average T_1 value for the PYD is larger than that of the CARD but the difference is only ~ 27 ms. This behavior can only be explained by largely diminished interdomain dynamics, which results in both domains tumbling almost as a rigid body.

The differences in T_2 values between the three isoforms is not as large as for T_1, but appreciable (**Figure 10C, Table 2**), and follow the expected trend matching the reduction of interdomain dynamics for the shorter linkers. Thus, we observe higher average T_2 values for ASC3X and lower for ASCb. However, based on the molecular weight we would expect the opposite result for globular proteins, which again shows the impact of interdomain dynamics on the NMR relaxation data. In addition, T_2 values are smaller for the PYD than for the CARD of ASC3X and ASC, again indicating significant interdomain flexibility with a trend toward the expected results for independent domains. Furthermore, the difference in T_2 values for the PYD and CARD is larger for ASC3X than for ASC due to the additional flexibility. In contrast, this difference is much smaller for the for PYD and CARD of ASCb, which indicates that the two domains tumble together. The different T_2 values of the PYD and CARD could also result from differences in the stability of the folded domains. However, the effect of the short ASCb linker cancelling this difference suggest that it is related to domain motion more than to domain stability.

To obtain more information on the degree of interdomain dynamics, an analysis of backbone amide ^{15}N T_1/T_2 ratios is particularly useful because these values are similar for domains tumbling together and different otherwise (45). The ^{15}N T_1/T_2 ratios of the PYD and CARD of ASC and ASC3X are noticeably different indicating that they reorient at different rates. In contrast, these values are more similar for the PYD and CARD of ASCb, suggesting that both domains tumble at similar rates (**Figure 10D, Table 2**). No significant differences are obtained in T_1/T_2 ratios for the PYD and CARD of ASC3X and ASC (~ 1.9 for both proteins), which suggests that the very long linker in ASC3X confers only marginally additional interdomain flexibility.

Table 2. Average ^{15}N relaxation parameters for ASC isoforms

^{15}N relaxation parameter	Protein isoform					
	ASC3X		ASC		ASCb	
	PYD	CARD	PYD	CARD	PYD	CARD
T_1 (ms)	674 ± 5	577 ± 12	722 ± 14	639 ± 19	925 ± 13	898 ± 13
T_2 (ms)	83.4 ± 0.3	94.2 ± 0.7	76.9 ± 0.6	83.6 ± 0.7	65.5 ± 0.3	66.7 ± 0.5
NOE	0.78 ± 0.02	0.78 ± 0.03	0.79 ± 0.03	0.79 ± 0.03	0.79 ± 0.02	0.81 ± 0.02
T_1/T_2	7.9 ± 0.5	6.0 ± 0.8	9.4 ± 0.6	7.5 ± 0.6	14.1 ± 0.8	13 ± 1

To further investigate differences in interdomain dynamics, we have obtained rotational correlation times (τ_c) for the full-length isoforms and the individual PYD and CARD domains by applying the Lipari-Szabo model free formalism to our NMR relaxation data (**Table 3**) (46, 48). As a reference for comparison, we show in **Table 3** the experimental and theoretical τ_c values obtained for PYD-only protein ASC2 (49) with similar size and structure to ASC individual domains, and for the N- and C-terminal domains of the protein calmodulin (45).

The NMR-derived τ_c values of both PYD and CARD in ASC3X and ASC (highlighted in bold in **Table 3**) are only slightly larger than the experimental τ_c value of ASC2, indicating that the two domains are independent at the dynamic level for both isoforms. These results suggest that the PYD and CARD dynamic behavior in ASC and ASC3X is closer to the extreme model in which each domain is dynamically independent. The slightly larger values for ASC and ASC3X compared to ASC2 indicate the dragging effect of the linker. This effect is more pronounced for ASC, resulting in larger differences with respect to ASC2, due to a shorter linker compared to ASC3X. In addition, we observe larger τ_c values for the PYD relative to the CARD, which matches the expected slower tumbling of the former due to the higher MW of the PYD. In contrast, τ_c values of the PYD and CARD in ASCb are significantly larger than the experimental values for ASC2. Moreover, the difference in τ_c values between the PYD and CARD in ASCb is very small and close to the experimental error. Both results indicate that ASCb dynamic behavior matches the model where both domains tumble as a rigid body. Interestingly, the experimental and theoretical τ_c values (based on molecular size) for the full-length proteins (highlighted in italics in **Table 3**) are very similar for ASCb (with a difference of ~ 1 ns), and disparate for ASC and ASC3X, reaching a difference of ~ 9 ns for the latter. These data point again to the independent dynamics of the PYD and CARD in ASC and ASC3X, and lack thereof in ASCb.

In summary, ASCb (4 amino acid linker) does not show significant interdomain flexibility, whereas ASC and ASC3X show substantial interdomain dynamics, slightly more accentuated in the latter despite the three-times longer linker. It has been reported that interdomain motion resulting from linker flexibility has important roles in protein function (4, 7). A well-known example is the multifunctional protein calmodulin with two domains connected by a relatively long linker (15 amino acids) that promiscuously binds to multiple partners (45, 50). NMR relaxation studies on calmodulin show that interdomain flexibility facilitates domain reorientations and simultaneous interactions of both domains with the different ligands (45, 51). Analogously to calmodulin, ASC and its isoform ASCb also interact with different inflammasome proteins (caspase-1 and sensor) and self-associate for inflammasome assembly. Each domain in ASC and ASCb bind to different molecules via homotypic interactions. Importantly, the NMR-derived τ_c values for the N- and C-terminus in calmodulin are significantly larger than the theoretical values, as previously reported (35) (**Table 3**), thus agreeing with the results obtained for ASC and ASC3X. Proteins within the Death Domain superfamily, such as FADD, have been reported to behave like ASCb at the dynamic level with domains tumbling together (52).

Table 3. Experimental and theoretics rotational correlation times (τ_c) for ASC3X, ASC and ASCb

Isoform	Experimental τ_c (ns)	Theoretical τ_c (ns)[a]
Full length ASC3X	*7.6 ± 0.1*	*16.8 (# residues = 241)*
$ASC3X^{PYD}$	**8.3 ± 0.2**	**6.7**
$ASC3X^{CARD}$	**7.1 ± 0.2**	**6.2**
Full length ASC	*8.6 ± 0.4*	*13.8 (# residues = 195)*
ASC^{PYD}	**9.2 ± 0.3**	**6.7**
ASC^{CARD}	**8.1 ± 0.3**	**6.2**
Full length ASCb	*11.4 ± 0.2*	*12.5 (# residues = 176)*
$ASCb^{PYD}$	**11.6 ± 0.2**	**6.7**
$ASCb^{CARD}$	**11.3 ± 0.2**	**6.2**

ASC2 [b]	*6.2*	*6.3 (# residue 84)*
Calmodulin (N-terminal) [b]	*7.1*	*4.1 (# residues 73)*
Calmodulin (C-terminal) [b]	*6.3*	*3.7 (# residues 66)*

a: obtained with a spherical model (53) using the number of residues specified and the corresponding temperature: ASC3X, ASC and ASCb (298 K), ASC2 (298 K), and calmodulin (308 K). b: reported experimental values for ASC2 (49) and calmodulin (45).

Discussion: ASC linker length is optimal for self-assembly

ASC and ASCb show differences in inflammasome activity as the former results in higher levels of released IL-1β than the latter (14). In addition, ASC forms the regular specks in the cytosol of activated macrophages, whereas ASCb forms filamentous polymers (14). These results suggest that ASC isoforms could impact the regulation of the inflammatory response by differential inflammasome activation. ASC and ASCb self-association are key in inflammasome assembly. Recently, we have studied the self-association capabilities of ASC and ASCb using several biophysical and biochemical techniques (16). Our studies show that ASC polymerizes faster and forms less polydisperse oligomers compared to ASCb, thus explaining at the molecular level ASC's more efficient inflammasome activation (16). We have suggested that ASC's long linker provides the flexibility needed for the multiple interactions required in filament formation. In contrast, the short linker in ASCb obstructs its participation in intermolecular interactions.

We hypothesize here whether a longer linker could confer additional flexibility thus enhancing isoform self-association. To test this hypothesis, we have engineered an artificial adaptor with a linker three times as long as ASC's linker (ASC3X). Our RT-NMR data indicate that ASC3X shows less effective polymerization resulting in lower intensity decrease of the overall NMR signal compared to ASC and ASCb. Importantly, pronounced differences in NMR data were observed between the PYD and CARD in ASC3X that were absent in ASCb and minimal in ASC. Specifically, NMR signals of the CARD domain decrease significantly, reaching values close to the baseline level, whereas PYD signals dimmish less than 25%.

The NMR results suggest that ASC3X assembles into CARD-driven oligomers bearing free (unbound) PYDs at the initial stages of self-association. To illustrate this behavior, we have used molecular docking to create models of ASC3X oligomeric structures via CARD-CARD interactions. The molecular docking is driven by the well-known type I interactions between Death Domains, which involve contacts between helices 1 and 4 of one CARD, and helices 2 and 3 the other interacting CARD (56–58). The smallest oligomer is a dimer to which additional ASC3X molecules are added by docking, resulting in a pentameric structure that closes the circle of interacting CARDs (**Figure 11A**). The molecular models shown that the free PYDs are far away from one another due to the very long linker, to form PYD-PYD interactions that are essential for filament formation (**Figure 11A**). In contrast, the shorter linker in ASC (**Figure 11B**) results in a dimer model formed by CARD-CARD interactions that positions the PYDs nearby for homotypic binding (**Figure 11C**).

Altogether, the RT-NMR data indicate that ASC3X polymerization is initially trapped into oligomers formed with little participation of the PYD. In contrast, both domains show similar participation in ASC and ASCb self-association leading to substantially more effective polymerization. The DLS data show that ASC3X forms oligomers with significantly higher polydispersity compared to ASC and ASCb (**Figure 9B**), indicating that the very long linker has perturbed the oligomerizing capabilities. In addition, SEC results show the presence of long-lived ASC3X low-order oligomer species that were not observed in analogous experiments for ASC or ASCb. In contrast, when the pH is close to neutral value, ASC3X assembles into

filaments of similar dimensions to those formed by ASC and ASCb. Most ASC3X macrostructures are two-filament bundles, which differs from ASC's tendency to form multiple-filament bundles.

Finally, NMR relaxation data indicate that the PYD and CARD domains in ASCb tumble at very similar rate, showing almost identical τ_c values, within the experimental error, for both domains. In contrast, ASC and ASC3X show PYD and CARD domains tumbling at different rates, hence different τ_c values were obtained. However, ASC3X shows marginally larger interdomain flexibility reported by the shorter T_1 and longer T_2 values compared to ASC. Overall, NMR relaxation data indicate that ASCb tumbles as a rod with no appreciable interdomain flexibility due to the short linker, whereas ASC and ASC3X domains are very flexible. Interdomain dynamics in both proteins are similar; however, ASC3X self-association is less effective, and oligomer polydispersity is larger. To explain this behavior, we need to consider the role that interdomain flexibility and linker length can play in filament formation.

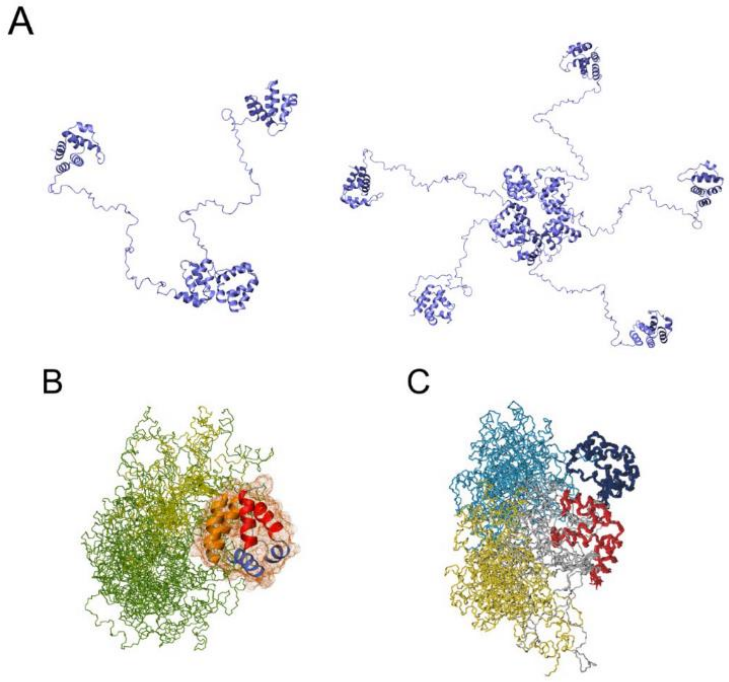

Figure 11. Molecular models for the self-association of ASC3X and ASC. *(A) Models derived from molecular docking for ASC3X dimer (left) and 5-member oligomer (right). (B). Experimental three-dimensional structure of ASC monomer showing interdomain flexibility (retrieved from ref* (35)*); (C) ASC dimer model formed by CARD-CARD binding, showing the proximity of the two free PYDs for additional interactions and dimer stabilization.*

We reported previously that both PYD and CARD are integral components of filament assembly based on ASC macrostructure characterization by ns-TEM and NMR analysis on protein-protein interactions (15). In addition, recent comparative studies on the kinetics of ASC and ASCb self-association corroborate PYD and CARD concomitant participation in oligomer formation (16). Certain interdomain flexibility will be required to favor the several types of interactions in which the PYD and CARD domains need to be involved. If we focus firstly on the formation of an ASC dimer, once one domain of a monomer (CARD) has interacted with its homologous in a nearby molecule, the second domain (PYD) will follow. As depicted

in **Figure 11C**, this process appears to be relatively simple for ASC, with a linker that allows both the required flexibility and sufficient proximity of the other interacting domain. Thus, the PYD and CARD of ASC readily interact to form oligomers with integral participation of both domains. In this case, intermediate oligomers are not observed experimentally, suggesting that they are short-lived likely leading to extensive polymerization into filament formation.

In contrast, dimer formation with simultaneous participation of both PYD and CARD domains is more difficult for ASC3X, as shown in **Figure 11A**. The PYDs of two ASC3X molecules bound through the CARD will need to find each other for dimerization and high-order oligomer formation due to the extra-long linker. Such behavior explains the large remaining NMR signal intensity and the presence of long-lived low-order oligomeric species based on the SEC results. Oligomers that do not readily polymerize would also lead to higher polydispersity, as observed by DLS. All in all, the comparison of the self-association behavior of the natural isoforms ASC and ASCb (16) to that of the engineered adaptor ASC3X shown here, together with the detailed study on the interdomain dynamics of the three isoforms, suggest that ASC has an optimal linker for self-association because it confers the needed flexibility while keeping both domains sufficiently close. The differential self-association observed for ASC, ASCb and ASC3X indicate that the length of the linker can control the function of multidomain proteins.

Experimental Procedures

Expression and purification of unlabeled and isotopically labelled ASC3X

The expression and purification of ASC and ASCb has been described previously (16, 34, 35). The expression and purification of ASC3X is analogous to the published protocols (16, 34, 35). Essentially, the purification of the three proteins is done under denaturing conditions via His-tag and Ni^{2+} affinity and the proteins are refolded upon denaturant removal.

Structure of ASC and model of ASC3X

A model of the three dimensional structure of ASC3X was created based on the structure of ASC (PDB 2KN6) (35) using the program Chimera (38). The 23 amino acid linker was tripled to make the 69-amino acid linker for ASC3X.

RT-NMR experiments

RT-NMR experiments performed on ASC3X as well as NMR data processing and analysis followed previously described procedures (16).

Chemical shift assignment of ASC3X by NMR Spectroscopy

ASC3X NMR samples were prepared at 200 μM in 300 μL containing 5% D_2O, 20 mM glycine and 1 mM TCEP at pH 3.8. Backbone chemical shift assignments of ASC3X were obtained from 2D [^{1}H-^{15}N]-HSQC, 3D HNCACB, and 3D CBCA(CO)NH (60, 61) that were acquired at 298 K on a Bruker Avance III 600 MH spectrometer equipped with a cryoprobe. Data were processed with NMRPipe and spectra were analyzed with Sparky (59, 62).

Backbone amide ^{15}N relaxation measurements by NMR

ASC, ASCb, and ASC3X samples were prepared in 20 mM glycine, 1 mM TCEP, pH 3.8 and 10 % D_2O/H_2O at a concentration of 200 μM. Relaxation experiments were performed at 298 K in a Bruker Avance spectrometer operating at a ^1H frequency of 600 MHz. The ^{15}N T_1, T_{1p} and $\{^1H\}$-^{15}N-NOE data were obtained with specific NMR pulse sequences (45, 63). The recycle delay to measure ^{15}N T_1 and $\{^1H\}$-^{15}N-NOE was 3 s, whereas T_{1p} experiments used 1.2 s. All experiments were acquired in an interleaved manner to minimize effects caused by spectrometer drift. Relaxation measurements of T_1 and T_{1p} were taken at eight different relaxation delays Δ = 23.987 ms, 103.843 ms, 263.555 ms, 503.123 ms, 762.655 ms, 1,002.223 ms, 1,301.683 ms, 1,601.143 ms for T_1 and Δ = 9.524 ms, 19.604 ms, 39.764 ms, 59.444 ms, 79.604 ms, 99.764 ms, 119.924 ms, 139.604 ms for T_{1p}. T_{1p} experiments used a ^{15}N continuous spin-lock field of 2.5 kHz. T_{1p} instead of T_2 relaxation times were acquired because resonance offset effects, significant in T_2 experiments, can be corrected in a straightforward manner for T_{1p} data using the following equation:

$$1/T_{1p} = \cos^2\theta/T_2 + \sin^2\theta/T_1 \qquad \text{eq. 3}$$

where $\theta = \tan^{-1}(\Omega_N/g_N B_1)$, Ω_N is the resonance offset and $\gamma_N B_1$ is the strength of the spin-lock field. T_2 values can be obtained from equation (3) as T_1, T_{1p} and θ are known. Relaxation times were calculated by fitting peak-intensity dependence with the experiment relaxation times to an exponential function given by $I(t) = I_0 e^{[(-1/T)t]}$ (T = T_1, T_{1p}). T_1 and T_{1p} values are averages of two separate measurements. The $\{^1H\}$-^{15}N-NOE values were calculated from the ratio of peak intensities obtained from experiments performed with and without ^1H presaturation. The ^1H frequency was shifted off-resonance in the unsaturated experiments. ^1H presaturation was achieved by a train of 120° pulses separated by 5 ms delays and was applied for a total of 3 s. The recycle time is reasonably long, however NOE values were corrected for incomplete ^1H magnetization recovery as previously described (63).

Relaxation data were analyzed using the Lipari-Szabo model-free approach (48), which assumes that the overall tumbling of the protein is decoupled from internal motions provided both differ by at least one order of magnitude. The correlation function for internal motion is given by:

$$C_i(t) = S^2 + (1 - S^2) + e^{(-\frac{t}{\tau e})} \qquad \text{eq. 4}$$

Where S^2 is a generalized order parameter describing the amplitude of motion of each N-H bond vector and τ_e is the effective correlation time. Under these assumptions, the spectra density function can be described as follows:

$$J(w) = \frac{S^2\tau_c}{1+(\omega\tau_c)^2} + \frac{(1-S^2)\tau}{1+(\omega\tau)^2} \qquad \text{eq. 5}$$

where $\frac{1}{\tau} = \frac{1}{\tau_c} + \frac{1}{\tau_e}$

Apparent rotational correlation times (τ_c) were obtained from T_1/T_2 ratios, which are independent of S^2 and τ_e values for amino acids with heteronuclear NOE values > 0.6 and without significant effects on T_2 from chemical exchange (46, 64).

Size-Exclusion Chromatography

ASC3X sample preparation for size exclusion chromatographic analysis was done following previously described procedures (16).

Dynamic Light Scattering

Dynamic light scattering (DLS) experiments and ASC3X sample preparation followed previously described procedures (16).

Transmission Electron Microscopy

ASC3X protein filaments were prepared as previously described (16). Images of ASC3X filaments were obtained using a Talos F200C G2 Transmission Electron Microscope equipped with a Field Emission Gun (X-FEG) at 200 kV. Analysis of ASC3X filaments was performed with ImageJ.

Mass Spectrometry

Mass spectrometry experiments on ASC3X were performed as previously indicated (16) with slight modifications. Briefly, NMR samples of ^{15}N-labeled ASC3X at ~ 700 μM were injected in an electrospray ionization mass spectrometer (Q-Exactive Hybrid Quadrupole-Orbitrap, Thermo). Protein samples were treated as follows: 1) dilution with a solution containing 95% acetonitrile, 4.9% water, 0.1% formic acid and injection to reverse phase column (Acclaim 200 C18, 3μm, Thermo operating at a flowrate of 0.3 mL/min) and subsequent mass spectrometer analysis; 2) dilution with 50% acetonitrile and direct injection to mass spectrometer. The spectra were analyzed as previously described (16).

Molecular Docking

The program HADDOCK (55) was used for molecular docking calculations. The ASC3X dimer model was built based on the modelled structure with Chimera (40) selecting as active residues those involved in Death Domain type I interactions (helices H1 and H4 in the CARD of one protomer, and helices H2 and H3 in the CARD of the other protomer) (57). Subsequent addition of ASC3X molecules was performed in a similar manner until the formation of the ASC3X 5-member oligomer. In all HADDOCK runs the N- and C-termini were considered charged and the 69-amino acid linker was set to be fully flexible. Each HADDOCK run started with 1,000 structures; out of which 200 were considered for refinement. The solvent used for each iteration was water. Structures were chosen based on best the HADDOCK score. ChimeraX was used to analyze ASC3X dimer and pentamer structures (65).

Supporting information

This article contains supporting information.

Data availability

The data that support the findings of this study are contained within the article and the supporting information. All source data generated for this study are available from the corresponding author (Dr. Eva de Alba; edealbabastarrechea@ucmerced.edu) upon reasonable request.

Funding

This research was funded by the National Institute of Allergy and Infectious Diseases of the National Institutes of Health under award number R15AI146780 to EdA, and by the NSF-CREST: Center for Cellular and Biomolecular Machines at the University of California, Merced (NSF-HRD-1547848 and NSF-HRD-2112675). The content of this publication is solely the responsibility of the authors and does not necessarily represent the official views of the National Institutes of Health or the National Science Foundation.

Acknowledgements

We are grateful to Dr Mourad Sadqi (NSF CREST Center for Cellular and Biomolecular Machines at the University of California, Merced) for mass spectrometry data. We would like to thank UC Merced Imaging Facility. We are grateful to Professor Son C. Nguyen for letting us use the dynamic light scattering equipment in his laboratory.

Conflict of Interest

The authors declare no conflict of interest.

List of Acronyms and Abbreviations:

NMR – Nuclear magnetic resonance
TEM – Transmission electron microscopy
SEC – Size-exclusion chromatography
DLS – Dynamic light scattering
ALR – Absent in melanoma 2-like receptor
NLR – Nucleotide-binding domain leucine-rich repeat containing receptor
ASC – Apoptosis-associated speck-like protein containing a CARD
CARD – Caspase activation and recruitment domain
PYD – Pyrin domain
IL-1β – Interleukin-1 beta
IL-18 – Interleukin-18
DED – Death Effector Domain

References

1. Bashton, M., and Chothia, C. (2007) The Generation of New Protein Functions by the Combination of Domains. *Structure.* **15**, 85–99
2. Vogel, C., Bashton, M., Kerrison, N. D., Chothia, C., and Teichmann, S. A. (2004) Structure, function and evolution of multidomain proteins. *Curr. Opin. Struct. Biol.* **14**, 208–216
3. Ma, B., Tsai, C.-J., Haliloğlu, T., and Nussinov, R. (2011) Dynamic allostery: linkers are not merely flexible. *Struct. Lond. Engl. 1993.* **19**, 907–917
4. Papaleo, E., Saladino, G., Lambrughi, M., Lindorff-Larsen, K., Gervasio, F. L., and Nussinov, R. (2016) The Role of Protein Loops and Linkers in Conformational Dynamics and Allostery. *Chem. Rev.* **116**, 6391–6423
5. Vishwanath, S., Brevern, A. G. de, and Srinivasan, N. (2018) Same but not alike: Structure, flexibility and energetics of domains in multi-domain proteins are influenced by the presence of other domains. *PLOS Comput. Biol.* **14**, e1006008
6. Wriggers, W., Chakravarty, S., and Jennings, P. A. (2005) Control of protein functional dynamics by peptide linkers. *Biopolymers.* **80**, 736–746
7. Bhaskara, R. M., de Brevern, A. G., and Srinivasan, N. (2013) Understanding the role of domain–domain linkers in the spatial orientation of domains in multi-domain proteins. *J. Biomol. Struct. Dyn.* **31**, 1467–1480
8. Yu, C.-H., Moecking, J., Geyer, M., and Masters, S. L. (2018) Mechanisms of NLRP1-Mediated Autoinflammatory Disease in Humans and Mice. *J. Mol. Biol.* **430**, 142–152
9. Luo, D., Wei, N., Doan, D. N., Paradkar, P. N., Chong, Y., Davidson, A. D., Kotaka, M., Lescar, J., and Vasudevan, S. G. (2010) Flexibility between the Protease and Helicase Domains of the Dengue Virus NS3 Protein Conferred by the Linker Region and Its Functional Implications. *J. Biol. Chem.* **285**, 18817–18827
10. Kostrhon, S., Kontaxis, G., Kaufmann, T., Schirghuber, E., Kubicek, S., Konrat, R., and Slade, D. (2017) A histone-mimicking interdomain linker in a multidomain protein modulates multivalent histone binding. *J. Biol. Chem.* **292**, 17643–17657
11. Park, H. H., Lo, Y.-C., Lin, S.-C., Wang, L., Yang, J. K., and Wu, H. (2007) The Death Domain Superfamily in Intracellular Signaling of Apoptosis and Inflammation. *Annu. Rev. Immunol.* **25**, 561–586
12. Masumoto, J., Taniguchi, S., Ayukawa, K., Sarvotham, H., Kishino, T., Niikawa, N., Hidaka, E., Katsuyama, T., Higuchi, T., and Sagara, J. (1999) ASC, a Novel 22-kDa Protein, Aggregates during Apoptosis of Human Promyelocytic Leukemia HL-60 Cells. *J. Biol. Chem.* **274**, 33835–33838
13. Matsushita, K., Takeoka, M., Sagara, J., Itano, N., Kurose, Y., Nakamura, A., and Taniguchi, S. (2009) A Splice Variant of ASC Regulates IL-1 β Release and Aggregates Differently from Intact ASC. *Mediators Inflamm.* **2009**, 1–6
14. Bryan, N. B., Dorfleutner, A., Kramer, S. J., Yun, C., Rojanasakul, Y., and Stehlik, C. (2010) Differential splicing of the apoptosis-associated speck like protein containing a caspase recruitment domain (ASC) regulates inflammasomes. *J. Inflamm.* **7**, 23
15. Nambayan, R. J. T., Sandin, S. I., Quint, D. A., Satyadi, D. M., and de Alba, E. (2019) The inflammasome adapter ASC assembles into filaments with integral participation of its two Death Domains, PYD and CARD. *J. Biol. Chem.* **294**, 439–452
16. Diaz-Parga, P., and de Alba, E. de (2022) Inflammasome regulation by adaptor isoforms, ASC and ASCb, via differential self-assembly. *J. Biol. Chem.* 10.1016/j.jbc.2022.101566
17. Martinon, F., Burns, K., and Tschopp, J. (2002) The Inflammasome: A Molecular Platform Triggering Activation of Inflammatory Caspases and Processing of proIL-β. *Mol. Cell.* **10**, 417–426

18. Sharma, D., and Kanneganti, T.-D. (2016) The cell biology of inflammasomes: Mechanisms of inflammasome activation and regulation. *J. Cell Biol.* **213**, 617–629
19. Jin, T., and Xiao, T. S. (2015) Activation and assembly of the inflammasomes through conserved protein domain families. *Apoptosis Int. J. Program. Cell Death.* **20**, 151–156
20. Sharma, D., and Kanneganti, T.-D. (2016) The cell biology of inflammasomes: Mechanisms of inflammasome activation and regulation. *J. Cell Biol.* **213**, 617–629
21. Sharma, M., and de Alba, E. (2021) Structure, Activation and Regulation of NLRP3 and AIM2 Inflammasomes. *Int. J. Mol. Sci.* 10.3390/ijms22020872
22. Schroder, K., and Tschopp, J. (2010) The Inflammasomes. *Cell.* **140**, 821–832
23. Seok, J. K., Kang, H. C., Cho, Y.-Y., Lee, H. S., and Lee, J. Y. (2021) Therapeutic regulation of the NLRP3 inflammasome in chronic inflammatory diseases. *Arch. Pharm. Res.* **44**, 16–35
24. Bauernfeind, F. G., Horvath, G., Stutz, A., Alnemri, E. S., MacDonald, K., Speert, D., Fernandes-Alnemri, T., Wu, J., Monks, B. G., Fitzgerald, K. A., Hornung, V., and Latz, E. (2009) Cutting Edge: NF-κB Activating Pattern Recognition and Cytokine Receptors License NLRP3 Inflammasome Activation by Regulating NLRP3 Expression. *J. Immunol.* **183**, 787–791
25. Kelley, N., Jeltema, D., Duan, Y., and He, Y. (2019) The NLRP3 Inflammasome: An Overview of Mechanisms of Activation and Regulation. *Int. J. Mol. Sci.* 10.3390/ijms20133328
26. Elliott, E. I., and Sutterwala, F. S. (2015) Initiation and perpetuation of NLRP3 inflammasome activation and assembly. *Immunol. Rev.* **265**, 35–52
27. Zhao, C., and Zhao, W. (2020) NLRP3 Inflammasome—A Key Player in Antiviral Responses. *Front. Immunol.* [online] https://www.frontiersin.org/article/10.3389/fimmu.2020.00211 (Accessed February 9, 2022)
28. Mariathasan, S., Weiss, D. S., Newton, K., McBride, J., O'Rourke, K., Roose-Girma, M., Lee, W. P., Weinrauch, Y., Monack, D. M., and Dixit, V. M. (2006) Cryopyrin activates the inflammasome in response to toxins and ATP. *Nature.* **440**, 228–232
29. Shi, J., Zhao, Y., Wang, K., Shi, X., Wang, Y., Huang, H., Zhuang, Y., Cai, T., Wang, F., and Shao, F. (2015) Cleavage of GSDMD by inflammatory caspases determines pyroptotic cell death. *Nature.* **526**, 660–665
30. Kayagaki, N., Stowe, I. B., Lee, B. L., O'Rourke, K., Anderson, K., Warming, S., Cuellar, T., Haley, B., Roose-Girma, M., Phung, Q. T., Liu, P. S., Lill, J. R., Li, H., Wu, J., Kummerfeld, S., Zhang, J., Lee, W. P., Snipas, S. J., Salvesen, G. S., Morris, L. X., Fitzgerald, L., Zhang, Y., Bertram, E. M., Goodnow, C. C., and Dixit, V. M. (2015) Caspase-11 cleaves gasdermin D for non-canonical inflammasome signalling. *Nature.* **526**, 666–671
31. Shi, J., Gao, W., and Shao, F. (2017) Pyroptosis: Gasdermin-Mediated Programmed Necrotic Cell Death. *Trends Biochem. Sci.* **42**, 245–254
32. Hayward, J. A., Mathur, A., Ngo, C., and Man, S. M. (2018) Cytosolic Recognition of Microbes and Pathogens: Inflammasomes in Action. *Microbiol. Mol. Biol. Rev.* **82**, e00015-18, /mmbr/82/4/e00015-18.atom
33. He, W., Wan, H., Hu, L., Chen, P., Wang, X., Huang, Z., Yang, Z.-H., Zhong, C.-Q., and Han, J. (2015) Gasdermin D is an executor of pyroptosis and required for interleukin-1β secretion. *Cell Res.* **25**, 1285–1298
34. Diaz-Parga, P., and de Alba, E. (2019) Protein interactions of the inflammasome adapter ASC by solution NMR. *Methods Enzymol.* **625**, 223–252
35. de Alba, E. (2009) Structure and Interdomain Dynamics of Apoptosis-associated Speck-like Protein Containing a CARD (ASC). *J. Biol. Chem.* **284**, 32932–32941
36. Man, S. M., Hopkins, L. J., Nugent, E., Cox, S., Gluck, I. M., Tourlomousis, P., Wright, J. A., Cicuta, P., Monie, T. P., and Bryant, C. E. (2014) Inflammasome activation causes dual recruitment of NLRC4 and NLRP3 to the same macromolecular complex. *Proc. Natl. Acad. Sci.* **111**, 7403–7408

37. Kleckner, I. R., and Foster, M. P. (2011) An introduction to NMR-based approaches for measuring protein dynamics. *Biochim. Biophys. Acta BBA - Proteins Proteomics.* **1814**, 942–968
38. Pettersen, E. F., Goddard, T. D., Huang, C. C., Couch, G. S., Greenblatt, D. M., Meng, E. C., and Ferrin, T. E. (2004) UCSF Chimera--a visualization system for exploratory research and analysis. *J. Comput. Chem.* **25**, 1605–1612
39. de Alba, E. (2007) 1H, 15N and 13C backbone and side chain chemical shifts of human ASC (apoptosis-associated speck-like protein containing a CARD domain). *Biomol. NMR Assign.* **1**, 135–137
40. Wishart, D. S., Bigam, C. G., Holm, A., Hodges, R. S., and Sykes, B. D. (1995) 1H, 13C and 15N random coil NMR chemical shifts of the common amino acids. I. Investigations of nearest-neighbor effects. *J. Biomol. NMR.* **5**, 67–81
41. Oroz, J., Barrera-Vilarmau, S., Alfonso, C., Rivas, G., and de Alba, E. (2016) ASC Pyrin Domain Self-associates and Binds NLRP3 Protein Using Equivalent Binding Interfaces. *J. Biol. Chem.* **291**, 19487–19501
42. Fawzi, N. L., Ying, J., Torchia, D. A., and Clore, G. M. (2010) Kinetics of Amyloid β Monomer-to-Oligomer Exchange by NMR Relaxation. *J. Am. Chem. Soc.* **132**, 9948–9951
43. Sengupta, I., Bhate, S. H., Das, R., and Udgaonkar, J. B. (2017) Salt-Mediated Oligomerization of the Mouse Prion Protein Monitored by Real-Time NMR. *J. Mol. Biol.* **429**, 1852–1872
44. Morin, S. (2011) A practical guide to protein dynamics from 15N spin relaxation in solution. *Prog. Nucl. Magn. Reson. Spectrosc.* **59**, 245–262
45. Barbato, G., Ikura, M., Kay, L. E., Pastor, R. W., and Bax, A. (1992) Backbone dynamics of calmodulin studied by nitrogen-15 relaxation using inverse detected two-dimensional NMR spectroscopy: the central helix is flexible. *Biochemistry.* **31**, 5269–5278
46. Kay, L. E., Torchia, D. A., and Bax, A. (1989) Backbone dynamics of proteins as studied by nitrogen-15 inverse detected heteronuclear NMR spectroscopy: application to staphylococcal nuclease. *Biochemistry.* **28**, 8972–8979
47. Chen, K., and Tjandra, N. (2011) Water proton spin saturation affects measured protein backbone 15 N spin relaxation rates. *J. Magn. Reson.* **213**, 151–157
48. Lipari, G., and Szabo, A. (1982) Model-free approach to the interpretation of nuclear magnetic resonance relaxation in macromolecules. 1. Theory and range of validity. *J. Am. Chem. Soc.* **104**, 4546–4559
49. Natarajan, A., Ghose, R., and Hill, J. M. (2006) Structure and Dynamics of ASC2, a Pyrin Domain-only Protein That Regulates Inflammatory Signaling. *J. Biol. Chem.* **281**, 31863–31875
50. Anthis, N. J., and Clore, G. M. (2013) The Length of the Calmodulin Linker Determines the Extent of Transient Interdomain Association and Target Affinity. *J. Am. Chem. Soc.* **135**, 9648–9651
51. Tjandra, N., Kuboniwa, H., Ren, H., and Bax, A. (1995) Rotational Dynamics of Calcium-Free Calmodulin Studied by 15N-NMR Relaxation Measurements. *Eur. J. Biochem.* **230**, 1014–1024
52. Carrington, P. E., Sandu, C., Wei, Y., Hill, J. M., Morisawa, G., Huang, T., Gavathiotis, E., Wei, Y., and Werner, M. H. (2006) The Structure of FADD and Its Mode of Interaction with Procaspase-8. *Mol. Cell.* **22**, 599–610
53. Daragan, V. A., and Mayo, K. H. (1997) Motional model analyses of protein and peptide dynamics using 13C and 15N NMR relaxation. *Prog. Nucl. Magn. Reson. Spectrosc.* **31**, 63–105
54. Lu, A., Li, Y., Schmidt, F. I., Yin, Q., Chen, S., Fu, T.-M., Tong, A. B., Ploegh, H. L., Mao, Y., and Wu, H. (2016) Molecular basis of caspase-1 polymerization and its inhibition by a new capping mechanism. *Nat. Struct. Mol. Biol.* **23**, 416–425
55. van Zundert, G. C. P., Rodrigues, J. P. G. L. M., Trellet, M., Schmitz, C., Kastritis, P. L., Karaca, E., Melquiond, A. S. J., van Dijk, M., de Vries, S. J., and Bonvin, A. M. J. J. (2016) The HADDOCK2.2

Web Server: User-Friendly Integrative Modeling of Biomolecular Complexes. *J. Mol. Biol.* **428**, 720–725
56. Ferrao, R., and Wu, H. (2012) Helical assembly in the death domain (DD) superfamily. *Curr. Opin. Struct. Biol.* **22**, 241–247
57. Qin, H., Srinivasula, S. M., Wu, G., Fernandes-Alnemri, T., Alnemri, E. S., and Shi, Y. (1999) Structural basis of procaspase-9 recruitment by the apoptotic protease-activating factor 1. *Nature.* **399**, 549–557
58. Weber, C. H., and Vincenz, C. (2001) A docking model of key components of the DISC complex: death domain superfamily interactions redefined. *FEBS Lett.* **492**, 171–176
59. Goddard, T., and Kneller, D. *Sparky 3*, University of California, San Francisco
60. Cavanagh, J., Fairbrother, W. J., III, A. G. P., and Skelton, N. J. (1995) *Protein NMR Spectroscopy: Principles and Practice*, Elsevier
61. Bax, A., and Grzesiek, S. (1993) Methodological advances in protein NMR. *Acc. Chem. Res.* **26**, 131–138
62. Delaglio, F., Grzesiek, S., Vuister, G. W., Zhu, G., Pfeifer, J., and Bax, A. (1995) NMRPipe: a multidimensional spectral processing system based on UNIX pipes. *J. Biomol. NMR.* **6**, 277–293
63. Grzesiek, S., and Bax, A. (1993) The importance of not saturating water in protein NMR. Application to sensitivity enhancement and NOE measurements. *J. Am. Chem. Soc.* **115**, 12593–12594
64. Clore, G. M., Driscoll, P. C., Wingfield, P. T., and Gronenborn, A. M. (1990) Analysis of the backbone dynamics of interleukin-1 beta using two-dimensional inverse detected heteronuclear 15N-1H NMR spectroscopy. *Biochemistry.* **29**, 7387–7401
65. Pettersen, E. F., Goddard, T. D., Huang, C. C., Meng, E. C., Couch, G. S., Croll, T. I., Morris, J. H., and Ferrin, T. E. (2021) UCSF ChimeraX: Structure visualization for researchers, educators, and developers. *Protein Sci. Publ. Protein Soc.* **30**, 70–82

Supporting Information:

Natural and engineered inflammasome adaptor proteins reveal optimum linker length for self-assembly

Pedro Diaz-Parga[1,2], Andrea Gould[1,3] and Eva de Alba[1]

[1] Department of Bioengineering, School of Engineering, University of California Merced, CA, USA.
[2] Quantitative Systems Biology Ph.D. Program, University of California Merced, CA, USA.

[3] Current address: Revolution Medicines. 700 Saginaw Dr. Redwood City, CA, USA.

Corresponding author: Eva de Alba. Department of Bioengineering, School of Engineering, University of California Merced. CA, USA.

Table S1: ^{15}N, $^{1}H_N$, $^{13}C_\alpha$, and $^{13}C_\beta$ Chemical Shifts of ASC3X

Residue	^{15}N (ppm)	^{15}NH (ppm)	$^{13}C_\alpha$ (ppm)	$^{13}C_\beta$ (ppm)
M1	120.962	8.347	55.611	33.032
G2	110.982	8.609	45.532	-
R3	120.226	8.290	57.309	30.771
A4	123.951	8.632	55.461	18.398
R5	117.246	8.531	60.138	29.713
D6	117.294	7.713	56.837	39.644
A7	122.635	7.695	54.987	18.751
I8	120.631	8.125	66.243	38.811
L9	119.737	7.945	57.758	41.657
D10	115.688	7.991	56.275	39.248
A11	120.081	7.387	54.795	18.131
L12	114.735	8.266	57.695	41.28
E13	116.465	8.802	57.279	28.1
N14	116.130	7.312	53.501	39.864
L15	119.411	6.912	54.453	41.265
T16	113.064	8.223	60.96	70.61
A17	123.426	8.929	55.836	17.858
E18	117.576	8.587	59.13	29.032
E19	119.474	7.680	58.441	29.931
L20	121.935	9.055	57.908	40.63
K21	118.623	7.528	60.168	32.231
K22	118.617	7.602	59.792	32.638
F23	122.143	8.796	61.461	39.533
K24	117.308	8.081	60.555	33.355
L25	115.859	7.715	57.813	41.314
K26	120.631	8.125	57.915	31.981
L27	120.799	7.913	57.279	41.233
L28	116.130	7.312	56.09	41.748
S29	111.009	7.455	57.997	65.397
V30	124.079	7.846	-	-
L32	122.652	8.235	52.693	46.18
R33	121.688	7.602	56.458	31.631
E34	122.240	8.479	57.778	28.662
G35	111.494	8.700	44.774	-
Y36	118.080	7.428	58.124	40.744
G37	108.980	8.970	43.581	-
R38	118.392	8.482	53.835	31.468
I39	128.499	8.217	-	-
R41	124.498	8.370	60.083	30.665
G42	104.805	8.777	46.747	-

A43	121.883	7.189	53.547	18.492
L44	117.047	7.808	57.204	43.14
L45	116.164	7.798	58.829	41.251
S46	112.031	7.674	58.762	63.905
M47	120.099	7.204	57.874	34.655
D48	121.942	8.706	51.104	38.929
A49	118.611	8.574	56.02	18.329
L50	121.570	7.881	58.536	41.41
D51	118.608	8.205	56.986	39.432
L52	120.694	8.705	57.522	41.905
T53	117.975	7.979	68.027	68.027
D54	118.176	7.714	56.947	39.103
K55	122.730	8.332	57.456	31.517
L56	120.629	8.957	58.846	42.642
V57	115.229	7.963	65.801	31.322
S58	116.728	8.192	61.666	63.643
F59	119.967	8.456	60.708	39.028
Y60	115.753	8.033	57.86	39.048
L61	111.977	7.389	57.173	40.63
E62	116.097	8.533	61.117	29.816
T63	112.202	7.933	65.723	67.716
Y64	122.682	8.673	58.416	35.965
G65	106.772	7.959	47.808	-
A66	124.224	7.715	55.507	18.373
E67	121.039	7.701	59.214	29.415
L68	120.893	8.908	57.685	42.033
T69	114.434	7.488	67.831	67.831
A70	122.167	8.064	55.89	17.936
N71	117.519	8.320	55.952	37.745
V72	121.974	8.407	67.177	30.961
L73	118.545	8.341	58.284	41.224
R74	119.130	8.419	60.776	29.419
D75	121.787	8.100	56.336	39.679
M76	116.607	7.852	56.663	35.047
G77	107.353	7.936	45.321	-
L78	124.636	8.042	52.819	38.855
Q79	118.782	7.807	59.729	28.071
E80	121.151	8.737	59.324	27.695
M81	119.810	8.048	58.93	33.496
A82	121.434	8.047	55.387	19.3
G83	104.981	8.258	46.942	-
Q84	122.257	7.917	58.465	28.245
L85	122.425	7.656	58.367	41.693
Q86	119.172	8.282	59.057	28.714
A87	121.504	8.015	54.675	18.108

A88	119.258	7.816	53.869	19.152
T89	105.292	7.460	61.804	69.592
H90	119.206	7.683	55.843	28.317
Q91	120.939	8.236	55.976	29.734
G92	110.387	8.439	45.138	-
L112	121.248	8.116	54.218	43.486
H113	125.772	9.483	58.698	31.626
F114	129.973	8.281	60.526	38.064
I115	115.825	11.286	64.527	38.076
D162	117.746	7.211	56.303	41.814
Q163	119.783	8.221	57.906	29.124
H164	110.626	7.146	53.119	28.091
R165	121.561	6.533	60.391	30.962
A166	118.502	8.178	55.522	17.803
A167	121.133	7.859	54.473	19.859
L168	116.766	8.093	57.571	41.678
I169	118.239	8.085	65.81	38.356
A170	115.195	7.127	53.87	20.213
R171	112.040	7.847	56.775	34.159
V172	121.068	7.755	64.634	31.862
T173	116.174	8.333	60.309	70.392
N174	119.632	8.079	52.541	37.036
V175	118.967	7.965	65.673	31.653
E176	119.203	8.558	60.168	28.151
W177	118.179	7.611	61.008	29.591
L178	116.130	7.312	57.81	41.393
L179	115.692	8.166	57.597	40.981
D180	117.643	8.205	56.607	38.443
A181	121.688	7.602	54.046	18.074
L182	114.330	7.413	54.739	43.272
Y183	126.314	7.980	60.728	37.713
G184	120.008	8.409	46.151	-
K185	120.123	7.473	57.767	33.76
V186	112.576	7.478	63.139	34.457
L187	117.267	7.212	53.51	44.617
T188	113.142	8.032	60.22	70.596
D189	120.334	8.929	58.479	40.611
E190	117.274	8.562	59.644	28.431
Q191	119.760	7.359	58.245	29.166
Y192	119.203	8.558	61.883	39.392
Q193	115.820	8.554	58.291	27.873
A194	121.208	7.872	54.802	18.564
V195	116.466	7.947	66.643	31.256
R196	117.694	7.842	59.341	29.956
A197	116.396	7.151	52.802	19.112

E198	119.360	7.487	-	-
T200	106.501	7.091	58.404	73.142
N201	120.764	9.526	-	-
S203	111.619	7.338	62.538	62.538
K204	125.309	8.680	60.723	35.03
M205	116.349	8.498	55.492	30.921
R206	120.558	8.791	60.426	30.35
K207	120.108	7.639	57.015	30.977
L208	122.988	8.572	58.403	41.622
F209	114.057	8.435	60.609	37.633
S210	118.416	7.659	60.845	62.474
F211	119.877	7.135	56.521	38.625
T212	110.180	6.839	-	-
A214	115.195	7.127	51.699	19.452
W215	120.631	8.125	55.379	30.954
N216	118.913	8.102	51.21	38.732
W217	120.812	8.752	61.446	29.207
T218	113.106	7.852	66.537	68.584
C219	119.691	8.010	63.812	26.651
K220	118.734	7.582	61.315	29.089
D221	119.904	8.521	57.139	39.486
L222	122.909	7.811	58.112	41.107
L223	120.617	7.453	58.448	40.718
L224	120.495	8.173	58.301	42.785
Q225	119.405	8.678	58.846	28.1
A226	121.462	7.824	55	18.119
L227	121.288	8.471	57.749	42.363
R228	119.351	8.516	60.135	29.911
E229	114.624	7.720	57.843	29.295
S230	110.396	7.492	59.075	64.772
Q231	124.464	8.568	54.494	29.095
S232	117.948	8.407	62.3	62.3
Y233	118.782	7.807	59.712	36.909
L234	122.879	6.936	57.235	41.401
V235	116.919	7.151	67.356	31.361
E236	116.651	8.043	58.785	28.277
D237	118.328	7.901	56.745	40.635
L238	118.069	7.890	56.422	41.905
E239	116.943	7.999	57.373	29.096
R240	118.133	7.321	56.539	30.678
S241	120.791	7.672	-	-

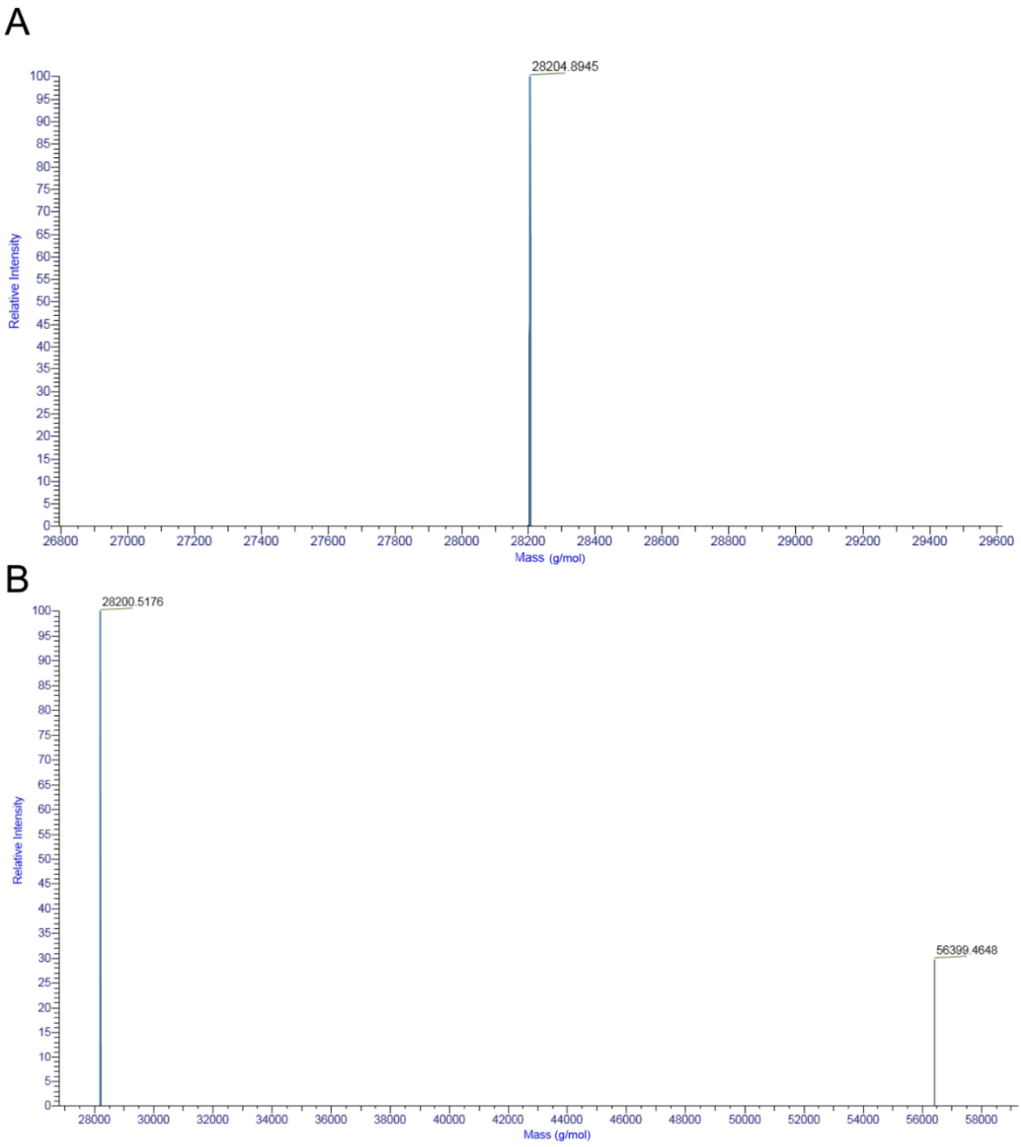

Figure S2. ASC3X monomer and dimer detected by mass spectrometry. *Mass spectra of ^{15}N-labeled ASC3X in the presence (A) and absence (B) of reverse phase chromatography immediately prior to injection in the mass spectrometer. Spectra were obtained several months after the start of oligomerization.*

ASC:

MGSSHHHHHH SSGLVPRGSH
10 20 30 40 50 60
MGRARDAILD ALENLTAEEL KKFKLKLLSV PLREGYGRIP RGALLSMDAL DLTDKLVSFY

70 80 90 100 110 120
LETYGAELTA NVLRDMGLQE MAGQLQAAT**H QGSGAAPAGI QAPPQSAAKP GL**HFIDQHRA

130 140 150 160 170 180
ALIARVTNVE WLLDALYGKV LTDEQYQAVR AEPTNPSKMR KLFSFTPAWN WTCKDLLLQA

190
LRESQSYLVE DLERS

ASCb:

MGSSHHHHHH SSGLVPRGSH

10 20 30 40 50 60
MGRARDAILD ALENLTAEEL KKFKLKLLSV PLREGYGRIP RGALLSMDAL DLTDKLVSFY

70 80 90 100 110 120
LETYGAELTA NVLRDMGLQE MAGQLQAAT**H QGL**HFIDQHR AALIARVTNV EWLLDALYGK

130 140 150 160 170
VLTDEQYQAV RAEPTNPSKM RKLFSFTPAW NWTCKDLLLQ ALRESQSYLV EDLERS

ASC3X:

MGSSHHHHHH SSGLVPRGSH
10 20 30 40 50 60
MGRARDAILD ALENLTAEEL KKFKLKLLSV PLREGYGRIP RGALLSMDAL DLTDKLVSFY

70 80 90 100 110 120
LETYGAELTA NVLRDMGLQE MAGQLQAAT**H QGSGAAPAGI QAPPQSAAKP GLHQGSGAAP**

130 140 150 160 170 180
AGIQAPPQSA AKPGLHQGSG AAPAGIQAPP QSAAKPGLHF IDQHRAALIA RVTNVEWLLD

190 200 210 220 230 240
ALYGKVLTDE QYQAVRAEPT NPSKMRKLFS FTPAWNWTCK DLLLQALRES QSYLVEDLER

S

Figure S1. Amino acid sequence of ASC, ASCb and ASC3X. *One-letter code amino acid sequence of full-length ASC, ASCb and ASC3X with residue numbering system. The His-tag and connecting linker to the native sequences is shown in red. Isoform linker is show in bold.*

7. Discussion

Regulation and formation of the inflammasome complex depends on the inclusion of the inflammatory adaptor ASC to the inflammasome complex. ASC plays a pivotal role in cellular death. The discovery of multiple isoforms of ASC (ASCb, ASCc, and ASCd) in macrophages further exemplifies its role in regulating pyroptosis. Each isoform has been shown to be expressed biologically depending on the cell type and serve to either lower inflammatory activity or inhibit inflammasome activation. Specifically, the biological activity of ASC relies on three integral parts: PYD domain, CARD domain, and linker length. As previously reported changes in either the domains or linker length have a significant effect on inflammasome activity. The studies presented above focused on establishing key differences between ASC and its isoform ASCb, in addition to, the effects of the linker on the dynamics between the PYD and CARD domain. The naturally occurring isoform, ASCb, and the engineered isoform, ASC3X, provide an ideal experimental design at two different extremes.

As shown by NMR, modulation in linker length does not alter the overall secondary structures the PYD and CARD domain. At a linker length of 3 aa (ASCb) and 23 aa (ASC) both domains remain intact and retain biological activity being able to complex with the PYD of NLRP3 and the CARD of procaspae-1 (18, 155). Similarly, at 69 aa (ASC3X) both domains also retain their secondary structure. As demonstrated by RT-NMR changes in linker length directly influence the self-association rate of each protein. At longer linker lengths > 23 amino acids the self-associating rate occurs in two kinetic phases, an initial fast phase, proceeded by a slower kinetic phase. While at smaller linker lengths self-association occurs as one slow kinetic phase or two identical slow phases. Analysis of the PYD and CARD domain at the amino acid level reveal equal participation of the PYD and CARD in ASCb self-association. At longer linker lengths the data suggests one domain predominantly drives the self-association process. At 23 aa acids the PYD-PYD interaction drives the self-association of ASC allowing it to produce the prototypical ASC speck. At 69 aa acids the CARD-CARD interaction drives the self-association process and forms a stable oligomer in solution.

Unexpectedly, as suggested by the RT-NMR data at longer linker lengths (ASC3X) the CARD-CARD interaction is the primary driver in self-associating behavior. The unusual loss of signal intensity for CARD residues suggests the formation of an stable CARD oligomer with non-interacting PYD domains as noted by the residual loss of signal intensity seen for PYD residues. Inexplicably, a CARD driven oligomer as a result of a longer linker does not allow for further PYD-PYD interactions; furthermore, the presence of a longer linker does not seem to increase the flexibility and thus, the interaction volume of each domain. Rather the added length seemingly acts as a deterrent for further PYD-PYD interactions reducing the overall effectiveness of its self-association properties. In

direct contrast, at significantly shorter lengths, ASCb, both the PYD and CARD domain drive the self-association process simultaneously resulting in a slower rate of self-association. Notably, at an intermediate linker length, ASC self-association is primarily driven by the PYD domain followed by the CARD-CARD interaction. The intermediate linker confers enough flexibility allowing both domains to interact through homotypic interactions. As evidenced by DLS studies of ASC, ASCb, ASC3X, indicate that at either extreme both ASCb and ASC3X lose the ability to form compact structures.

SEC studies monitoring the effects of pH, time, and concentration further enhance the self-association capabilities of each protein. Curiously, SEC studies of ASC3X appear to show the presence of a long-lived dimer indicating the presence of a stable dimer and monomer in solution. However, under similar conditions this phenomenon was not observed in both ASC and ASCb. Both ASC and ASC3X follow a similar trend, at longer linker lengths the self-association ability of each protein is enhanced readily producing an oligomer > 600 kDa in size. At a linker length of 3 aa ASCb retains a monomeric population after 2 days and at higher pH's compared to ASC and ASC3X. Despite differences in linker length, at neutral pH ASC, ASCb, and ASC3X assemble into similarly sized filaments.

Further insight into the interdomain dynamics using NMR relaxation reveal an already optimized linker length suited for inflammasome regulation. As previously stated, changes in linker length did not affect the overall structure of the PYD and CARD domain as indicated by [^{1}H-^{15}N] NOE values. Furthermore, the linker region remains disordered and highly flexible even at a significantly increased length. From the data, it is evident a reduced distance between both domains, as seen with ASCb, causes them to tumble together as a rod rather than two separate entities, resulting in a protein mimicking the behavior of a larger protein. The lack of a sufficiently long linker and interdomain flexibility between the two domains interferes with the capabilities of each domain to participate in homotypic interactions resulting in different behavior and biological function compared to ASC; increasing the distance between the two domains at longer linker lengths (69 aa) also produced behavior different from ASC. Surprisingly, the presence of a 69 aa linker did not produce a substantial change in both T_1 and T_2 values suggesting an upper limit to the effects of linker length on interdomain dynamics. Further increases would result in similar values as the linker would still provide sufficient drag to each domain. The flexibility afforded to each domain offers diminished returns at longer lengths and is comparable to that of ASC.

The results obtained from these studies demonstrate the importance of linker length on biological function. Changes in linker length have a dramatic effect on the inherent capabilities of the inflammasome adaptor ASC. ASCb and ASC3X fail to produce uniform structures *in vitro* instead forming different sized populations in solution. It is known ASCb produces a lower inflammatory response compared to ASC and that both ASC and ASCb can colocalize in the cell producing irregular sized filaments presumably affecting inflammasome complexation. Further studies monitoring the rate of formation of ASC and

ASCb colocalization are needed to determine the rate of formation as well as the specific type of macrostructures formed in solution. Secondly, RT-NMR experiments on the ASC^{PYD} and ASC^{CARD} are needed in determining the inherent rate of self-association for each domain. Determination of the rate for each domain will allow for a comparison to the PYD and CARD domain of ASC at longer linker lengths. Lastly, *in vitro* experiments monitoring the activity of ASC, ASCb, and ASC3X to the activation of procaspase-1 are necessary to further correlate linker length to biological function.

References

1. Chaplin, D. D. (2010) Overview of the Immune Response. *J. Allergy Clin. Immunol.* **125**, S3-23
2. Parkin, J., and Cohen, B. (2001) An overview of the immune system. *The Lancet*. **357**, 1777–1789
3. Marshall, J. S., Warrington, R., Watson, W., and Kim, H. L. (2018) An introduction to immunology and immunopathology. *Allergy Asthma Clin. Immunol.* **14**, 49
4. Hoebe, K., Janssen, E., and Beutler, B. (2004) The interface between innate and adaptive immunity. *Nat. Immunol.* **5**, 971–974
5. Kumar, H., Kawai, T., and Akira, S. (2011) Pathogen Recognition by the Innate Immune System. *Int. Rev. Immunol.* **30**, 16–34
6. Netea, M. G., Schlitzer, A., Placek, K., Joosten, L. A. B., and Schultze, J. L. (2019) Innate and Adaptive Immune Memory: an Evolutionary Continuum in the Host's Response to Pathogens. *Cell Host Microbe*. **25**, 13–26
7. Bonilla, F. A., and Oettgen, H. C. (2010) Adaptive immunity. *J. Allergy Clin. Immunol.* **125**, S33–S40
8. Buchmann, K. (2014) Evolution of Innate Immunity: Clues from Invertebrates via Fish to Mammals. *Front. Immunol.* [online] https://www.frontiersin.org/article/10.3389/fimmu.2014.00459 (Accessed April 29, 2022)
9. Riera Romo, M., Pérez-Martínez, D., and Castillo Ferrer, C. (2016) Innate immunity in vertebrates: an overview. *Immunology*. **148**, 125–139
10. Janeway, C. A., and Medzhitov, R. (2002) Innate immune recognition. *Annu. Rev. Immunol.* **20**, 197–216
11. Stegelmeier, A. A., van Vloten, J. P., Mould, R. C., Klafuric, E. M., Minott, J. A., Wootton, S. K., Bridle, B. W., and Karimi, K. (2019) Myeloid Cells during Viral Infections and Inflammation. *Viruses*. **11**, 168
12. Takeuchi, O., and Akira, S. (2010) Pattern Recognition Receptors and Inflammation. *Cell*. **140**, 805–820
13. Amarante-Mendes, G. P., Adjemian, S., Branco, L. M., Zanetti, L. C., Weinlich, R., and Bortoluci, K. R. (2018) Pattern Recognition Receptors and the Host Cell Death Molecular Machinery. *Front. Immunol.* [online] https://www.frontiersin.org/article/10.3389/fimmu.2018.02379 (Accessed April 29, 2022)
14. Kawai, T., and Akira, S. (2009) The roles of TLRs, RLRs and NLRs in pathogen recognition. *Int. Immunol.* **21**, 317–337
15. Dranoff, G. (2004) Cytokines in cancer pathogenesis and cancer therapy. *Nat. Rev. Cancer*. **4**, 11–22
16. Martinon, F., and Burns, K. The Inflammasome: A Molecular Platform Triggering Activation of Inflammatory Caspases and Processing of proIL-□. *Mol. Cell*
17. Schroder, K., and Tschopp, J. (2010) The Inflammasomes. *Cell*. **140**, 821–832
18. Bryan, N. B., Dorfleutner, A., Kramer, S. J., Yun, C., Rojanasakul, Y., and Stehlik, C. (2010) Differential splicing of the apoptosis-associated speck like protein containing a caspase recruitment domain (ASC) regulates inflammasomes. *J. Inflamm.* **7**, 23

19. Sharma, D., and Kanneganti, T.-D. (2016) The cell biology of inflammasomes: Mechanisms of inflammasome activation and regulation. *J. Cell Biol.* **213**, 617–629
20. Bergsbaken, T., Fink, S. L., and Cookson, B. T. (2009) Pyroptosis: host cell death and inflammation. *Nat. Rev. Microbiol.* **7**, 99–109
21. Shi, J., Zhao, Y., Wang, K., Shi, X., Wang, Y., Huang, H., Zhuang, Y., Cai, T., Wang, F., and Shao, F. (2015) Cleavage of GSDMD by inflammatory caspases determines pyroptotic cell death. *Nature*. **526**, 660–665
22. Stojanov, S., and Kastner, D. L. (2005) Familial autoinflammatory diseases: genetics, pathogenesis and treatment. *Curr. Opin. Rheumatol.* **17**, 586–599
23. McDermott, M. F., Aksentijevich, I., Galon, J., McDermott, E. M., Ogunkolade, B. W., Centola, M., Mansfield, E., Gadina, M., Karenko, L., Pettersson, T., McCarthy, J., Frucht, D. M., Aringer, M., Torosyan, Y., Teppo, A.-M., Wilson, M., Karaarslan, H. M., Wan, Y., Todd, I., Wood, G., Schlimgen, R., Kumarajeewa, T. R., Cooper, S. M., Vella, J. P., Amos, C. I., Mulley, J., Quane, K. A., Molloy, M. G., Ranki, A., Powell, R. J., Hitman, G. A., O'Shea, J. J., and Kastner, D. L. (1999) Germline Mutations in the Extracellular Domains of the 55 kDa TNF Receptor, TNFR1, Define a Family of Dominantly Inherited Autoinflammatory Syndromes. *Cell*. **97**, 133–144
24. Dombrowski, Y., Peric, M., Koglin, S., Kammerbauer, C., Göß, C., Anz, D., Simanski, M., Gläser, R., Harder, J., Hornung, V., Gallo, R. L., Ruzicka, T., Besch, R., and Schauber, J. (2011) Cytosolic DNA Triggers Inflammasome Activation in Keratinocytes in Psoriatic Lesions. *Sci. Transl. Med.* **3**, 82ra38
25. Esser, N., L'homme, L., De Roover, A., Kohnen, L., Scheen, A. J., Moutschen, M., Piette, J., Legrand-Poels, S., and Paquot, N. (2013) Obesity phenotype is related to NLRP3 inflammasome activity and immunological profile of visceral adipose tissue. *Diabetologia*. **56**, 2487–2497
26. Sun, X., Pang, H., Li, J., Luo, S., Huang, G., Li, X., Xie, Z., and Zhou, Z. (2020) The NLRP3 Inflammasome and Its Role in T1DM. *Front. Immunol.* [online] https://www.frontiersin.org/article/10.3389/fimmu.2020.01595 (Accessed April 29, 2022)
27. Grant, R., and Dixit, V. (2013) Mechanisms of disease: inflammasome activation and the development of type 2 diabetes. *Front. Immunol.* [online] https://www.frontiersin.org/article/10.3389/fimmu.2013.00050 (Accessed April 29, 2022)
28. Gora, I. M., Ciechanowska, A., and Ladyzynski, P. (2021) NLRP3 Inflammasome at the Interface of Inflammation, Endothelial Dysfunction, and Type 2 Diabetes. *Cells*. **10**, 314
29. Shao, B.-Z., Wang, S.-L., Pan, P., Yao, J., Wu, K., Li, Z.-S., Bai, Y., and Linghu, E.-Q. (2019) Targeting NLRP3 Inflammasome in Inflammatory Bowel Disease: Putting out the Fire of Inflammation. *Inflammation*. **42**, 1147–1159
30. Zhen, Y., and Zhang, H. (2019) NLRP3 Inflammasome and Inflammatory Bowel Disease. *Front. Immunol.* **10**, 276
31. Friker, L. L., Scheiblich, H., Hochheiser, I. V., Brinkschulte, R., Riedel, D., Latz, E., Geyer, M., and Heneka, M. T. (2020) β-Amyloid Clustering around ASC Fibrils Boosts Its Toxicity in Microglia. *Cell Rep.* **30**, 3743-3754.e6

32. Heneka, M. T., McManus, R. M., and Latz, E. (2018) Inflammasome signalling in brain function and neurodegenerative disease. *Nat. Rev. Neurosci.* **19**, 610–621
33. Yu, J. R., and Leslie, K. S. (2011) Cryopyrin-Associated Periodic Syndrome: An Update on Diagnosis and Treatment Response. *Curr. Allergy Asthma Rep.* **11**, 12–20
34. Neven, B., Prieur, A.-M., and dit Maire, P. Q. (2008) Cryopyrinopathies: update on pathogenesis and treatment. *Nat. Clin. Pract. Rheumatol.* **4**, 481–489
35. Kwon, H. S., and Koh, S.-H. (2020) Neuroinflammation in neurodegenerative disorders: the roles of microglia and astrocytes. *Transl. Neurodegener.* **9**, 42
36. Guzman-Martinez, L., Maccioni, R. B., Andrade, V., Navarrete, L. P., Pastor, M. G., and Ramos-Escobar, N. (2019) Neuroinflammation as a Common Feature of Neurodegenerative Disorders. *Front. Pharmacol.* [online] https://www.frontiersin.org/article/10.3389/fphar.2019.01008 (Accessed May 1, 2022)
37. Wyss-Coray, T., and Mucke, L. (2002) Inflammation in Neurodegenerative Disease—A Double-Edged Sword. *Neuron*. **35**, 419–432
38. Knopman, D. S., Amieva, H., Petersen, R. C., Chételat, G., Holtzman, D. M., Hyman, B. T., Nixon, R. A., and Jones, D. T. (2021) Alzheimer disease. *Nat. Rev. Dis. Primer*. **7**, 33
39. Vassar, R., Bennett, B. D., Babu-Khan, S., Kahn, S., Mendiaz, E. A., Denis, P., Teplow, D. B., Ross, S., Amarante, P., Loeloff, R., Luo, Y., Fisher, S., Fuller, J., Edenson, S., Lile, J., Jarosinski, M. A., Biere, A. L., Curran, E., Burgess, T., Louis, J.-C., Collins, F., Treanor, J., Rogers, G., and Citron, M. (1999) β-Secretase Cleavage of Alzheimer's Amyloid Precursor Protein by the Transmembrane Aspartic Protease BACE. *Science*. **286**, 735–741
40. Halle, A., Hornung, V., Petzold, G. C., Stewart, C. R., Monks, B. G., Reinheckel, T., Fitzgerald, K. A., Latz, E., Moore, K. J., and Golenbock, D. T. (2008) The NALP3 inflammasome is involved in the innate immune response to amyloid-β. *Nat. Immunol.* **9**, 857–865
41. Pirzada, R. H., Javaid, N., and Choi, S. (2020) The Roles of the NLRP3 Inflammasome in Neurodegenerative and Metabolic Diseases and in Relevant Advanced Therapeutic Interventions. *Genes*. **11**, 131
42. Murray, C. A., and Lynch, M. A. (1998) Evidence that increased hippocampal expression of the cytokine interleukin-1 beta is a common trigger for age- and stress-induced impairments in long-term potentiation. *J. Neurosci. Off. J. Soc. Neurosci.* **18**, 2974–2981
43. Yin, J., Zhao, F., Chojnacki, J. E., Fulp, J., Klein, W. L., Zhang, S., and Zhu, X. (2018) NLRP3 Inflammasome Inhibitor Ameliorates Amyloid Pathology in a Mouse Model of Alzheimer's Disease. *Mol. Neurobiol.* **55**, 1977–1987
44. Kitazawa, M., Cheng, D., Tsukamoto, M. R., Koike, M. A., Wes, P. D., Vasilevko, V., Cribbs, D. H., and LaFerla, F. M. (2011) Blocking IL-1 Signaling Rescues Cognition, Attenuates Tau Pathology, and Restores Neuronal β-Catenin Pathway Function in an Alzheimer's Disease Model. *J. Immunol.* **187**, 6539–6549
45. Codolo, G., Plotegher, N., Pozzobon, T., Brucale, M., Tessari, I., Bubacco, L., and de Bernard, M. (2013) Triggering of inflammasome by aggregated α-synuclein, an inflammatory response in synucleinopathies. *PloS One*. **8**, e55375

46. Gustot, A., Gallea, J. I., Sarroukh, R., Celej, M. S., Ruysschaert, J.-M., and Raussens, V. (2015) Amyloid fibrils are the molecular trigger of inflammation in Parkinson's disease. *Biochem. J.* **471**, 323–333
47. Mao, Z., Liu, C., Ji, S., Yang, Q., Ye, H., Han, H., and Xue, Z. (2017) The NLRP3 Inflammasome is Involved in the Pathogenesis of Parkinson's Disease in Rats. *Neurochem. Res.* **42**, 1104–1115
48. Yan, Y., Jiang, W., Liu, L., Wang, X., Ding, C., Tian, Z., and Zhou, R. (2015) Dopamine controls systemic inflammation through inhibition of NLRP3 inflammasome. *Cell*. **160**, 62–73
49. Zhang, Z., Shen, P., Lu, X., Li, Y., Liu, J., Liu, B., Fu, Y., Cao, Y., and Zhang, N. (2017) In Vivo and In Vitro Study on the Efficacy of Terpinen-4-ol in Dextran Sulfate Sodium-Induced Mice Experimental Colitis. *Front. Immunol.* **8**, 558
50. De la Fuente, M., Franchi, L., Araya, D., Díaz-Jiménez, D., Olivares, M., Álvarez-Lobos, M., Golenbock, D., González, M.-J., López-Kostner, F., Quera, R., Núñez, G., Vidal, R., and Hermoso, M. A. (2014) Escherichia coli isolates from inflammatory bowel diseases patients survive in macrophages and activate NLRP3 inflammasome. *Int. J. Med. Microbiol. IJMM*. **304**, 384–392
51. Mao, L., Kitani, A., Similuk, M., Oler, A. J., Albenberg, L., Kelsen, J., Aktay, A., Quezado, M., Yao, M., Montgomery-Recht, K., Fuss, I. J., and Strober, W. (2018) Loss-of-function CARD8 mutation causes NLRP3 inflammasome activation and Crohn's disease. *J. Clin. Invest.* **128**, 1793–1806
52. Hanaei, S., Sadr, M., Rezaei, A., Shahkarami, S., Ebrahimi Daryani, N., Bidoki, A. Z., and Rezaei, N. (2018) Association of NLRP3 single nucleotide polymorphisms with ulcerative colitis: A case-control study. *Clin. Res. Hepatol. Gastroenterol.* **42**, 269–275
53. Zhang, H., Wang, Z., Lu, X., Wang, Y., Zhong, J., and Liu, J. (2014) NLRP3 gene is associated with ulcerative colitis (UC), but not Crohn's disease (CD), in Chinese Han population. *Inflamm. Res. Off. J. Eur. Histamine Res. Soc. Al.* **63**, 979–985
54. Ruiz, P. A., Morón, B., Becker, H. M., Lang, S., Atrott, K., Spalinger, M. R., Scharl, M., Wojtal, K. A., Fischbeck-Terhalle, A., Frey-Wagner, I., Hausmann, M., Kraemer, T., and Rogler, G. (2017) Titanium dioxide nanoparticles exacerbate DSS-induced colitis: role of the NLRP3 inflammasome. *Gut*. **66**, 1216–1224
55. Fenini, G., Karakaya, T., Hennig, P., Di Filippo, M., and Beer, H.-D. (2020) The NLRP1 Inflammasome in Human Skin and Beyond. *Int. J. Mol. Sci.* **21**, E4788
56. Nestle, F. O., Di Meglio, P., Qin, J.-Z., and Nickoloff, B. J. (2009) Skin immune sentinels in health and disease. *Nat. Rev. Immunol.* **9**, 679–691
57. Eckert, R. L., and Rorke, E. A. (1989) Molecular biology of keratinocyte differentiation. *Environ. Health Perspect.* **80**, 109–116
58. Pasparakis, M., Haase, I., and Nestle, F. O. (2014) Mechanisms regulating skin immunity and inflammation. *Nat. Rev. Immunol.* **14**, 289–301
59. Feldmeyer, L., Keller, M., Niklaus, G., Hohl, D., Werner, S., and Beer, H.-D. (2007) The inflammasome mediates UVB-induced activation and secretion of interleukin-1beta by keratinocytes. *Curr. Biol. CB*. **17**, 1140–1145
60. Faustin, B., and Reed, J. C. (2008) Sunburned skin activates inflammasomes. *Trends Cell Biol.* **18**, 4–8

61. Park, H. H., Lo, Y.-C., Lin, S.-C., Wang, L., Yang, J. K., and Wu, H. (2007) The Death Domain Superfamily in Intracellular Signaling of Apoptosis and Inflammation. *Annu. Rev. Immunol.* **25**, 561–586
62. Feinstein, E., Kimchi, A., Wallach, D., Boldin, M., and Varfolomeev, E. (1995) The death domain: a module shared by proteins with diverse cellular functions. *Trends Biochem. Sci.* **20**, 342–344
63. Steward, A., McDowell, G. S., and Clarke, J. (2009) Topology is the principal determinant in the folding of a complex all-alpha Greek key death domain from human FADD. *J. Mol. Biol.* **389**, 425–437
64. McIlwain, D. R., Berger, T., and Mak, T. W. (2013) Caspase Functions in Cell Death and Disease. *Cold Spring Harb. Perspect. Biol.* **5**, a008656–a008656
65. Fink, S. L., and Cookson, B. T. (2005) Apoptosis, Pyroptosis, and Necrosis: Mechanistic Description of Dead and Dying Eukaryotic Cells. *Infect. Immun.* **73**, 1907–1916
66. Gentle, I. E. (2019) Supramolecular Complexes in Cell Death and Inflammation and Their Regulation by Autophagy. *Front. Cell Dev. Biol.* [online] https://www.frontiersin.org/article/10.3389/fcell.2019.00073 (Accessed May 20, 2022)
67. Qin, H., Srinivasula, S. M., Wu, G., Fernandes-Alnemri, T., Alnemri, E. S., and Shi, Y. (1999) Structural basis of procaspase-9 recruitment by the apoptotic protease-activating factor 1. *Nature*. **399**, 549–557
68. Ferrao, R., and Wu, H. (2012) Helical assembly in the death domain (DD) superfamily. *Curr. Opin. Struct. Biol.* **22**, 241–247
69. Park, H. H. (2019) Caspase recruitment domains for protein interactions in cellular signaling (Review). *Int. J. Mol. Med.* **43**, 1119–1127
70. Indramohan, M., Stehlik, C., and Dorfleutner, A. (2018) COPs and POPs Patrol Inflammasome Activation. *J. Mol. Biol.* **430**, 153–173
71. Dorfleutner, A., Chu, L., and Stehlik, C. (2015) Inhibiting the inflammasome: one domain at a time. *Immunol. Rev.* **265**, 205–216
72. Kumar, S. (2007) Caspase function in programmed cell death. *Cell Death Differ.* **14**, 32–43
73. Jang, T., Kim, S. H., Jeong, J.-H., Kim, S., Kim, Y.-G., and Park, H. H. (2015) Crystal structure of caspase recruiting domain (CARD) of apoptosis repressor with CARD (ARC) and its implication in inhibition of apoptosis. *Sci. Rep.* **5**, 9847
74. Li, Y., Fu, T.-M., Lu, A., Witt, K., Ruan, J., Shen, C., and Wu, H. (2018) Cryo-EM structures of ASC and NLRC4 CARD filaments reveal a unified mechanism of nucleation and activation of caspase-1. *Proc. Natl. Acad. Sci.* **115**, 10845–10852
75. Humke, E. W., Shriver, S. K., Starovasnik, M. A., Fairbrother, W. J., and Dixit, V. M. (2000) ICEBERG: A Novel Inhibitor of Interleukin-1β Generation. *Cell*. **103**, 99–111
76. Li, S., Yang, X., Shao, J., and Shen, Y. (2012) Structural Insights into the Assembly of CARMA1 and BCL10. *PLOS ONE*. **7**, e42775
77. Lu, A., Li, Y., Schmidt, F. I., Yin, Q., Chen, S., Fu, T.-M., Tong, A. B., Ploegh, H. L., Mao, Y., and Wu, H. (2016) Molecular basis of caspase-1 polymerization and its inhibition by a new capping mechanism. *Nat. Struct. Mol. Biol.* **23**, 416–425

78. Ancient missense mutations in a new member of the RoRet gene family are likely to cause familial Mediterranean fever. The International FMF Consortium (1997) *Cell*. **90**, 797–807
79. Chu, L. H., Gangopadhyay, A., Dorfleutner, A., and Stehlik, C. (2015) An updated view on the structure and function of PYRIN domains. *Apoptosis Int. J. Program. Cell Death*. **20**, 157–173
80. Kersse, K., Verspurten, J., Berghe, T. V., and Vandenabeele, P. (2011) The death-fold superfamily of homotypic interaction motifs. *Trends Biochem. Sci.* **36**, 541–552
81. Jin, T., Perry, A., Smith, P., Jiang, J., and Xiao, T. S. (2013) Structure of the absent in melanoma 2 (AIM2) pyrin domain provides insights into the mechanisms of AIM2 autoinhibition and inflammasome assembly. *J. Biol. Chem.* **288**, 13225–13235
82. Stehlik, C., Krajewska, M., Welsh, K., Krajewski, S., Godzik, A., and Reed, J. C. (2003) The PAAD/PYRIN-only protein POP1/ASC2 is a modulator of ASC-mediated nuclear-factor-kappa B and pro-caspase-1 regulation. *Biochem. J.* **373**, 101–113
83. Ratsimandresey, R. A., Chu, L. H., Khare, S., de Almeida, L., Gangopadhyay, A., Indramohan, M., Misharin, A. V., Greaves, D. R., Perlman, H., Dorfleutner, A., and Stehlik, C. (2017) The PYRIN domain-only protein POP2 inhibits inflammasome priming and activation. *Nat. Commun.* **8**, 15556
84. Khare, S., Ratsimandresey, R. A., de Almeida, L., Cuda, C. M., Rellick, S. L., Misharin, A. V., Wallin, M. C., Gangopadhyay, A., Forte, E., Gottwein, E., Perlman, H., Reed, J. C., Greaves, D. R., Dorfleutner, A., and Stehlik, C. (2014) The PYRIN domain–only protein POP3 inhibits ALR inflammasomes and regulates responses to infection with DNA viruses. *Nat. Immunol.* **15**, 343–353
85. Oroz, J., Barrera-Vilarmau, S., Alfonso, C., Rivas, G., and de Alba, E. (2016) ASC Pyrin Domain Self-associates and Binds NLRP3 Protein Using Equivalent Binding Interfaces. *J. Biol. Chem.* **291**, 19487–19501
86. Liepinsh, E., Barbals, R., Dahl, E., Sharipo, A., Staub, E., and Otting, G. (2003) The Death-domain Fold of the ASC PYRIN Domain, Presenting a Basis for PYRIN/PYRIN Recognition. *J. Mol. Biol.* **332**, 1155–1163
87. Natarajan, A., Ghose, R., and Hill, J. M. (2006) Structure and Dynamics of ASC2, a Pyrin Domain-only Protein That Regulates Inflammatory Signaling. *J. Biol. Chem.* **281**, 31863–31875
88. Sharma, M., and de Alba, E. (2021) Structure, Activation and Regulation of NLRP3 and AIM2 Inflammasomes. *Int. J. Mol. Sci.* 10.3390/ijms22020872
89. Hayward, J. A., Mathur, A., Ngo, C., and Man, S. M. (2018) Cytosolic Recognition of Microbes and Pathogens: Inflammasomes in Action. *Microbiol. Mol. Biol. Rev.* **82**, e00015-18, /mmbr/82/4/e00015-18.atom
90. Bürckstümmer, T., Baumann, C., Blüml, S., Dixit, E., Dürnberger, G., Jahn, H., Planyavsky, M., Bilban, M., Colinge, J., Bennett, K. L., and Superti-Furga, G. (2009) An orthogonal proteomic-genomic screen identifies AIM2 as a cytoplasmic DNA sensor for the inflammasome. *Nat. Immunol.* **10**, 266–272
91. Fernandes-Alnemri, T., Yu, J.-W., Datta, P., Wu, J., and Alnemri, E. S. (2009) AIM2 activates the inflammasome and cell death in response to cytoplasmic DNA. *Nature*. **458**, 509–513

92. Khare, S., Dorfleutner, A., Bryan, N. B., Yun, C., Radian, A. D., de Almeida, L., Rojanasakul, Y., and Stehlik, C. (2012) An NLRP7-Containing Inflammasome Mediates Recognition of Microbial Lipopeptides in Human Macrophages. *Immunity*. **36**, 464–476
93. Man, S. M., and Kanneganti, T.-D. (2015) Regulation of inflammasome activation. *Immunol. Rev.* **265**, 6–21
94. Vladimer, G. I., Weng, D., Paquette, S. W. M., Vanaja, S. K., Rathinam, V. A. K., Aune, M. H., Conlon, J. E., Burbage, J. J., Proulx, M. K., Liu, Q., Reed, G., Mecsas, J. C., Iwakura, Y., Bertin, J., Goguen, J. D., Fitzgerald, K. A., and Lien, E. (2012) The NLRP12 Inflammasome Recognizes Yersinia pestis. *Immunity*. **37**, 96–107
95. Guo, H., Callaway, J. B., and Ting, J. P.-Y. (2015) Inflammasomes: mechanism of action, role in disease, and therapeutics. *Nat. Med.* **21**, 677–687
96. Mariathasan, S., Weiss, D. S., Newton, K., McBride, J., O'Rourke, K., Roose-Girma, M., Lee, W. P., Weinrauch, Y., Monack, D. M., and Dixit, V. M. (2006) Cryopyrin activates the inflammasome in response to toxins and ATP. *Nature*. **440**, 228–232
97. Dostert, C., Petrilli, V., Van Bruggen, R., Steele, C., Mossman, B. T., and Tschopp, J. (2008) Innate Immune Activation Through Nalp3 Inflammasome Sensing of Asbestos and Silica. *Science*. **320**, 674–677
98. Savage, C., Lopez-Castejon, G., Denes, A., and Brough, D. (2012) NLRP3-Inflammasome Activating DAMPs Stimulate an Inflammatory Response in Glia in the Absence of Priming Which Contributes to Brain Inflammation after Injury. *Front. Immunol.* [online] https://www.frontiersin.org/article/10.3389/fimmu.2012.00288 (Accessed May 26, 2022)
99. Bauernfeind, F. G., Horvath, G., Stutz, A., Alnemri, E. S., MacDonald, K., Speert, D., Fernandes-Alnemri, T., Wu, J., Monks, B. G., Fitzgerald, K. A., Hornung, V., and Latz, E. (2009) Cutting Edge: NF-κB Activating Pattern Recognition and Cytokine Receptors License NLRP3 Inflammasome Activation by Regulating NLRP3 Expression. *J. Immunol.* **183**, 787–791
100. Franchi, L., Eigenbrod, T., and Núñez, G. (2009) Cutting Edge: TNF-α Mediates Sensitization to ATP and Silica via the NLRP3 Inflammasome in the Absence of Microbial Stimulation. *J. Immunol.* **183**, 792–796
101. Zheng, D., Liwinski, T., and Elinav, E. (2020) Inflammasome activation and regulation: toward a better understanding of complex mechanisms. *Cell Discov.* **6**, 1–22
102. Swanson, K. V., Deng, M., and Ting, J. P.-Y. (2019) The NLRP3 inflammasome: molecular activation and regulation to therapeutics. *Nat. Rev. Immunol.* **19**, 477–489
103. Vajjhala, P. R., Mirams, R. E., and Hill, J. M. (2012) Multiple binding sites on the pyrin domain of ASC protein allow self-association and interaction with NLRP3 protein. *J. Biol. Chem.* **287**, 41732–41743
104. He, W., Wan, H., Hu, L., Chen, P., Wang, X., Huang, Z., Yang, Z.-H., Zhong, C.-Q., and Han, J. (2015) Gasdermin D is an executor of pyroptosis and required for interleukin-1β secretion. *Cell Res.* **25**, 1285–1298
105. Liu, X., Zhang, Z., Ruan, J., Pan, Y., Magupalli, V. G., Wu, H., and Lieberman, J. (2016) Inflammasome-activated gasdermin D causes pyroptosis by forming membrane pores. *Nature*. **535**, 153–158

106. Sborgi, L., Rühl, S., Mulvihill, E., Pipercevic, J., Heilig, R., Stahlberg, H., Farady, C. J., Müller, D. J., Broz, P., and Hiller, S. (2016) GSDMD membrane pore formation constitutes the mechanism of pyroptotic cell death. *EMBO J.* **35**, 1766–1778
107. Wei, S., Ma, W., Zhang, B., and Li, W. (2021) NLRP3 Inflammasome: A Promising Therapeutic Target for Drug-Induced Toxicity. *Front. Cell Dev. Biol.* [online] https://www.frontiersin.org/article/10.3389/fcell.2021.634607 (Accessed May 21, 2022)
108. Kayagaki, N., Warming, S., Lamkanfi, M., Walle, L. V., Louie, S., Dong, J., Newton, K., Qu, Y., Liu, J., Heldens, S., Zhang, J., Lee, W. P., Roose-Girma, M., and Dixit, V. M. (2011) Non-canonical inflammasome activation targets caspase-11. *Nature*. **479**, 117–121
109. Rathinam, V. A. K., Vanaja, S. K., Waggoner, L., Sokolovska, A., Becker, C., Stuart, L. M., Leong, J. M., and Fitzgerald, K. A. (2012) TRIF licenses caspase-11-dependent NLRP3 inflammasome activation by gram-negative bacteria. *Cell*. **150**, 606–619
110. Gurung, P., Malireddi, R. K. S., Anand, P. K., Demon, D., Vande Walle, L., Liu, Z., Vogel, P., Lamkanfi, M., and Kanneganti, T.-D. (2012) Toll or interleukin-1 receptor (TIR) domain-containing adaptor inducing interferon-β (TRIF)-mediated caspase-11 protease production integrates Toll-like receptor 4 (TLR4) protein- and Nlrp3 inflammasome-mediated host defense against enteropathogens. *J. Biol. Chem.* **287**, 34474–34483
111. Shi, J., Zhao, Y., Wang, Y., Gao, W., Ding, J., Li, P., Hu, L., and Shao, F. (2014) Inflammatory caspases are innate immune receptors for intracellular LPS. *Nature*. **514**, 187–192
112. Downs, K. P., Nguyen, H., Dorfleutner, A., and Stehlik, C. (2020) An overview of the non-canonical inflammasome. *Mol. Aspects Med.* **76**, 100924
113. D'Osualdo, A., Weichenberger, C. X., Wagner, R. N., Godzik, A., Wooley, J., and Reed, J. C. (2011) CARD8 and NLRP1 Undergo Autoproteolytic Processing through a ZU5-Like Domain. *PLOS ONE*. **6**, e27396
114. Mitchell, P. S., Sandstrom, A., and Vance, R. E. (2019) The NLRP1 inflammasome: new mechanistic insights and unresolved mysteries. *Curr. Opin. Immunol.* **60**, 37–45
115. Liu, S., Miller-Randolph, S., Crown, D., Moayeri, M., Sastalla, I., Okugawa, S., and Leppla, S. H. (2010) Anthrax Toxin Targeting of Myeloid Cells through the CMG2 Receptor Is Essential for Establishment of Bacillus anthracis Infections in Mice. *Cell Host Microbe*. **8**, 455–462
116. Hellmich, K. A., Levinsohn, J. L., Fattah, R., Newman, Z. L., Maier, N., Sastalla, I., Liu, S., Leppla, S. H., and Moayeri, M. (2012) Anthrax Lethal Factor Cleaves Mouse Nlrp1b in Both Toxin-Sensitive and Toxin-Resistant Macrophages. *PLOS ONE*. **7**, e49741
117. Chavarría-Smith, J., Mitchell, P. S., Ho, A. M., Daugherty, M. D., and Vance, R. E. (2016) Functional and Evolutionary Analyses Identify Proteolysis as a General Mechanism for NLRP1 Inflammasome Activation. *PLOS Pathog.* **12**, e1006052

118. Squires, R. C., Muehlbauer, S. M., and Brojatsch, J. (2007) Proteasomes Control Caspase-1 Activation in Anthrax Lethal Toxin-mediated Cell Killing. *J. Biol. Chem.* **282**, 34260–34267
119. Sandstrom, A., Mitchell, P. S., Goers, L., Mu, E. W., Lesser, C. F., and Vance, R. E. (2019) Functional degradation: a mechanism of NLRP1 inflammasome activation by diverse pathogen enzymes. *Science*. **364**, eaau1330
120. Taabazuing, C. Y., Griswold, A. R., and Bachovchin, D. A. (2020) The NLRP1 and CARD8 inflammasomes. *Immunol. Rev.* **297**, 13–25
121. Franchi, L., Stoolman, J., Kanneganti, T.-D., Verma, A., Ramphal, R., and Núñez, G. (2007) Critical role for Ipaf in Pseudomonas aeruginosa-induced caspase-1 activation. *Eur. J. Immunol.* **37**, 3030–3039
122. Suzuki, T., Franchi, L., Toma, C., Ashida, H., Ogawa, M., Yoshikawa, Y., Mimuro, H., Inohara, N., Sasakawa, C., and Nuñez, G. (2007) Differential Regulation of Caspase-1 Activation, Pyroptosis, and Autophagy via Ipaf and ASC in Shigella-Infected Macrophages. *PLoS Pathog.* **3**, e111
123. Amer, A., Franchi, L., Kanneganti, T.-D., Body-Malapel, M., Ozören, N., Brady, G., Meshinchi, S., Jagirdar, R., Gewirtz, A., Akira, S., and Núñez, G. (2006) Regulation of Legionella phagosome maturation and infection through flagellin and host Ipaf. *J. Biol. Chem.* **281**, 35217–35223
124. Tenthorey, J. L., Kofoed, E. M., Daugherty, M. D., Malik, H. S., and Vance, R. E. (2014) Molecular Basis for Specific Recognition of Bacterial Ligands by NAIP/NLRC4 Inflammasomes. *Mol. Cell*. **54**, 17–29
125. Wen, J., Xuan, B., Liu, Y., Wang, L., He, L., Meng, X., Zhou, T., and Wang, Y. (2021) Updating the NLRC4 Inflammasome: from Bacterial Infections to Autoimmunity and Cancer. *Front. Immunol.* [online] https://www.frontiersin.org/article/10.3389/fimmu.2021.702527 (Accessed May 13, 2022)
126. Diez, E., Lee, S.-H., Gauthier, S., Yaraghi, Z., Tremblay, M., Vidal, S., and Gros, P. (2003) Birc1e is the gene within the Lgn1 locus associated with resistance to Legionella pneumophila. *Nat. Genet.* **33**, 55–60
127. Karki, R., Lee, E., Place, D., Samir, P., Mavuluri, J., Sharma, B. R., Balakrishnan, A., Malireddi, R. K. S., Geiger, R., Zhu, Q., Neale, G., and Kanneganti, T.-D. (2018) IRF8 Regulates Transcription of Naips for NLRC4 Inflammasome Activation. *Cell*. **173**, 920-933.e13
128. Kortmann, J., Brubaker, S. W., and Monack, D. M. (2015) Cutting Edge: Inflammasome Activation in Primary Human Macrophages Is Dependent on Flagellin. *J. Immunol.* **195**, 815–819
129. Rayamajhi, M., Zak, D. E., Chavarria-Smith, J., Vance, R. E., and Miao, E. A. (2013) Cutting Edge: Mouse NAIP1 Detects the Type III Secretion System Needle Protein. *J. Immunol.* **191**, 3986–3989
130. Kofoed, E. M., and Vance, R. E. (2011) Innate immune recognition of bacterial ligands by NAIPs determines inflammasome specificity. *Nature*. **477**, 592–595
131. Duncan, J. A., and Canna, S. W. (2018) The NLRC4 Inflammasome. *Immunol. Rev.* **281**, 115–123

132. Albrecht, M., Choubey, D., and Lengauer, T. (2005) The HIN domain of IFI-200 proteins consists of two OB folds. *Biochem. Biophys. Res. Commun.* **327**, 679–687
133. Liao, J. C. C., Lam, R., Brazda, V., Duan, S., Ravichandran, M., Ma, J., Xiao, T., Tempel, W., Zuo, X., Wang, Y.-X., Chirgadze, N. Y., and Arrowsmith, C. H. (2011) Interferon-Inducible Protein 16: Insight into the Interaction with Tumor Suppressor p53. *Structure*. **19**, 418–429
134. Jin, T., Perry, A., Jiang, J., Smith, P., Curry, J. A., Unterholzner, L., Jiang, Z., Horvath, G., Rathinam, V. A., Johnstone, R. W., Hornung, V., Latz, E., Bowie, A. G., Fitzgerald, K. A., and Xiao, T. S. (2012) Structures of the HIN Domain:DNA Complexes Reveal Ligand Binding and Activation Mechanisms of the AIM2 Inflammasome and IFI16 Receptor. *Immunity*. **36**, 561–571
135. Shaw, N., and Liu, Z.-J. (2014) Role of the HIN Domain in Regulation of Innate Immune Responses. *Mol. Cell. Biol.* **34**, 2–15
136. Wang, B., Bhattacharya, M., Roy, S., Tian, Y., and Yin, Q. (2020) Immunobiology and Structural Biology of AIM2 Inflammasome. *Mol. Aspects Med.* **76**, 100869
137. Lu, A., Magupalli, V. G., Ruan, J., Yin, Q., Atianand, M. K., Vos, M. R., Schröder, G. F., Fitzgerald, K. A., Wu, H., and Egelman, E. H. (2014) Unified Polymerization Mechanism for the Assembly of ASC-Dependent Inflammasomes. *Cell*. **156**, 1193–1206
138. Heilig, R., and Broz, P. (2018) Function and mechanism of the pyrin inflammasome. *Eur. J. Immunol.* **48**, 230–238
139. Centola, M., Wood, G., Frucht, D. M., Galon, J., Aringer, M., Farrell, C., Kingma, D. W., Horwitz, M. E., Mansfield, E., Holland, S. M., O'Shea, J. J., Rosenberg, H. F., Malech, H. L., and Kastner, D. L. (2000) The gene for familial Mediterranean fever, MEFV, is expressed in early leukocyte development and is regulated in response to inflammatory mediators. *Blood*. **95**, 3223–3231
140. French FMF Consortium (1997) A candidate gene for familial Mediterranean fever. *Nat. Genet.* **17**, 25–31
141. Xu, H., Yang, J., Gao, W., Li, L., Li, P., Zhang, L., Gong, Y.-N., Peng, X., Xi, J. J., Chen, S., Wang, F., and Shao, F. (2014) Innate immune sensing of bacterial modifications of Rho GTPases by the Pyrin inflammasome. *Nature*. **513**, 237–241
142. Malik, A., and Kanneganti, T.-D. (2017) Inflammasome activation and assembly at a glance. *J. Cell Sci.* **130**, 3955–3963
143. Gao, W., Yang, J., Liu, W., Wang, Y., and Shao, F. (2016) Site-specific phosphorylation and microtubule dynamics control Pyrin inflammasome activation. *Proc. Natl. Acad. Sci. U. S. A.* **113**, E4857-4866
144. Masumoto, J., Taniguchi, S., Ayukawa, K., Sarvotham, H., Kishino, T., Niikawa, N., Hidaka, E., Katsuyama, T., Higuchi, T., and Sagara, J. (1999) ASC, a Novel 22-kDa Protein, Aggregates during Apoptosis of Human Promyelocytic Leukemia HL-60 Cells. *J. Biol. Chem.* **274**, 33835–33838
145. de Alba, E. (2009) Structure and Interdomain Dynamics of Apoptosis-associated Speck-like Protein Containing a CARD (ASC). *J. Biol. Chem.* **284**, 32932–32941

147. Moriya, M., Taniguchi, S., Wu, P., Liepinsh, E., Otting, G., and Sagara, J. (2005) Role of Charged and Hydrophobic Residues in the Oligomerization of the PYRIN Domain of ASC †. *Biochemistry*. **44**, 575–583
148. Pettersen, E. F., Goddard, T. D., Huang, C. C., Meng, E. C., Couch, G. S., Croll, T. I., Morris, J. H., and Ferrin, T. E. (2021) UCSF ChimeraX: Structure visualization for researchers, educators, and developers. *Protein Sci. Publ. Protein Soc.* **30**, 70–82
149. Conway, K. E., McConnell, B. B., Bowring, C. E., Donald, C. D., Warren, S. T., and Vertino, P. M. (2000) TMS1, a novel proapoptotic caspase recruitment domain protein, is a target of methylation-induced gene silencing in human breast cancers. *Cancer Res.* **60**, 6236–6242
150. McConnell, B. B., and Vertino, P. M. (2004) TMS1/ASC: The cancer connection. *Apoptosis*. **9**, 5–18
151. McConnell, B. B., and Vertino, P. M. (2000) Activation of a Caspase-9-mediated Apoptotic Pathway by Subcellular Redistribution of the Novel Caspase Recruitment Domain Protein TMS11. *Cancer Res.* **60**, 6243–6247
152. Fernandes-Alnemri, T., Wu, J., Yu, J.-W., Datta, P., Miller, B., Jankowski, W., Rosenberg, S., Zhang, J., and Alnemri, E. S. (2007) The pyroptosome: a supramolecular assembly of ASC dimers mediating inflammatory cell death via caspase-1 activation. *Cell Death Differ.* **14**, 1590–1604
153. Man, S. M., Hopkins, L. J., Nugent, E., Cox, S., Gluck, I. M., Tourlomousis, P., Wright, J. A., Cicuta, P., Monie, T. P., and Bryant, C. E. (2014) Inflammasome activation causes dual recruitment of NLRC4 and NLRP3 to the same macromolecular complex. *Proc. Natl. Acad. Sci.* **111**, 7403–7408
154. Nambayan, R. J. T., Sandin, S. I., Quint, D. A., Satyadi, D. M., and de Alba, E. (2019) The inflammasome adapter ASC assembles into filaments with integral participation of its two Death Domains, PYD and CARD. *J. Biol. Chem.* **294**, 439–452
155. Matsushita, K., Takeoka, M., Sagara, J., Itano, N., Kurose, Y., Nakamura, A., and Taniguchi, S. (2009) A Splice Variant of ASC Regulates IL-1 β Release and Aggregates Differently from Intact ASC. *Mediators Inflamm.* **2009**, 1–6
156. Shalini, S., Dorstyn, L., Dawar, S., and Kumar, S. (2015) Old, new and emerging functions of caspases. *Cell Death Differ.* **22**, 526–539
157. Boucher, D., Monteleone, M., Coll, R. C., Chen, K. W., Ross, C. M., Teo, J. L., Gomez, G. A., Holley, C. L., Bierschenk, D., Stacey, K. J., Yap, A. S., Bezbradica, J. S., and Schroder, K. (2018) Caspase-1 self-cleavage is an intrinsic mechanism to terminate inflammasome activity. *J. Exp. Med.* **215**, 827–840
158. Aglietti, R. A., Estevez, A., Gupta, A., Ramirez, M. G., Liu, P. S., Kayagaki, N., Ciferri, C., Dixit, V. M., and Dueber, E. C. (2016) GsdmD p30 elicited by caspase-11 during pyroptosis forms pores in membranes. *Proc. Natl. Acad. Sci. U. S. A.* **113**, 7858–7863
159. Ding, J., Wang, K., Liu, W., She, Y., Sun, Q., Shi, J., Sun, H., Wang, D.-C., and Shao, F. (2016) Pore-forming activity and structural autoinhibition of the gasdermin family. *Nature*. **535**, 111–116
160. Cavanagh, J., Skelton, N. J., Fairbrother, W. J., Rance, M., and III, A. G. P. (2010) *Protein NMR Spectroscopy: Principles and Practice*, Elsevier

161. Keeler, J. (2011) *Understanding NMR Spectroscopy*, John Wiley & Sons
162. Levitt, M. H. (2008) *Spin Dynamics: Basics of Nuclear Magnetic Resonance*, Wiley
163. Goldenberg, D. (2016) *Principles of NMR Spectroscopy*, University Science Books
164. Wishart, D. S., and Case, D. A. (2001) Use of chemical shifts in macromolecular structure determination. *Methods Enzymol.* **338**, 3–34
165. Morin, S. (2011) A practical guide to protein dynamics from 15N spin relaxation in solution. *Prog. Nucl. Magn. Reson. Spectrosc.* **59**, 245–262
166. Kleckner, I. R., and Foster, M. P. (2011) An introduction to NMR-based approaches for measuring protein dynamics. *Biochim. Biophys. Acta BBA - Proteins Proteomics*. **1814**, 942–968
167. Chao, F.-A., and Byrd, R. A. (2020) Protein Dynamics revealed by NMR Relaxation Methods. *Emerg. Top. Life Sci.* **2**, 93–105
168. Gáspári, Z., and Perczel, A. (2010) Chapter 2 - Protein Dynamics as Reported by NMR. in *Annual Reports on NMR Spectroscopy* (Webb, G. A. ed), pp. 35–75, Academic Press, **71**, 35–75
169. Lipari, G., and Szabo, A. (1982) Model-free approach to the interpretation of nuclear magnetic resonance relaxation in macromolecules. 1. Theory and range of validity. *J. Am. Chem. Soc.* **104**, 4546–4559
170. Clore, G. M., Szabo, A., Bax, A., Kay, L. E., Driscoll, P. C., and Gronenborn, A. M. (1990) Deviations from the simple two-parameter model-free approach to the interpretation of nitrogen-15 nuclear magnetic relaxation of proteins. *J. Am. Chem. Soc.* **112**, 4989–4991
171. Franken, L. E., Grünewald, K., Boekema, E. J., and Stuart, M. C. A. (2020) A Technical Introduction to Transmission Electron Microscopy for Soft-Matter: Imaging, Possibilities, Choices, and Technical Developments. *Small*. **16**, 1906198
172. Williams, D. B., and Carter, C. B. (2013) *Transmission Electron Microscopy: A Textbook for Materials Science*, Springer Science & Business Media
173. Luo, Z. (2015) *A Practical Guide to Transmission Electron Microscopy: Fundamentals*, Momentum Press
174. Spence, J. C. H. (2009) *High-Resolution Electron Microscopy*, Oxford University Press
175. Ayache, J., Beaunier, L., Boumendil, J., Ehret, G., and Laub, D. (2010) *Sample Preparation Handbook for Transmission Electron Microscopy: Methodology*, Springer Science & Business Media
176. Stetefeld, J., McKenna, S. A., and Patel, T. R. (2016) Dynamic light scattering: a practical guide and applications in biomedical sciences. *Biophys. Rev.* **8**, 409–427
177. Pereira, A. S., Tavares, P., and Limão-Vieira, P. (2020) *Radiation in Bioanalysis: Spectroscopic Techniques and Theoretical Methods*, Springer International Publishing
178. Li, Y., Lubchenko, V., and Vekilov, P. G. (2011) The use of dynamic light scattering and brownian microscopy to characterize protein aggregation. *Rev. Sci. Instrum.* **82**, 053106